Adjoint-Based Sensitivity and Optimization of Turbulent Reacting Flows

by

Ali Kord

A dissertation submitted in partial fulfillment
of the requirements for the degree of
Doctor of Philosophy
(Mechanical Engineering)
in The University of Michigan
2022

Doctoral Committee:

Assistant Professor Jesse Capecelatro, Chair
Associate Professor Karthik Duraisamy
Associate Professor Eric Johnsen
Professor Venkat Raman

Ali Kord
akord@umich.edu
ORCID iD: 0000-0002-6355-708X

To my mother and wife.

ACKNOWLEDGMENTS

There is an old Persian poem that says: "*This book ends, but the story remains*." Although I summarized major achievements of my Ph.D. career in this *book* (i.e., the dissertation), the *story* that never ends is my gratitude to those who supported me during this journey.

First, I want to thank my advisor, Prof. Jesse Capecelatro, for allowing me to join his research team. He assisted me in pursuit of my degree and was also available whenever I needed his feedback. I always say that the most valuable skills that I have learned from him are critical thinking, presentation, and scientific manuscript writing, which cannot be obtained from other textbooks or classes. This dissertation would not have existed without his continued support.

Next, I want to thank my committee members, Professor Karthik Duraisamy, Professor Eric Johnsen, and Professor Venkat Raman, for their thoughtful comments to improve my dissertation. Also, I am grateful for the opportunity to collaborate with Prof. Cheng Huang, Dr. David Buchta, and Dr. Seung Whan Chung, which resulted in the advancements of this work.

To my lab-siblings, Yuan Yao, Mehdi Khalloufi, Sarah Beetham, Greg Shallcross, Pedram Pakseresht, Aaron Lattanzi, Meet Patel, Archana Sridhar, John (Jack) Wakefield, Max Herzog, Rebecca Grawe, Connor Boerman, thank you for being a source of support in this journey. I value the time that we spent laughing, thinking,

and learning together.

Next, I want to express my gratitude to my mother for her constant support in my life. She encouraged me to apply for a Ph.D. program in the USA and broaden my professional experience. Unfortunately, I didn't have many chances to see her in person and give her my regards during my Ph.D. program, but she always sent me her best wishes from thousands of miles away. My brother also cared a lot for me, especially after my father passed away, and always assisted me in my life decisions or school work even though he was busy. I would also like to thank my family-in-law. The gatherings and the time we spent together provided me with a break from the stresses of the program, and I was fortunate to have their support when the workload became heavy.

Finally, I want to give my kindest words to my beloved wife, Faezeh, who brought enthusiasm into my life and inspired me to put forth my best performance, and I am grateful for being with her during the last years of my Ph.D.

A portion of computing resources was provided by the National Science Foundation via grant 1531752 MRI: Acquisition of Conflux, A Novel Platform for Data-Driven Computational Physics (Technical Monitor: Ed Walker).

Finally, the computing resources and assistance provided by the staff of the Advanced Research Computing at the University of Michigan are greatly appreciated.

TABLE OF CONTENTS

LIST OF FIGURES

Figure

LIST OF TABLES

Table

LIST OF APPENDICES

Appendix

ABSTRACT

Turbulent reacting flows drive many energy conversion devices and play crucial roles in the power generation and transportation sectors. Due to their chaotic and multi-scale nature, predicting and optimizing such systems is challenging. Over the past several decades, direct numerical simulation (DNS) and large-eddy simulation (LES) have gained in popularity within the scientific and engineering community for simulating this class of flows. However, owing to their high computational cost, they have primarily been used to investigate micro-scale physics or develop sub-grid scale models. Meanwhile, optimizing new engineering systems or improving existing devices requires iterating upon many design/input parameters. A brute-force trial-and-error approach involves performing many simulations and is thus not practical even with modern computational resources. Current approaches typically reduce the complexity of the model, which compromises its fidelity and decreases dimensionality of the physical system.

Discrete adjoint-based methods provide exact sensitivity of a quantity of interest (QoI) to many input parameters with a tractable computational cost. The sensitivity gradient obtained from an adjoint solution provides a direction to adjust parameters for minimizing (i.e., improving) the QoI. However, computing discrete adjoint sensitivity from high-fidelity numerical simulations like DNS or LES is challenging. Modern numerical methods are typically developed for solving the original governing equations and are not necessarily consistent with the discrete adjoint formulation.

The objective of this dissertation is to develop a high-fidelity numerical framework that provides exact sensitivity of a QoI for turbulent reacting flows. This builds off state-

of-the-art numerical discretization methods and extends them to be compatible with a discrete adjoint solver. The adjoint sensitivity is combined with gradient-based optimization techniques to find optimal parameters. The numerical framework solves the multi-component compressible Navier–Stokes equations using high-order narrow-stencil finite difference operators that satisfy the summation-by-parts (SBP) property. Simultaneous-approximation-term boundary treatment is used to enforce the boundary conditions. A SBP adaptive artificial dissipation scheme with a compatible adjoint solver is introduced to minimize boundedness errors in the scalars and retain high-order accuracy of the solution. In addition, a flamelet/progress variable approach is employed for combustion modeling, and its adjoint is formulated. This approach avoids transporting many chemical species and makes the adjoint solver flexible with respect to the choice of chemical reactions. The adjoint solver makes use of an efficient check-pointing scheme, and it computes analytic Jacobians of the Navier–Stokes equations instead of automatically differentiating them. The cost of the combined forward-adjoint simulation is about 3–3.5 times the cost of the forward run.

The framework is applied to several challenging cases to assess its performance and demonstrate its efficacy in optimizing various QoIs. The methodology is used to enhance and suppress mixing and growth of high-resolution multi-mode Rayleigh–Taylor instabilities by strategically manipulating the interfacial perturbations. This example demonstrates the utility of the adjoint framework on chaotic variable-density flows before introducing complexities associated with chemical reactions and unboundedness of the mass fraction. Next, a momentum actuator is optimized to control the temporal evolution of scalar mixing in a shear layer, where more than one hundred million parameters are manipulated simultaneously by the adjoint solver. Using a coarse grid necessitates the adaptive dissipation scheme to preserve scalar boundedness. Finally, the adjoint solver is used to identify optimal forcing to control flame position in a non-premixed turbulent round jet.

CHAPTER 1

Introduction

1.1 Predicting turbulent reacting flows

Many engineering systems involve turbulent reacting flows, examples include industrial burners and furnaces; stationary gas turbine engines; and internal combustion and aircraft engines. Predicting the flow dynamics within these devices is challenging due to the complexities of turbulence, combustion, and their interactions.

Turbulent flows are characterized by chaotic, random, and unsteady behavior, and their kinetic energy is distributed among a broad spectrum of length and time scales. Large-scale eddies, whose sizes are constrained by the geometry of the device, are unstable and break down into smaller ones. This 'cascade' of energy ceases at the Kolmogorov length scale, where molecular viscosity eventually dissipates the kinetic energy associated with the eddies. According to Kolmogorov's hypothesis, these small-scale eddies are homogeneous and isotropic at sufficiently high Reynolds (Re) numbers. Re is defined as the ratio of inertia to dissipation forces, also distinguishing the ratio of the largest (l_0) to the smallest (η) length scales, given by (e.g., see Pope, 2000)

$$\mathrm{Re} \sim \left(\frac{l_0}{\eta}\right)^{4/3}, \tag{1.1}$$

where η denotes the Kolmogorov length scale.

Combustion typically involves many chemical species and reactions even with simple fuels such as hydrogen and methane (e.g., see Li *et al.*, 2004). The rate at which chemical species are

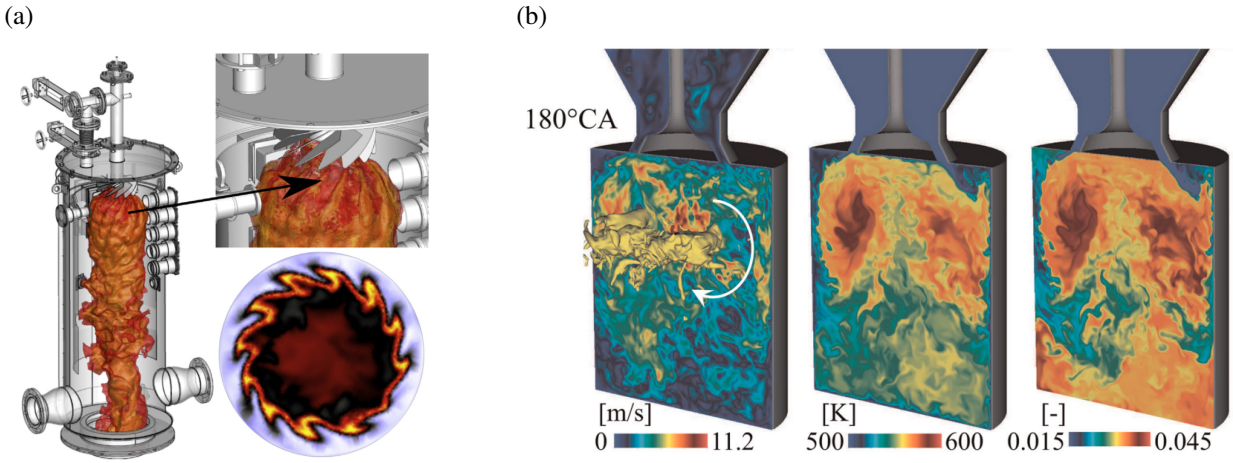

Figure 1.1: (*a*) Isosurfaces of the temperature (1700 K and 2000 K) and its contours in a medium size model of industrial gas turbine combustor via LES. Adapted from Tyliszczak *et al.* (2016). (*b*) From left to right: Distribution of velocity magnitude, temperature, and mass fraction of H_2O on vertical slices of an internal combustion engine model, using DNS. Adapted from Schmitt *et al.* (2016).

consumed or produced can vary by orders of magnitude. The chemical length scale associated with the flame thickness is typically smaller than the Kolmogorov length scale. The Karlovitz number denotes the ratio of a chemical length scale δ to the Kolmogorov length scale, given by

$$\mathrm{Ka} = \left(\frac{\delta}{\eta}\right)^2, \tag{1.2}$$

which is typically $\mathrm{Ka} < 1$.

Two-way coupling between turbulence and combustion further complicates the system dynamics. High kinetic energy and inertial forces associated with turbulent velocity fluctuations are able to either enhance fuel-oxygen mixing and increase the heat release rate or quench the flame (e.g., see Poinsot *et al.*, 1991). On the other hand, temperature variations associated with the released heat could change local molecular diffusion, altering the dissipation rate of turbulent fluctuations.

Recent advancements in numerical methods and growing computational resources have made high-fidelity simulations appealing for studying turbulent reacting flows. Over the past several decades, direct numerical simulation (DNS) and large-eddy simulation (LES) have become at-

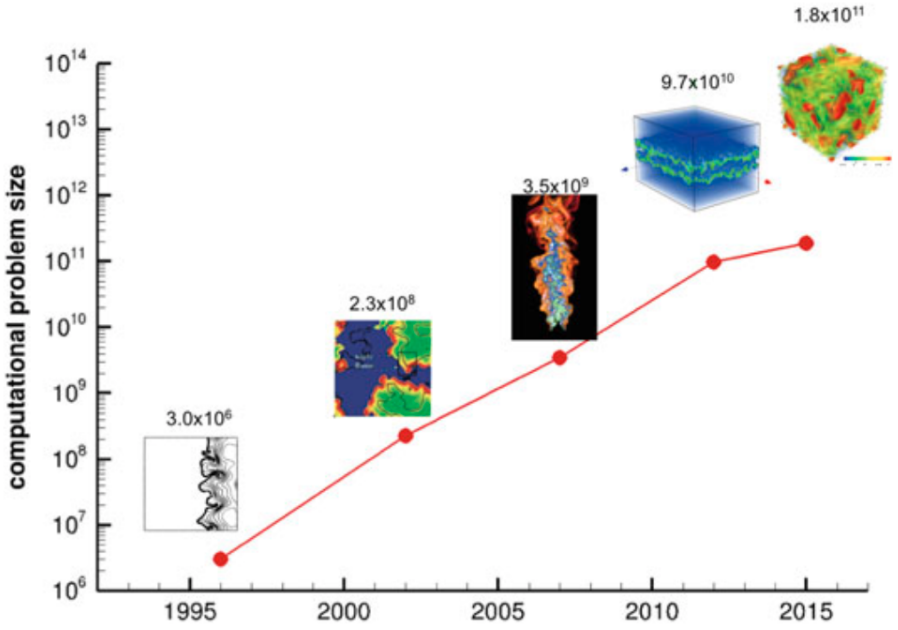

Figure 1.2: Historical trend of the growth of computational problem size and DNS of turbulent reacting flows by showing five representative examples. Adapted from Kolla & Chen (2018).

tractive among the scientific and engineering community. DNS solves the governing conservation equations, i.e., the reacting Navier–Stokes equations, without any assumption on turbulence. Thus, the computational grid must be able to resolve all scales of turbulence and combustion. The computational cost of DNS of an unsteady three-dimensional non-reacting and reacting turbulent simulations are $O\left(\mathrm{Re}^3\right)$ and $O\left(\mathrm{Re}^3/\mathrm{Ka}^2\right)$, respectively, according to (1.1) and (1.2). On the other hand, LES captures large eddies by solving the filtered Navier–Stokes equations and models sub-grid scale fluctuations.

Both DNS and LES have been used for simulating non-reacting and reacting turbulent flows within engineering systems (see Fig. 1.1). Figure 1.1a shows an LES study performed on a medium size model of an industrial gas turbine combustor (Tyliszczak *et al.*, 2016). This figure demonstrates a variety of length scales and the unsteady behavior of a swirling turbulent flame in an engineering device, which cannot be obtained by low-fidelity simulations. Figure 1.1b shows instantaneous snapshots of flow quantities obtained from DNS of an internal combustion engine model (Schmitt *et al.*, 2016). This figure reveals crucial flow features that was captured by DNS,

i.e., mixing, randomness, and the multi-scale nature of the turbulence. However, due to the high computational cost of DNS and LES, they have mainly been employed to investigate micro-scale physics or develop new sub-grid scale models (see Fig. 1.2).

1.2 Beyond prediction of turbulent reacting flows

As described above, turbulent reacting flows play crucial roles in many energy conversion devices involved in the power generation and transportation sectors. Because of economic, public health, and environmental concerns, reducing fuel consumption and pollutant emission from these devices have historically been a crucial target. Despite new advancements in technologies that employ renewable resources for electricity generation and transportation fuels, it is still expected that petroleum and natural gas will remain the most-consumed fuels in the U.S. over the upcoming decades (see Fig. 1.3a). This is anticipated to result in a large increase in carbon dioxide and other pollutant emissions in the environment (see Fig. 1.3b), which has negative impacts on public health and the environment. Thus, it is necessary to improve engineering systems involving turbulent reacting flows by decreasing fuel consumption and reducing pollutant emission, just to cite a few examples.

Despite decades of research focused on this class of flows (e.g., see Peters, 2000; Poinsot & Veynante, 2005; Pitsch, 2006, and references therein), improvements of relevant engineering applications remain challenging due to the chaotic behavior of turbulent flows, nonlinear and multi-scale nature of turbulent combustion, and nonlinear response of system outputs to inputs, as discussed in the previous section. Improving designs (e.g., increasing efficiency or mitigating negative effects associated with pollutants) and measuring sensitivity of quantities of interest to design parameters remain challenging and impractical via a trial-and-error approach. This is associated with high computational cost (see Fig. 1.2) and a large number of input/design/control parameters that influence quantities of interest. Existing approaches typically compromise model fidelity and/or reduce dimensionality of the physical system (e.g., via Reynolds-averaged Navier–Stakes, RANS,

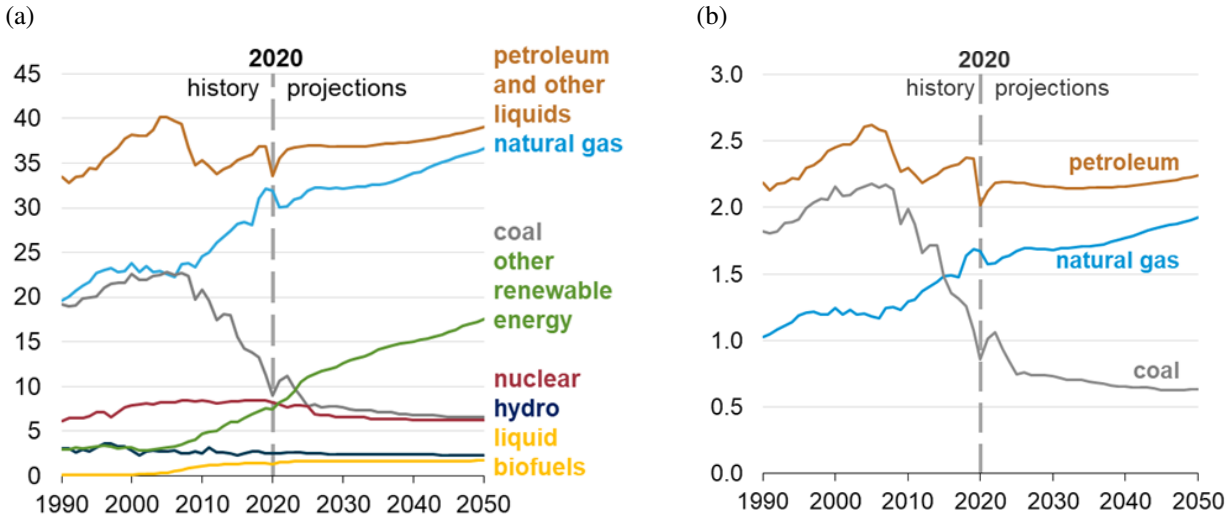

Figure 1.3: (*a*) Energy consumption (in quadrillion British thermal units) and (*b*) energy-related carbon dioxide emissions (billion metric tons) by fuel over the past three decades with future predictions. Adapted from U.S. Energy Information Administration, Annual Energy Outlook 2021.

equations). However, low-fidelity simulations cannot sufficiently capture small-scale physics that significantly contributes to flow and flame dynamics.

1.3 Adjoint-based optimization

In recent years, adjoint-based methods have emerged as a powerful technique to measure parametric sensitivity. These methods provide sensitivity of a quantity of interest (QoI) to a large number of design parameters with a computational cost comparable to the cost of the primal simulation that predicts the flow. Combining adjoint-based methods with gradient-based optimization techniques results in a scalable solution for 'improving' engineering systems dealing with turbulent reacting flows without compromising model fidelity. Adjoint-based sensitivity is computed via two different approaches: continuous and discrete adjoint formulation.

In continuous adjoint methods, the adjoint equations are first derived via linearizing the partial differential equations (PDEs) governing the system (also called the primal equations). Adjoint solutions are then obtained via discretizing and solving the corresponding adjoint PDEs. However, the sensitivity obtained from the adjoint solution can be susceptible to spatial and temporal trun-

cation errors that are known to become significant in unsteady or chaotic flows (Lea *et al.*, 2000; Nadarajah & Jameson, 2000; Vishnampet *et al.*, 2015). Discrete adjoint methods address this by taking into account the numerical discretization prior to perturbing and linearizing the flow equations, which provides sensitivity that is exact up to machine-precision roundoff errors (Nadarajah & Jameson, 2001). Because of the exact sensitivity, discrete adjoint methods are more effective in optimizing chaotic flows compared to its continuous counterpart (e.g., see Vishnampet *et al.*, 2015).

Adjoint methods have successfully been employed in many fluid dynamic application, including shape optimization and drag reduction for aerostructures (Jameson, 1989; Jameson & Martinelli, 2000; Martins *et al.*, 2004), aeroacoustic control of free shear flows (Wei & Freund, 2006; Vishnampet *et al.*, 2015), scalar mixing (Vikhansky, 2002; Liu, 2006; Thiffeault, 2012; Foures *et al.*, 2014b; Miles, 2018; Vermach & Caulfield, 2018), and variable-density instabilities (Lopez-Zazueta *et al.*, 2016; Kord & Capecelatro, 2019).

Only recently have adjoint methods been applied to reactive flows. For instance, adjoint methods were effective in computing sensitivity of the parameters appearing in combustion models, which has been studied in one- and two-dimensional laminar configurations (Braman *et al.*, 2015; Hassan *et al.*, 2021). Adjoint sensitivity can also be employed to find optimal control parameters in reacting flows. This has been done in one- and two-dimensional laminar flame configurations, where the numerical solutions obtained by solving compressible Navier–Stokes equations with single-step chemistry are compared with a desired/trusted solution, e.g., experimental investigations, and the adjoint gradient is then used to reduce this discrepancy by either manipulating chemistry and diffusion parameters (Gray *et al.*, 2017) or an external source term (Lemke *et al.*, 2014). In another work, gradient-based optimization combined with discrete adjoint sensitivity was able to enhance ignition in steady and unsteady laminar non-premixed jets, where the Navier–Stokes equations in an axisymmetric coordinate are solved with a simple one-step reaction (Qadri *et al.*, 2021). Capecelatro *et al.* (2016) used discrete-adjoint sensitivity to control ignition in a two-dimensional hydrogen-air mixing layer, where the compressible Navier–Stokes equations are

solved with a single-step chemistry model. Adjoint-based methods have been also used for hydrodynamic stability analysis of a lifted flame in a laminar reacting jet (Qadri *et al.*, 2015) and frequency response analysis of premixed (Skene & Schmid, 2019) and diffusion flames (Sayadi & Schmid, 2021), all of them used a single-step chemistry model. Also, risk assessment of scramjet unstart via an inviscid flow solver with a simple heat-release model is studied using discrete adjoint schemes (Wang *et al.*, 2012).

Only a few studies have applied adjoint methods for turbulent reacting flows. In one study, the discrete adjoint-based method was used for uncertainty quantification and adaptive mesh-refinement in low-fidelity turbulent flows (i.e., RANS) with combustion modeling of a flamelet/progress variable approach (Duraisamy & Alonso, 2012). Also, Capecelatro *et al.* (2017, 2018) employed discrete adjoint sensitivity and optimization for improving localized ignition applied on a non-premixed turbulent flame, using DNS and one-step chemistry.

However, to date, discrete-adjoint methods of high-fidelity reacting flow solvers with detailed chemistry are non-existent. Indeed, most of the aforementioned studies have been employed simple one-step chemistry even for laminar reacting flows. Deriving an adjoint-based formalism from a high-fidelity numerical framework combined with advanced combustion models is still challenging due to the chaotic and nonlinear behaviors of the flow and complexities associated with the adjoint-based formulation. In the following section, these challenges are reviewed.

1.4 Challenges of employing adjoint methods to turbulent reacting flows

1.4.1 Adjoint compatible flow solver

Despite huge progress in state-of-the-art numerical schemes for predicting turbulent reacting flows, most existing approaches are not necessarily compatible with the discrete adjoint formulation. As mentioned before, discrete adjoint sensitivity is obtained via linearizing the variations of dis-

cretized governing equations with respect to the state variables. However, most existing models designed for turbulent reacting flows (e.g., subgrid-scale turbulence closures, flux discretization schemes, shock capturing) are typically developed for solving the primal equations governing the flow and may not be differentiable. For instance, a low-order upwinding scheme is able to handle numerical discontinuities such as shocks. However, its operator coefficients locally vary from one grid point to another depending on the flow direction. This makes it a non-differentiable technique with respect to flow variables. This issue becomes more pronounced when advanced shock-capturing techniques such as weighted essentially non-oscillatory (WENO) methods are considered.

Even turbulent reacting flows in low Mach number regimes can involve discontinuities. Turbulent fluctuations enhance mixing of species and generate high gradients in their mass fractions. Also, enhancement in fuel-air mixing results in localized released heat that generates sharp gradients in temperature. Thus, the flame thickness could vary within few grid points. It is necessary to avoid spurious oscillations leading to non-physical overshoots and undershoots on flow variables. Developing a robust and high-order accurate technique for this purpose with an efficient and compatible adjoint solver is thus required.

A high-order numerical framework with a discrete adjoint solver was recently developed for compressible non-reacting (Vishnampet, 2015) and reacting (Capecelatro *et al.*, 2018) turbulent flows. It employs high-order centered finite difference operators satisfying the summation-by-parts (SBP) property (Kreiss & Scherer, 1974; Strand, 1994) combined with simultaneous-approximation-term (SAT) boundary treatments (Carpenter *et al.*, 1994; Svärd *et al.*, 2007; Svärd & Nordström, 2008). Combined SBP-SAT schemes provide an energy stable numerical framework (e.g., see Fernández *et al.*, 2014, and references therein). In addition, their discrete adjoint formulation can be 'consistent' with their continuous counterpart since the SBP property is the discrete version of integrating by parts that is employed in formulating continuous adjoint equations. Such 'consistency' between continuous and discrete adjoint solvers, also called dual-consistency, mitigate spurious numerical waves observed in discrete adjoint solutions (e.g., see Hicken & Zingg,

2014; Vishnampet, 2015). In addition, dual consistent SBP-SAT schemes yield 'superconvergence' in computing the QoI (Hicken & Zingg, 2011). These properties make the combined SBP-SAT formalism a natural framework for computing adjoint-based sensitivity. Adjoint sensitivity derived from a SBP-SAT numerical framework has shown great success in controlling different flow configurations if sufficient grid resolution is applied (e.g., see Vishnampet *et al.*, 2015; Kord & Capecelatro, 2019). However, this framework may not be able to effectively capture numerical discontinuities in under-resolved flow simulations.

High-order centered finite difference operators yield dispersion errors that generate spurious oscillations when the flow field is not sufficiently resolved. These oscillations can lead to excursion errors (i.e., unphysical overshoots and undershoots) in the flow state variables, including passive scalars. Many of these scalars have physical limits, e.g., the mass fraction of a chemical species must be bounded in $[0, 1]$. To suppress unresolved spurious modes, high-order artificial dissipation operators that preserve stability and accuracy of SBP schemes were introduced by Mattsson *et al.* (2004), and their dual consistency was also verified by Hicken & Zingg (2014). However, these schemes are not effective at absorbing spurious oscillations in regions with sharp gradients. Although high-order dissipation operators of Mattsson *et al.* (2004) were extended and improved to handle sharp gradients and discontinuities (e.g., see Svärd & Mishra, 2009; Craig P. & Zingg, 2018; Ranocha *et al.*, 2018), these approaches are not readily usable in an adjoint solver.

To the best of our knowledge, a straightforward, robust, and high-fidelity numerical framework based on SBP operators with a dual consistent adjoint formulation for turbulent reacting flows does not exist. The numerical scheme must be able to effectively capture discontinuities in under-resolved flow simulations or ensure their realizability constraints such as scalar boundedness. Moreover, the numerical scheme should retain high-order accuracy of predictive simulations.

1.4.2 Combustion modeling and its adjoint formulation

Accounting for detailed chemistry typically requires tracking many reactions and transporting a large number of chemical species. For instance, Li *et al.* (2004) has provided detailed mechanism

of H_2-O_2 reaction, i.e., the simplest combustion mechanism, which involves at least nine chemical species. This becomes more sophisticated for hydrocarbon fuels. In addition, changing the chemistry in the primal equations requires reformulating, implementing, and verifying its adjoint solver, which is a tedious task. Although automatic differentiation techniques can be used to address this issue, they typically increase the computation cost. As mentioned in the previous section, it is typical to employ simple chemistry models in predicting laminar and turbulent flames when adjoint sensitivity is computed.

Flamelet approaches address this by mapping the chemical kinetics into a pre-calculated lookup table (e.g., see Peters, 1984, 1986; Cook *et al.*, 1997; Pitsch *et al.*, 1998; Pitsch & Steiner, 2000; Pitsch, 2000; Pierce & Moin, 2004). Altering the chemical reaction, thus, requires updating the lookup table only, and the flow and adjoint equations remain unchanged. Flamelet/progress variable (FPV) approaches (Pierce, 2001; Pierce & Moin, 2004) have gained in popularity within the combustion community over the past two decades. The FPV approach is formulated by transporting two or three additional scalars (as opposed to each chemical species): a mixture fraction representing the degree of mixing between the fuel and oxidizer; and a progress variable accounting for the progress of the chemical reaction. The state quantities associated with the chemical reaction are precomputed and tabulated as a function of the mixture fraction and the progress variable (and their statistics if required), and their values are interpolated from a lookup table.

Although FPV approaches have shown great success in predicting flame dynamics or pollutant emissions such as soot and NOx in turbulent reacting flows (e.g., see Ihme & Pitsch, 2008a,b,c; Mueller & Pitsch, 2012; Saghafian *et al.*, 2015; Yang *et al.*, 2019), their adjoint counterpart has only been used in limited studies (see Duraisamy & Alonso, 2012). In FPV approaches, thermochemical quantities are interpolated from the lookup table, and linear interpolation is commonly used as an efficient and straightforward estimation. As mentioned before, adjoint equations are obtained by computing variations of the primal equations to flow variables. However, linear interpolation provides a piecewise continuous function that its derivatives do not smoothly change. To address this issue, high-order interpolation methods such as B-spline interpolation can be considered in the

flamelet approach (Bode *et al.*, 2019). However, they increase the computational cost since their interpolation algorithm performs more arithmetic operations.

1.4.3 Chaos and divergence of adjoint sensitivity

Previous studies have confirmed that adjoint sensitivity in chaotic dynamical systems can exponentially diverge when their equations are integrated over a long-time horizon (e.g., see Lea *et al.*, 2000; Wang & Gao, 2013). This is a well-known limitation of adjoint methods and other approaches that compute sensitivity in turbulent flows or other chaotic dynamical systems. The divergence of adjoint sensitivity is associated with the amplification of roundoff errors by chaos. These errors are generated due to operating finite-precision floating-point arithmetic, and they cannot be prohibited even by using a discrete adjoint formulation. However, it is shown that the adjoint formulation can be successfully employed when adjoint equations are integrated over finite- but not long-time intervals (e.g., see Wang, 2013; Kord & Capecelatro, 2019). Different techniques have been introduced to enable adjoint sensitivity over long time horizons, including ensemble-averaging of adjoint sensitivities (e.g., see Lea *et al.*, 2000, 2002; Eyink *et al.*, 2004), Lyapunov eigenvector decomposition (Wang, 2013), least squares shadowing (e.g., see Wang *et al.*, 2014; Blonigan, 2017; Ni & Talnikar, 2019), and the approaches developed based on the probability distribution function (PDF) (Thuburn, 2005). The least squares shadowing approach has also been tested in turbulent flows (e.g., see Blonigan, 2017; Ni & Talnikar, 2019). Although these approaches can increase the accuracy of adjoint sensitivity in chaotic systems, they tend to increase the computational cost (Thuburn, 2005; Wang, 2013; Wang *et al.*, 2014; Blonigan, 2017), and they may not provide exact sensitivity (Lea *et al.*, 2000, 2002) or slowly converge to it (Eyink *et al.*, 2004).

Only limited work has been introduced to improve optimization procedures of chaotic dynamical systems with adjoint-based methods. Recently, Chung & Freund (2021) introduced a multi-step penalty method for addressing the non-convexity of QoIs caused by the chaos. They addressed this issue by breaking the time domain into multiple shorter intervals. This method, combined

with adjoint sensitivity, was successfully tested in a series of problems, including the Kolmogorov turbulent flow. This method showed better performance compared to standard gradient search techniques. However, to date, a computationally efficient approach to make use of adjoint sensitivity in turbulent flows over long time horizons for general flow configurations remains an outstanding challenge.

1.5 Objectives of the dissertation

The main objective of this dissertation is to develop a high-order numerical framework capable of providing sensitivity from high-fidelity simulations of turbulent reacting flows. The aim is to combine the sensitivity gradient obtained from the adjoint solution with gradient-based optimization techniques to provide a means of minimizing/maximizing a well-defined QoI. We demonstrate its utility on a series of challenging problems dealing with flow instabilities, combustion, and turbulence. Throughout this dissertation, we make use of and extend state-of-the-art numerical methods developed for DNS and LES of turbulent reacting flows in a manner that is compatible with a discrete adjoint formulation. The specific objectives of this dissertation include:

(i) Compute exact sensitivity using discrete-adjoint methods and apply it to gradient-based optimization techniques to find optimal quantities of interest associated with high-fidelity simulations of turbulent combustion.

(ii) Formulate the discrete-adjoint method to be compatible with the state-of-the-art numerical schemes and models without compromising flow solver properties (i.e., stability, high-order accuracy, robustness, and scalar boundedness).

(iii) Develop a flexible flow-adjoint solver for different chemical mechanisms using the flamelet/progress variable approach.

(iv) Demonstrate capabilities of the developed adjoint-based framework via a variety of challenging flow problems, including variable-density instabilities, scalar mixing, and turbulent

combustion.

1.6 Organization of the dissertation

This dissertation includes seven chapters. Its material is reorganized from journal publications and conference presentations that are either in print or have been submitted. The rest of this dissertation is organized as follows.

Chapter 2 (Kord & Capecelatro, 2019, 2021, 2022) introduces a high-order numerical framework with its adjoint formulation developed for turbulent reacting flows. This chapter provides governing equations of reacting flows and briefly describes the high-order spatial and temporal discretization schemes and their adjoint counterpart. A flamelet/progress variable approach and its adjoint formulation is also presented in this chapter. Finally, details on the optimization algorithms that make use of the sensitivity gradient obtained from the adjoint solution are provided.

An adaptive artificial dissipation technique is presented in Chapter 3 (Kord & Capecelatro, 2021, 2022) as an effective and efficient approach to preserve scalar boundedness. This chapter starts with an overview of standard first derivative and dissipation operators that satisfy the summation-by-parts property. The order of accuracy of the dissipation operator and its effectiveness in absorbing energy from different modes of the solution are studied. We leverage this property by locally adjusting the order of accuracy of the dissipation operator in regions of overshoots and undershoots to reduce boundedness errors. The corresponding adjoint formulation is also derived and provided. The accuracy and effectiveness in preserving scalar boundedness are assessed with a series of numerical tests. Their adjoint formulation combined with a gradient-based optimization technique is also tested.

Chapter 4 (Kord & Capecelatro, 2019) employs the adjoint-based optimization solver on high-resolution multi-mode Rayleigh–Taylor (RT) instabilities to perform sensitivity analysis and optimization of unsteady multi-component flows. These flow instabilities isolate the effects of chaos and turbulent mixing before introducing complexities associated with combustion. Different quan-

tities of interest are presented to measure mixing and growth, and their adjoint sensitivity to interfacial perturbation modes is studied at different RT regimes, which target the most unstable interfacial modes. Finally, the adjoint-based framework combined with a gradient-based optimization solver is used to suppress and enhance multi-mode RT instabilities.

Chapters 5 and 6 (Kord & Capecelatro, 2022) demonstrate the efficacy of the adjoint-based solver in finding optimal space-time fields that contain a massive number of control parameters. A solenoidal momentum actuator is applied to a free shear flow to control scalar mixing evolution in Chapter 5. A diffusion H_2-air flame in a three-dimensional turbulent reacting jet is also studied in Chapter 6, and its combustion is modeled by the flamelet/progress variable approach. An optimal external acoustic forcing is manipulated in space and time via the adjoint sensitivity to control the flame lift-off position. The adaptive dissipation scheme is employed to preserve scalar boundedness in both chapters.

Finally, Chapter 7 summarizes the major achievements and contributions of this dissertation and provides an outlook on the future of controlling turbulent reacting flows using high-fidelity simulations.

CHAPTER 2

Adjoint-Based Optimization Framework

2.1 Quantity of interest

Numerical simulations provide a quantity of interest (QoI), denoted by $\mathcal{J}$, that depends on the flow solution $\vec{Q}$ (density, momentum, energy, and species mass fractions for multi-component flows) and a set of design/control parameters $\vec{f}$ (e.g., external body forces, boundary conditions) within the simulation domain $\mathbb{D}$ and time horizon $[t_0, t_f]$. The QoI (also referred to as the objective function interchangeably throughout this dissertation) is given by

$$\mathcal{J}(\vec{Q}[\vec{f}], \vec{f}) = \int_{t_0}^{t_f} \int_{\mathbb{D}} \mathcal{I}(\vec{Q}, \vec{f}) \mathcal{W}_{\text{Tar}}(\boldsymbol{x}, t) \, \mathrm{d}\boldsymbol{x} \, \mathrm{d}t, \tag{2.1}$$

where the integrand $\mathcal{I}$ denotes the local temporal value of QoI provided by a high-fidelity simulation that solves the governing equations (see Chapters 2.2 and 2.3). The weighting function $\mathcal{W}_{\text{Tar}}(\boldsymbol{x})$ specifies a region of interest within $\mathbb{D}$. The choice of $\mathcal{I}$ in (2.1) is critical for measuring the QoI, and it has to be defined carefully depending on the goal of each optimization problem.

Different QoIs have been employed in the previous studies. For instance, pressure or velocity distributions over a body (such as an airfoil) or their drag and lift coefficients are widely considered as a QoI for shape optimization and drag reduction of aerostructures (Jameson & Martinelli, 2000; Martins *et al.*, 2004). Quantifying mixing is also desired for different applications such as those that involve combustion. Mathew *et al.* (2005) proposed the so-called mix-norm to measure the

degree of mixing of an advected scalar, which is effective for targeting small-scale variations in chaotic flows. Minimizing the mix-norm has also been considered as a practical approach for enhancing mixing (e.g., see Mathew *et al.*, 2007; Foures *et al.*, 2014b; Vermach & Caulfield, 2018). Heat release and temperature distribution have also been considered as a QoI to optimize ignition location and timing in reacting flows (e.g., see Capecelatro *et al.*, 2018; Qadri *et al.*, 2021). Data-driven techniques such as machine learning and data assimilation define a QoI as the discrepancy between a numerical solution and trusted data (i.e., from experiments or high-fidelity solutions), and minimizing such a QoI is performed for developing new numerical models or adapting some model parameters (e.g., see Gray *et al.*, 2017; Singh *et al.*, 2017).

The vector $\vec{f}$ contains a set of parameters associated with an 'actuator' or a controller, by which the flow and eventually the value of $\mathcal{J}$ is modified. Several types of actuators have been imposed in non-reacting and reacting flows (e.g., see Kral, 2000; Cattafesta III & Sheplak, 2011, and references therein). A reacting flow can be controlled passively (i.e., without an external source of energy), where the geometry of a combustion chamber is modified, or external obstacles such as swirlers and bluff-bodies are placed within the flow field (Schadow & Gutmark, 1992) to enhance fuel-oxidizer mixing and stabilize the flame. An external source of energy can also be applied to change the flame dynamics, and its location and timing are strategically manipulated to achieve the desired flame behavior. For instance, combustion instabilities are controlled by acoustic forcing that can be applied via loudspeakers located upstream of nozzle exits (e.g., see McManus *et al.*, 1993; Baillot & Demare, 2002; Dowling & Morgans, 2005; Baillot & Demare, 2007, and references therein). Acoustic forcing has been applied on lifted flames to control their stability (Chao *et al.*, 2002; Abdurakipov *et al.*, 2013), reduce emissions (Chao *et al.*, 1996), avoid anchoring the flame (Demare & Baillot, 2004), and modify flame shapes (Kozlov *et al.*, 2013).

2.2 Governing equations

The objective of this dissertation is to develop an approach capable of measuring sensitivity in high-fidelity simulations of turbulent reacting flows. To this end, this work is built upon the multi-component compressible Navier–Stokes equations, written compactly as

$$\vec{\mathcal{N}}(\vec{Q}) = \frac{\partial \vec{Q}}{\partial t} + \frac{\partial}{\partial x_i}\left(\vec{F}_i^I - \vec{F}_i^V\right) - \vec{S} = 0, \tag{2.2}$$

where $\vec{Q} = [\rho,\ \rho\boldsymbol{u},\ \rho E,\ \rho Y_1,\ \ldots,\ \rho Y_{N-1}]^\mathsf{T}$ is the vector of conserved variables that contains density ρ, velocity vector $\boldsymbol{u} = [u_1,\ u_2,\ u_3]^\mathsf{T}$, total energy E, and mass fraction Y_n for $n = 1, ..., N$ with N number of chemical species. To ensure global mass conservation, Y_N does not appear in $\vec{Q}$, and instead is computed according to $Y_N = 1 - \sum_{n=1}^{N-1} Y_n$.

The inviscid flux $\vec{F}_i^I$, viscous flux $\vec{F}_i^V$, and volumetric source term $\vec{S}$ are given in non-dimensional form by

$$\vec{F}_i^I = \begin{bmatrix} \rho u_i \\ \rho u_1 u_i + p\delta_{i1} \\ \rho u_2 u_i + p\delta_{i2} \\ \rho u_3 u_i + p\delta_{i3} \\ u_i(\rho E + p) \\ \rho Y_1 u_i \\ \vdots \\ \rho Y_{N-1} u_i \end{bmatrix}, \quad \vec{F}_i^V = \begin{bmatrix} 0 \\ \tau_{1i} \\ \tau_{2i} \\ \tau_{3i} \\ u_j\tau_{ij} - q_i \\ -f_{1,i}^V \\ \vdots \\ -f_{N-1,i}^V \end{bmatrix}, \quad \vec{S} = \begin{bmatrix} 0 \\ 0 \\ -\rho/\mathrm{Fr}_c \\ 0 \\ -\rho u_2/\mathrm{Fr}_c \\ \dot{\omega}_1 \\ \vdots \\ \dot{\omega}_{N-1} \end{bmatrix}, \tag{2.3}$$

respectively. Non-dimensional pressure p is obtained from the total energy E, according to

$$p = (\gamma - 1)\rho\left(E - \frac{1}{2}u_i u_i + \frac{T_f^0}{W} - \sum_{n=1}^{N} \Delta h_{f,n}^0 Y_n\right), \tag{2.4}$$

where γ is the ratio of specific heats, Y_n is the mass fraction of species n with mass enthalpy of

formation $\Delta h^0_{f,n}$ at temperature T^0_f and molecular weight W_n, for $n = 1, \ldots, N$, and the mixture molecular weight W is given by

$$\frac{1}{W} = \sum_{n=1}^{N} \frac{Y_n}{W_n}. \tag{2.5}$$

The viscous stress tensor τ_{ij} is given in non-dimensional form as

$$\tau_{ij} = \frac{\mu}{\mathrm{Re}_c}\left(\frac{\partial u_i}{\partial x_j} + \frac{\partial u_j}{\partial x_i}\right) + \frac{\lambda}{\mathrm{Re}_c}\frac{\partial u_k}{\partial x_k}\delta_{ij}, \tag{2.6}$$

where $\mathrm{Re}_c = \mathrm{Re}/\mathrm{Ma}$ with the Mach number $\mathrm{Ma} = u^\star_\infty / c^\star_\infty$ and Reynolds number $\mathrm{Re} = \rho^\star_\infty u^\star_\infty L^\star_\infty / \mu^\star_\infty$. The subscript ∞ denotes a reference value, and dimensional quantities are denoted via superscript $\star$ in this dissertation. $\rho^\star_\infty$, $u^\star_\infty$, $c^\star_\infty$, $L^\star_\infty$, and $\mu^\star_\infty$ are the reference density, velocity, speed of sound, length scale, and viscosity, respectively. μ and λ denote the first and second viscosities, respectively, related to each other by $\lambda = \mu_B - 2/3\mu$ with bulk viscosity μ_B. The first viscosity has a temperature dependence through power b according to

$$\mu = (T/T_\infty)^b \tag{2.7}$$

with reference temperature $T_\infty = 1/(\gamma - 1)$. The non-dimensional heat flux q_i and mass species flux $f^V_{n,i}$ are given by

$$q_i = -\frac{\mu}{\mathrm{Re}_c \, \mathrm{Pr}}\frac{\partial T}{\partial x_i} - \frac{\mu}{\mathrm{Re}_c}\sum_{n=1}^{N}\left(\frac{T - T^0_f}{W_n \mathrm{Sc}_n} + \frac{\Delta h^0_{f,n}}{\mathrm{Sc}_n}\right)\frac{\partial Y_n}{\partial x_i}, \tag{2.8}$$

and

$$f^V_{n,i} = -\frac{\mu}{\mathrm{Re}_c \mathrm{Sc}_n}\frac{\partial Y_n}{\partial x_i}, \quad \text{for } n = 1, 2, \ldots, N-1, \tag{2.9}$$

respectively, with the Prandtl number $\mathrm{Pr} = C^\star_{p,\infty}\mu^\star/\kappa^\star$ and Schmidt number $\mathrm{Sc}_n = \mu^\star/\rho^\star \mathcal{D}^\star_n$ for $n = 1, \ldots, N-1$. Here, $C^\star_{p,\infty}$ is the reference specific heat at constant pressure, and κ denotes the

thermal conductivity. $\mathcal{D}_n^\star$ is mass diffusivity of species n. Pr and Sc_n for $n = 1, \ldots, N-1$ remain constant through the entire domain. Temperature is given by the non-dimensional equation of state for a mixture of ideal gases, i.e.,

$$T = \frac{\gamma p W}{(\gamma - 1)\rho}. \tag{2.10}$$

Finally, the Froude number is $\mathrm{Fr}_c = {c_\infty^\star}^2/(g^\star L_\infty^\star)$ in (2.3) with gravity $g^\star$ acting in the negative x_2-direction, which accounts for buoyancy effects, and chemical reaction source terms are denoted by $\dot{\omega}_n$ for $n = 1, \ldots, N-1$.

2.3 Discretization of the governing equations

In the present work, physical coordinates $\mathbf{x} = (x_1, x_2, x_3)$ are transformed into computational space $\boldsymbol{\xi} = (\xi_1, \xi_2, \xi_3)$ by the Jacobian matrix $J = \det\left(\partial \xi_i / \partial x_j\right)$ and normalized metrics $\mathrm{M}_{ij} = J^{-1} \partial \xi_i / \partial x_j$. Thus, the governing equations (2.2) are rewritten in the computational space according to

$$\vec{\mathcal{N}}(\vec{Q}) = \frac{\partial \vec{Q}}{\partial t} + J \frac{\partial}{\partial \xi_i} \left[\mathrm{M}_{ij} \left(\vec{F}_j^I - \vec{F}_j^V \right) \right] - \vec{S} = 0. \tag{2.11}$$

Spatial derivatives appearing in the governing equations (2.11) and (2.6)–(2.9) are obtained via narrow-stencil finite difference operators that satisfy the summation-by-part (SBP) property (Kreiss & Scherer, 1974; Strand, 1994, see Chapter 3.2.1 for more details). Second and mixed derivatives are obtained by applying the first derivative consecutively. High-order SBP dissipation operators (Mattsson *et al.*, 2004; Vishnampet, 2015) are employed to damp spurious numerical waves that arise due to repeated first derivatives (see Chapter 3.2.2 for more details). The dissipation operators of Mattsson *et al.* (2004) are extended to preserve scalar boundedness $Y_n \in [0, 1]$ in Chapter 3. The flow equations are integrated in time using a standard fourth-order Runge–Kutta (RK4) scheme.

The SBP scheme is combined with the simultaneous-approximation-term (SAT) boundary

treatment to ensure provable stability (Carpenter *et al.*, 1994; Svärd *et al.*, 2007; Svärd & Nordström, 2008; Bodony, 2010; Vishnampet, 2015). Different boundary conditions including walls (impenetrable, isothermal, and adiabatic walls), inflows/outflows, and characteristic non-refracting far-field boundary conditions are available for different problems, where more details can be found in Vishnampet (2015), and a review of them is also provided in Appendix B with new treatments for imposing inflow and outflow conditions.

As discussed later, the SBP property will benefit the discrete-adjoint solver since it is equivalent to the integration-by-parts property that is employed in deriving the continuous-adjoint equation. The consistency between the continuous- and discrete adjoint solvers, also called dual consistency, mitigates spurious numerical waves generated in discrete adjoint methods (e.g., see Hicken & Zingg, 2014; Vishnampet, 2015). In addition, dual consistent SBP–SAT schemes yield 'superconvergence' in computing the QoI (Hicken & Zingg, 2011). This is favorable in cases where accuracy of a QoI is preferred instead of accuracy of flow state quantities, such as optimization problems.

2.4 Adjoint-based sensitivity approach

We seek the sensitivity of a QoI, $\mathcal{J}$, with respect to control parameters $\vec{f}$. The sensitivity can be used within a gradient-based optimization technique (see Chapter 2.6) to find values of $\vec{f}$ for 'improving' $\mathcal{J}$. Considering the variations of $\mathcal{J}$ with respect to $\vec{f}$, the sensitivity is given by the chain rule as (note that $\vec{Q}$ depends on $\vec{f}$)

$$\frac{\delta \mathcal{J}}{\delta \vec{f}} = \frac{\partial \mathcal{J}}{\partial \vec{Q}} \frac{\delta \vec{Q}}{\delta \vec{f}} + \frac{\partial \mathcal{J}}{\partial \vec{f}}, \tag{2.12}$$

where δ denotes small variations. A brute-force approach for evaluating $\delta\vec{Q}/\delta\vec{f}$ would require perturbing each control parameter individually and performing a new simulation for each to measure the change in flow solution $\delta\vec{Q}$. Thus, that would require N_f solutions of the time-dependent multicomponent Navier–Stokes equations, with N_f denoting the size of $\vec{f}$, resulting in a prohibitively large number of simulations when many control parameters are involved. An alternative, more

computationally efficient approach is to solve the corresponding adjoint equations by linearizing the perturbed flow equations. The adjoint solution yields the sensitivity of a desired QoI to a set of parameters with a cost independent of the number of parameters, as described in the following section.

2.4.1 Continuous adjoint formulation

In order to obtain the sensitivity gradient, we consider the Lagrangian $\mathcal{L}$ of $\mathcal{J}$ constrained by the governing equations $\vec{\mathcal{N}}$, given by

$$\mathcal{L}(\vec{Q}, \vec{f}, \vec{Q}^{\dagger}) = \mathcal{J}(\vec{Q}, \vec{f}) - \int_0^{t_f} \int_{\mathbb{D}} \vec{Q}^{\dagger\mathsf{T}} \vec{\mathcal{N}}(\vec{Q}, \vec{f}) \, \mathrm{d}\boldsymbol{x} \, \mathrm{d}t, \tag{2.13}$$

where $\vec{Q}^{\dagger} = \left[\rho^{\dagger}, \, \boldsymbol{u}^{\dagger}, \, E^{\dagger}, \, Y_1^{\dagger}, \, \ldots, \, Y_{N-1}^{\dagger}\right]^{\mathsf{T}}$ with $\boldsymbol{u}^{\dagger} = \begin{bmatrix} u_1^{\dagger} & u_2^{\dagger} & u_3^{\dagger} \end{bmatrix}^{\mathsf{T}}$ is the Lagrange multiplier, referred to here as the adjoint variable. Variations of $\mathcal{L}$ are expressed as

$$\delta\mathcal{L}(\vec{Q}, \vec{A}) = \delta\mathcal{J}(\vec{Q}, \vec{A}) - \int_0^{t_f} \int_{\mathbb{D}} \delta\vec{Q}^{\dagger\mathsf{T}} \vec{\mathcal{N}}(\vec{Q}, \vec{A}) \, \mathrm{d}\boldsymbol{x} \, \mathrm{d}t - \int_0^{t_f} \int_{\mathbb{D}} \vec{Q}^{\dagger\mathsf{T}} \delta\vec{\mathcal{N}}(\vec{Q}, \vec{A}) \, \mathrm{d}\boldsymbol{x} \, \mathrm{d}t. \tag{2.14}$$

The last two terms on the right-hand side of (2.14) are always zero according to (2.11), leading to $\delta\mathcal{L} = \delta\mathcal{J}$. Taking variations of $\delta\mathcal{J}$ and $\delta\vec{\mathcal{N}}$ and substituting them into (2.14) yields

$$\begin{aligned} \delta\mathcal{J} = &\int_0^{t_f} \int_{\mathbb{D}} \left[\left(\frac{\partial \mathcal{I}}{\partial \vec{Q}} \right)^{\mathsf{T}} \mathcal{W}_{\mathrm{Tar}} - \vec{Q}^{\dagger\mathsf{T}} \frac{\partial \vec{\mathcal{N}}}{\partial \vec{Q}} \right] \delta\vec{Q} \, \mathrm{d}\boldsymbol{x} \, \mathrm{d}t \\ &+ \int_0^{t_f} \int_{\mathbb{D}} \left[\left(\frac{\partial \mathcal{I}}{\partial \vec{f}} \right)^{\mathsf{T}} \mathcal{W}_{\mathrm{Tar}} - \vec{Q}^{\dagger\mathsf{T}} \frac{\partial \vec{\mathcal{N}}}{\partial \vec{f}} \right] \delta\vec{f} \, \mathrm{d}\boldsymbol{x} \, \mathrm{d}t. \end{aligned} \tag{2.15}$$

The adjoint variables $\vec{Q}^{\dagger}$ are chosen such that the first line of (2.15) vanishes, leading to the adjoint partial differential equations provided in Appendix A. Putting this together, the local temporal

sensitivity of $\mathcal{J}$ to $\vec{f}$ denoted by $\vec{g} = \delta\mathcal{J}/\delta\vec{f}$ is given by

$$\vec{g} = \frac{\partial \mathcal{I}}{\partial \vec{f}} \mathcal{W}_{\text{Tar}} - \left(\frac{\partial \vec{\mathcal{N}}}{\partial \vec{f}} \right)^{\mathsf{T}} \vec{Q}^{\dagger}, \tag{2.16}$$

and the total sensitivity is obtained via integrating $\vec{g}$ in space and time. Note that it is not required to repeat primal simulations for each parameter to compute adjoint sensitivity according to (2.16). Also, $\partial/\partial\vec{f}$ is not the total derivative, and thus, not computationally expensive as compared to $\delta\vec{Q}/\delta\vec{f}$ in (2.12). Thus, adjoint methods are powerful for computing sensitivity when a large number of parameters exist. The first-term on the right-hand side of (2.16) is typically zero since most QoIs do not explicitly depend on parameters $\vec{f}$. However, we keep it here for the sake of generality.

In this section, we derived the corresponding adjoint equation directly from the governing equations without taking into account the numerical discretization. Discretization of the adjoint PDEs need not be the same as the forward (or primal) equations. The sensitivity provided by the adjoint solution after discretizing (2.16) is known to induce truncation errors accumulated in $\vec{Q}^{\dagger}$ that may become significant in unsteady or chaotic flows (Nadarajah & Jameson, 2000; Carnarius *et al.*, 2010). Simulations of turbulent reacting flows are particularly sensitive to this since the numerical resolution is often close to the limits of the discretization. In addition, we have ignored spatial and temporal boundary conditions for adjoint equations in the this section. Obtaining these conditions for adjoint PDEs can be challenging when complicated boundary conditions are imposed in the primal simulation. These issues are addressed via the discrete adjoint formulation in the next section.

2.4.2 Discrete adjoint formulation

Adjoint-based sensitivity can also be obtained from the discretized primal PDEs with imposed boundary conditions (e.g., through SAT boundary treatments), which are a set of algebraic equations considered as primal equations. Transposing them into adjoint space leads to algebraic adjoint equations and sensitivity. Thus, discrete adjoint sensitivity is exact up to the machine precision

roundoff error, and employing discrete adjoint sensitivity instead of continuous one can accelerate the optimization process (e.g., see Vishnampet *et al.*, 2015).

In the discrete adjoint formulation, the governing equations are discretized prior to being perturbed and linearized. Here, $\boldsymbol{\mathcal{N}}(\vec{\mathcal{Q}})$ denote the discretized governing equations (2.11) , given by

$$\boldsymbol{\mathcal{N}}[\boldsymbol{\mathcal{Q}}, \vec{f}] \equiv \boldsymbol{D}_t \boldsymbol{\mathcal{Q}} - \boldsymbol{R}[\boldsymbol{\mathcal{Q}}, \vec{f}] \equiv 0, \tag{2.17}$$

where $\boldsymbol{\mathcal{Q}} = \left[\vec{\mathcal{Q}}^0, \vec{\mathcal{Q}}^{1,1}, \vec{\mathcal{Q}}^{1,2}, \ldots, \vec{\mathcal{Q}}^{N_t,3}, \vec{\mathcal{Q}}^{N_t,4}\right]^\mathsf{T}$ is the vector of space-time discrete conserved variables with N_t time steps. $\vec{\mathcal{Q}}^{n,s}$ for $n = 1, \ldots, N_t$ and $s = 1, 2, 3, 4$ (for a standard fourth-order Runge–Kutta scheme) denote the conserved flow variables discretized in space at time step 'n' and sub-step 's', and $\vec{\mathcal{Q}}^0$ are the discretized initial conditions. The right-hand side vector $\boldsymbol{R}[\boldsymbol{\mathcal{Q}}]$ contains all unsteady terms in (2.2) as well as the SAT boundary terms, artificial dissipation, and damping (absorbing sponge) terms. Matrix $\boldsymbol{D}_t$ is a discrete representation of the standard fourth-order Runge–Kutta scheme, and $\boldsymbol{\mathcal{N}} = \left[\vec{\mathcal{N}}^{1,1}, \vec{\mathcal{N}}^{1,2}, \ldots, \vec{\mathcal{N}}^{N_t,3}, \vec{\mathcal{N}}^{N_t,4}\right]^\mathsf{T}$.

Similar to the continuous adjoint approach given in Chapter2.4, the Lagrangian is defined according to (Vishnampet *et al.*, 2015)

$$\mathcal{L}[\boldsymbol{\mathcal{Q}}, \boldsymbol{\mathcal{Q}}^\dagger, \vec{f}] = \mathcal{J}[\boldsymbol{\mathcal{Q}}, \vec{f}] - \sum_{n=1}^{N_t} \sum_{s=1}^{4} \beta^{n,s} \Delta t \left(\vec{\mathcal{Q}}^{\dagger n,s}\right)^T \left(P \otimes I_{N_q}\right) \vec{\mathcal{N}}^{n,s}[\boldsymbol{\mathcal{Q}}, \vec{f}], \tag{2.18}$$

where $\vec{\mathcal{Q}}^{\dagger n,s}$ for $n = 1, \ldots, N_t$ and $s = 1, 2, 3, 4$ denote the space-time discrete adjoint variables. N_q is the number of state variables in $\vec{\mathcal{Q}}$, e.g., $N_q = 5 + N - 1$ for three-dimensional multi-component flows with N species. In (2.18), $\otimes$ is the Kronecker product, and $P = P_x \otimes P_y \otimes P_z$ with a diagonal positive-definite matrix $P_{x_i} \in \mathbb{R}^{N_{x_i}}$ in direction x_i that satisfies the SBP property (Kreiss & Scherer, 1974; Strand, 1994, see Chapter 3.2.1 for a review of SBP). Δt is the timestep size, and $\beta^{n,s}$ denotes the temporal quadrature weight coefficients. Vishnampet *et al.* (2015) discussed possible choices of $\beta^{n,s}$ and noted that the discrete adjoint time integrator is at least an $\mathcal{O}(\Delta t)$ approximation of the continuous adjoint equations if $\beta^{n,1} = \beta^{n,4} = 1/6$ and $\beta^{n,2} = \beta^{n,3} = 1/3$.

Similarly, the objective function is computed discretely as

$$\mathcal{J}[\boldsymbol{Q}, \vec{f}] = \sum_{n=1}^{N_t} \sum_{s=1}^{4} \beta^{n,s} \Delta t \left(\vec{\mathcal{I}}^{n,s}\right)^{\mathsf{T}} P \vec{\mathcal{W}}^{n,s}_{\text{Tar}}, \tag{2.19}$$

where $\vec{\mathcal{I}}^{n,s} = \mathcal{I}(\vec{\mathcal{Q}}^{n,s})$ is the integrand defined in (2.1) evaluated at time step 'n' and sub-step 's'. $\vec{\mathcal{W}}^{n,s}_{\text{Tar}}$ also denotes the discrete space-time vector of the weighting function $\mathcal{W}_{\text{Tar}}$ defined in (2.1). Similar to the continuous adjoint formulation provided in Chapter 2.4 and Appendix A, variations of the Lagrangian (2.18) with respect to $\vec{f}$ and $\vec{\mathcal{Q}}^{n,s}$ for $n = 1, \ldots, N_t$ and $s = 1, 2, 3, 4$ are set to zero, where the latter provides the discrete adjoint equations, given by

$$\boldsymbol{\mathcal{N}}^{\dagger}[\boldsymbol{Q}, \boldsymbol{Q}^{\dagger}, \vec{f}] \equiv \boldsymbol{D}_t^{\dagger} \boldsymbol{Q}^{\dagger} - \boldsymbol{R}^{\dagger}[\boldsymbol{Q}, \vec{f}] \boldsymbol{Q}^{\dagger} = \boldsymbol{G} \tag{2.20}$$

with

$$\boldsymbol{R}^{\dagger}[\boldsymbol{Q}, \vec{f}] = \left(P \otimes I_{N_q}\right)^{-1} \left(\frac{\partial \boldsymbol{R}}{\partial \boldsymbol{Q}}\right)^{\mathsf{T}} \left(P \otimes I_{N_q}\right) \tag{2.21}$$

and

$$\boldsymbol{G} = \left[\frac{1}{2}\vec{G}^{1,1}, \vec{G}^{1,2}, 2\,\vec{G}^{1,3}, \vec{G}^{1,4}, \ldots, \frac{1}{2}\vec{G}^{N_t,1}, \vec{G}^{N_t,2}, 2\,\vec{G}^{N_t,3}, \vec{G}^{N_t,4}\right]^{\mathsf{T}}, \tag{2.22}$$

and the former yields the sensitivity of $\mathcal{J}$ to control parameters. $\vec{G}^{n,s} = \left(\partial \vec{\mathcal{I}}^{n,s} / \partial \vec{\mathcal{Q}}^{n,s}\right) \circ \vec{\mathcal{W}}^{n,s}_{\text{Tar}}$, where $\circ$ denotes the element-wise multiplication. The initial adjoint solution is also given by

$$\vec{\mathcal{Q}}^{\dagger N_t,4} = \frac{\Delta t}{6} \left(\frac{\partial \vec{\mathcal{I}}^{N_t,4}}{\partial \vec{\mathcal{Q}}^{N_t,4}}\right) \circ \vec{\mathcal{W}}^{N_t,4}_{\text{Tar}}. \tag{2.23}$$

To this end, the dissertation has presented a discrete-adjoint method that provides sensitivity with accuracy independent of the underlying numerical scheme and is only limited by machine-precision roundoff error. This is achieved by considering the discrete counterpart of the inner product (2.1) and the fully discretized Navier–Stokes equations (in space and time) prior to employing

the Lagrangian (2.13). Details of the space-time discrete adjoint formulation consistent with the SBP–SAT discretization outlined in Chapter 2.3 and advanced in time with the standard fourth-order Runge–Kutta scheme can be found in Vishnampet (2015) for unsteady single-component flows. It can easily be extended for multi-component reacting flows and is not provided here.

2.5 Combustion modeling

Employing detailed chemistry requires transporting a large number of chemical species that are governed by many intermediate chemical mechanisms. Thus, it is preferred to reduce complexity of combustion modeling by decreasing the number of scalars being transported. In addition, combustion modeling depends strongly on the chemical mechanism under consideration. Implementing a new combustion model in the flow solver requires adding/modifying a source term to the governing equations. As shown in Chapter 2.4, the adjoint-based formulation is based on linearizing the perturbed governing equations. Thus, altering chemical mechanisms requires reformulating, implementing, and verifying adjoint equations, which is not a tractable solution for a broad dissemination of adjoint-based methods for turbulent reacting flows. Most previous studies applying adjoint methods to reacting flow simulations considered simplified chemistry. For instance, adjoint sensitivity was used to manipulate chemistry and diffusion parameters (Gray *et al.*, 2017), to enhance ignition in non-premixed flames (Capecelatro *et al.*, 2018; Qadri *et al.*, 2021), and to perform frequency response analysis of premixed (Skene & Schmid, 2019) and diffusion flames (Sayadi & Schmid, 2021), all of them used a one-step chemistry model.

To address the aforementioned issues, we decouple the flow and adjoint field computations from the detailed chemistry using a flamelet approach. In this approach, the thermodynamical quantities are precomputed, using detail mechanisms, and stored in lookup tables. Therefore, both the flow and adjoint solvers achieve flexibility with respect to the choice of chemical reactions.

2.5.1 Flamelet approach

Flamelet approaches have been widely used due to their computational efficiency and simplicity of implementation (e.g., see Peters, 1984, 1986; Cook *et al.*, 1997; Pitsch *et al.*, 1998; Pitsch & Steiner, 2000; Pitsch, 2000; Pierce & Moin, 2004). In these approaches, thermochemical quantities ϕ are mapped into a low-dimensional space according to

$$\phi = \mathcal{G}(\vec{q}), \tag{2.24}$$

where $\vec{q}$ is a set of state variables by which ϕ is formulated via the mapping function (i.e., the combustion model) $\mathcal{G}$. In flamelet approaches, $\mathcal{G}(\vec{q})$ is usually obtained by gathering diffusion flamelet solutions of standard laminar flames (e.g., counterflow diffusion flames), which are solved via considering detailed chemistry.

Flamelets are thin flame regions assumed to have a one-dimensional structure with infinity fast chemical reactions. In other words, the flow timescale is supposed to be much greater than the chemical reaction timescale, leading to an infinite Damköhler number (Da). Da is defined as the ratio of the flow timescale to the chemical timescale. Thus, the mixing of fuel and oxidizer is the determining factor in forming a flamelet. It is common to map amounts of fuel and oxidizer into a conserved variable, called mixture fraction Z, to measure the degree of mixing, given by

$$Z = \frac{sY_F - Y_O + Y_O^0}{sY_F^0 + Y_O^0}, \tag{2.25}$$

where s denotes the mass stoichiometric ratio. Y_F and Y_O are fuel and oxidizer mass fractions, respectively, and their reference values are denoted by Y_F^0 and Y_O^0, respectively. It has been shown that the distributions of species mass fractions and temperature in a laminar diffusion flame with infinity fast chemistry only depends on Z (e.g., see Poinsot & Veynante, 2005). Thus, the mixture fraction is typically considered as an input variable $\vec{q}$ for the mapping function $\mathcal{G}$ in diffusion flames.

However, the flow timescale in turbulent flows is much smaller compared to laminar flows, and the assumption of an infinite Da is not valid in turbulent flows. In steady flamelet approaches, the scalar dissipation rate, χ, given by

$$\chi = 2\mathcal{D}\frac{\partial Z}{\partial x_i}\frac{\partial Z}{\partial Xi}, \tag{2.26}$$

is also included into $\vec{q}$ to account for the strain rate effects of the flow on flame dynamics (Peters, 1983, 1984; Cook *et al.*, 1997). It has been shown that the stoichiometric scalar dissipation rate χ_{st} is proportional to the inverse of Da (e.g., see Cuenot & Poinsot, 1996; Vervisch & Poinsot, 1998), and the scalar dissipation rate at the flame front is proportional to the flow strain rate of a one-dimensional diffusion counterflow flame with irreversible infinity fast chemistry (Poinsot & Veynante, 2005).

Although using Z and χ_{st} is a straightforward and non-expensive approach to model complex chemistry in turbulent flows, this approach is not suitable for some events such as local extinction and reignition, and it is not also a robust technique to simulate lifted flames (Pierce & Moin, 2004). To better demonstrate these drawbacks, the maximum flamelet temperature with respect to stoichiometric scalar dissipation rates is plotted for a H_2-air counterflow diffusion flame at 300 K (see Fig. 2.1). The FlameMaster solver (Pitsch, 1998) was used to generate the laminar flamelet solutions. As shown in Fig. 2.1, considering a specific value of χ_{st} would not give a unique maximum flamelet temperature, and three different branches exist (also see Pierce & Moin, 2004, for more detials). The bottom branch corresponds to the non-burning (or complete extinction) solution, i.e., only mixing of fuel and oxidizer occurs. The middle branch contains the unstable solutions corresponding to partially extinguished events, which are important for modeling extinction stages. The upper branch includes the stable burning solutions. The steady-flamelet approach only considers the stable burning and non-burning branches. Because of not considering the intermediate branch, some important flame dynamics such as extinction or reignition stages have been missed in this approach.

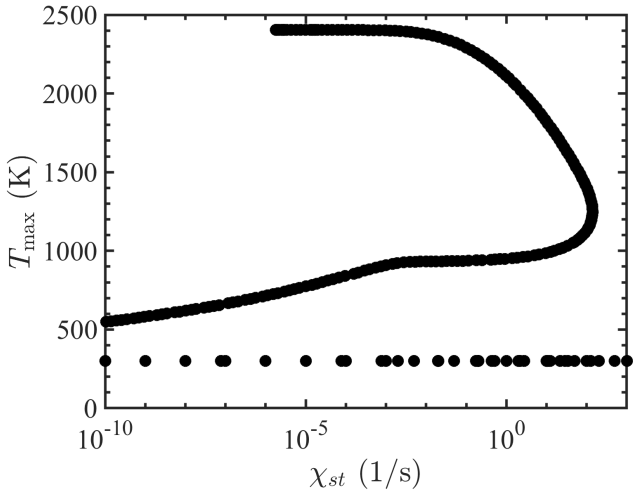

Figure 2.1: Maximum flamelet temperature with respect to the stoichiometric scalar dissipation rate for counterflow diffusion flame of H_2-air with temperatures of 300 K.

2.5.2 Flamelet/progress variable approach

The flamelet/progress variable (FPV) approach (Pierce, 2001) was developed to address the aforementioned issues. To achieve this goal, all three branches of Fig. 2.1 have to be accounted into the tabulated chemistry, which cannot be done via χ_{st}. Thus, a new quantity, called the progress variable, was defined to account for the progress of the chemical reaction, given by

$$C = \sum_{\text{Seleceted Products}} Y_{\text{Seleceted Products}} \,, \tag{2.27}$$

where mass fractions of selected products depend on the chemical reaction. Although these selected products are determined by the user, they should account for certain features of flame dynamics such as the reignition stages. For instance, Y_{CH_4}, Y_{H_2O}, Y_{CO}, and Y_{H_2} are typically taken to define the progress variable for methane-air reactions. Also, it is common to normalize the progress variable such that $C \in [0, 1]$. Unlike the scalar dissipation rate, the progress variable can also be used for generating a lookup table for premixed flames (e.g., see van Oijen *et al.*, 2001). The FPV approaches were used successfully for studying flame behaviors or pollutant emissions such as soot and NOx in complex problems involving turbulent reacting flows (e.g., see Ihme

& Pitsch, 2008a,b,c; Mueller & Pitsch, 2012; Saghafian *et al.*, 2015; Yang *et al.*, 2019). In the following section, details on the generation of the lookup table are provided.

2.5.3 Generating lookup tables

As mentioned before, thermochemical quantities have to be obtained through Eq. (2.24). In the steady-flamelet and FPV approaches, laminar flamelet solutions are first collected by solving steady flamelet equations to compute thermochemical quantities within laminar diffusion flames, given by (e.g., see Poinsot & Veynante, 2005)

$$\begin{aligned} -\frac{1}{2}\rho\chi\frac{\partial^2 Y_n}{\partial Z \partial Z} &= \dot{\omega}_n, \\ -\frac{1}{2}\rho\chi\frac{\partial^2 T}{\partial Z \partial Z} &= \dot{\omega}_T, \end{aligned} \tag{2.28}$$

where $\dot{\omega}_T$ is the energy source term. Thus, thermochemical quantities ϕ (e.g., $Y_n, \dot{\omega}_n, T, \rho, \mu, C_p$) only depend on Z, χ (which also depends on Z), and boundary conditions (i.e., mass fraction, velocity, and temperature of the fuel and oxidizer). Considering the counterflow diffusion flame, which is typically used for the FPV approach, χ_{st} depends on the flow strain rate of the counterflow configuration. Thus, different values of χ_{st} are set for each flamelet simulation, and $\phi(Z,\chi_{st})$ is stored. Each point in Fig. 2.1 corresponds to a laminar flamelet simulation. It is important to make sure all three branches of Fig. 2.1 are captured via the set of flamelet simulations.

Recall that the laminar flamelet solutions contain distributions of chemical products that will be used to compute the progress variable, and they are functions of Z and χ_{st}. However, as discussed before, χ_{st} is not an appropriate choice to parameterize the flamelet solutions. It is favorable to parameterize them with other quantities instead of χ_{st}, such as the maximum value of C or the temperature value at stoichiometric Z (Pierce & Moin, 2004). The former parameter is used here, and we denote this parameter with λ, given by

$$\lambda = \max\left\{\sum_{\text{Seleceted Products}} Y_{\text{Seleceted Products}}\right\}. \tag{2.29}$$

The FPV approach is originally developed for LES. Thus, its lookup table provides Favre (density-weighted) filtered values of thermochemical quantities $\widetilde{\phi}$, given by

$$\widetilde{\phi} = \int_0^1 \int_0^1 \phi(Z, C) P(Z, C) \mathrm{d}Z \mathrm{d}C, \tag{2.30}$$

where $P(Z, C)$ is the probability distribution function (PDF). Details of generating $\widetilde{\phi}$ from the laminar flamelet solutions were provided by (Pierce & Moin, 2004). We use a similar approach, which is reviewed here. It is necessary to choose a joint PDF $P(Z, C)$ to compute $\widetilde{\phi}$ according to (2.30), which is assumed to be (using Bayes' theorem)

$$P(Z, C) = P(C|Z) P(Z). \tag{2.31}$$

A beta-distribution is used for $P(Z)$, given by

$$P(Z; a, b) = \frac{\Gamma(a + b)}{\Gamma(a)\Gamma(b)} Z^{a-1} (1 - Z)^{b-1}, \tag{2.32}$$

where Γ denotes the gamma function, and a and b are given by

$$a = \frac{\widetilde{Z}\left[\widetilde{Z} - \left(\widetilde{Z}\right)^2 - \widetilde{Z''^2}\right]}{\widetilde{Z''^2}}, \qquad b = \frac{\left(1 - \widetilde{Z}\right)\left[\widetilde{Z} - \left(\widetilde{Z}\right)^2 - \widetilde{Z''^2}\right]}{\widetilde{Z''^2}}, \tag{2.33}$$

respectively, with the mean (or filtered) $\widetilde{Z}$ and variance $\widetilde{Z''^2}$ of the mixture fraction.

It is also required to determine the conditional PDF $P(C|Z)$. If it is assumed that each grid point in $\widetilde{Z} - \widetilde{C}$ space (i.e., the chemical space, not to be confused with the spatial grid) belongs to a single flamelet solution with a corresponding λ_0 value, a delta-distribution can then be taken to describe the conditional PDF, given by

$$P(C|Z) = \delta(C - \widetilde{C|Z}) \qquad \text{with } \widetilde{C|Z} = C(Z, \lambda_0), \tag{2.34}$$

where λ_0 is a reference parameter corresponding to the appropriate flamelet solution. If multiple flamelet solutions exist at a single grid point in the chemical space, either one of the flamelet solutions or their average can be taken. Putting this together leads to

$$\widetilde{\phi}(\widetilde{Z}, \widetilde{Z''^2}, \lambda_0) = \int_0^1 \phi(Z, \lambda_0) P(Z; \widetilde{Z}, \widetilde{Z''^2}) \mathrm{d}Z. \tag{2.35}$$

Finally, the value of λ_0 has to be taken such that the below constraint is satisfied (Pierce & Moin, 2004)

$$\widetilde{C} = \int_0^1 C(Z, \lambda_0) P(Z; \widetilde{Z}, \widetilde{Z''^2}) \mathrm{d}Z. \tag{2.36}$$

Thus, all thermochemical quantities now depend on statistics of the mixture fraction and the progress variable, given by

$$\widetilde{\phi} = \mathcal{G}(\widetilde{Z}, \widetilde{Z''^2}, \widetilde{C}), \tag{2.37}$$

and it is required to solve transport equations of $\widetilde{Z}$ and $\widetilde{C}$. Also, $\widetilde{Z''^2}$ can either be (dynamically) modelled (e.g., see Pierce & Moin, 1998) or solved through its partial differential equation (e.g., see Saghafian *et al.*, 2015). If DNS is used instead of LES, then $\widetilde{Z''^2} = 0$ (i.e., no sub-grid-scale exists). In this work, we assume that small scale physics of flame dynamics are captured by the spatial grid spacing, leading to $\widetilde{Z} = Z$, $\widetilde{C} = C$, and $\widetilde{Z''^2} = 0$.

2.5.4 Forward simulation using a lookup table

In the FPV approach, the flow governing equations (2.11) are considered with conserved variables $\vec{Q} = [\rho, \rho\boldsymbol{u}, \rho E, \rho Z, \rho C]^\mathsf{T}$. The non-dimensional species flux $f^V_{n,i}$ in (2.9) is rewritten according to

$$f^V_{Z,i} = -\frac{\mu}{\mathrm{Re}_c \mathrm{Sc}_Z} \frac{\partial Z}{\partial x_i}, \quad f^V_{C,i} = -\frac{\mu}{\mathrm{Re}_c \mathrm{Sc}_C} \frac{\partial C}{\partial x_i}, \tag{2.38}$$

where the Schmidt numbers are defined according to $\mathrm{Sc}_Z = \mu/\rho\mathcal{D}_Z$ and $\mathrm{Sc}_C = \mu/\rho\alpha\mathcal{D}_C$ with $\mathcal{D}_Z$ and $\mathcal{D}_C$ denoting the mass diffusivity of Z and C, respectively. A unity Lewis number is commonly taken among all species with the FPV approach, leading to $\mathrm{Pr} = \mathrm{Sc}_Z = \mathrm{Sc}_C = \mathrm{Sc}_n$ for species $n = 1, \ldots, N$ with N chemical species. It can be shown that the mixture fraction is a conserved variable, i.e., $\dot{\omega}_Z = 0$ (Poinsot & Veynante, 2005). As explained in the previous section, the species mass fraction Y_n for $n = 1, \ldots, N$ and the source term for the progress variable $\dot{\omega}_C$ are precomputed by solving quasi-steady laminar flame equations with complex chemistry models, in which all chemical species and intermediate chemical schemes are considered. These values are stored in a lookup table as a function of Z and C. When the flow governing equations are being solved, values of Y_n for $n = 1, \cdots, N$ in (2.4) and (2.8) and also values of $\dot{\omega}_C$ in (2.3) are obtained by interpolation (and extrapolation if necessary) of the flamelet lookup table.

The most straightforward and common interpolation technique used for the FPV approach is linear interpolation. In this case, $\mathcal{G}$ would be a piecewise continuous function but not a smooth function since the derivatives of $\mathcal{G}$ to Z and C do not continuously change. Although this approach has been successful in predicting turbulent reacting flows using tabulated chemistry, it is not desired for the adjoint formulation since it makes the system of governing equations not differentiable with respect to $\vec{Q}$. In other words, it could impact dual consistency of the numerical framework and generate spurious waves in the adjoint solution (see Chapter 3.3.4 for more details on dual consistency). Instead, high-order interpolation techniques can be used, such as the high-order B-spline interpolation, which also increases the accuracy of the predictive solution (Bode *et al.*, 2019). Using high-order interpolation requires performing more arithmetic operations during the simulation. But, the memory cost can be reduced by taking a fewer number of grid points in the $Z-C$ space because a higher-order of accuracy would be achieved by the interpolation (Bode *et al.*, 2019).

In this dissertation, both linear and cubic Hermit spline interpolation are implemented in the flow and adjoint solver. The latter one provides a continuously differentiable interpolation (i.e., their derivatives are continuous).

2.5.4.1 Linear interpolation

Linear interpolation is performed according to

$$\begin{aligned}\phi(Z,C) =& w_{21}(C;C_k,C_{k+1})\left(w_{11}(Z;Z_k,Z_{k+1})\widehat{\phi}(Z_k,C_k) + w_{12}(Z;Z_k,Z_{k+1})\widehat{\phi}(Z_{k+1},C_k)\right)\\ &+w_{22}(C;C_k,C_{k+1})\left(w_{11}(Z;Z_k,Z_{k+1})\widehat{\phi}(Z_k,C_{k+1}) + w_{12}(Z;Z_k,Z_{k+1})\widehat{\phi}(Z_{k+1},C_{k+1})\right),\end{aligned} \tag{2.39}$$

where ϕ denotes either Y_n or $\dot{\omega}_C$, and $\widehat{\phi}$ is the corresponding value in the lookup table, and $Z_k < Z < Z_{k+1}$ and $C_k < C < C_{k+1}$. If Z or C are either smaller than 0 or greater than 1, extrapolation is employed by considering the closest boundary points in the lookup table. The weights on the above relation are given by

$$\begin{aligned} w_{11}(Z;Z_k,Z_{k+1}) &= \frac{Z_{k+1}-Z}{Z_{k+1}-Z_k}, \qquad & w_{12}(Z;Z_k,Z_{k+1}) &= 1-w_{11},\\ w_{21}(C;C_k,C_{k+1}) &= \frac{C_{k+1}-C}{C_{k+1}-C_k}, \qquad & w_{22}(C;C_k,C_{k+1}) &= 1-w_{21}. \end{aligned} \tag{2.40}$$

2.5.4.2 Cubic Hermit spline interpolation

Cubic Hermit spline (CHS) interpolation employs a third-degree polynomial such that the slopes of the obtained function remain continuous at the grid points. First, we perform CHS interpolation for $Z_k < Z < Z_{k+1}$ at a fixed C_k. Also, we assume that the slopes of ϕ with respect to Z at Z_k and Z_{k+1} are known and given by $m_k(C_k)$ and $m_{k+1}(C_k)$, respectively. Using CHS provides a third-degree polynomial $p_{CHS,Z}$, given by

$$\begin{aligned}p_{CHS,Z}(Z;Z_k,Z_{k+1},C_k) =& \mathcal{H}_{00}(Z;Z_k,Z_{k+1})\widehat{\phi}(Z_k,C_k) + \mathcal{H}_{10}(Z;Z_k,Z_{k+1})(Z_{k+1}-Z_k)m_k(C_k)\\ &+\mathcal{H}_{01}(Z;Z_k,Z_{k+1})\widehat{\phi}(Z_{k+1},C_k) + \mathcal{H}_{11}(Z;Z_k,Z_{k+1})(Z_{k+1}-Z_k)m_{k+1}(C_k),\end{aligned} \tag{2.41}$$

where

$$\begin{aligned}
\mathcal{H}_{00}(X; X_k, X_{k+1}) &= 2\bar{X}^3 - 3\bar{X}^2 + 1, \\
\mathcal{H}_{10}(X; X_k, X_{k+1}) &= \bar{X}^3 - 2\bar{X}^2 + \bar{X}, \\
\mathcal{H}_{01}(X; X_k, X_{k+1}) &= -2\bar{X}^3 + 3\bar{X}^2, \\
\mathcal{H}_{11}(X; X_k, X_{k+1}) &= \bar{X}^3 - \bar{X}^2
\end{aligned} \tag{2.42}$$

with $\bar{X} = (X - X_k)/(X_{k+1} - X_k)$. Note that the slopes m_k and m_{k+1} are typically not known, but they can be estimated by finite-different approximations, such as a centered finite difference method given by

$$m_k(C_k) = \frac{\widehat{\phi}(Z_{k+1}, C_k) - \widehat{\phi}(Z_{k-1}, C_k)}{2\,(Z_{k+1} - Z_{k-1})}. \tag{2.43}$$

Using (2.43) yields a Catmull-Rom spline. When Z_{k-1} and Z_{k+1} do not exist, a first-order forward or backward finite-difference approximation are used, respectively.

Then, CHS interpolation is preformed for $C_k < C < C_{k+1}$ according to

$$\begin{aligned}
\phi_{chs}(Z, C) =& \mathcal{H}_{00}(C; C_k, C_{k+1}) p_{chs,Z}(Z; Z_k, Z_{k+1}, C_k) \\
&+ \mathcal{H}_{10}(C; C_k, C_{k+1})\,(C_{k+1} - C_k)\,\frac{p_{chs,Z}(Z; Z_k, Z_{k+1}, C_{k+1}) - p_{chs,Z}(Z; Z_k, Z_{k+1}, C_{k-1})}{2\,(C_{k+1} - C_{k-1})} \\
&+ \mathcal{H}_{01}(C; C_k, C_{k+1}) p_{chs,Z}(Z; Z_k, Z_{k+1}, C_{k+1}) \\
&+ \mathcal{H}_{11}(C; C_k, C_{k+1})\,(C_{k+1} - C_k)\,\frac{p_{chs,Z}(Z; Z_k, Z_{k+1}, C_{k+2}) - p_{chs,Z}(Z; Z_k, Z_{k+1}, C_k)}{2\,(C_{k+2} - C_k)}.
\end{aligned} \tag{2.44}$$

2.5.5 Adjoint of the flamelet/progress variable approach

As mentioned in Chapter 2.4, the adjoint equations are derived by considering variations of the governing equations (2.11) with respect to conserved variables $\vec{Q}$ (see Appendix A for more details). We employ the chain rule for computing variations of the lookup table output $\phi(Z, C)$ to $\vec{Q}$,

given by

$$\frac{\partial \phi}{\partial \vec{Q}} \delta \vec{Q} = -\frac{1}{\rho}\left(Z\frac{\partial \phi}{\partial Z} + C\frac{\partial \phi}{\partial C}\right)\delta\rho + \frac{1}{\rho}\frac{\partial \phi}{\partial Z}\delta(\rho Z) + \frac{1}{\rho}\frac{\partial \phi}{\partial C}\delta(\rho C). \tag{2.45}$$

If linear interpolation was used in the forward (predictive) simulation, derivatives of ϕ with respect to Z and C are obtained according to (2.39), given by

$$\begin{aligned}\frac{\partial \phi}{\partial Z} =& w_{21}(C; C_k, C_{k+1})\left(\frac{\mathrm{d}w_{11}(Z; Z_k, Z_{k+1})}{\mathrm{d}Z}\widehat{\phi}(Z_k, C_k) + \frac{\mathrm{d}w_{12}(Z; Z_k, Z_{k+1})}{\mathrm{d}Z}\widehat{\phi}(Z_{k+1}, C_k)\right) \\ &+ w_{22}(C; C_k, C_{k+1})\left(\frac{\mathrm{d}w_{11}(Z; Z_k, Z_{k+1})}{\mathrm{d}Z}\widehat{\phi}(Z_k, C_{k+1}) + \frac{\mathrm{d}w_{12}(Z; Z_k, Z_{k+1})}{\mathrm{d}Z}\widehat{\phi}(Z_{k+1}, C_{k+1})\right),\end{aligned} \tag{2.46}$$

and

$$\begin{aligned}\frac{\partial \phi}{\partial C} =& \frac{\mathrm{d}w_{21}(C; C_k, C_{k+1})}{\mathrm{d}C}\left(w_{11}(Z; Z_k, Z_{k+1})\widehat{\phi}(Z_k, C_k) + w_{12}(Z; Z_k, Z_{k+1})\widehat{\phi}(Z_{k+1}, C_k)\right) \\ &+ \frac{\mathrm{d}w_{22}(C; C_k, C_{k+1})}{\mathrm{d}C}\left(w_{11}(Z; Z_k, Z_{k+1})\widehat{\phi}(Z_k, C_{k+1}) + w_{12}(Z; Z_k, Z_{k+1})\widehat{\phi}(Z_{k+1}, C_{k+1})\right),\end{aligned} \tag{2.47}$$

respectively, where

$$\begin{aligned}\frac{\mathrm{d}w_{11}(Z; Z_k, Z_{k+1})}{\mathrm{d}Z} &= -\frac{1}{Z_{k+1} - Z_k}, \qquad \frac{\mathrm{d}w_{12}(Z; Z_k, Z_{k+1})}{\mathrm{d}Z} = -\frac{\mathrm{d}w_{11}(Z; Z_k, Z_{k+1})}{\mathrm{d}Z}, \\ \frac{\mathrm{d}w_{21}(C; C_k, C_{k+1})}{\mathrm{d}C} &= -\frac{1}{C_{k+1} - C_k}, \qquad \frac{\mathrm{d}w_{22}(C; C_k, C_{k+1})}{\mathrm{d}C} = -\frac{\mathrm{d}w_{21}(C; C_k, C_{k+1})}{\mathrm{d}C}.\end{aligned} \tag{2.48}$$

This method is employed to compute variations of the pressure, heat flux, etc. to $\vec{Q}$ (see Appendix A for more details).

If CHS interpolation was employed instead of linear interpolation, variations of ϕ_{CHS} with

respect to Z and C are computed by

$$\begin{aligned}\frac{\partial \phi_{chs}}{\partial Z} =& \mathcal{H}_{00}(C; C_k, C_{k+1}) \frac{\mathrm{d}p_{chs,Z}(Z; Z_k, Z_{k+1}, C_k)}{\mathrm{d}Z} \\ &+ \mathcal{H}_{10}(C; C_k, C_{k+1}) \frac{C_{k+1} - C_k}{2\,(C_{k+1} - C_{k-1})} \left(\frac{\mathrm{d}p_{chs,Z}(Z; Z_k, Z_{k+1}, C_{k+1})}{\mathrm{d}Z} - \frac{\mathrm{d}p_{chs,Z}(Z; Z_k, Z_{k+1}, C_{k-1})}{\mathrm{d}Z} \right) \\ &+ \mathcal{H}_{01}(C; C_k, C_{k+1}) \frac{\mathrm{d}p_{chs,Z}(Z; Z_k, Z_{k+1}, C_{k+1})}{\mathrm{d}Z} \\ &+ \mathcal{H}_{11}(C; C_k, C_{k+1}) \frac{C_{k+1} - C_k}{2\,(C_{k+2} - C_k)} \left(\frac{\mathrm{d}p_{chs,Z}(Z; Z_k, Z_{k+1}, C_{k+2})}{\mathrm{d}Z} - \frac{\mathrm{d}p_{chs,Z}(Z; Z_k, Z_{k+1}, C_k)}{\mathrm{d}Z} \right),\end{aligned} \tag{2.49}$$

and

$$\begin{aligned}\frac{\partial \phi_{chs}}{\partial C} =& \frac{\mathrm{d}\mathcal{H}_{00}(C; C_k, C_{k+1})}{\mathrm{d}C} p_{chs,Z}(Z; Z_k, Z_{k+1}, C_k) \\ &+ \frac{\mathrm{d}\mathcal{H}_{10}(C; C_k, C_{k+1})}{\mathrm{d}C} (C_{k+1} - C_k) \frac{p_{chs,Z}(Z; Z_k, Z_{k+1}, C_{k+1}) - p_{chs,Z}(Z; Z_k, Z_{k+1}, C_{k-1})}{2\,(C_{k+1} - C_{k-1})} \\ &+ \frac{\mathrm{d}\mathcal{H}_{01}(C; C_k, C_{k+1})}{\mathrm{d}C} p_{chs,Z}(Z; Z_k, Z_{k+1}, C_{k+1}) \\ &+ \frac{\mathrm{d}\mathcal{H}_{11}(C; C_k, C_{k+1})}{\mathrm{d}C} (C_{k+1} - C_k) \frac{p_{chs,Z}(Z; Z_k, Z_{k+1}, C_{k+2}) - p_{chs,Z}(Z; Z_k, Z_{k+1}, C_k)}{2\,(C_{k+2} - C_k)},\end{aligned} \tag{2.50}$$

respectively, where

$$\begin{aligned}p_{CHS,Z}(Z; Z_k, Z_{k+1}, C_k) =& \frac{\mathrm{d}\mathcal{H}_{00}(Z; Z_k, Z_{k+1})}{\mathrm{d}Z} \widehat{\phi}(Z_k, C_k) + \frac{\mathrm{d}\mathcal{H}_{10}(Z; Z_k, Z_{k+1})}{\mathrm{d}Z} (Z_{k+1} - Z_k) m_k(C_k) \\ &+ \frac{\mathrm{d}\mathcal{H}_{01}(Z; Z_k, Z_{k+1})}{\mathrm{d}Z} \widehat{\phi}(Z_{k+1}, C_k) + \frac{\mathrm{d}\mathcal{H}_{11}(Z; Z_k, Z_{k+1})}{\mathrm{d}Z} (Z_{k+1} - Z_k) m_{k+1}(C_k),\end{aligned} \tag{2.51}$$

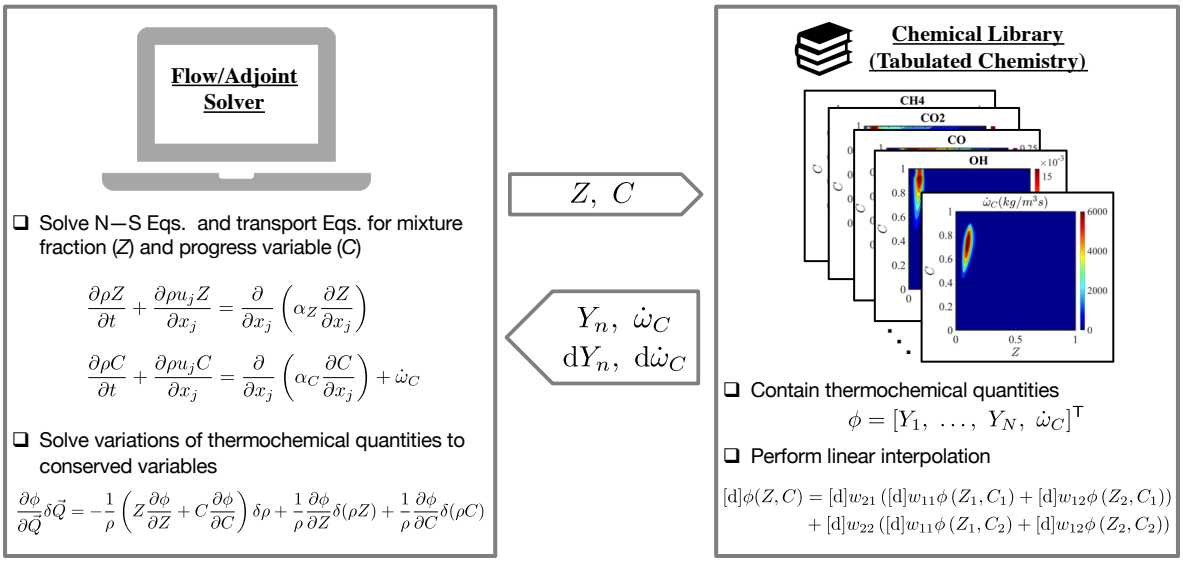

Figure 2.2: Summary of the flamelet/progress variable approach and its adjoint formulation.

and

$$\begin{aligned}
\frac{\mathrm{d}\mathcal{H}_{00}(X;X_k,X_{k+1})}{\mathrm{d}X} &= \frac{1}{X_{k+1}-X_k}\left(6\bar{X}^2 - 6\bar{X}\right),\\
\frac{\mathrm{d}\mathcal{H}_{10}(X;X_k,X_{k+1})}{\mathrm{d}X} &= \frac{1}{X_{k+1}-X_k}\left(3\bar{X}^2 - 4\bar{X} + 1\right),\\
\frac{\mathrm{d}\mathcal{H}_{01}(X;X_k,X_{k+1})}{\mathrm{d}X} &= \frac{1}{X_{k+1}-X_k}\left(-6\bar{X}^2 + 6\bar{X}\right),\\
\frac{\mathrm{d}\mathcal{H}_{11}(X;X_k,X_{k+1})}{\mathrm{d}X} &= \frac{1}{X_{k+1}-X_k}\left(3\bar{X}^2 - 2\bar{X}\right).
\end{aligned} \tag{2.52}$$

Figure 2.2 summarizes the FPV approach with linear interpolation and its adjoint formulation.

2.6 Optimization

The sensitivity of a QoI $\mathcal{J}$ to $\vec{f}$ obtained from the adjoint-based method described in the previous sections is used within a gradient-based optimization framework to find optimal values of $\mathcal{J}$ (see Fig. 2.3). Once the sensitivity (i.e., gradient $\nabla\mathcal{J} = \delta\mathcal{J}/\delta\vec{f}$) is provided by the adjoint solver, the optimizer determines a 'search direction' based on the gradient. The search direction could be set as $-\nabla\mathcal{J}$ in the steepest descent algorithm; however, it can also be computed based on the history

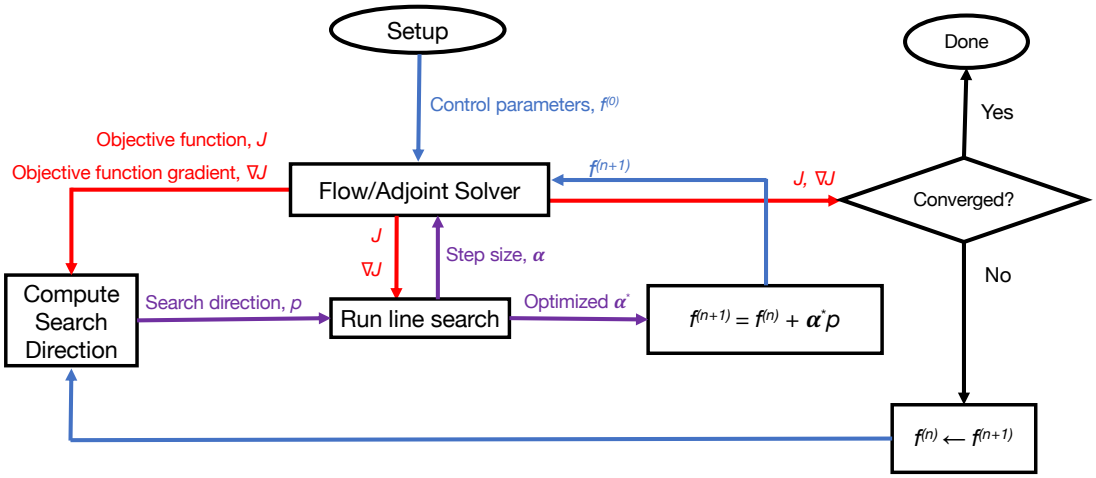

Figure 2.3: Adjoint-based optimization framework.

of previous gradients as in the conjugate gradient method. Then, a line-search algorithm is used to obtain an 'optimal value' within this search direction. Depending on the line search algorithm, this 'optimal value' either provides a new $\mathcal{J}$ that is smaller than the baseline $\mathcal{J}$ (e.g., the sufficient decrease condition), is based on how much the magnitude of its gradient, $|\nabla\mathcal{J}|$, is reduced (e.g., the sufficient curvature condition), or combination of both, e.g., the strong Wolfe conditions (see Martins & Ning, 2021, for more details). Depending on a user-defined tolerance, either the adjoint-based optimization is terminated, or a new optimization iteration restarts to obtain a new search direction.

In this work, the following gradient-based optimization algorithms have been implemented as an in-house optimization library:

(i) Steepest descent,

(ii) Conjugate gradient,

(iii) Broyden-Fletcher-Goldfarb-Shanno (BFGS),

with the following line search algorithms:

(i) Backtracking,

(ii) Bracketing with the pinpoint function.

More information about these algorithms can be found in Martins & Ning (2021). In addition, the FORTRAN-based code solving the Navier–Stokes and adjoint equations communicates with the `SciPy minimize` package, an open-source Python library (Jones *et al.*, 2001; Oliphant, 2007; Millman & Aivazis, 2011) providing many optimization solvers. With this, the `SciPy minimize` solver updates design parameters and sends them back to the flow or adjoint code for recomputing the QoI (and its sensitivities if requested). This is repeated until the optimization procedure converges to a threshold tolerance.

2.6.1 Seeking an optimal space-time field

As previously mentioned, the computational cost of adjoint-based methods does not significantly depend on the number of control parameters $\vec{f}$; thus, they are very powerful in cases when a large number of control parameters are involved. In some applications, $\vec{f}$ is a space-time field, and its size, denoted by $N_f = N_{ct} \times N_t \times N_{st}$, is thus proportional to the grid size of the control region (N_{ct}) and the number of timesteps N_t and sub-steps N_{st}, where $N_{st} = 4$ for the standard fourth-order Runge–Kutta time integrator. In these cases, it might not be possible to store all values of $\vec{f} \in \mathbb{R}^{N_f}$ and the gradient $\nabla\mathcal{J} \in \mathbb{R}^{N_f}$ when the flow or adjoint governing equations are integrated in time. Instead, their values are saved on disk, and only a portion of them is stored in memory. Thus, efficient data management for reading from/writing to disk is required. It is also necessary to store flow state variables $\vec{Q}$ for the adjoint simulation. Adjoint equations typically have to be integrated reversely in time as shown in Chapter 3.3.1, and adjoint equations depends on $\vec{Q} \in \mathbb{R}^{N_q \times N_g \times N_t \times N_{st}}$ with N_q conserved/state variables and N_g grid points in the computational domain. Unlike $\vec{f}$ and $\nabla\mathcal{J}$, it would not be practical to store all values of $\vec{Q}$ in disk since the control region is typically a small portion of the domain, i.e., $N_{ct} \ll N_g$. Instead, checkpointing is performed (e.g., see Vishnampet, 2015). Note that flow solutions at sub-timesteps do also have to be known during the discrete adjoint simulation. For continuous adjoint, on the other hand, flow state solutions at fractional sub-steps can be approximated via interpolation (Vishnampet *et al.*, 2015), which reduces the computational cost. Also, the adjoint equations are linear with respect to

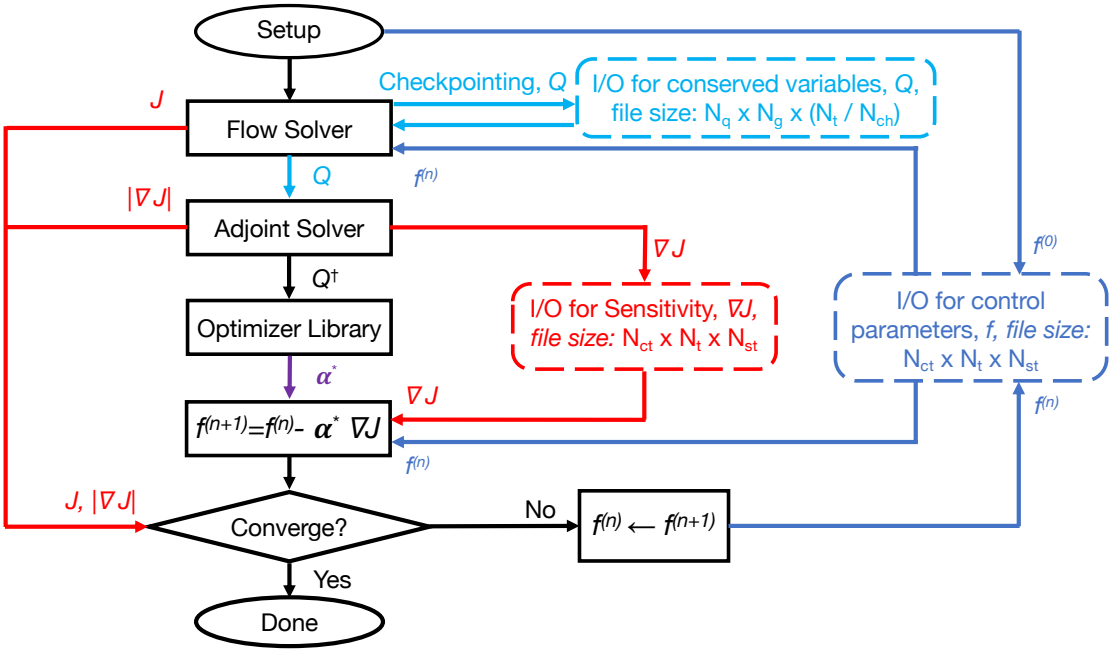

Figure 2.4: Adjoint-based optimization framework with space-time field $\vec{f}$. Dashed boxes are disk storages, and arrows toward/from them means writing/reading data to/from disk.

adjoint variables according to (2.20), and making use of this property in time integration and data management accelerates the time-integration portion of the discrete-adjoint solver (e.g., see Skene *et al.*, 2021).

The adjoint-based optimizer is extended to manage subset values of $\vec{f}$ during the simulation via reading them from/writing them to disk, which is summarized in Fig. 2.4. After setting-up the problem configuration, the flow solver integrates the Navier–Stokes equations from $t = 0$ to $t = t_f$ with constant timestep $\Delta t = t_f/N_t$, and snapshots of the flow solution $\vec{Q}$ are frequently written to disk at $t = 0,\ N_{ch}\Delta t,\ 2N_{ch}\Delta_t,\ \ldots,\ N_t\Delta_t$ with $N_{ch} < N_t$ denoting the checkpointing frequency. A subset of $\vec{f}$ with a size of $N_{ct} \times N_{ch} \times N_{st}$ that is required within $t \in [0, N_{ch}\Delta t]$, $t \in [N_{ch}\Delta t, 2N_{ch}\Delta t]$, $\ldots$, $t \in [(N_t - N_{ch})\Delta t, N_t\Delta t]$ is read from disk at $t = 0$, $N_{ch}\Delta t$, $\ldots$, and $(N_t - N_{ch})\Delta t$, respectively, and stored in memory. After finishing the flow simulation, the adjoint solver initializes the adjoint solution at $t = t_f$ according to (2.23) via reading the corresponding snapshot of the flow solution $\vec{Q}$ from the disk . Then, the solver reads the subset of $\vec{f}$ for $t \in [(N_t - N_{ch}), N_t\Delta t]$ and stores them in memory, but it reads the snapshot of $\vec{Q}$ at $t = (N_t - N_{ch})\Delta t$ from disk and integrates the flow

governing equations from $t = (N_t - N_{ch})\Delta t - N_t \Delta t$, during which $\vec{Q}$ values are now stored in memory. Then, the adjoint simulation integrates reversely in time for $t = N_t \Delta t - (N_t - N_{ch})\Delta t$, using the stored $\vec{Q}$ and $\vec{f}$ values in memory. The adjoint sensitivity is computed and stored in memory during this time horizon and then writes to disk when the adjoint simulation reaches $t = (N_t - N_{ch})\Delta t$. This procedure repeats until the adjoint simulation approaches $t = 0$. Then, the optimizer framework starts a new flow simulation to obtain $\mathcal{J}^{(n+1)}$, during which the control parameters $f^{(n+1)}$ are updated using the steepest descent method according to

$$f^{(n+1)} = f^{(n)} - \alpha^{(n)} g^{(n)}, \tag{2.53}$$

where superscript n denotes the optimization iteration, g is the local temporal sensitivity in the control region, and $\alpha^{(n)} > 0$ is a step length. Note that subsets of $\vec{f}^{(n)}$ and $\vec{g}^{(n)}$ have to be read from disk and stored in memory with a timestep frequency of N_{ch} during integrating the flow equations.

Several line searching algorithms exist to obtain an optimal value of $\alpha^{(n)}$. In this work, a backtracking algorithm is implemented as follows. If $\mathcal{J}^{(n+1)}$ does sufficiently decrease with respect to $\mathcal{J}^{(n)}$, i.e.,

$$\mathcal{J}^{(n+1)} \leq \mathcal{J}^{(n)} - \mu_{ls} \alpha^{(n)} \int_{t=t_0}^{t=t_f} \int_{\boldsymbol{x}} g^{(n)} \cdot g^{(n)} \, \mathrm{d}\boldsymbol{x} \, \mathrm{d}t, \tag{2.54}$$

then $\alpha^\star = \alpha^{(n)}$. The inequality (2.54) is called the sufficient decrease condition or Armijo condition (e.g., see Martins & Ning, 2021), and a user-defined parameter $\mu_{ls} = 10^{-4}$ is used. Then, the new $\vec{f}$ according to (2.53) is updated and written to disk, and a new optimization iteration begins (next optimization iteration $n + 1$) until the optimization procedure converges. If (2.54) has not been satisfied yet, a new line searching iteration is performed with a smaller step, i.e., $\alpha^{(n)} \leftarrow 10^{-1/4} \alpha^{(n)}$. Note that $-g^{(n)} \cdot g^{(n)}$ in (2.54) denotes the negative directional derivative, which is the opposite of adjoint sensitivity, as used in the steepest descent method.

CHAPTER 3

Adaptive Dissipation Framework for Preserving Scalar Boundedness

3.1 Introduction

In this dissertation, we seek a robust numerical framework and its discrete adjoint counterpart for compressible flows involving scalar mixing, turbulence, chemical reactions, and potentially, shocks. The numerical framework should provide high-fidelity predictions of such complex flow problems with a manageable computational cost. Therefore, we leverage high-order discretization methods. Although advanced numerical techniques exist for this purpose, they could yield oscillatory discrete adjoint solutions. Discrete adjoint equations are derived by computing variations of discretized governing equations with their numerical models (e.g., flux limiters) to flow state variables. Thus, it is challenging to obtain a high-order numerical framework with a compatible discrete adjoint solution for complex flow problems.

Despite huge progress in developing high-order numerical schemes, applications of high-order methods to under-resolved simulations of turbulent flows remain challenging. Namely, without the aid of numerical diffusion, dispersion errors generate spurious oscillations when sharp gradients are not sufficiently resolved (Johnsen *et al.*, 2010). This results in excursion errors (i.e., unphysical overshoots and undershoots) in flow state variables, which can violate realizability constraints. For example, the mass fraction of a chemical species, Y, must be bounded $Y \in [0, 1]$.

Several methods have been proposed in recent years to preserve scalar boundedness in high-

fidelity numerical solvers. Examples include flux correction and limiter schemes (Herrmann *et al.*, 2006; Subbareddy *et al.*, 2017; Sharan *et al.*, 2018) and artificial dissipation operators (Cook, 2007; Kawai & Lele, 2008). High-order artificial dissipation operators that retain stability and accuracy of SBP schemes were introduced by Mattsson *et al.* (2004) to suppress unresolved spurious modes, and their dual consistency was also verified by Hicken & Zingg (2014). However, the proposed high-order dissipation operators are not capable of absorbing oscillations in regions with sharp gradients and could generate excursion errors. SBP operators have been extended to upwind-based (Mattsson *et al.*, 2004; Svärd *et al.*, 2005; Mattsson *et al.*, 2007; Mattsson, 2017), monotonic upstream-centered scheme for conservation laws (MUSCL) (Abbas *et al.*, 2010), weighted essentially non-oscillatory (WENO) (Yamaleev & Carpenter, 2009b,a), and adaptive discretization (Abbas *et al.*, 2009; Eriksson *et al.*, 2011; Eriksson & Nordström, 2018) schemes. Yet, these approaches could be computationally expensive. Also, these schemes may add remarkable numerical dissipation and suppress physical fluctuations such as small-scale turbulent eddies and acoustic waves (e.g., see Herrmann *et al.*, 2006; Matheou & Dimotakis, 2016).

In this chapter, an adaptive dissipation operator is presented to preserve scalar boundedness in turbulent flows in a computationally efficient manner that retains overall high-order accuracy and is compatible with the adjoint solver. Its effects on the boundedness error and accuracy of the solution are studied via a series of numerical tests, including a three-dimensional turbulent round jet. Adjoint formulation for adaptive dissipation operators is derived, and it is studied via a few numerical simulations.

3.2 High-order SBP framework with scalar boundedness

In this section, we present an adaptive dissipation operator to yield scalar boundedness in convection-dominated flows. A one-dimensional advection equation of a passive scalar is first considered, which isolates the dispersive behavior that generates excursion errors. An energy estimate of the proposed adaptive SBP dissipation operators is then presented.

3.2.1 An overview of SBP operators

Consider a one-dimensional linear advection equation of a scalar quantity u, given by

$$\begin{aligned} &\frac{\partial u}{\partial t} + a\frac{\partial u}{\partial x} = 0, \qquad -l \le x \le l, \\ &u(x, t = 0) = u_0(x), \\ &u(x = -l, t) = u_L(t), \end{aligned} \tag{3.1}$$

where $a > 0$ is a constant advection velocity, and u must be bounded within $u_{\min} \le u \le u_{\max}$. For example, if u represents the mass fraction of a chemical species we require $u \in [0, 1]$. Initial and left boundary conditions are denoted by $u_0(x)$ and $u_L(t)$, respectively.

The spatial coordinate x is uniformly discretized with N_x grid points, resulting in grid spacing $\Delta x = L_x/(N_x - 1)$, where $L_x = 2l$ is the domain length. The discrete counterpart of x is denoted by $\vec{x} = [x_1,\ x_2,\ \ldots,\ x_{N_x}]^\mathsf{T}$ with $x_i = (i-1)\Delta x$ for $i = 1, 2, \ldots, N_x$. The semi-discrete form of (3.1) can be expressed as

$$\frac{\mathrm{d}\vec{u}}{\mathrm{d}t} + a\mathrm{D}_{2s}\vec{u} = \vec{\mathrm{R}}_{\mathrm{SAT}}, \tag{3.2}$$

where $\vec{u} = [u(x_1),\ u(x_2),\ \ldots,\ u(x_{N_x})]^\mathsf{T}$ contains the numerical approximation of $u(x)$ via a solution to (3.2) at time t. The first-derivative operator $\mathrm{D}_{2s} \in \mathbb{R}^{N_x} \times \mathbb{R}^{N_x}$ is a finite difference approximation of a smooth solution $u(x)$ with $2s$-order of accuracy for the interior grid points, i.e., $\mathrm{D}_{2s}u = \partial u/\partial x + O(\Delta x^{2s})$. In this work, D_{2s} satisfies the summation-by-parts (SBP) property (Kreiss & Scherer, 1974; Strand, 1994)

$$\mathrm{P}_{2s}\mathrm{D}_{2s} + (\mathrm{P}_{2s}\mathrm{D}_{2s})^\mathsf{T} = \mathrm{diag}[-1, 0, \ldots, 0, 1] \in \mathbb{R}^{N_x}, \tag{3.3}$$

where P_{2s} is a symmetric positive-definite matrix (the SBP norm matrix). We consider D_{2s} to be a skew-symmetric operator that contains centered finite-difference stencils for interior grid points

and specific boundary closures that satisfy (3.3). If P_{2s} is a diagonal matrix, first derivative operators D_{2s} satisfying (3.3) provide $2s$-order of accuracy in the interior domain and s-order of accuracy near the boundaries with global accuracy of $s+1$ (e.g., see Kreiss & Scherer, 1974; Strand, 1994, for $s = 1, 2, 3, 4$). Diagonal norms also preserve the SBP property under a coordinate transformation for arbitrary orders of accuracy (Svärd, 2004).

Boundary conditions are enforced weakly via the simultaneous-approximation-term (SAT) boundary treatment, given by $\vec{\mathrm{R}}_{\mathrm{SAT}}$ in (3.2). The combined SBP–SAT formulation ensures energy stability of the discrete system (Bodony, 2010). Details on the specific SAT treatment used in this dissertation are provided in Appendix B. The interested reader may refer to Carpenter *et al.* (1994); Svärd *et al.* (2007); Svärd & Nordström (2008); Nordström *et al.* (2009) for further details on SAT boundary conditions.

The SBP property (3.3) is the discrete counterpart of the integration by parts. This yields numerical stability of combined SBP–SAT schemes. Dual consistency of SBP–SAT can also yield superconvergence (Hicken & Zingg, 2011). This results in a $2s$-order of accuracy when a cost functional of u is numerically approximated even though the u has a $(s+1)$-order of accuracy due to boundary restrictions. In fluid dynamic applications, this function can be a drag force depending on the flow velocity and pressure fields.

3.2.2 Standard SBP dissipation operators

It is well known that centered finite difference operators are capable of generating spurious oscillations due to dispersion errors. A common approach to alleviate this, which is adopted here, is to introduce artificial dissipation. Following Mattsson *et al.* (2004), a $2s$-order dissipation operator, denoted by $\mathrm{D}_{2s}^{(\mathrm{diss})}$, is added to the right-hand side of (3.2) (neglecting the SAT term for brevity) according to

$$\frac{\mathrm{d}\vec{u}}{\mathrm{d}t} + a\mathrm{D}_{2s}\vec{u} = \mathrm{D}_{2s}^{(\mathrm{diss})}\vec{u}, \tag{3.4}$$

which is given by (Mattsson *et al.*, 2004)

$$\mathrm{D}_{2s}^{(\mathrm{diss})} = -\sigma_{2s}^{(\mathrm{diss})}\widetilde{\mathrm{P}}_{2s}^{-1}\widetilde{\mathrm{D}}^{(s)^{\mathsf{T}}}\mathrm{B}\widetilde{\mathrm{D}}^{(s)} = -\sigma_{2s}^{(\mathrm{diss})}\widetilde{\mathrm{P}}_{2s}^{-1}\mathrm{R}_{2s}, \tag{3.5}$$

where B is a positive semidefinite matrix that will be defined later, and $\widetilde{\mathrm{D}}^{(s)}$ is an undivided difference operator such that $\mathrm{D}^{(s)} = \Delta x^{-s}\widetilde{\mathrm{D}}^{(s)}$ is a consistent approximation of $\partial^s/\partial x^s$ with minimum stencil size. Similarly, $\widetilde{\mathrm{P}}_{2s} = \Delta x^{-1}\mathrm{P}_{2s}$, where the SBP norm matrix P_{2s} corresponds to the first derivative operator of D_{2s} according to (3.3). In this expression, $\sigma_{2s}^{(\mathrm{diss})} > 0$ is a user defined coefficient that controls the amount of dissipation, whose magnitude depends upon the grid spacing and order of accuracy of the dissipation operator, i.e., $\sigma_{2s}^{(\mathrm{diss})} \propto \Delta x^{-1}2^{-2s}$. The factor 2^{-2s} in $\sigma^{(\mathrm{diss})}$ was suggested by Diener *et al.* (2007) to ensure the strength of the numerical dissipation is independent of s at high wavenumbers.

Mattsson *et al.* (2004) showed that when a diagonal P_{2s} is considered and $\mathrm{B} = c\mathrm{I}$ (a constant value multiplied by the identity matrix I), $\mathrm{D}_{2s}^{\mathrm{diss}}$ has $2s$-order of accuracy for interior grid points and s-order of accuracy near the boundaries, consistent with the first derivative operator D_{2s} in (3.4). It is possible to modify B near the boundaries to increase accuracy of the dissipation operator as shown by Mattsson *et al.* (2004). The original dissipation operator (3.5) has since been extended and improved, namely through modifications of B, e.g., by making it dependent on the local grid metrics (Vishnampet, 2015) or advection velocity (Nordström, 2006). Dissipation operators satisfying the SBP property with provable entropy-stability have also been developed (Ranocha *et al.*, 2018; Craig P. & Zingg, 2018). Also, dissipation operators (3.5) are extended and improved by modifying B to create MUSCL schemes (Abbas *et al.*, 2009, 2010). In the current work, B is taken to be an identity matrix for the standard scheme and will be modified for the proposed adaptive scheme.

When examining the numerical stability of (3.4), it is useful to define an inner product operator

according to

$$\left\langle \vec{f}, \vec{g} \right\rangle_{\mathrm{P}} = \vec{f}^{\mathsf{T}} \mathrm{P}_{2s} \vec{g}, \tag{3.6}$$

where $\vec{f}$ and $\vec{g}$ are projections of arbitrary smooth functions $f(x)$ and $g(x)$, respectively, on the grid. The corresponding norm is given by $\|f\|_{\mathrm{P}}^2 = \vec{f}^{\mathsf{T}} \mathrm{P}_{2s} \vec{f}$. Thus, numerical stability of the dissipation term in (3.4) is determined by evaluating $\mathrm{d}\,\|u\|_{\mathrm{P}}^2 / \mathrm{d}t = (\mathrm{d}\vec{u}/\mathrm{d}t)^{\mathsf{T}} \mathrm{P}_{2s} \vec{u} + \vec{u}^{\mathsf{T}} \mathrm{P}_{2s} (\mathrm{d}\vec{u}/\mathrm{d}t)$, given by (Mattsson *et al.*, 2004)

$$\frac{\mathrm{d}}{\mathrm{d}t} \|u\|_P^2 = -\Delta x \sigma_{2s}^{(\mathrm{diss})} \left(\widetilde{\mathrm{D}}^{(s)} \vec{u} \right)^{\mathsf{T}} \left(\mathrm{B}^{\mathsf{T}} + \mathrm{B} \right) \left(\widetilde{\mathrm{D}}^{(s)} \vec{u} \right), \tag{3.7}$$

where the advection term is neglected. The right-hand side of the above equation is always non-positive if B is a positive semidefinite matrix.

To evaluate the efficacy of the dissipation operator (3.5) in absorbing energy across different wavenumbers, we consider a periodic domain and obtain the solution of (3.5) at a grid point $x_i = i\Delta x$ in Fourier space via $u(x_i, t) = \sum_\omega \sum_\kappa \hat{u}(\kappa, t) e^{j\omega t} e^{j\kappa i \Delta x}$, where κ and ω are spatial and temporal modes, respectively, and $j = \sqrt{-1}$. Inserting this into (3.4) yields (Mattsson *et al.*, 2004)

$$j\omega(\kappa) = -2^{2s} \sigma_{2s}^{(\mathrm{diss})} \sin^{2s} \left(\frac{\kappa \Delta x}{2} \right). \tag{3.8}$$

Note that $j\omega$ is a non-positive real number according to (3.8); thus, it determines the strength of exponential decay (i.e., dissipation) of the solution through time with $u \propto e^{j\omega t}$. As previously mentioned, we may consider

$$\sigma_{2s}^{(\mathrm{diss})} = \widetilde{\sigma}^{(\mathrm{diss})} / 2^{2s}; \tag{3.9}$$

thus, the factor of 2^{2s} on the right-hand side of (3.8) cancels with $\sigma_{2s}^{(\mathrm{diss})}$.

Figure 3.1a shows $-j\omega(\kappa)$ with $2^{2s}\sigma_{2s}^{(\mathrm{diss})} = 1$. According to (3.8), $-j\omega(\kappa)$ is positive except for

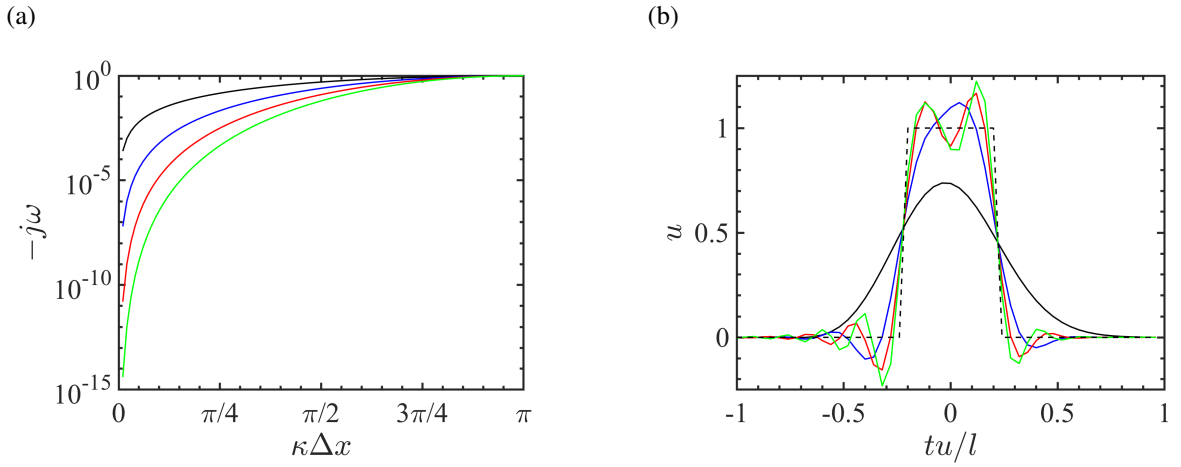

Figure 3.1: (*a*) Exponential decay (dissipation strength) according to (3.8) corresponding to the dissipation operator (3.5). (*b*) Numerical solution to (3.4) with an initial conditions of a rectangular pulse (−−) advanced in time for one rotation using second-order ($s = 1$; black), fourth-order ($s = 2$; blue), sixth-order ($s = 3$; red), and eighth-order ($s = 4$; green) operators.

$\kappa = 0$, where $-j\omega(\kappa) = 0$. This confirms that the numerical solution of (3.4) exponentially decays with time for $s \geq 1$ except for mode $\kappa = 0$ whose solution remains constant. As can be seen, all dissipation operators exhibit similar amount of dissipation at the highest resolvable wavenumbers ($\kappa\Delta x \to \pi$), when normalizing the dissipation amount by 2^{2s}. However, important differences can be observed at smaller wavenumbers. Namely, the exponential factor $-j\omega$ drops sharply as the wavenumber decreases for high-order dissipation operators (i.e., dissipation operators using high-order derivatives target the smallest scale fluctuations only). On the other hand, dissipation using low-order derivatives exhibit larger values of $-j\omega$ at small κ, resulting in broadband energy reduction (dissipation across all scales).

Figure 3.1b shows the solution to Eq. (3.4) for a square pulse advected in a periodic domain of length $2l = 1$ discretized using with $N_x = 51$ points after one rotation for dissipation orders $s = 1, 2, 3, 4$. In each case, dissipation and first derivative operators have the same order of accuracy, and $\widetilde{\sigma}^{(\text{diss})} = \Delta x^{-1}$. The initial condition is a rectangular pulse (see Fig 3.1b). To eliminate temporal truncation errors, the solution is advanced in time using an explicit first-order Euler method with a small Courant–Friedrichs–Lewy (CFL) number of $\Delta t a/\Delta x = 0.02$, where Δt is the timestep size. It can be seen that all dissipation operators, except for $s = 1$, yield spurious fluctuations with

overshoots/undershoots near discontinuities. On the other hand, the second-order scheme provides an overly diffused solution. In summary, the second-order solution is bounded while higher-order operators yield unbounded solutions with improved accuracy. Therefore, it is favorable to employ second-order dissipation in regions with sharp gradients, such as regions with shocks or when the solution is locally unbounded, but use high-order dissipation operators in smooth regions to retain small scale fluctuations. Such a procedure is presented in the following section.

3.2.3 Adaptive dissipation for preserving scalar boundedness

We begin with the $2s$-order dissipation term (3.5) in its continuous form, given by (Mattsson *et al.*, 2004)

$$\frac{\partial u}{\partial t} = (-1)^{s-1} \frac{\partial^s}{\partial x^s} \left(b \frac{\partial^s u}{\partial x^s} \right), \tag{3.10}$$

where $b(x)$ is a non-negative smooth function that represents the continuous counterpart of B in (3.5). Here, $\partial^s / \partial x^s$ corresponds to the difference operator $\mathrm{D}^{(s)} = \Delta x^{-s} \widetilde{\mathrm{D}}^{(s)}$, where $\widetilde{\mathrm{D}}^{(s)}$ is used in (3.5).

To demonstrate the dissipative behavior of the right-hand side of (3.10), we define the continuous counterpart of (3.6), given by

$$\langle f, g \rangle = \int_{x=-l}^{x=l} f(x) g(x) \, \mathrm{d}x, \tag{3.11}$$

where f and g are arbitrary smooth functions. A corresponding norm is also defined according to $\|f\|^2 = \int_{-l}^{l} f^2 \, \mathrm{d}x$. Multiplying both sides of (3.10) by u and integrating by parts yields

$$\frac{1}{2} \frac{\mathrm{d}}{\mathrm{d}t} \|u\|^2 = (-1)^{2s-1} \int_{-l}^{l} b \left(\frac{\partial^s u}{\partial x^s} \right)^2 \mathrm{d}x, \tag{3.12}$$

where the boundary terms of b and their derivatives are assumed to be zero for simplicity. The

right-hand side of (3.12) is always non-positive since $b(x) \geq 0$, consequently the energy of the continuous system decays in time. In other words, the dissipation term on the right-hand side of (3.10) effectively 'absorbs' global energy of the system. In the previous section, we demonstrated how this dissipative property dampens spurious oscillations generated in the discrete equations. Namely, the discrete second-order dissipation operator absorbs a broad range of spurious oscillation modes, especially at low wavenumbers. Thus, we propose to locally switch to second-order in regions that exhibit excursion errors. To dampen spurious high wavenumber unresolved modes, the high-order dissipation operator is employed in the rest of the domain.

A sensor, ψ, is introduced to locally switch between dissipation operators, where $\psi = 0$ and $\psi = 1$ activate the high-order and second-order operators, respectively, and therefore we require $\psi \in [0, 1]$. Several sensors have been introduced in the literature (e.g., see Zhao *et al.*, 2020, and references therein), which are typically defined based on variations of a flow state variable (Harten, 1978; Jameson *et al.*, 1981; Ren *et al.*, 2003). Physics-based sensors have also been considered based on vorticity and the rate of dilatation (Ducros *et al.*, 1999; Larsson *et al.*, 2007; White *et al.*, 2012). In the present study, as motivated by Herrmann *et al.* (2006), the sensor activates the second-order dissipation operator in unbounded regions, according to

$$\psi(u) = \begin{cases} 1; & u > u_{\max} + \epsilon \quad \text{or} \quad u < u_{\min} - \epsilon \\ 0; & \text{otherwise,} \end{cases} \tag{3.13}$$

where $\epsilon \geq 0$ is a user-defined tolerance. In some cases, even a small amount of unboundedness cannot be handled by the computational solver, in which case $\epsilon = 0$ should be considered. However, $\epsilon = 0$ could potentially activate the second-order operator in undesired regions of the flow, e.g., where u slightly exceeds its limits due to round off errors, which could result in an overly dissipative system. Thus, a trade-off between accuracy of the solution and unboundedness is made, which will be evaluated in later sections.

3.2.3.1 Unconditionally stable formulation

The sensor can be applied to the dissipation operator (3.10) in a number of ways. We first propose to blend the second-order ($s = 1$) and high-order ($s > 1$) operators by replacing b with ψ for the former and $b = 1 - \psi$ for the latter, according to

$$\frac{\partial u}{\partial t} + a\frac{\partial u}{\partial x} = \frac{\partial}{\partial x}\left(\psi\frac{\partial u}{\partial x}\right) + (-1)^{s-1}\frac{\partial^s}{\partial x^s}\left[(1-\psi)\frac{\partial^s u}{\partial x^s}\right]. \tag{3.14}$$

Its discrete counterpart is given by

$$\begin{aligned}\frac{\mathrm{d}\vec{u}}{\mathrm{d}t} + \frac{a}{\Delta x}\mathrm{D}_{2s}\vec{u} = &-\sigma_2^{(\mathrm{diss})}\widetilde{\mathrm{P}}_{2s}^{-1}\widetilde{\mathrm{D}}^{(1)^{\mathsf{T}}}\Psi\widetilde{\mathrm{D}}^{(1)}\vec{u} \\ &-\sigma_{2s}^{(\mathrm{diss})}\widetilde{\mathrm{P}}_{2s}^{-1}\widetilde{\mathrm{D}}^{(s)^{\mathsf{T}}}\left(\mathrm{I}_{N_x} - \Psi\right)\widetilde{\mathrm{D}}^{(s)}\vec{u},\end{aligned} \tag{3.15}$$

where Ψ is a diagonal matrix whose diagonal elements are $\psi(x_i)$, and I_{N_x} denotes a $N_x \times N_x$ identity matrix. A similar approach was used in Abbas *et al.* (2009) and Eriksson *et al.* (2011) for activating a MUSCL-type SBP dissipation operator near discontinuities. In their approach, the right-hand side of (3.15) is replaced with $-\mathrm{P}^{-1}\widetilde{\mathrm{D}}^{1^{\mathsf{T}}}\Psi\mathrm{B}_M\widetilde{\mathrm{D}}^{1}\vec{u}$ with diagonal matrix B_M, resulting in the standard MUSCL formulation near shocks when $\psi = 1$.

If $0 \leq \psi \leq 1$ is a smooth function, (3.14) and (3.15) will not add energy to the system according to (3.12) and (3.7), respectively (note that Ψ and $\mathrm{I}_{N_x} - \Psi$ are positive semidefinite matrices). In other words, the right-hand side of (3.14) is dissipative and its discrete counterpart (3.15) is numerically stable. However, expressing ψ in terms of a Heaviside function, as is done in (3.13), results in a non-differentiable function that could generate local dispersion errors. However, to distinguish between the formulation presented below, we refer to this scheme as unconditionally stable. Its effect on preserving boundedness will be assessed in later sections. Note that (3.13) could be replaced by a smooth sensor (e.g., a regularized Heaviside function), which would indeed provide an energy estimate, but could result in overly dissipative solution near gradients.

Regarding the discrete form of the adaptive dissipation (3.15), note that both low- and high-

order operators use the same SBP norm matrix P_{2s} given by (3.3). P_{2s} corresponds to the $2s$-order first-derivative operator D_{2s} of the advection term on the left-hand side of (3.15). This is essential to preserve numerical stability of the scheme with respect to the P_{2s} inner product (3.6) as shown in (3.7).

3.2.3.2 Conditionally stable formulation

An alternative approach is to place the sensor outside of the dissipation operator to avoid differentiating (a potentially non-differentiable) ψ, according to

$$\frac{\partial u}{\partial t} + a\frac{\partial u}{\partial x} = \psi\frac{\partial^2 u}{\partial x^2} + (-1)^{s-1}(1-\psi)\frac{\partial^{2s} u}{\partial x^{2s}}, \tag{3.16}$$

where b in (3.10) is set to unity. However, this form does not guarantee an energy estimate in general. Considering the second-order dissipation term in (3.16) and neglecting the advection term, its stability is analyzed according to

$$\frac{1}{2}\frac{\mathrm{d}}{\mathrm{d}t}\|u\|^2 = -\int_{-l}^{l}\frac{\partial \psi u}{\partial x}\frac{\partial u}{\partial x}\,\mathrm{d}x = -\int_{-l}^{l}\psi\left(\frac{\partial u}{\partial x}\right)^2\,\mathrm{d}x - \int_{-l}^{l}u\frac{\partial \psi}{\partial x}\frac{\partial u}{\partial x}\,\mathrm{d}x, \tag{3.17}$$

where integration by part has been applied and resulting boundary terms are neglected. It can be seen that the first term on the right-hand side of (3.17) is always non-positive since $\psi \geq 0$, and thus does not add energy to the system. However, the second term can be positive or negative and thus may add energy to the system. Noting that ψ given by (3.13) is expressed as a Heaviside function in terms of u, the chain rule can be employed, such that $\partial\psi/\partial x = (\mathrm{d}\psi/\mathrm{d}u)(\partial u/\partial x)$ where $\mathrm{d}\psi/\mathrm{d}u$ yields a Dirac delta function in regions where the sensor changes. Thus, it is reasonable to assume that the amount of energy added to the system via the second term on the right-hand side of (3.17) is minimal. A similar analysis is performed on the high-order dissipation term (the second term on the right-hand side of (3.16)) in Appendix C, which yields similar results. Thus, we consider the formulation in (3.16) to be conditionally stable.

Finally, the discrete form of (3.16) is given by

$$\frac{\mathrm{d}\vec{u}}{\mathrm{d}t} + \frac{a}{\Delta x}\mathrm{D}_{2s}\vec{u} = -\sigma_2^{(\mathrm{diss})}\Psi\widetilde{\mathrm{P}}_{2s}^{-1}\mathrm{R}_2\vec{u} - \sigma_{2s}^{(\mathrm{diss})}(\mathrm{I}_{N_x} - \Psi)\widetilde{\mathrm{P}}_{2s}^{-1}\mathrm{R}_{2s}\vec{u}, \tag{3.18}$$

where $\mathrm{R}_{2s} = -\widetilde{\mathrm{D}}^{(s)^{\mathsf{T}}}\mathrm{B}\widetilde{\mathrm{D}}^{(s)}$ is a positive semi-definite matrix given by (3.5). Similar to the conditionally stable formulation (3.15), we use P_{2s}^{-1} for both dissipation operators in (3.18). Thus, it can be shown that

$$\begin{aligned}\frac{\mathrm{d}}{\mathrm{d}t}\left\|\vec{u}\right\|_{\mathrm{P}_{2s}}^2 = &-\Delta x\sigma_2^{(\mathrm{diss})}\vec{u}^{\mathsf{T}}\left[(\Psi\mathrm{R}_{2s})^{\mathsf{T}} + \Psi\mathrm{R}_{2s}\right]\vec{u} \\ &-\Delta x\sigma_{2s}^{(\mathrm{diss})}\vec{u}^{\mathsf{T}}\left\{\left[(\mathrm{I}_{N_x} - \Psi)\mathrm{R}_{2s}\right]^{\mathsf{T}} + (\mathrm{I}_{N_x} - \Psi)\mathrm{R}_{2s}\right\}\vec{u}.\end{aligned} \tag{3.19}$$

Here, we applied the identify $\mathrm{P}_{2s}^{-1}\Psi = \Psi\mathrm{P}_{2s}^{-1}$ since both Ψ and P_{2s} are diagonal matrices. While R_2, Ψ, R_{2s}, and $\mathrm{I}_N - \Psi$ are positive semidefinite matrices, $\mathrm{R}_2\Psi$ and $\mathrm{R}_{2s}(\mathrm{I}_N - \Psi)$ will not necessarily be. However, as previously mentioned, the right-hand side of (3.19) is not expected to be positive in the majority of the flow.

3.3 Adjoint-based formulation

3.3.1 Continuous adjoint formulation with standard dissipation

In this section, the corresponding adjoint equation of linear advection equation (3.1) with dissipation (3.10) is presented. We rewrite the governing equation (also known as the primal equation) of (3.1) and (3.10) according to

$$\mathcal{N}_{1d}[u;\vec{f}] \equiv \frac{\partial u}{\partial t} + a\frac{\partial u}{\partial x} - (-1)^{s-1}\frac{\partial^s}{\partial x^s}\left(b\frac{\partial^s u}{\partial x^s}\right) = 0. \tag{3.20}$$

A QoI $\mathcal{J}$ is computed, based on state values u and control parameter $\vec{f}$, over a time horizon $t \in [0, t_f]$ and domain space $x \in [-l, l]$, given by

$$\mathcal{J}[u; \vec{f}] = \int_{t=0}^{t=t_f} \int_{x=-l}^{x=l} \mathcal{I}[u; \vec{f}] \, \mathrm{d}x \, \mathrm{d}t, \tag{3.21}$$

where integrand $\mathcal{I}$ determines local and temporal values of the QoI, and it should be specified depending on the problem of interest. Following what was done in Chapter 2.4.1 yields the adjoint PDE and sensitivity, given by

$$\frac{\partial u^\dagger}{\partial t} + a\frac{\partial u^\dagger}{\partial x} = -(-1)^{s-1}\frac{\partial^s}{\partial x^s}\left(b\frac{\partial^s u^\dagger}{\partial x^s}\right) - \frac{\partial \mathcal{I}}{\partial u}, \tag{3.22}$$

and

$$\frac{\delta \mathcal{J}}{\delta \vec{f}} = \int_{t=0}^{t=t_f} \int_{x=-l}^{x=l} \frac{\partial \mathcal{I}}{\partial \vec{f}} \, \mathrm{d}x \, \mathrm{d}t - \int_{t=0}^{t=t_f} \int_{x=-l}^{x=l} u^\dagger \frac{\partial \mathcal{N}}{\partial \vec{f}} \, \mathrm{d}x \, \mathrm{d}t, \tag{3.23}$$

respectively. Here, it is assumed that b in (3.10) is independent of u. The first term on the right-hand side of (3.23) is typically zero since most of QoIs do not explicitly depend on $\vec{f}$. However, we keep it here for the sake of generality.

Neglecting the right-hand side of the adjoint equation (3.22), it is the same as the primal linear advection equation (3.1) with the same advection velocity a in the same direction. As can be seen on the first term of the right-hand side of the adjoint equation, the dissipation term has an opposite sign compared to the primal dissipation term (3.10). Thus, the dissipation term adds energy to the adjoint energy $\left\|u^\dagger\right\|^2/2$ instead of dissipating it. To overcome this issue, adjoint equations must be integrated reversely in time, which is from t_f to t_0. This results in a moving wave in the opposite direction of the primal simulation. In addition, the QoI controls adjoint solutions and applies as an external source term in (3.22) via $\partial \mathcal{I}/\partial u$. In other words, the adjoint solution completely depends on the definition of the QoI.

3.3.2 Discrete adjoint formulation with standard dissipation

We first show the semi-discrete adjoint formulation and briefly describe the full-discrete one later. We rewrite the spatially discretized primal equation according to

$$\frac{\mathrm{d}\vec{u}}{\mathrm{d}t} - \vec{\mathcal{R}}\left[\vec{u}; \vec{f}\right] = 0, \tag{3.24}$$

where $\vec{\mathcal{R}}\left[\vec{u}; \vec{f}\right]$ includes all the advection and dissipation terms discretized via the SBP operators and also contains SAT boundary terms as shown in (3.2) and (3.4). Following what was done in 2.4.2, the discrete adjoint equation and sensitivity are obtained, given by

$$\frac{\mathrm{d}\vec{u}^{\dagger}}{\mathrm{d}t} = -\mathrm{P}_{2s}^{-1}\left(\frac{\partial\vec{\mathcal{R}}}{\partial\vec{u}}\right)^{\mathsf{T}}\mathrm{P}_{2s}\vec{u}^{\dagger} - \frac{\partial\mathcal{I}}{\partial\vec{u}}, \tag{3.25}$$

and

$$\frac{\delta\mathcal{J}}{\delta\vec{f}} = \int_{t=t_0}^{t=t_f}\left[\frac{\partial\mathcal{I}}{\partial\vec{f}} - \vec{u}^{\dagger\,\mathsf{T}}\mathrm{P}_{2s}\left(\frac{\partial\vec{\mathcal{R}}}{\partial\vec{f}}\right)\right]\Delta x\,\mathrm{d}t, \tag{3.26}$$

respectively. Substituting the terms of $\vec{\mathcal{R}}$ from (3.2) and (3.4) into the adjoint equation (3.25) yields

$$\frac{\mathrm{d}\vec{u}^{\dagger}}{\mathrm{d}t} = a\mathrm{P}_{2s}^{-1}\mathrm{D}_{2s}{}^{\mathsf{T}}\mathrm{P}_{2s}\vec{u}^{\dagger} - \mathrm{P}_{2s}^{-1}\mathrm{D}_{2s}^{(\mathrm{diss})^{\mathsf{T}}}\mathrm{P}_{2s}\vec{u}^{\dagger} - \mathrm{P}_{2s}^{-1}\left(\frac{\partial\vec{\mathrm{R}}_{\mathrm{SAT}}}{\partial\vec{u}}\right)^{\mathsf{T}}\mathrm{P}_{2s}\vec{u}^{\dagger} - \frac{\partial\mathcal{I}}{\partial\vec{u}}. \tag{3.27}$$

Neglecting all terms on the right-hand side excluding the dissipation and substituting (3.5) into it yields

$$\frac{\mathrm{d}\vec{u}^{\dagger}}{\mathrm{d}t} = \sigma_{2s}^{(\mathrm{diss})}\widetilde{\mathrm{P}}_{2s}^{-1}\widetilde{\mathrm{D}}^{(s)^{\mathsf{T}}}\mathrm{B}^{\mathsf{T}}\widetilde{\mathrm{D}}^{(s)}\vec{u}^{\dagger} = \sigma_{2s}^{(\mathrm{diss})}\widetilde{\mathrm{P}}_{2s}^{-1}\mathrm{R}_{2s}^{\mathsf{T}}\vec{u}^{\dagger}. \tag{3.28}$$

Except a minus sign behind the adjoint dissipation, it is equal to the primal dissipation (3.5) if B is a symmetric matrix, e.g., a diagonal matrix.

For simplicity, we only showed semi-discrete adjoint formulation in this section. Once the time integrator is determined, the full-discrete primal equation (3.10), inner product (3.11), and quantity of interest (3.21) are considered, and the corresponding discrete adjoint equation and sensitivity are obtained similar to the procedure presented before. In this work, we consider a standard fourth-order Runge–Kutta (RK) time integrator. For brevity, we skip fully discrete adjoint formulation in this section. The fully-discrete QoI formulation and adjoint equations for such a time integrator can be found in Chapter 2.4.2, and its full description is provided by Vishnampet *et al.* (2015).

3.3.3 Adjoint formulation of adaptive dissipation

3.3.3.1 Unconditionally stable adaptive dissipation

Adjoint equations of the adaptive dissipation schemes are computed through a similar approach performed for the standard SBP dissipation operator. Corresponding adjoint equations for the stable scheme (3.14) is given by

$$\begin{aligned}\frac{\partial u^\dagger}{\partial t} + a\frac{\partial u^\dagger}{\partial x} = &-\frac{\partial}{\partial x}\left(\psi\frac{\partial u^\dagger}{\partial x}\right) - (-1)^{s-1}\frac{\partial^s}{\partial x^s}\left[(1-\psi)\frac{\partial^s u^\dagger}{\partial x^s}\right] - \frac{\partial \mathcal{I}}{\partial u} \\ &+ \frac{\partial \psi}{\partial u}\frac{\partial u}{\partial x}\frac{\partial u^\dagger}{\partial x} + \frac{\partial(1-\psi)}{\partial u}\frac{\partial^s u}{\partial x^s}\frac{\partial^s u^\dagger}{\partial x^s}.\end{aligned} \tag{3.29}$$

Note that ψ depends on u. Besides changing of sign in the dissipation term and the added source term of the QoI, additional terms exist in the adjoint equation compared to the adjoint formulation of the standard dissipation operator (3.22). These terms come from variations of the sensor ψ with respect to u. In this work, ψ is combinations of Heaviside functions according to (3.13); thus, $\mathrm{d}\psi/\mathrm{d}u$ is combinations of Dirac delta functions. If the sensor is activated only in small regions of the domain, $\mathrm{d}\psi/\mathrm{d}u$ is non-zero only in a few areas of the domain. In this case, we could neglect $\mathrm{d}\psi/\mathrm{d}u$ in (3.29).

Similar to the primal equation (3.14), it would be preferred that the sensor ψ smoothly changes with u since its spatial derivatives have appeared in the adjoint equation as well. In this case, both

primal and adjoint solutions would be smooth. However, it may not be able to sufficiently preserve boundedness or could add more dissipation to the state solutions.

Similarly, the semi-discrete adjoint formulation of unconditionally stable dissipation scheme is given by

$$\frac{\mathrm{d}\vec{u}^{\dagger}}{\mathrm{d}t} = \sigma_2^{(\mathrm{diss})}\widetilde{\mathrm{P}}_{2s}^{-1}\widetilde{\mathrm{D}}^{(1)^{\mathsf{T}}}\Psi\widetilde{\mathrm{D}}^{(1)}\vec{u}^{\dagger} + \sigma_{2s}^{(\mathrm{diss})}\widetilde{\mathrm{P}}_{2s}^{-1}\widetilde{\mathrm{D}}^{(s)^{\mathsf{T}}}\left(\mathrm{I}_{N_x} - \Psi\right)\widetilde{\mathrm{D}}^{(s)}\vec{u}^{\dagger} - \frac{\partial \mathcal{I}}{\partial \vec{u}}, \tag{3.30}$$

where the advection term, SAT boundary terms, and the variations of the sensor to u have been neglected.

3.3.3.2 Conditionally stable adaptive dissipation

We can similarly derive an adjoint equation of (3.16), given by

$$\begin{aligned}\frac{\partial u^{\dagger}}{\partial t} + a\frac{\partial u^{\dagger}}{\partial x} =& -\frac{\partial^2 \psi u^{\dagger}}{\partial x^2} - (-1)^{s-1}\frac{\partial^{2s}(1-\psi)u^{\dagger}}{\partial x^{2s}} - \frac{\partial \mathcal{I}}{\partial u} \\ &- \frac{\partial \psi}{\partial u}\frac{\partial^2 u}{\partial x^2}u^{\dagger} - (-1)^{s-1}\frac{\partial(1-\psi)}{\partial u}\frac{\partial^{2s}u}{\partial x^{2s}}u^{\dagger}.\end{aligned} \tag{3.31}$$

We can similarly neglect addition terms on the second line of the above equation as mentioned before unless ψ smoothly changes with u. In contrast to the adjoint formulation of the unconditional stable adaptive dissipation, we can see that the adjoint of the conditionally stable dissipation operator is different than its corresponding primal dissipation term. In the primal equation, ψ is outside of $\partial^{2s}/\partial x^{2s}$, which makes the method effective when the sensor is not a smooth function. However, the sensor should be $2s$-times differentiable in its adjoint equations, and we will show that the adjoint solution can become noisy if a discontinuous sensor such as (3.13) is employed.

Similarly, the semi-discrete adjoint dissipation of conditionally adaptive dissipation (3.18) is

given by

$$\frac{\mathrm{d}\vec{u}^{\dagger}}{\mathrm{d}t} = \sigma_2^{(\mathrm{diss})}\widetilde{\mathrm{P}}_{2s}^{-1}\mathrm{R}_2^{\mathsf{T}}\Psi\vec{u}^{\dagger} + \sigma_{2s}^{(\mathrm{diss})}\widetilde{\mathrm{P}}_{2s}^{-1}\mathrm{R}_{2s}^{\mathsf{T}}(\mathrm{I}_{N_x} - \Psi)\vec{u}^{\dagger} - \frac{\partial\mathcal{I}}{\partial\vec{u}} + \sigma_2^{(\mathrm{diss})}\widetilde{\mathrm{P}}_{2s}^{-1}\left(\mathrm{R}_2 u\right)^{\mathsf{T}}\frac{\mathrm{d}\Psi}{\mathrm{d}u}\vec{u}^{\dagger} + \sigma_{2s}^{(\mathrm{diss})}\widetilde{\mathrm{P}}_{2s}^{-1}\left(\mathrm{R}_{2s}u\right)^{\mathsf{T}}\left(-\frac{\mathrm{d}\Psi}{\mathrm{d}u}\right)\vec{u}^{\dagger}, \tag{3.32}$$

where the advection and SAT boundary terms are neglected, and $\mathrm{d}\Psi/\mathrm{d}\vec{u}$ is a diagonal matrix whose diagonal values are $\mathrm{d}\psi(u_i)/\mathrm{d}u_i$. This matrix may be neglected when ψ is combinations of Heaviside functions of u. Equation (3.32) is similar to continuous adjoint dissipation formulation of the conditionally adaptive scheme (3.31) according to definition of R_{2s} in (3.5).

3.3.4 Dual consistency of adaptive schemes

Employing SBP–SAT discretization and artificial dissipation operators of Mattsson *et al.* (2004) provide consistency between continuous and discrete adjoint formulation if special care is considered in SAT parameters and discretization of the QoI (Hicken & Zingg, 2011, 2014; Vishnampet, 2015). This 'dual consistency' has two major outcomes: (*i*) A discrete adjoint sensitivity is not contaminated by spurious waves associated with discretizing governing equations (Vishnampet, 2015), and (*ii*) Accuracy of an appropriately discretized QoI is equal to interior accuracy used in the SBP discretization, also known as superconvergent functional estimates (Hicken & Zingg, 2011).

Recall that discrete adjoint formulation is obtained from discretized primal PDEs. Thus, numerical modes associated with the discretization scheme can strongly affect adjoint stability and generate oscillations in the adjoint solutions even though they are not observed in primal simulations (e.g., see Sirkes & Tziperman, 1997). However, consistency between discrete and continuous adjoint formulations (i.e., dual consistent property) avoids these oscillations (e.g., see Hicken & Zingg, 2014; Vishnampet, 2015).

The superconvergence outcome of dual consistency is also important since overall accuracy of state variables is usually restricted by the accuracy of boundary stencils. In many practical

applications, however, accuracy of a cost functional or a QoI is instead favorable, especially in optimization applications. When a coordinate transformation is required for complex geometries (e.g., flow passing an airfoil), the stability of SBP schemes constrains its accuracy (Svärd, 2004). In other words, we have to use SBP operators whose order of accuracy for boundary and interior stencils is 's' and '$2s$', respectively, resulting in global accuracy of '$s+1$'. Despite boundary restriction on global accuracy, it is shown that a properly discrete approximation of a QoI has $2s$-order of accuracy (superconvergence) due to dual consistency of SBP–SAT (Hicken & Zingg, 2011).

Provided smooth primal and adjoint solutions, it is shown that including the standard SBP dissipation (3.5) to the Euler equations discretized by an SBP–SAT scheme does not impact dual consistency (Hicken & Zingg, 2014). Inspecting dual consistency of the proposed adaptive SBP dissipation operators is beyond the scope of this work; however, the same procedure of Hicken & Zingg (2014) would illustrate that including adaptive dissipation operators (3.15) and (3.18) should be dual consistency.

In adjoint formulation of both unconditionally- and conditionally stable adaptive dissipation schemes, the sensor and its high-order derivatives have to be continuous according to (3.29) and (3.31), respectively. However, we introduced a sensor (3.13) that employs Heaviside functions and is not thus differentiable. We study a one-dimensional numerical test in Chapter 3.4.2, which shows that using a discontinuous sensor could result in spurious oscillations in the adjoint solution especially with the conditionally stable adaptive scheme (3.18). Thus, we expect that both adaptive dissipation schemes would not be dual consistent when a non-differentiable sensor is employed, as we will show its noisy adjoint solution in Fig. 3.4d. Even if the sensor choice does not affect dual consistency, we anticipate that superconvergent functional estimates are not observed in both adaptive schemes when their continuous adjoint solution is not smooth (Hicken & Zingg, 2011).

Alternatively, a regularized Heaviside function can be used as a sensor to ensure being differentiable. In this case, more than one user-defined parameter as ϵ in (3.13) should be required to be manipulated. Also, such a sensor will potentially add more second-order dissipation in the so-

lution and damp more physical fluctuations. In addition, it might not be able to properly preserve boundedness of scalars. We will show that employing adjoint-based optimization of conditionally stable adaptive dissipation (3.32) with a simple sensor of (3.13) is able to suppress mixing even though the SBP–SAT scheme would not be dual consistent.

3.4 1D advection equation

In this section, the accuracy and unboundedness of the adaptive dissipation schemes are evaluated for both smooth and non-smooth solutions. In addition, their adjoint formulations are studied on a non-smooth solution, and an adjoint-based optimizer is employed to improve boundedness via manipulating the sensor (3.13).

3.4.1 Smooth initial condition

The one-dimensional advection equation (3.1) is solved with initial condition $u_0(x) = \sin^4(\pi x)$ in a domain of $x \in [-1/2, 1/2]$ with periodic boundary conditions discretized using $N_x = 33$, 65, 129, and 257 grid points. The sixth-order first derivative operator is used for all of the tests. Comparisons are made between the sixth-order dissipation operator and the unconditionally stable and conditionally stable formulations, with a dissipation coefficient of $\sigma_{2s}^{(\text{diss})}$ of (3.5) set to 2^{-2s}. The sensor threshold in (3.13) is set to $\epsilon = 0$. The simulation is integrated for one rotation of the initial condition with a standard explicit fourth-order Runge–Kutta scheme. The timestep size is kept the same in each case, with CFL=0.02 for the finest grid. Thus, temporal discretization errors are expected to be minimal.

To assess the accuracy of the solution, L_p norm errors are computed according to

$$L_2(t) = \sqrt{\frac{1}{L_x} \sum_{i=1}^{N_x-1} [u_i(t) - u_{\text{exact}}(x_i, t)]^2 \ \Delta x} \,, \tag{3.33}$$

and

$$L_\infty(t) = \max_{i=1,\ldots,N_x-1} |u_i(t) - u_{\text{exact}}(x_i, t)|\,, \tag{3.34}$$

where $u_{\text{exact}}(x_i, t)$ denotes the exact solution at a grid point x_i and time t. The degree of local unboundedness is measured according to

$$\varepsilon^b(x_i, t) = \begin{cases} 0 & \text{if} \quad 0 \le u(x_i, t) \le 1 \\ -u(x_i, t) & \text{if} \quad u(x_i, t) < 0 \\ u(x_i, t) - 1 & \text{if} \quad u(x_i, t) > 1. \end{cases} \tag{3.35}$$

With this, the following norms are considered:

$$\varepsilon_1^b(t) = \frac{1}{L_x} \sum_{i=1}^{N_x-1} \varepsilon^b(x_i, t)\, \Delta x, \tag{3.36}$$

and

$$\varepsilon_\infty^b(t) = \max_{i=1,\ldots,N_x-1} \varepsilon^b(x_i, t). \tag{3.37}$$

We briefly note that because periodic boundary conditions are enforced, the value at $i = N_x$ is omitted.

A summary of these norms after one-rotation of the initial condition is provided in Table 3.1. It can be seen that the order of accuracy, as given by the L_p norms, remains relatively unchanged between the sixth-order and adaptive formulations, exhibiting sixth-order convergence under grid refinement. As previously mentioned, the adaptive schemes consider $\epsilon = 0$, which provides the most second-order dissipation, yet this is not seen to impact the order of accuracy. Also, the conditionally stable formulation is seen to preserve boundedness for all of the grid sizes considered. The unconditionally stable formulation provides lower boundedness error compared to the traditional (high-order) scheme for the coarsest grids, and preserves boundedness with finer resolution.

Table 3.1: Accuracy and boundedness errors for $u_0 = \sin^4(\pi x)$.

Dissipation scheme	N_x	L_2 error	L_2 order	L_∞ error	L_∞ order	ε^b_∞ error	ε^b_∞ order
Sixth-order	33	2.87e-05	—	4.11e-05	—	6.45e-06	—
	65	4.58e-07	5.97	6.66e-07	5.95	1.04e-07	5.96
	129	7.20e-09	5.99	1.05e-08	5.99	1.64e-09	5.99
	257	1.13e-10	6.00	1.64e-10	6.00	2.56e-11	6.00
Adaptive	33	2.86e-05	—	4.19e-05	—	2.65e-06	—
(unconditionally	65	4.58e-07	5.96	6.71e-07	5.96	7.16e-09	8.53
stable)	129	7.20e-09	5.99	1.05e-08	6.00	0	—
	257	1.13e-10	6.00	1.64e-10	6.00	0	—
Adaptive	33	2.85e-05	—	4.14e-05	—	0	—
(conditionally	65	4.58e-07	5.96	6.67e-07	5.95	0	—
stable)	129	7.20e-09	5.99	1.05e-08	5.99	0	—
	257	1.13e-10	6.00	1.64e-10	6.00	0	—

It is evident from these results that the conditionally stable scheme is more effective at preserving boundedness compared to its unconditionally stable counterpart. In addition, the adaptive schemes retain high-order accuracy for the smooth solution considered here.

3.4.2 Discontinuous initial condition

The one-dimensional advection equation (3.1) is solved with a canonical discontinuous initial condition (Jiang & Shu, 1996) as shown in Fig 3.2. A domain of size $2l = 2$ with periodic boundary conditions is discretized with $N_x = 129$ grid points. The solution is integrated in time by a standard fourth-order Runge–Kutta scheme with CFL = 0.5. Simulations were performed for four rotations of the initial condition using sixth-order derivative operators combined with different artificial dissipation schemes. Both unconditionally- and conditionally-stable schemes are considered with $\epsilon = 0$ and $\sigma^{\text{diss}}_{2s} = \Delta x^{-1} 2^{-2s}$.

As can be seen in Fig. 3.2a, the second-order scheme provides an overly diffused solution. The sixth-order scheme, however, produces a more accurate result, albeit with maximum over/undershoots of $\varepsilon^b_\infty = 0.092$ after four rotations (see Fig. 3.2b). On the other hand, both the unconditionally- and conditionally-stable adaptive schemes significantly reduce the excursion errors, with maximum boundedness errors of $\varepsilon^b_\infty = 0.021$ and $\varepsilon^b_\infty = 0$, respectively. The condition-

(a) 2nd-order scheme

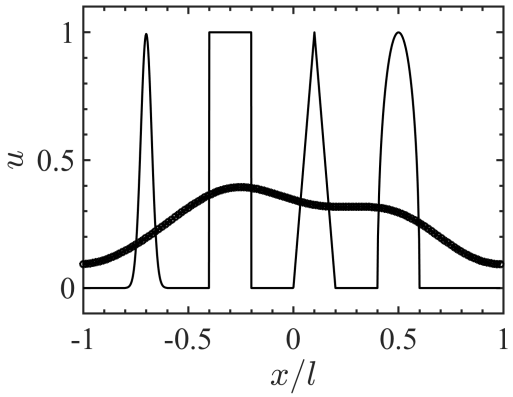

(b) 6th-order scheme

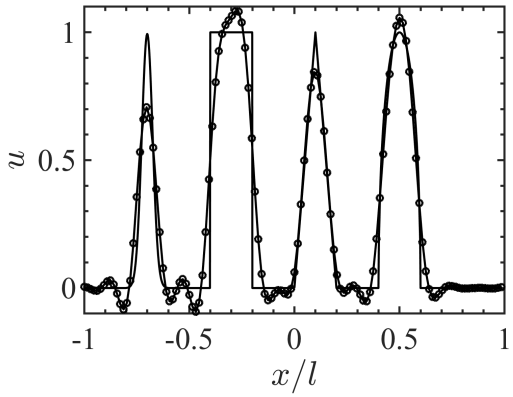

(c) Adaptive (unconditionally stable)

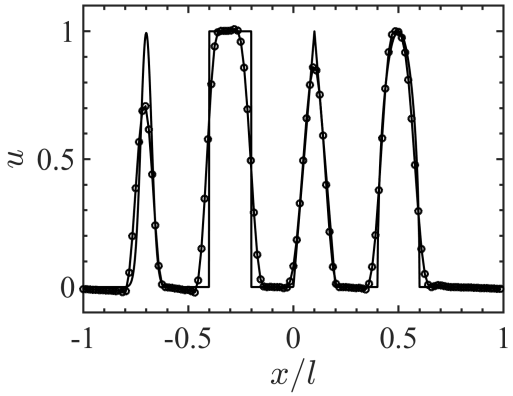

(d) Adaptive (conditionally stable)

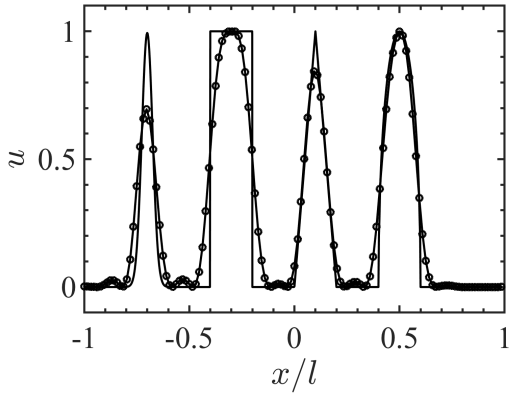

Figure 3.2: Effect of artificial dissipation scheme after four rotations from the initial condition. Numerical solution (∘), exact solution (–).

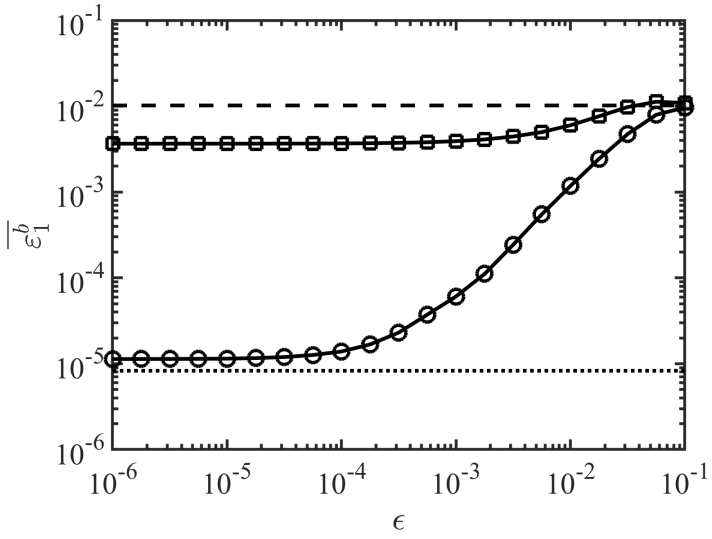

Figure 3.3: Time-averaged boundedness of the one-dimensional advection equation with discontinuous initial condition as a function of sensor thresholds ϵ for the unconditionally stable ($\square$) and conditionally stable ($\bigcirc$) formulations. Standard dissipation with sixth-order ($--$) and second-order ($\ldots$) operators shown for reference.

ally stable dissipation scheme is more successful in preserving boundedness (compare Figs. 3.2c and 3.2d) since the non-smooth sensor ψ is outside of the spatial derivatives.

The time-averaged boundedness norms ε_1^b for various schemes are reported in Fig. 3.3. The threshold ϵ controls the level of unboundedness, with large values producing errors similar to those that would be produced from the high-order dissipation operator, and small values yielding smaller errors comparable to the second-order operator. As before, the error associated with the conditionally-stable formulation is always smaller than the unconditionally-stable scheme.

The boundedness norm approaches a (non-zero) constant when $\epsilon < 10^{-3}$ for the unconditionally stable formulation and $\epsilon < 10^{-5}$ for the conditionally stable formulation. Because the norm is averaged over all timesteps, these errors could be produced during an early stage and eventually dissipate. It should be emphasized that the adaptive dissipation scheme is activated after the solution has become unbounded. Thus, it may require several timesteps to suppress any excursion errors, especially in cases with discontinuous initial conditions. An alternative approach is to identify regions of unboundedness at the end of each timestep and recompute the solution with the updated dissipation scheme within a timestep. This could be done iteratively until a desired

threshold is met. A similar approach is employed in the bounded quadratic-upwind biased interpolative convective (BQUICK) scheme (Herrmann *et al.*, 2006). This potentially increases the computational cost, and is not considered in the present study. Thus, the proposed adaptive dissipation could still lead to some small amount of excursion errors even when $\epsilon = 0$, but significantly reduces the boundedness error without remarkable effect on the accuracy or computational cost.

In summary, the present case demonstrates that the conditionally stable adaptive scheme is more effective in preserving scalar boundedness compared with the unconditionally stable formulation. According to Fig. 3.3, $\epsilon = 10^{-5} - 10^{-4}$ could be a reasonable choice to sufficiently reduce the unboundedness while avoiding adding excessive dissipation. However, if 1% boundedness error is acceptable, $\epsilon \approx 10^{-3} - 10^{-2}$ may be chosen according to Fig. 3.3.

We also study adjoint solutions of unconditionally- and conditionally-stable adaptive dissipation schemes introduced in the previous sections. The solution of the one-dimensional advection equation is taken as the primal solution, and the fully-discrete adjoint solver is employed to obtain its adjoint solution. As mentioned, the corresponding adjoint equation (3.22) contains an advection term with the same velocity as the primal equation but opposite sign in dissipation, and it requires to be integrated reversely in time. Also, the adjoint solution depends on the definition of the QoI because of the $\partial \mathcal{I}/\partial u$ term on the right-hand side of (3.22). We want to merely focus on the effect of the dissipation term on the adjoint equation. For this purpose, we set the adjoint simulation at $t = t_f$ as the exact solution of the primal solution at $t = t_f$ when the artificial dissipation term is not included, and we set $\partial \mathcal{I}/\partial u = 0$ during the adjoint simulation. Thus, the adjoint solution at $t = t_f$ is the same as the primal solution at $t = 0$ (since the primal solution was advected for four rotations). By integrating reversely in time, the adjoint solution moves in negative x-direction while adjoint dissipation acts on it. With this consideration, we are able to compare adjoint results between different dissipation operators. Recall that sensor ψ depends on the primal solution instead of the adjoint one.

Figure (3.4) illustrates adjoint solution at $t = 0$ compared with its 'exact solution' (when dissipation is zero). Similar to the primal solution, the adjoint solution using the second-order

(a) 2nd-order scheme

(b) 6th-order scheme

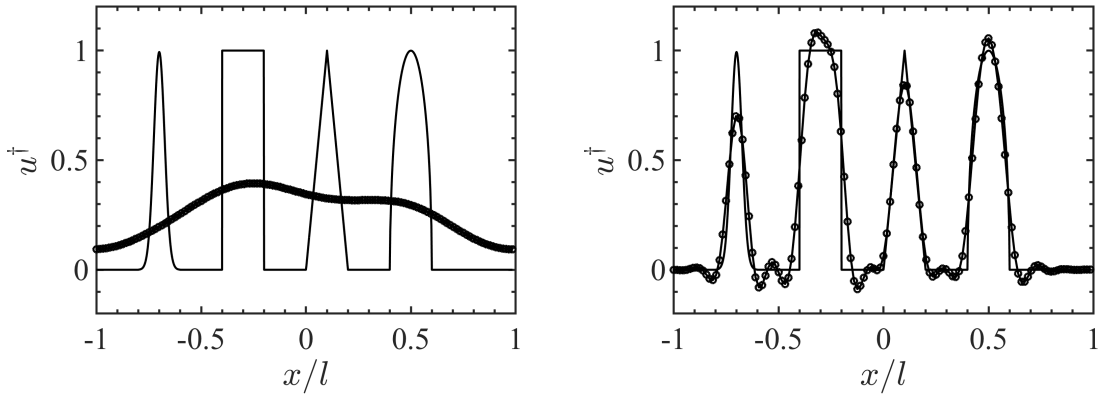

(c) Adaptive (unconstionally stable)

(d) Adaptive (conditionally stable)

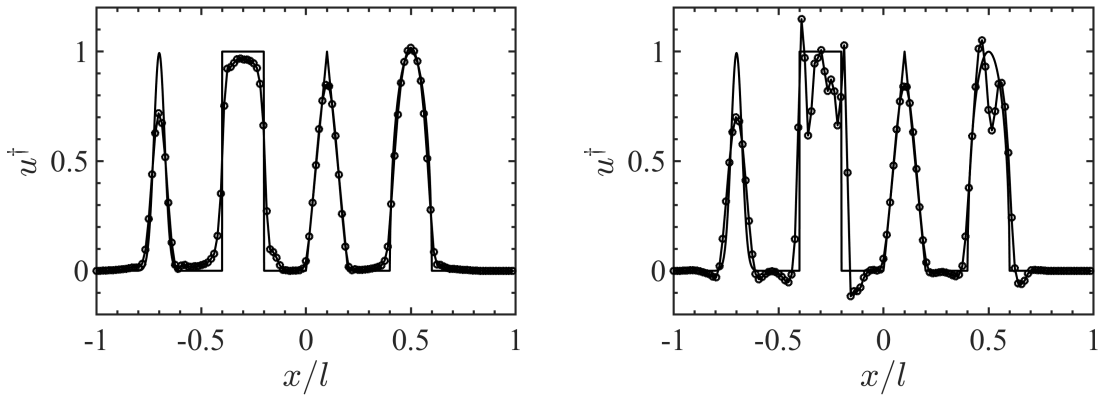

Figure 3.4: Effect of artificial dissipation scheme on the adjoint solution at $t = 0$, which is after four rotations of the adjoint simulation. Numerical solution (∘), exact solution (–). The adjoint solutions correspond to the primal solutions of Fig. 3.2.

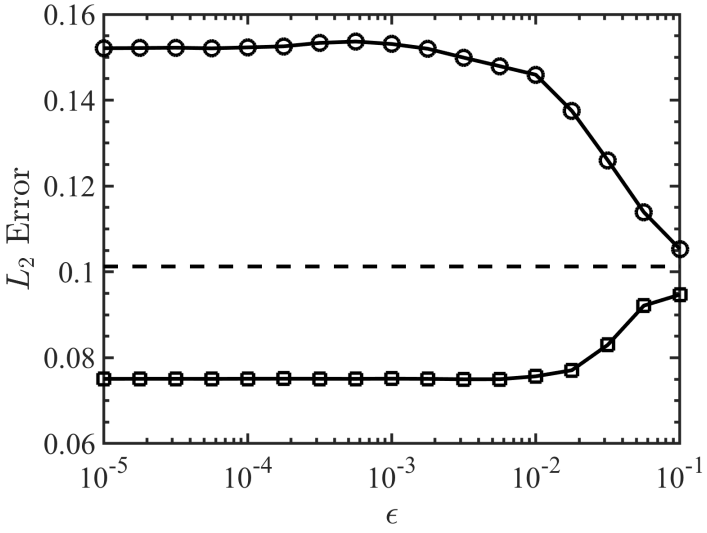

Figure 3.5: L_2 norm error of adjoint solutions of Fig. 3.4 as a function of sensor thresholds ϵ for the unconditionally stable (□) and conditionally stable (◯) formulations. Standard dissipation with sixth-order (−−) shown for reference.

dissipation is extremely diffused, and employing the traditional six-order scheme yields overshoots/undershoots. On the other hand, the solution of the unconditionally stable adaptive scheme is well-bounded at $t = 0$ and close to the exact solution, and several oscillations are observed when the conditionally stable adaptive formulation is employed.

The adjoint solutions of the adaptive dissipation schemes are in contrast with the primal solutions. In the primal solutions, the conditionally stable operator is more successful in preserving boundedness rather than the unconditionally stable one. The difference can be interpreted by comparing adaptive adjoint dissipation terms with their corresponding primal ones. The conditionally stable adaptive scheme involves the sensor ψ outside of the dissipation operators. On the other hand, the sensor is set inside of the dissipation operator in adjoint equations (compare Eqs. (3.16) and (3.31)). This results oscillations in adjoint solutions when a non-continuous sensor (3.13) is employed as can be seen in 3.4d. However, the unconditionally stable adaptive dissipation operator and its adjoint formulation are similar (compare Eqs. (3.14) and (3.29)), which provides similar primal and adjoint solutions (compare Figs. 3.2c and 3.4c). Therefore, the conditionally stable scheme is preferred for preserving boundedness in the primal problem, but it could give oscillatory

adjoint solutions. On the other hand, the unconditionally stable formulation provides smoother adjoint solutions as well as decreasing overshoots/undershoots in the primal solution (but less than the conditionally stable one).

We also study the effect of the sensor threshold ϵ on the accuracy of adjoint solutions. Figure 3.5 shows the L_2 norm error

$$L_2 = \sqrt{\frac{1}{L_x}\sum_{i=1}^{N_x-1}(u_i^\dagger(t) - u_{\text{exact}}^\dagger(x_i,t))^2\,\Delta x} \tag{3.38}$$

of the adjoint solution at $t = 0$. The L_2 error of the adjoint solution increases by decreasing ϵ for the conditionally stable scheme. Surprisingly, it is shown that this behavior is opposite for the unconditionally stable scheme, and its L_2 norm error is even better than the six-order adjoint solution. In other words, increasing the amount of second-order dissipation leads to damping oscillations in the adjoint solution and makes it closer to its exact one. This can be observed by comparing the adjoint solutions to the exact one in Figs. 3.4b and 3.4c.

3.4.3 Adjoint-based optimization

In the previous sections, we have demonstrated how the adaptive dissipation schemes are employed to preserve scalar boundedness, and their adjoint equations have been formulated to compute sensitivity of a QoI to a set of input/design parameters. We also studied effects of parameter ϵ of (3.13) in the accuracy and excursion errors. Generally, selecting an appropriate sensor function can be challenging in complex problems such as supersonic or turbulent reacting flows. Several methods are available for computing sensor values as mentioned before (e.g., see Zhao *et al.*, 2020, and references therein). In this section, we use the adjoint method to 'design' a sensor.

For this purpose, a QoI is defined based on an L_2 norm error of the numerical solution with

respect to the exact solution of an advection equation (3.1), u_{exact}, given by

$$\mathcal{J}_{L_2}[u;\vec{f}] = \int_{t=0}^{t=t_f}\int_{x=-l}^{x=l} (u - u_{\text{exact}}(x,t))^2\, \mathcal{W}(x,t)\, \mathrm{d}x\, \mathrm{d}t, \tag{3.39}$$

where $\mathcal{W}$ is a weight function to locally or temporally limit $\mathcal{J}_{L_2}$. The goal is to minimize this error by locally manipulating the sensor values. As discussed before, sensor is a function of state value u. In order to obtain optimal values of $\psi(u)$, we subdivide it into N_f discrete values in u-space, given by

$$\psi(u) = \begin{cases} \psi_1; & u < u_{\min} \\ \psi_2; & u_{\min} \le u < u_{\min} + \Delta u \\ \vdots & \vdots \\ \psi_{N_f-1}; & u_{\max} - \Delta u \le u < u_{\max} \\ \psi_{N_f}; & u_{\max} \le u \end{cases}, \tag{3.40}$$

where N_f, $u_{\min}$, $u_{\max}$ are user-defined parameters, and $\Delta u = (u_{\max} - u_{\min})/(N_f - 2)$. For instance, the previous sensor (3.13) can be obtained by considering $N_f = 3$, $u_{\min} = -\epsilon$ and $u_{\max} = 1 + \epsilon$. Thus, optimized values of parameters $\vec{f} = \left[\psi_1,\ \psi_2,\ \ldots,\ \psi_{N_f}\right]^{\mathsf{T}}$ are sought such that the QoI (3.39) is minimized, resulting in the minimum value of the L_2-norm error between numerical and exact solutions. Sensitivity of $\mathcal{J}_{L_2}$ to ψ_i is obtained via the adjoint method according to (3.23), i.e.,

$$\frac{\delta \mathcal{J}_{L_2}}{\delta f_i} = \int_{t=0}^{t=t_f}\int_{x=-l}^{x=l} u^{\dagger}\left[\frac{\partial}{\partial x}\left(\frac{\mathrm{d}\psi}{\mathrm{d}f_i}\frac{\partial u}{\partial x}\right) - (-1)^{s-1}\frac{\partial^s}{\partial x^s}\left(\frac{\mathrm{d}\psi}{\mathrm{d}f_i}\frac{\partial^s u}{\partial x^s}\right)\right], \tag{3.41}$$

and

$$\frac{\delta \mathcal{J}_{L_2}}{\delta f_i} = \int_{t=0}^{t=t_f}\int_{x=-l}^{x=l} u^{\dagger}\frac{\mathrm{d}\psi}{\mathrm{d}f_i}\left(\frac{\partial^2 u}{\partial x^2} - (-1)^{s-1}\frac{\partial^{2s} u}{\partial x^{2s}}\right)\mathrm{d}x\, \mathrm{d}t, \tag{3.42}$$

for unconditionally- and conditionally stable adaptive dissipation schemes, respectively, where f_i

denotes ψ_i for $i = 1, \ldots, N_f$. Values of $\mathrm{d}\psi/\mathrm{d}f_i$ are obtained via (3.40), given by

$$\frac{\mathrm{d}\psi}{\mathrm{d}f_1}(u) = \begin{cases} 1; & u < u_{\min} \\ 0; & \text{otherwise} \end{cases},$$

$$\frac{\mathrm{d}\psi}{\mathrm{d}f_i}(u) = \begin{cases} 1; & u_{\min} + (i-2)\Delta u \le u < u_{\min} + (i-1)\Delta u \\ 0; & \text{otherwise} \end{cases}, \quad \text{for } i = 2, \ldots, N_f,$$

$$\frac{\mathrm{d}\psi}{\mathrm{d}f_{N_f}}(u) = \begin{cases} 1; & u_{\max} \le u \\ 0; & \text{otherwise} \end{cases}. \tag{3.43}$$

We employ a simple test case with discontinuities to find optimal sensor values for non-smooth problems. The advection equation (3.1) is solved with $N = 51$ grid points in a domain of length $2l = 1$ and periodic boundary conditions. The initial condition is a rectangular pulse as depicted in Fig. 3.6, and it is marched through time for a one rotation via a standard fourth-order RK time integrator and with CFL=0.5. $\widetilde{\sigma}^{(diss)} = \Delta x^{-1}$ is taken as dissipation strength. Due to the discontinuities in the exact solution and the fact that $a\Delta t < \Delta x$ (CFL< 1), the L_2 error (3.39) is computed when the exact solution passes one grid point, i.e., through each $\Delta x/a\Delta t = 2$ timesteps. Thus, the weight function of (3.39) is set to $\mathcal{W} = 2\Delta t$ when $t = i\Delta t$ for $i = 2, 4, \ldots, N_t$ and zero otherwise, where $N_t = 100$ is the total number of timesteps. The Sixth-order first derivative operator is used with standard sixth-order and adaptive dissipation operators (see Fig. 3.6). We first consider combinations of Heaviside functions according to (3.13) with $\epsilon = 0$ as the reference case (also called the Heaviside sensor in this work). Similar to the previous one-dimensional solutions of Fig. 3.2, the sixth-order scheme yields overshoots/undershoots while adaptive schemes significantly reduce them. At $t = t_f$, the boundedness error ε^b_∞ is about 0.09 for sixth-order scheme, which drops to 0.05 for the unconditionally stable adaptive scheme and a negligible error for the conditionally stable scheme (see Table 3.2). Similar to the previous sections, the conditionally stable scheme was able to significantly reduce overshoots/undershoots, and the stable scheme only slightly decreases them.

The standard L_2 norm errors (3.33) at $t = t_f$ are also summarized in Table (3.2). It is interesting

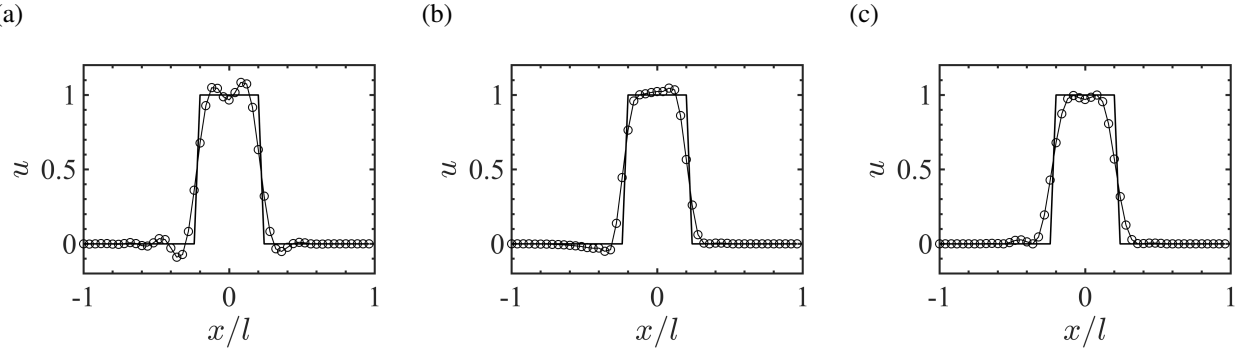

Figure 3.6: Numerical solution (– ◯ –) compared to its exact solution (–) after marching one rotation of the initial condition (–). Sixth-order first-derivative operator is employed with (*a*) sixth-order dissipation, (*b*) unconditionally stable adaptive dissipation, and (*c*) conditionally stable adaptive dissipation.

that the sixth-order scheme results lower error value while it contains more overshoots/undershoots compared to adaptive schemes. As can be seen in Fig. 3.6a, the sixth-order solution is closer to the discontinuities of the exact solution despites its overshoots/undershoots. Although the L_2 norm error is computed at $t = t_f$, we conclude that $\mathcal{J}_{L_2}$ is not a sufficient measure of boundedness, and we expect that an optimal solution of (3.39) cannot significantly preserve boundedness (as will be shown later). Thus, we modify (3.39) such that it only computes at locations that unboundedness occurs, given by

$$\mathcal{J}_b[u;\vec{f}] = \int_{t=0}^{t=t_f}\int_{x=-l}^{x=l} (u - u_{\text{exact}}(x,t))^2\, \psi_{\text{step}}(u)\mathcal{W}(x,t)\,\mathrm{d}x\,\mathrm{d}t, \tag{3.44}$$

where ψ_{step} is determined from (3.13) with $\epsilon = 0$. Thus, we only compute the error where overshoots/undershoots exist. In addition to (3.44), we also consider a linear combination of $\mathcal{J}_{L_2}$ and $\mathcal{J}_b$ to decrease error as well as to preserve boundedness of the solution simultaneously, given by

$$\mathcal{J}_{L_2 b}[\vec{u};\vec{\psi};\lambda] = \lambda\mathcal{J}_b + (1-\lambda)\mathcal{J}_{L_2}, \quad 0 \le \lambda \le 1, \tag{3.45}$$

where λ is a user-defined parameter. If $\lambda = 1$, the QoI only computes the boundedness error, i.e., (3.44), and $\lambda = 0$ makes it equivalent to the L_2 norm error of (3.39).

Table 3.2: Accuracy and boundedness errors for adaptive dissipation schemes with the Heaviside sensor (3.13) with $\epsilon = 0$ and the optimized sensor (3.40). The objective function is (3.45) with different values considered for λ. The corresponding values using the standard sixth-order dissipation operator are L_2 error =0.104 and ε^b_∞ error=8.94e-2. See Fig. 3.6 for problem configuration.

Dissipation Type	Quantity at $t = t_f$	Heaviside Sensor ($\epsilon = 0$)	Optimized Sensor				
			$\lambda = 0$	$\lambda = 0.8$	$\lambda = 0.9$	$\lambda = 0.95$	$\lambda = 1$
Unconditionally Stable (3.14)	L_2 error	0.106	0.105	0.107	0.108	0.104	0.185
	ε^b_∞ error	4.99e-2	2.27e-2	2.05e-2	6.01e-4	0	0
Conditionally Stable (3.16)	L_2 error	0.117	0.104	0.109	0.112	0.113	0.147
	ε^b_∞ error	4.45e-7	5.21e-2	2.03e-2	1.20e-2	6.94e-3	0

3.4.3.1 Verification of adjoint sensitivity

We provided continuous QoI and adjoint sensitivity formulations in the previous section, but their discrete-counterparts are used to obtain exact sensitivity. To verify adjoint gradients, they are compared with complex-step derivative approximations (Squire & Trapp, 1998; Martins *et al.*, 2000, 2001, 2003) with different step sizes, h (see Fig. 3.7), which provides derivatives with second-order accuracy, i.e., $O(\mathrm{h}^2)$, and this scheme is not susceptible to subtraction cancellations. For this purpose, a three-parameter sensor (3.40) is considered ($N_f = 3$) with $u_{\min} = 0$ and $u_{\max} = 1$, and also $\vec{f} = [\psi_1, \psi_2, \psi_3]^\mathsf{T} = \vec{0}$, where $\vec{0}$ is a zero vector.

Adjoint sensitivity for unconditionally stable (3.41) and conditionally stable (3.42) formulations are verified. We can see that the adjoint gradients are converged to the complex-step approximations with a second-order rate when the step size approaches zero (see Fig. 3.7), illustrating that adjoint sensitivities are exact within machine precision roundoff errors. As mentioned, complex-step derivative approximations are second-order accurate and not affected with subtraction cancellations in contrast with standard finite difference methods.

3.4.3.2 Optimizing sensor parameters using adjoint sensitivity

For improving the sensor, we subdivide sensor (3.40) into $N_f = 122$ discrete values with $u_{\min} = -0.1$, $u_{\max} = 1.1$, and $\Delta u = 0.01$, in which all ψ_i for $i = 1, \ldots N_f$ are initially set to zero (baseline solution). Thus, the baseline solution is equivalent to a standard six-order dissipation operator,

(a) Stable adaptive dissipation

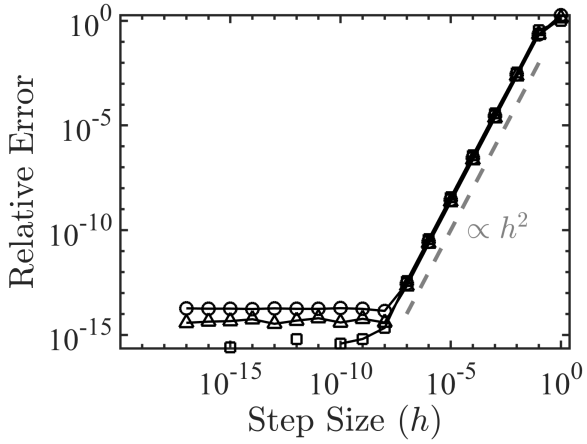

(b) Conditionally stable adaptive dissipation

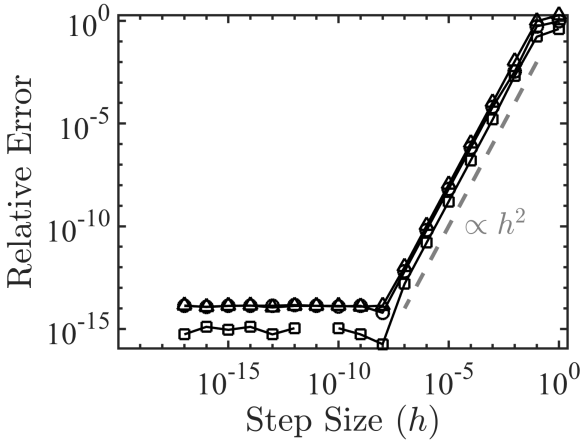

Figure 3.7: Sensitivity $\delta\mathcal{J}_{L_2}/\delta\vec{f}$ with $\vec{f} = [\psi_1, \psi_2, \psi_3]^\mathsf{T} = \vec{0}$ is computed by the adjoint method, and its error with respect to complex-step derivative approximations (normalized with adjoint sensitivity) is depicted for each parameter ψ_1 (○), ψ_2 (□), and ψ_3 (△) as a function of step sizes (h). See Fig. 3.6 for problem configuration.

and the goal is to manipulate the sensor parameters such that both boundedness and accuracy will be improved. During the optimization procedure, all sensor parameters can continuously vary between 0 and 1, i.e., $0 \leq \psi_i \leq 1$ for $i = 1, \ldots N_f$. Thus, 'blended' dissipation of high- and low-order operators could be locally achieved when the sensor value is between 0 and 1. The problem configuration and numerical scheme are described in the previous sections and in Fig. 3.6, in which a rectangular pulse initial condition is integrated over one rotation within the domain. The QoI is defined by (3.45), and different λ values are taken. Its adjoint sensitivity is incorporated with the `SciPy minimize` package, an open source Python library (Jones *et al.*, 2001; Oliphant, 2007; Millman & Aivazis, 2011), in which a Sequential Least SQuares Programming (SLSQP) algorithm (Kraft, 1988) is employed to find minimum values of $\mathcal{J}_{L_2 b}$ with constrain $0 \leq \psi_i \leq 1$ for $i = 1, \ldots N_f$.

Accuracy and boundedness errors of the optimized solution at $t = t_f$ is summarized in Table 3.2 for different values of λ, and they are compared with the adaptive dissipation operators using the Heaviside sensor (3.13). Both unconditionally- and conditionally stable dissipation schemes are employed. When a conditionally stable dissipation scheme is used, the optimized sensors are

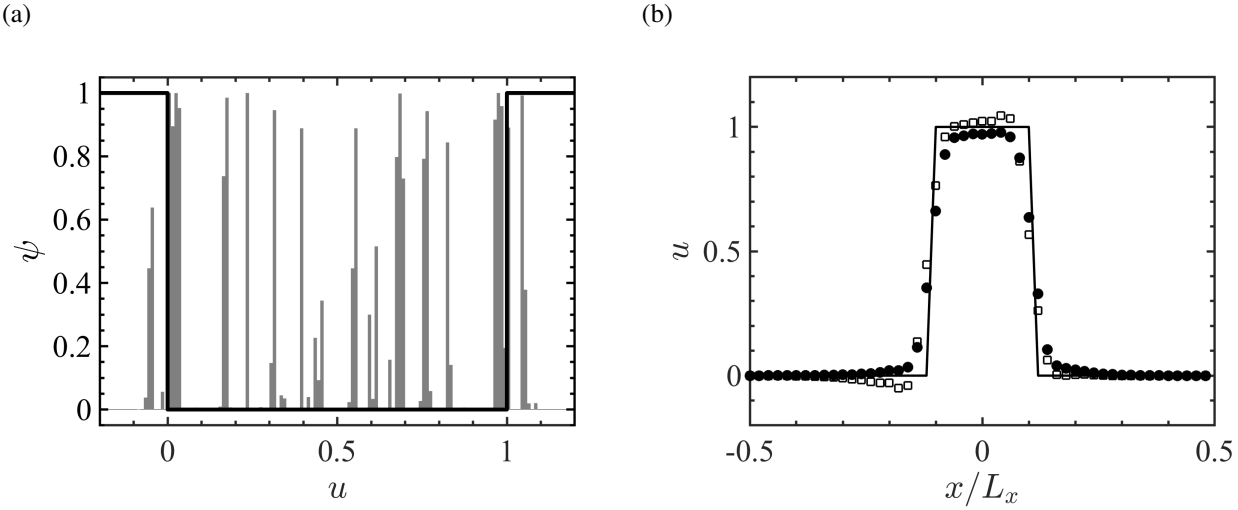

Figure 3.8: (*a*) The Heaviside sensor (–) and optimized sensor (gray) as function of u, the optimal sensor is obtained in problem of Fig. 3.6 via minimizing $\mathcal{J}_{L2b}$ (3.45) with $\lambda = 0.95$ using a 'unconditionally stable' dissipation scheme (3.14). (*b*) Numerical solution after one rotation of initial condition. Unconditionally stable adaptive dissipation with optimal sensor of (*a*) (•), Heaviside sensor (3.13) with $\epsilon = 0$ (□), and the exact solution (–).

not able to reduce overshoots/undershoots compared to the Heaviside sensor (see Table 3.2) even though the L_2 error has been reduced. In the unconditionally stable dissipation scheme, the optimal sensor performs better in preserving overshoots/undershoots compared to the Heaviside sensor. Especially, we observed that L_2 error is decreased as well as the solution is bounded with $\lambda = 0.95$ compared to the Heaviside sensor solution (see Table 3.2 and Fig.3.8). However, the optimized ψ is not a trivial function of u that can be applied on other applications (see Fig. 3.8a). We can see that the sensor ψ is activated around $u = 0$ and $u = 1$ to avoid unboundedness. Besides, it is surprising that the sensor is also activated for some values of $0.1 < u < 0.9$.

The numerical solution of u when the unconditionally stable adaptive dissipation is employed with the optimized sensor and the Heaviside sensor (3.13) are also compared (see Fig. 3.8b). As can be seen, using the optimized sensor yields a bounded solution after one rotation of the initial condition.

3.5 Turbulent round jet

In this section, we take a configuration of a three-dimensional turbulent round jet and apply the conditionally stable adaptive dissipation operator on compressible Navier–Stokes equations to solve the flow, and effects of the adaptive scheme on the accuracy and scalar boundedness of a passive scalar Z is investigated.

3.5.1 Governing equations and discretization

The non-reacting compressible Navier–Stokes equations (2.11) are solved for conserved variables $\vec{Q} = [\rho,\ \rho u_i,\ \rho E,\ \rho Z]$. A Reynolds number of $\mathrm{Re} = \rho_\infty U_j D_j/\mu_\infty$, where the viscosity remains constant in the domain, i.e., $b = 0$ in (2.7), and the bulk viscosity is $\mu_B = 0$. The Prandtl and Schmidt numbers are given by $\mathrm{Pr} = C_{p,\infty}\mu/\kappa = 0.7$ and $\mathrm{Sc} = \mu/(\rho\mathcal{D}) = 0.7$, respectively, with reference specific heat at constant pressure $C_{p,\infty}$, conductivity κ, and mass diffusivity $\mathcal{D}$. The reference Mach number is given by $\mathrm{Ma} = \mathrm{Re}/\mathrm{Re}_c = U_j/c_\infty = 0.36$. Mixing fraction Z is taken as a passive scalar; thus, the pressure (2.4) and heat flux (2.8) equations and the equation state of state (2.10) are modified, given

$$p = (\gamma - 1)\rho\left(E - \frac{1}{2}u_i u_i\right), \tag{3.46}$$

$$q_i = -\frac{\mu}{\mathrm{Re}_c\,\mathrm{Pr}}\frac{\partial T}{\partial x_i}, \tag{3.47}$$

and

$$T = \frac{\gamma p}{(\gamma - 1)\rho}, \tag{3.48}$$

respectively. Finally, buoyancy effects are neglected in this configuration, i.e., $\mathrm{Fr}_c \to \infty$.

The governing equations (2.11) are discretized using SBP finite difference operators with sixth-

order accuracy in the interior and third-order near the boundaries ($s = 3$), resulting in fourth-order global accuracy (see Chapter 3.2.1). Second and mixed derivatives are obtained by consecutively applying the first-derivative operators. The standard (high-order) SBP dissipation operator is applied to density, momentum, and energy equations, while the conditionally stable adaptive dissipation scheme is applied to the passive scalar to enforce $Z \in [0, 1]$. The governing equations are advanced in time using a standard fourth-order explicit Runge–Kutta scheme.

3.5.2 Flow configuration

A round jet with exit velocity U_j enters a rectangular domain of size $16D_j \times 12D_j \times 12D_j$, corresponding to Re = 3000. The domain is discretized with $265 \times 193 \times 193$ grid points. Axial grid spacing decreases exponentially towards the jet inlet, leading to minimum axial grid spacing of $\Delta x_{\min} = 0.04D_j$. Grid stretching is applied in the radial direction with minimum grid resolution in the cross-flow directions of $\Delta y_{\min} = \Delta z_{\min} = 0.02D$, and nearly uniform grid resolution with 49×49 points across the jet region $-D_j/2 < y, z < D_j/2$.

A top-hat profile is considered for the mean jet exit velocity, given by

$$\overline{U}(\boldsymbol{x}) = \frac{U_j + U_c}{2} - \frac{U_j - U_c}{2} \tanh\left[\frac{1}{4}\frac{R}{\delta_\theta}\left(\frac{r}{R} - \frac{R}{r}\right)\right], \tag{3.49}$$

where an overbar denotes a time-averaged quantity, r is the radial distance from the jet centerline, $R = D_j/2$ is the jet radius, and a co-flow velocity of $U_c = 0.03U_j$ is considered. The momentum thickness of the initial shear layer is given by $\delta_\theta = 0.05R$, whose value is consistent with previous works at similar Reynolds numbers (da Silva & Métais, 2002; Tyliszczak & Geurts, 2014; Tyliszczak, 2015b, 2018). The passive scalar Z varies from $Z = 1$ at the jet centerline to $Z = 0$ at lateral boundaries via a similar top-hat profile (Nichols *et al.*, 2007; Tyliszczak, 2018), according to

$$Z = \frac{1}{2} - \frac{1}{2} \tanh\left[\frac{1}{4}\frac{R}{\delta_\theta}\left(\frac{r}{R} - \frac{R}{r}\right)\right]. \tag{3.50}$$

Following Wang *et al.* (2010a,b), turbulence is seeded at the inflow via time-dependent three-dimensional pseudo-turbulent velocity perturbations generated by a digital filtering technique (Klein *et al.*, 2003) superimposed to (3.49) in a region of $-D_j < y, z < D_j$ with a turbulence intensity of 4% and an integral length scale of $\approx 0.2D$. The resulting velocity perturbations are multiplied by $0.5\{1 + \tanh[R/(4\delta_\theta)(R/r - r/R)]\}$ to decay smoothly towards zero outside the jet radius. The mean radial velocity and its perturbations are set to zero at the jet exit.

Boundary conditions are weakly imposed via the SAT boundary treatment. Non-reflecting boundary conditions (Svärd *et al.*, 2007; Vishnampet, 2015) are enforced at the lateral boundaries. The standard non-reflecting SAT boundary condition at the outflow plane is modified to weakly enforce a Neumann condition (see B.5). In addition, a new SAT treatment is employed at the inlet that weakly imposes time-dependent inflow conditions to facilitate the digital filtering technique (see B.4). As shown in Appendix B.7, the modified SAT treatment was found to minimize domain size effects on turbulence statistics.

3.5.3 Accuracy and boundedness

Instantaneous snapshots of the turbulent round jet are shown in Fig. 3.9. Comparisons are made between the standard (high order) dissipation and the proposed conditionally stable adaptive dissipation scheme with $\epsilon = 0.001$. The vorticity magnitude remains unchanged between each case since the adaptive dissipation is only applied to the mixture fraction. The contour of $Z = 0.055$ (corresponding to the stoichiometric mixture fraction of methane-air combustion) is also qualitatively similar. However, the traditional dissipation scheme using high-order derivative operators exhibits overshoots and undershoots in mixture fraction near the shear layer. The adaptive dissipation scheme using $\epsilon = 0.001$ does not show any regions of overshoots and undershoots greater than 0.001.

Instantaneous profiles of mixture fraction at various axial locations are reported in Fig. 3.10. It can be seen that the adaptive dissipation scheme ensures Z remains bounded without significant changes to the solution in regions where it was already bounded

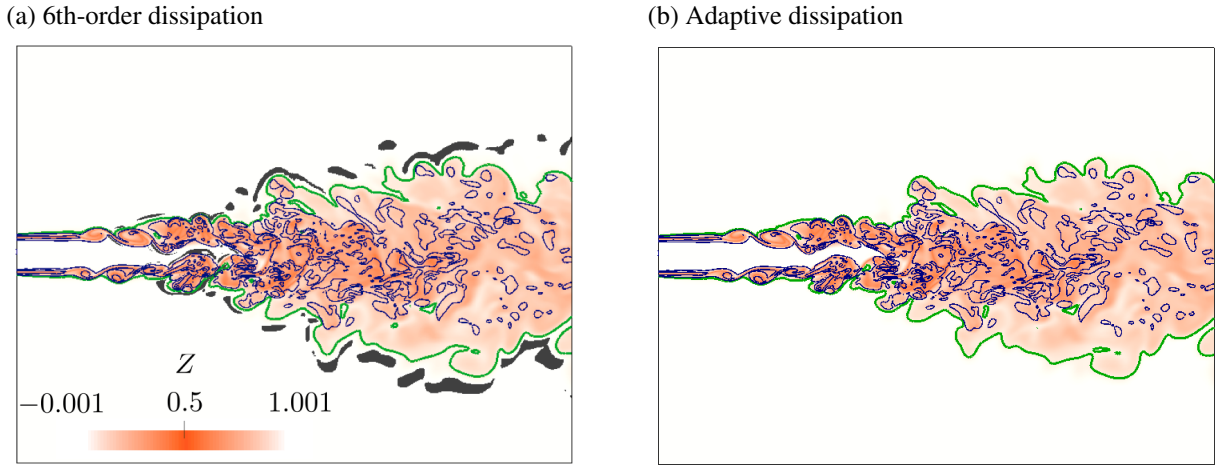

Figure 3.9: Instantaneous snapshots of the jet simulation in the $z = 0$ plane with different dissipation schemes applied to the ρZ equation in (2.11). Mixture fraction (orange). The black regions indicate overshoots and undershoots in Z greater than 0.001. Contour of $Z = 0.055$ (green line) and vorticity magnitude (navy).

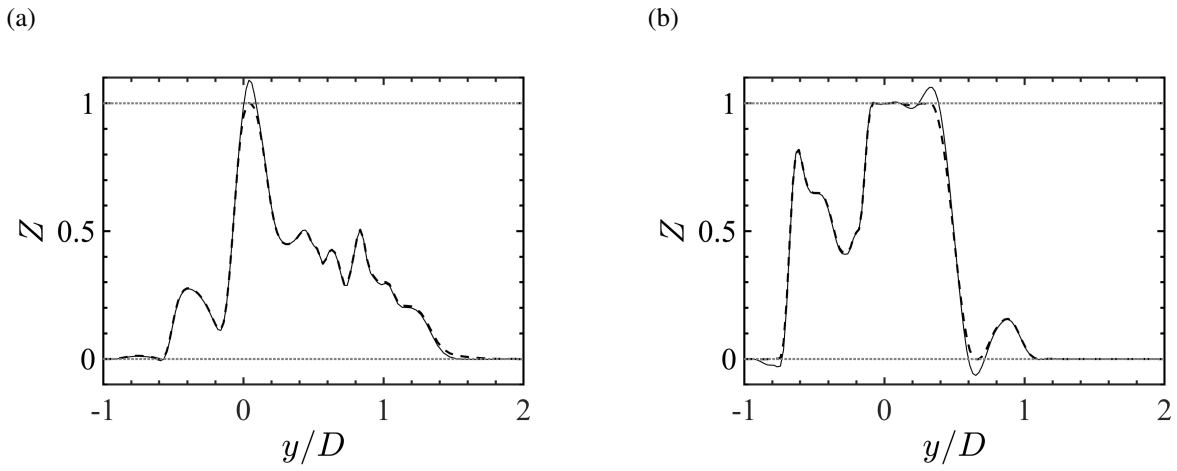

Figure 3.10: Instantaneous distribution of mixture fraction associated with jet simulation at $z = 0$, (a) $x/D_j = 5.70$, and $tU_j/D_j = 504$, and (b) $x/D_j = 4.07$, and $tU_j/D_j = 918$ with high-order (–) and adaptive dissipation operators (−−).

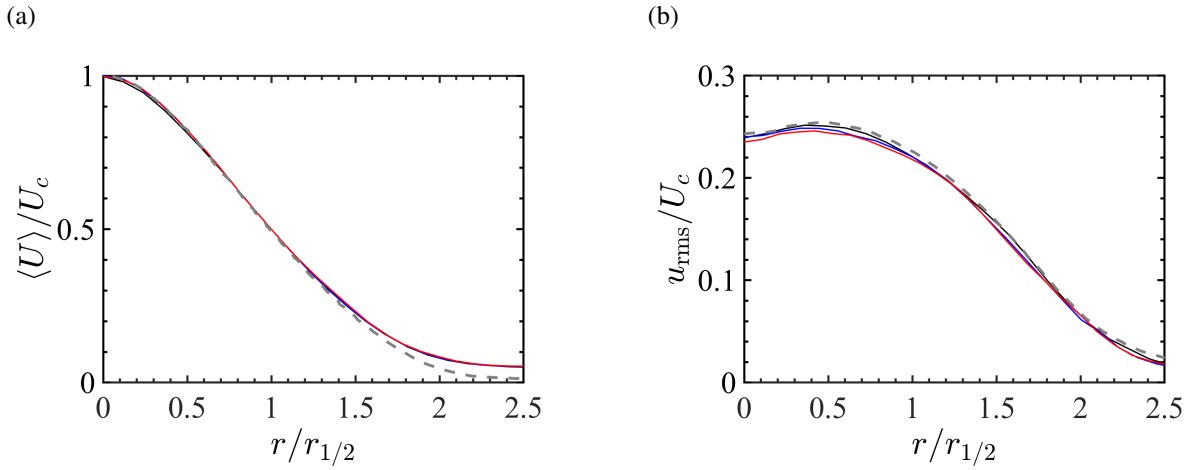

Figure 3.11: (*a*) Mean axial velocity and (*b*) RMS velocity across the jet at $x = 12D_j$ (black), $x = 13D_j$ (blue), and $x = 14D_j$ (red) when adaptive dissipation is used. Experimental data (Panchapakesan & Lumley, 1993) (−−).

As shown in Fig. 3.11, the mean axial velocity, $\langle U \rangle$, and root-mean-square (RMS) velocity, $u_{\mathrm{rms}} = \langle (U - \langle U \rangle)^2 \rangle^{1/2}$, agree well with experimental data of Panchapakesan & Lumley (1993). Angles brackets $\langle \cdot \rangle$ denote averages over both time and azimuthal directions. For a consistent comparison, results are shown as a function of the jet half-width $r_{1/2}$, which represents the radial location where the mean axial velocity $\overline{U} = 0.5U_c$, with U_c the mean centerline velocity. The mean and RMS mixture fraction statistics also exhibit excellent agreement with the experimental data of Dowling & Dimotakis (1990) (see Fig. 3.12). Here, $r_{Z/2}$ is the scalar half-width that represents the radial location where $\overline{Z} = 0.5Z_c$ with Z_c the mean centerline mixture fraction.

Comparisons between the adaptive dissipation scheme and standard approach using high-order operators are shown in Fig. 3.13. A small reduction in mixture fraction fluctuations can be seen when the adaptive dissipation is used, but the changes are not noticeable unless sufficiently zoomed in. It can be seen that using different values of ϵ does not significantly change the mixture fraction statistics, though it does impact the boundedness errors.

Finally, the temporal evolution of the maximum boundedness norm ε_∞^b is given in Fig. 3.14a. The maximum unboundedness over all simulation timesteps is: 0.1281 (high-order dissipation); 0.0111 (adaptive dissipation with $\epsilon = 10^{-2}$); 0.0043 (adaptive dissipation with $\epsilon = 10^{-3}$); and

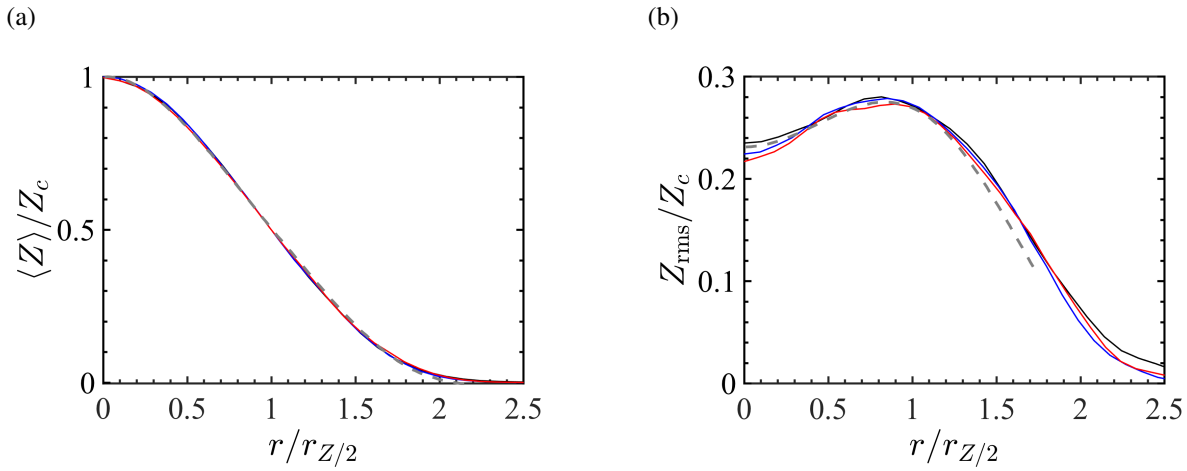

Figure 3.12: Radial profiles of (a) the mean mixture fraction and (b) its fluctuations at $x = 12D_j$ (black), $x = 13D_j$ (blue), and $x = 14D_j$ (red) when adaptive dissipation (–) is used. Experimental data (Dowling & Dimotakis, 1990) (−−).

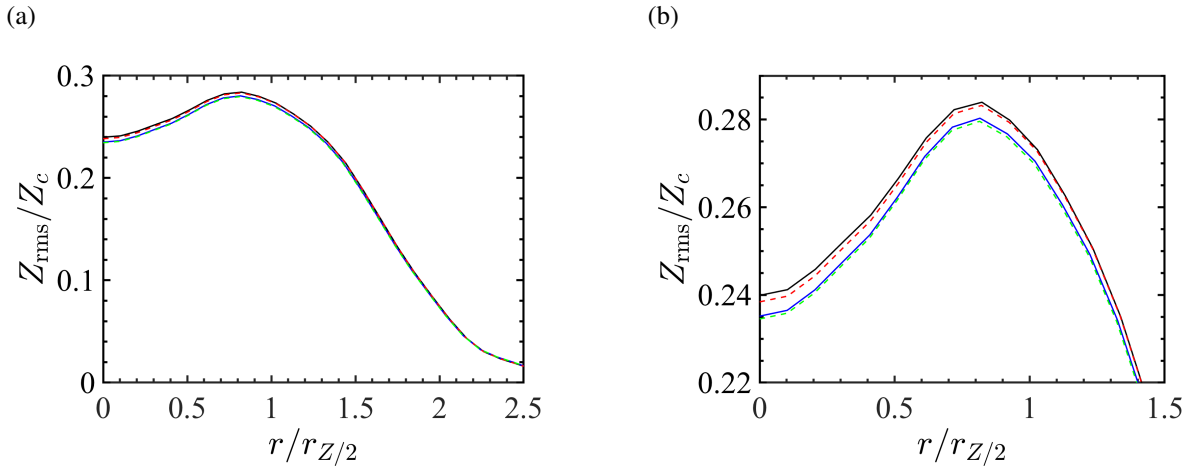

Figure 3.13: (a) Mixture fraction fluctuations across the jet at $x = 12D_j$ and (b) zoom-in view near the maximum value for high-order (black) and adaptive dissipation with $\epsilon = 10^{-2}$ (red), $\epsilon = 10^{-3}$ (blue), and $\epsilon = 0$ (green).

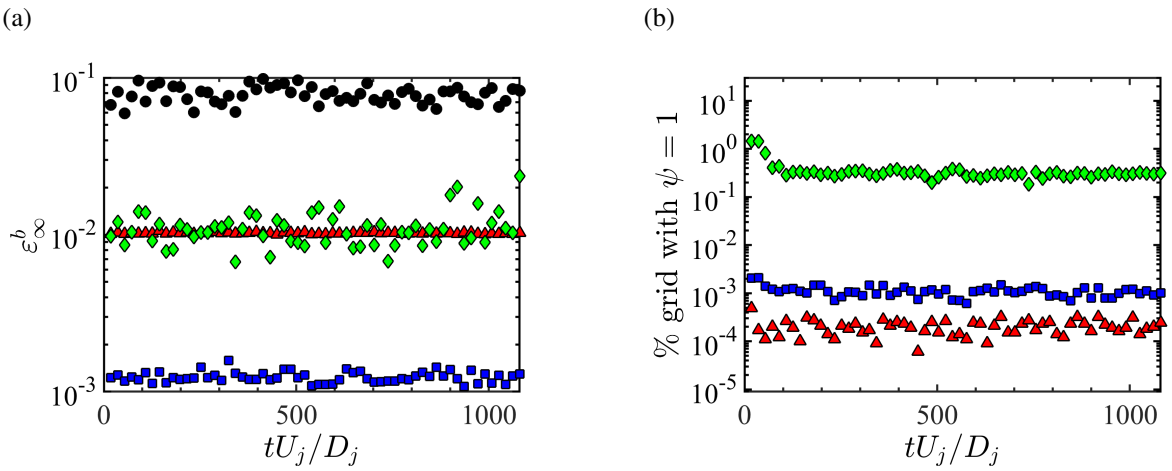

Figure 3.14: Temporal evolution of (*a*) maximum boundedness errors and (*b*) the fraction of grid points that second-order dissipation is activated. High-order dissipation (black circles) and adaptive dissipation with $\epsilon = 10^{-2}$ (red triangles), $\epsilon = 10^{-3}$ (blue squares), and $\epsilon = 0$ (green diamonds).

0.0360 (adaptive dissipation with $\epsilon = 0$). The fraction of the grid points where the sensor is activated is also reported. It can be seen that lower values of ϵ results in more activation of second-order dissipation (see Fig. 3.14b).

3.6 Conclusions

A discrete adjoint framework for sensitivity analysis and optimization of compressible flows involving scalar mixing, turbulence, chemical reactions, and potentially shocks has been provided. The numerical solver is able to provide high-fidelity solutions to such flows. Moreover, an efficient scheme to preserve scalar boundedness and possibly being dual consistent was a matter of interest in this work. Also, the discrete-adjoint solver yields exact sensitivity up to machine precision roundoff errors with a tractable computational cost, making it more effective for chaotic dynamical systems such as turbulent flows.

We reviewed the first derivative and dissipation operators that satisfy the summation-by-parts (SBP) property. It was demonstrated that the standard SBP dissipation operator that relies on high-order derivatives is effective at absorbing the highest wavenumber components, but the dissipation operator based on second derivatives absorbs energy across all scales. Thus, locally adjusting

between the two is a natural choice for controlling dispersion errors.

A sensor was used that activates the lower-order dissipation operator where the solution is unbounded. We considered two formulations, one in which places the sensor inside the derivative operator that ensures an energy estimate for continuous sensors (unconditionally stable formulation), and another where the sensor is placed outside the derivatives (conditionally stable formulation). Adjoint formulations of both adaptive schemes were also provided.

The various formulations were assessed in a series of one-dimensional numerical experiments. In each case, both adaptive dissipation formulations provided lower excursion errors compared to the standard high-order dissipation operator. However, due to the placement of the sensor inside the derivative in the unconditionally stable formulation, the conditionally stable approach systematically provided better performance, especially in flows with discontinuous solutions. On the other hand, numerical oscillations were found in the adjoint solution of the conditionally stable approach. The unconditionally stable adaptive method provides smoother adjoint solutions, but greater amounts of excursion errors are found in its primal simulation, compared to the other adaptive scheme.

We employed a data assimilation technique to find the optimized sensor that preserves boundedness and accuracy of the solution with an adaptive dissipation scheme. A one-dimensional numerical test with a discontinuous initial condition was employed. We were not able to improve the conditionally stable scheme compared to the Heaviside sensor; however, it was succeeded in the optimized sensor of the unconditionally stable adaptive dissipation scheme. Its optimized sensor was not a trivial function of the state values, which makes its implementation more difficult for fluid dynamic applications.

We applied the adaptive dissipation scheme to the compressible Navier–Stokes equations to assess its utility in preserving boundedness in a three-dimensional turbulent round jet. Overall good performance is observed. The proposed approach is found to reduce boundedness errors without significant effects on small-scale fluctuations.

A numerical solver with the adaptive scheme is able to preserve scalar boundedness, and its

discrete adjoint formulation can be efficiently implemented for gradient-based optimization. We note that a similar approach can be adopted in other applications for reducing dispersion errors in the presence of discontinuities (e.g., shock capturing).

CHAPTER 4

Sensitivity Analysis and Optimization of Rayleigh–Taylor Instabilities

4.1 Introduction

Turbulent mixing of variable density flows is ubiquitous in nature and plays an important role in many engineering applications. Such examples include supernova explosions and neutron stars (Woosley & Weaver, 1986; Janka & Müller, 1996; Fujimoto, 1993; Piro & Bildsten, 2007), turbulent combustion (Peters, 2000; Pitsch, 2006, and references therein) and inertial confinement fusion (ICF) (Lindl, 1995; Nakai & Takabe, 1996). Turbulent mixing directly affects the overall performance of many engineering systems. For example, hydrodynamic instabilities that induce mixing decrease the efficiency of implosion performance in ICF (Nakai & Takabe, 1996; Lindl, 1995). Hydrodynamic mixing in ICF is thought to be controlled by Rayleigh–Taylor (RT) and Richtmyer–Meshkov instabilities originating from non-uniformities associated with irradiation laser intensity and the fuel target surface (Nakai & Takabe, 1996). Control of RT-induced mixing is therefore of great importance to improve the performance of such devices.

Since the 1950s, a large number of theoretical (e.g., Chandrasekhar, 1961; Duff *et al.*, 1962), numerical (e.g., Cook & Dimotakis, 2001; Cabot & Cook, 2006) and experimental (e.g., Read, 1984; Roberts & Jacobs, 2016) studies have provided a great deal of insight into the mixing properties of RT instabilities. In addition, several studies have been conducted to determine stabilizing or suppressing agents of RT growth, e.g., via shear rate and surface tension actions (Babchin *et al.*,

1983), wall oscillations (Halpern & Frenkel, 2001) and electric fields imposed on dielectric fluids (Cimpeanu *et al.*, 2014). It has also been observed that the RT growth rate can be modified by altering the structure of initial interfacial perturbations (Cook & Dimotakis, 2001; Ristorcelli & Clark, 2004; Ramaprabhu *et al.*, 2005; Youngs, 2009; Banerjee & Andrews, 2009; Xie *et al.*, 2017), suggesting that one might be able to control the extent of fluid mixing by carefully adjusting the initial conditions. While such a strategy for manipulating fluid mixing might appear impractical in practice, it is interesting to note that Carles *et al.* (2006) and Huang *et al.* (2007) recently demonstrated that it is feasible to impose *precise and arbitrary* controlled initial perturbations using magnetic fields.

Several studies in the literature have examined the importance of initial perturbations on RT growth rates, yet it remains unclear to what extent details of the initial perturbations are retained throughout evolutionary stages of the instability. Many studies have shown that variations of initial interfacial perturbations in spectral space can affect the growth rate (e.g., Cook & Dimotakis, 2001; Ristorcelli & Clark, 2004; Ramaprabhu *et al.*, 2005; Youngs, 2009; Banerjee & Andrews, 2009; Xie *et al.*, 2017). For example, Banerjee & Andrews (2009) simulated several three-dimensional multi-mode RT configurations with different interfacial perturbation spectra, and obtained different growth rates in some cases. Xie *et al.* (2017) showed that it is possible to suppress or enhance growth by perturbing the amplitude of an individual mode of a two-dimensional multi-mode RT instability. In addition, it has been observed that including low wavenumber modes in the initial perturbations increases the late-time RT growth (Cook & Dimotakis, 2001; Youngs, 2003; Ramaprabhu *et al.*, 2005; Banerjee & Andrews, 2009). Despite the dependence of large scale mixing and penetration on initial perturbations, it has been seen that small scale features (e.g., molecular mixing) are usually less sensitive to the distribution of initial perturbations (Dimonte *et al.*, 2004; Ramaprabhu *et al.*, 2005; Banerjee & Andrews, 2009). Contrary to these observations, some studies have shown that the RT growth rate can be insensitive to changes in initial interfacial perturbations (e.g., Livescu *et al.*, 2011; Roberts & Jacobs, 2016), especially if the growth is dominated by nonlinear mode-coupling effects (e.g., Dimonte *et al.*, 2004; Ramaprabhu *et al.*, 2005; Banerjee

& Andrews, 2009).

Despite recent progress, practical methods to control mixing of multi-component fluids remain limited, and the extent to which instabilities can be altered remains an open question. In recent years, advancements in numerical methods and growing computational resources have enabled predictive simulations of realistic multi-component turbulent flows. Yet, the use of high-fidelity simulations for optimization in general remains challenging due to the high computational cost and large number of parameters capable of influencing mixing. In recent years, adjoint-based methods have emerged as a powerful technique to measure parametric sensitivity in fluid dynamic applications, including shape optimization and drag reduction for aerostructures (Jameson, 1989; Jameson & Martinelli, 2000; Martins *et al.*, 2004), sensitivity analysis of laminar flames (Braman *et al.*, 2015), aeroacoustic control of free shear flows (Wei & Freund, 2006; Vishnampet *et al.*, 2015), scalar mixing (Vikhansky, 2002; Liu, 2006; Thiffeault, 2012; Foures *et al.*, 2014b; Miles, 2018; Vermach & Caulfield, 2018) and hydrodynamic instability of lifted diffusion flames (Qadri *et al.*, 2015). Only recently have adjoint methods been applied to multi-component unsteady flows, including variable-density Kelvin–Helmholtz instabilities (Lopez-Zazueta *et al.*, 2016) and turbulent combustion (Capecelatro *et al.*, 2016, 2017, 2018).

The sensitivity obtained from the adjoint solution can be susceptible to spatial and temporal truncation errors that are known to become significant in unsteady or chaotic flows (Lea *et al.*, 2000; Nadarajah & Jameson, 2000; Vishnampet *et al.*, 2015). Discrete-adjoint methods address this by taking into account the numerical discretization prior to perturbing and linearizing the flow equations, which provides sensitivity that is exact up to machine roundoff errors. Such an approach is expected to accelerate and improve optimization for simulations of turbulence. For example, the discrete adjoint method has been shown to improve the minimum drag coefficient for flow around a rotating cylinder (Carnarius *et al.*, 2010), and achieve 2.2× more reduction in aeroacoustic noise compared to the continuous-adjoint approach (Vishnampet *et al.*, 2015). Vishnampet *et al.* (2015) recently developed a discrete-adjoint method for unsteady turbulent flows using high-order spatial and temporal discretization. In this work, we extend the space–time discrete adjoint approach

of Vishnampet *et al.* (2015) to buoyancy-driven variable density flows and measure sensitivity of multi-mode RT growth to local perturbations of the fluid interface. In Chapter 4.2, the RT configuration, governing equations and discretization are presented. In Chapter 4.3, different means for quantifying mixing are discussed, and the adjoint method is formulated for quantifying their sensitivity. Local sensitivity is analysed in Chapter 4.4 at different times during the evolution of the instability. In Chapter 4.5, the sensitivity obtained from the adjoint method is employed in gradient-based optimization to both suppress and enhance the growth rate, and the optimal perturbations associated with different RT regimes are evaluated.

4.2 Predictive model

4.2.1 System configuration

We consider two miscible fluids with molecular weight ratio $W_2/W_1 = 3$, corresponding to an Atwood number

$$\mathrm{At} = \frac{W_2 - W_1}{W_2 + W_1} \tag{4.1}$$

of At = 0.5. The fluids are contained within a box of length $L \times 2L \times L$ with $L = 2\pi$. Gravity g is aligned in the negative y-direction. Periodic boundary conditions are imposed in the homogeneous x- and z-directions. A no-slip wall is enforced at the upper and lower boundaries, i.e., $y = \pm 2\pi$. The reference velocity is taken to be $u_\infty = \sqrt{gl}$ with the reference length scale $l = L/2\pi$, resulting in a Froude number $\mathrm{Fr} = {u_\infty}^2/(gl) = 1$. The subscript ∞ denotes a reference quantity throughout the remainder of this chapter.

The domain is discretized on a mesh with $256 \times 1025 \times 256$ grid points, corresponding to grid spacing $\Delta x = \Delta z = 0.025l$ in the horizontal directions and $\Delta y = 0.012l$ in the vertical direction. The average kinematic viscosity at the interface $\bar{\nu}$ is chosen such that the Kolmogorov length scale

η is properly resolved, as determined by the Reynolds number

$$\mathrm{Re} = \frac{u_\infty l}{\bar{\nu}} = \left(\frac{l}{\eta}\right)^{\frac{4}{3}}, \tag{4.2}$$

which is taken to be $\mathrm{Re} = 353.3$ with $\eta = \Delta x/2$. The average kinematic viscosity is related to the light (μ_1) and heavy (μ_2) fluid viscosities via $\bar{\nu} = (\mu_1 + \mu_2)/(\rho_1 + \rho_2)$, where ρ_1 and ρ_2 are the densities of the fluid below and above the interface, respectively. The dynamic viscosity of the mixture, μ, is taken to be constant, i.e., $\mu = \mu_1 = \mu_2 = \mu_\infty$.

4.2.2 Governing equations

In this work, we consider the non-dimensional non-reacting Navier–Stokes equations of (2.11) for the non-dimensional conserved variables $\vec{Q} = [\rho \quad \rho\boldsymbol{u} \quad \rho E \quad \rho Y]^\mathsf{T}$, where ρ is the mixture density, $\boldsymbol{u} = [u \quad v \quad w]^\mathsf{T}$ is the velocity vector, E is the total non-chemical energy (including thermal and kinetic energy), Y is the heavy fluid mass fraction with $1 - Y$ the mass fraction of the light fluid, and p is the pressure given by $p = (\gamma - 1)(\rho E - \rho u_i u_i/2)$, where $\gamma = 1.4$ is the specific heat ratio. In (2.11) , $\mathrm{Fr}_c = \mathrm{Fr}/\mathrm{Ma}^2$ and $\mathrm{Re}_c = \mathrm{Re}/\mathrm{Ma}$ denote the Froude and Reynolds numbers, respectively, based on the reference sound speed $c_\infty = \sqrt{\gamma p_I/\rho_I}$ with interfacial pressure p_I and density $\rho_I = (\rho_1+\rho_2)/2$. The Mach number $\mathrm{Ma} = u_\infty/c_\infty = 0.189$ is taken such that compressibility effects on the RT instability are not important (Livescu, 2004). The viscosity remains constant in the domain, i.e., $b = 0$ in (2.7), and the bulk viscosity is $\mu_B = 0$. The non-dimensional heat flux (2.8) is simplified for the non-reacting case according to

$$q_i = -\frac{1}{\mathrm{Re}_c \mathrm{Pr}} \frac{\partial T}{\partial x_i} - \frac{T}{\mathrm{Re}_c \mathrm{Sc}} \left[\frac{1}{W_1} \frac{\partial (1 - Y)}{\partial x_i} + \frac{1}{W_2} \frac{\partial Y}{\partial x_i} \right], \tag{4.3}$$

where T is the temperature that is determined by the ideal gas law for a mixture (2.10) with the mixture molecular weight, $\overline{W}$ given by

$$\overline{W} = \left(\frac{Y}{W_2} + \frac{1 - Y}{W_1} \right)^{-1}. \tag{4.4}$$

In (4.3), $\mathrm{Pr} = C_{p,\infty}\mu/\kappa$ is the Prandtl number with κ and $C_{p,\infty}$ the thermal conductivity and reference specific heat at constant pressure, respectively, and $\mathrm{Sc} = \mu/(\rho\mathcal{D})$ is the Schmidt number with mass diffusivity $\mathcal{D}$. Values of $\kappa/C_{p,\infty}$ and $\rho\mathcal{D}$ are chosen to be constant such that $\mathrm{Pr} = 0.7$ and $\mathrm{Sc} = 1$.

4.2.3 Initialization

The mole fraction of the heavy fluid, $X = Y\overline{W}/W_2$, is initialized as

$$X = \frac{1}{2} \left\{ 1 + \mathrm{erf} \left[\frac{y - h_0(x, z)}{\delta_D} \right] \right\}, \tag{4.5}$$

where $\delta_D = 5\Delta y$ is the initial diffusion thickness of the interface, and $h_0(x, z)$ denotes the interfacial perturbations, composed of M modes in the x-direction and N modes in the z-direction, according to

$$h_0(x, z) = \sum_{m=1}^{M} \sum_{n=1}^{N} A_{m,n} \cos\left(k_{x,m}x + \theta_{x,m}\right) \cos\left(k_{z,n}z + \theta_{z,n}\right). \tag{4.6}$$

Here, $k_{x,m} = 2\pi/\lambda_{x,m}$ and $k_{z,n} = 2\pi/\lambda_{z,n}$ are the perturbation wavenumbers with wavelengths $\lambda_{x,m}$ and $\lambda_{z,n}$ in x- and z-direction, respectively, with phase shift $\theta_{x,m}$ and $\theta_{z,n}$, and amplitude $A_{m,n}$.

The fluid is taken to be initially at rest, i.e., $u_i = 0$, and thus the momentum conservation equation of (2.2) provides a hydrostatic relation for pressure, given by $\partial p/\partial y = -\rho/\mathrm{Fr}_c$. Substituting ρ for p in the hydrostatic equation via (2.10) and integrating from $y = h_0(x, z)$ to an arbitrary vertical position y yields

$$p = p_I \exp\left(-\frac{\gamma}{(\gamma - 1)T_0} \frac{1}{\mathrm{Fr}_c} \left[\overline{W}\left(y - h_0\right) + \frac{\delta_D \left(W_2 - W_1\right)}{2\sqrt{\pi}} \left\{ \exp\left[-\frac{\left(y - h_0\right)^2}{\delta_D^2} \right] - 1 \right\} \right] \right). \tag{4.7}$$

Here, p_I is the fluid interface pressure and T_0 denotes the initial temperature that is assumed to be constant throughout the entire domain, resulting in an initially isothermal state. The density is initialized by substituting the resulting pressure into (2.10). It is important to note that employing stationary initial conditions with the hydrostatic pressure distribution $\partial p/\partial y = -\rho/\mathrm{Fr}_c$ will generate spurious acoustic waves near the interface. These waves originate from pressure disturbances as a result of non-zero enthalpy diffusion that appears in the energy equation (Cook, 2009; Livescu, 2013; Reckinger *et al.*, 2016). Recent work has shown that the spurious waves can be suppressed by modifying the velocity field near the interface (Movahed, 2014; Reckinger *et al.*, 2016). In the current work, we follow a similar approach described by Reckinger *et al.* (2016) to eliminate these spurious oscillations, resulting in the following initial velocity

$$u_i = -\frac{1}{\mathrm{Re}_c \mathrm{Sc}} \frac{1}{\rho \overline{W}} \frac{\partial \overline{W}}{\partial x_i}. \tag{4.8}$$

4.2.4 Discretization of the governing equations

In the present work, spatial derivatives appearing in the governing equations (2.11) and (2.6)–(4.3) are obtained via a narrow-stencil finite difference operator that satisfies the summation-by-part (SBP) property (Kreiss & Scherer, 1974; Strand, 1994). We employ spatial derivatives with eighth-order accuracy in the interior domain and fourth-order near the boundaries, resulting in fifth-order global accuracy. Second and mixed derivatives are obtained by applying the first derivative consecutively. Sixth-order SBP dissipation operators (Mattsson *et al.*, 2004; Vishnampet, 2015) are employed to damp spurious numerical waves that arise due to repeated first derivatives. The flow equations are integrated in time using a standard fourth-order Runge–Kutta scheme. A constant simulation timestep of $\Delta t = 2.67^{-4}\tau$ with $\tau = \sqrt{\mathrm{Fr}_c L/l\mathrm{At}}$ a characteristic time scale is maintained such that the Courant–Friedrichs–Lewy (CFL) condition remains below $\mathrm{CFL} < 0.9$.

The SBP scheme is combined with the simultaneous-approximation-term (SAT) boundary treatment to ensure provable stability (Carpenter *et al.*, 1994; Svärd & Nordström, 2008; Bodony, 2010; Vishnampet, 2015). The SAT treatment is used to impose no-slip isothermal boundary con-

ditions at $y = \pm 2\pi$ (Svärd & Nordström, 2008; Vishnampet, 2015). In addition, absorbing sponge regions (Freund, 1997) are applied near the walls by adding a damping term to suppress numerical acoustic waves and to enforce the solution to a target state $\vec{Q}_t$ (taken to be the unperturbed initial conditions). The damping term $\sigma_s(y)\left(\vec{Q} - \vec{Q}_t\right)$ is added to the right-hand side of the governing equations, where the sponge strength $\sigma_s(y)$ varies quadratically in the y-direction from unity at the walls to zero at $\approx 0.7l$ away from the wall.

4.3 Controlling the Rayleigh–Taylor instability

We seek to control RT growth by manipulating individual mode amplitudes $A_{m,n}$ of the initial perturbations at the fluid interface h_0, given by (4.6). Sensitivity of the instability with respect to each mode provides a direction that is useful in gradient-based optimization. In order to calculate this sensitivity, a quantitative measure of the RT instability is required. In this section, important features and concepts of RT growth are summarized. We then introduce various definitions of mixing that will be considered and provide a formal methodology for measuring its sensitivity to each individual amplitude $A_{m,n}$.

4.3.1 A background on Rayleigh–Taylor growth

RT instabilities are known to undergo a range of stages during their growth. In the limit that either the Schmidt number, the perturbation amplitude, or gravity is sufficiently small, the initial growth will be dominated by diffusion (Duff *et al.*, 1962; Cook & Dimotakis, 2001; Wei & Livescu, 2012). Following diffusional growth, the perturbation amplitude grows exponentially with time according to linear stability theory (Chandrasekhar, 1961; Duff *et al.*, 1962; Livescu, 2004). The exponential growth holds when the perturbation amplitude h is significantly smaller than the perturbation wavelength λ, i.e., $h \ll \lambda$. When h is not sufficiently small, nonlinearities become important, and bubbles and spikes form as the two fluids penetrate each other, resulting in a growing mixing zone. During the nonlinear regime, the bubble tip velocity of a single-mode RT instability

is known to reach a constant value proportional to $\sqrt{g\lambda}$ (Layzer, 1955; Baker & Freeman, 1981; Hecht *et al.*, 1994; Goncharov, 2002). After sufficiently long time, the mixing zone grows quadratically (Anuchina *et al.*, 1978; Youngs, 1984), and the acceleration of bubbles and spikes becomes constant, given by (Read, 1984; Youngs, 1984)

$$h_{b/s}(t) = \alpha_{b/s} \mathrm{At} g t^2, \tag{4.9}$$

where indices 'b' and 's' denote bubbles and spikes, respectively, and α is the growth parameter. There are two primary mechanisms responsible for bubbles approaching self similarity. The first mechanism, referred to as bubble competition, suggests that each ambient mode grows independently and exponentially until reaching its saturation limit, resulting in a set of saturated bubbles (Hecht *et al.*, 1994; Alon *et al.*, 1994; Dimonte, 2004; Ramaprabhu *et al.*, 2005; Banerjee & Andrews, 2009). Such a mechanism results in a weak correlation between α_b and the amplitudes of the interfacial perturbations (Dimonte, 2004; Ramaprabhu *et al.*, 2005; Banerjee & Andrews, 2009). The second mechanism, referred to as bubble merger, suggests that different bubbles merge and couple nonlinearly to create larger and faster bubbles (Sharp, 1984; Alon *et al.*, 1994; Dimonte, 2004; Dimonte *et al.*, 2004; Ramaprabhu *et al.*, 2005; Banerjee & Andrews, 2009). In contrast to bubble competition, the resulting α_b of pure mode-coupling does not depend on initial perturbations (Alon *et al.*, 1994; Dimonte *et al.*, 2004; Ramaprabhu *et al.*, 2005; Banerjee & Andrews, 2009). Thus, no universal value for α exists, and a wide range of growth parameters have been reported from experiments and numerical simulations, ranging from $0.015 \lessapprox \alpha \lessapprox 0.085$ (Dimonte *et al.*, 2004; Ramaprabhu *et al.*, 2005). In order to more effectively control RT instabilities, it is important to identify to what extent α is influenced by the structure of the initial interfacial perturbations.

4.3.2 Quantifying mixing

In this work, the objective function, $\mathcal{J}$, is defined within the simulation domain $\mathbb{D}$ and time horizon $[0, t_f]$ as

$$\mathcal{J}(\vec{Q}, \vec{A}) = \int_0^{t_f} \int_{\mathbb{D}} \mathcal{I}(\vec{Q}, \vec{A}) \mathcal{W}(y) \, \mathrm{d}\boldsymbol{x} \, \mathrm{d}t, \tag{4.10}$$

where the integrand $\mathcal{I}$ denotes the local temporal mixing provided by a high-fidelity simulation that solves the governing equations (2.11), and $\vec{A} = [A_{1,1}, \cdots, A_{M,N}]^\mathsf{T}$. The weighting function $\mathcal{W}(y)$ enforces compact support near the interface and smoothly decays to zero towards the vertical boundaries, given by

$$\mathcal{W}(y) = \frac{1}{2} \left\{ \tanh\left[\sigma_\mathcal{W} \left(y + 1 - f_\mathcal{W}/2\right)\right] - \tanh\left[\sigma_\mathcal{W} \left(y - 1 + f_\mathcal{W}/2\right)\right] \right\}, \tag{4.11}$$

where $\sigma_\mathcal{W} = 25.0/l$ determines the slope, and $f_\mathcal{W} = 0.25l$ controls the fraction of the span for which $\mathcal{W}$ is maximum. The choice of these parameters have negligible effect on the results reported here.

The choice of $\mathcal{I}$ in (4.10) is critical for measuring mixing and growth of the RT instability. Several definitions for $\mathcal{I}$ can be found in the literature. One measure is the bubble-spike distance h_t (e.g., see Cook & Dimotakis, 2001), given by

$$h_t = h_b - h_s. \tag{4.12}$$

For multi-mode RT instabilities, thresholds on spanwise-averaged mole, volume or mass fraction are typically used to measure bubble and spike heights (e.g., see Cook & Dimotakis, 2001; Dimonte *et al.*, 2004; Movahed, 2014). In the present work, we consider $\langle X \rangle = 0.99$ and $\langle X \rangle = 0.01$ thresholds for determining bubble h_b and spike h_s heights, respectively, where $\langle \cdot \rangle$ denotes a span-

wise average, given by

$$\langle\phi\rangle(y) = \frac{1}{L^2}\int_{-L/2}^{L/2}\int_{-L/2}^{L/2}\phi(x,y,z)\,\mathrm{d}z\,\mathrm{d}x, \tag{4.13}$$

where ϕ can be the mole, volume or mass fraction. Another common measure is the mixing width, given by (e.g., see Dimonte *et al.*, 2004; Cabot, 2006)

$$w = \int_{-L}^{L}\langle\phi\rangle\left(1-\langle\phi\rangle\right)\,\mathrm{d}y. \tag{4.14}$$

In addition, mixed fluid can be defined as the product of a hypothetical fast-kinetic reversible chemical reaction between two pure fluids, such that a corresponding mixing length is given by (e.g., see Cook & Dimotakis, 2001; Movahed, 2014)

$$h_m = \int_{-L}^{L}\phi_m\left(\langle\phi\rangle\right)\,\mathrm{d}y, \tag{4.15}$$

where h_m is the mixing height, and $\phi_m(\phi)$ is a corresponding mixed fluid fraction, where $\phi_m = 2\phi$ for $\phi \leq 0.5$; $\phi_m = 2\left(1-\phi\right)$ otherwise. In the current work, $\langle\phi\rangle = \langle X\rangle$ is considered in (4.14) and (4.15).

In the present work, the adjoint of the perturbed and linearized governing equations is solved to determine the sensitivity of mixing and growth, which requires the objective function to be differentiable with respect to flow variables $\vec{Q}$ and perturbation parameters $\vec{A}$. However, computing derivatives of the aforementioned quantities can be problematic, and thus necessitates a new measure of mixing. An initial candidate for $\mathcal{I}$ in (4.10) is to utilize the form of (4.14) with $\mathcal{I} = X\left(1-X\right)$, leading to $\mathcal{J}$ that quantifies mixing, defined as

$$\mathrm{MIX} = \int_{0}^{t_f}\int_{\mathbb{D}} X\left(1-X\right)\mathcal{W}(y)\,\mathrm{d}\boldsymbol{x}\,\mathrm{d}t, \tag{4.16}$$

in which its maximum value occurs at $X = 0.5$ (representing the fully mixed fluid), and MIX = 0 within a pure fluid. It is important to note that due to the initial smooth distribution of X as given by (4.5), MIX($t = 0$) $\neq 0$ even for an unperturbed interface.

Alternatively, the definition of mixing can be defined based on the perturbation kinetic energy (Aamo *et al.*, 2003; Foures *et al.*, 2014b; Lopez-Zazueta *et al.*, 2016; Vermach & Caulfield, 2018). Because the interfacial fluid movement is closely related to the local velocity of the interface, it is reasonable to consider an L^2-norm of vertical velocity v, resulting in $\mathcal{J}$ that quantifies the kinetic energy, given by

$$\mathrm{KE} = \int_0^{t_f} \int_{\mathbb{D}} v^2 \mathcal{W}(y)\, \mathrm{d}\boldsymbol{x}\, \mathrm{d}t. \tag{4.17}$$

Foures *et al.* (2014b) and Vermach & Caulfield (2018) showed that maximizing the perturbation kinetic energy does not effectively enhance mixing of a passive scalar in plane channel flows. Even so, the utility of this definition for controlling RT growth will be analysed in later sections.

In addition to the definitions above, we consider a third quantity that represents the deviation of mole fraction from its unperturbed initial value X_∞, according to

$$\mathrm{VAR} = \int_0^{t_f} \int_{\mathbb{D}} (X - X_\infty)^2\, \mathcal{W}(y)\, \mathrm{d}\boldsymbol{x}\, \mathrm{d}t, \tag{4.18}$$

where X_∞ is determined by (4.5) with $h_0(x, z) = 0$. VAR can be considered as the 'variance' of X with respect to the unperturbed field X_∞.

4.3.3 Quantifying sensitivity of mixing

The flow variables $\vec{Q}$ and initial perturbation amplitudes $\vec{A}$ are governed by the Navier–Stokes equations and its initial conditions, given by

$$\vec{\mathcal{M}}(\vec{Q}, \vec{A}) = \vec{\mathcal{N}}(\vec{Q}) + \left[\vec{Q}(\vec{A}) - \vec{Q}_0\right] \delta_{t=0} \equiv 0, \tag{4.19}$$

where $\vec{\mathcal{N}}$ denotes the flow equations (2.11), $\vec{Q}_0(\vec{A})$ are the flow variables at $t = 0$, and $\delta_{t=0}$ denotes the Dirac Delta function, which is unity for $t = 0$ and zero otherwise. The last term in (4.19) enforces the initial conditions and is presented as such to obtain the sensitivity of $\mathcal{J}$ to $\vec{A}$. A similar formulation can be found in Foures *et al.* (2014b). Following what was done in Chapter 2.4, the adjoint sensitivity is computed as

$$\frac{\delta \mathcal{J}}{\delta \vec{A}} = \int_{\mathbb{D}} \vec{Q}_0^{\dagger \mathsf{T}} \frac{\partial \vec{Q}_0}{\partial \vec{A}} \, \mathrm{d}\boldsymbol{x} \text{ at } t = 0. \tag{4.20}$$

To avoid measuring sensitivity near the domain boundaries, we multiply a weighting function, $\mathcal{W}_\Gamma$, with initial perturbation $h_0(x, z)$ that enforces compact support near the interface, and approaches zero towards the walls in a similar manner as (4.11). Therefore, the initial mole fraction equation (4.5) is modified according to

$$X = \frac{1}{2}\left\{1 + \mathrm{erf}\left[\frac{y - h_0(x,z)\mathcal{W}_\Gamma(y)}{\delta_D}\right]\right\}. \tag{4.21}$$

This modification does not significantly change the initial conditions provided that the weighting function is near unity in the vicinity of the interface and the imposed perturbation h_0 is small.

The sensitivity provided by the adjoint solution after discretizing (4.20) can induce truncation errors accumulated in $\vec{Q}^\dagger$ that may become significant in unsteady or chaotic flows (Nadarajah & Jameson, 2000; Carnarius *et al.*, 2010). Simulations of turbulent mixing like the ones considered here are particularly sensitive to this since the numerical resolution is often close to the limits of the discretization. To this end, the present work employs the discrete counterpart of the inner product (4.10) and the fully discretized Navier–Stokes equations (in space and time) prior to employing the Lagrangian (2.13). Details of the space-time discrete adjoint formulation consistent with the SBP-SAT discretization outlined in Chapter 4.2.4, and verification of its sensitivity gradient, can be found in Vishnampet *et al.* (2015); Capecelatro *et al.* (2018).

4.3.4 Verification of the adjoint sensitivity

The accuracy of the adjoint sensitivity (2.16), i.e., (4.20) for this problem, can be verified by comparing to finite difference approximations of $\delta\mathcal{J}/\delta\vec{f}$. For this purpose, $\mathcal{J}$ is recomputed via perturbing the parameter $\vec{f}$ (i.e., $\vec{A}$ in this case) in the direction of the adjoint sensitivity. The modified $\mathcal{J}$ is related to the baseline QoI by considering the first-order Taylor series, given by

$$\mathcal{J}\left(\vec{Q}+\delta\vec{Q},\vec{f}+\varepsilon\frac{\delta\mathcal{J}}{\delta\vec{f}}\right)=\mathcal{J}(Q,\vec{f})+\varepsilon\frac{\delta\mathcal{J}}{\delta\vec{f}}\cdot\frac{\delta\mathcal{J}}{\delta\vec{f}}+O(\varepsilon^2)+O_t(\Delta x_i^{a'},\Delta t^{b'}), \tag{4.22}$$

where $\delta\mathcal{J}/\delta\vec{f}$ is computed via (2.16), and ε denotes the step size of the finite difference approximation. $O_t(\Delta x_i^{a'},\Delta t^{b'})$ represents truncation errors due to discretizing the governing equations (2.11) and adjoint equations provided in Appendix A. Δx_i and Δt denotes the grid spacing and timestep size, respectively. A sensitivity error is obtained by rearranging (4.22), given by

$$\frac{\mathcal{J}\left(\vec{Q}+\delta\vec{Q},\vec{f}+\varepsilon\frac{\delta\mathcal{J}}{\delta\vec{f}}\right)-\mathcal{J}(\vec{Q},\vec{f})}{\varepsilon}-\frac{\delta\mathcal{J}}{\delta\vec{f}}\cdot\frac{\delta\mathcal{J}}{\delta\vec{f}}=O(\varepsilon)+O_t(\Delta x_i^{a},\Delta t^{b}). \tag{4.23}$$

As can be seen, the above expression compares the adjoint sensitivity solution $\delta\mathcal{J}/\delta\vec{f}$ with a first-order finite difference approximation that uses ε as its step size. The truncation error $O_t(\Delta x_i^{a},\Delta t^{b})$ is zero in discrete-adjoint methods since the adjoint sensitivity is obtained via perturbing the discretized flow equations. Thus, the discrete-adjoint equations are algebraic equations instead of partial differential equations and no discretization is required.

The adjoint sensitivity of a two-dimensional RT instability is investigated according to (4.23) as can be seen in Fig. 4.1, which suggests that the error is proportional to the step size as expected by (4.23) until machine-precision roundoff errors become dominate.

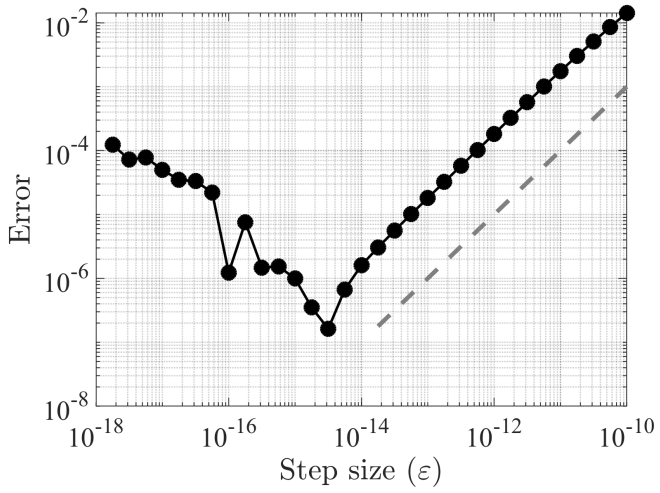

Figure 4.1: Verification of the adjoint sensitivity of a two-dimensional RT instability by comparing its error $(- \bullet -)$ (4.23) with a linear slope $(--)$.

.

4.4 Sensitivity of a three-dimensional RT instability

4.4.1 Rayleigh–Taylor growth

In this section a three-dimensional multi-mode RT instability is considered. The interfacial amplitudes $A_{m,n}$ are initially distributed uniformly, i.e., $A_{m,n} = A_0$ for $m = 1, \ldots, M$ and $n = 1, \ldots, N$, and the phases are distributed randomly, $0 \leq \theta_{m,x},\ \theta_{n,z} \leq 2\pi$. Thirty-two modes are considered in each horizontal direction (i.e., $M = N = 32$), and the smallest wavelength in each direction is $\lambda_{\min} = 8\Delta x$. Linear stability theory predicts that the exponential growth rate of the incompressible ($p_I \to \infty$) RT instability is negative for $k > 21$ (Duff *et al.*, 1962). Thus, the present configuration should account for all active modes. The root-mean-square (RMS) of initial perturbation $h_{0,\mathrm{RMS}} = 3.15 \times 10^{-4} L$ is chosen based on Banerjee & Andrews (2009), which leads to $A_0 = 1.97 \times 10^{-5} L$.

The evolution of bubble height h_b and tip velocity $\dot{h}_b$ in Fig. 4.2a depict the various stages of RT growth up to $t = 4\tau$. The instability begins in the diffusion growth (DG) regime until $t \approx \tau$. Afterwards, gravitational effects become important, leading to the exponential growth (EG)

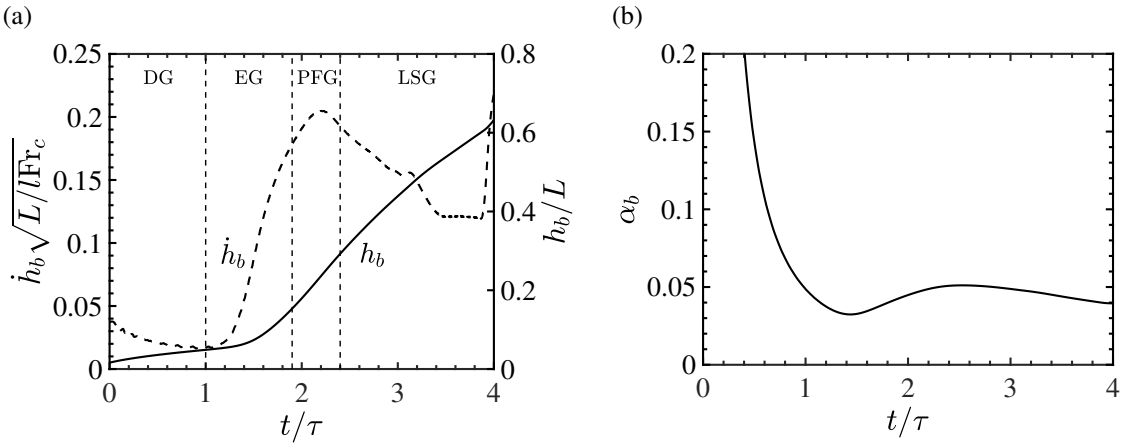

Figure 4.2: (*a*) Evolution of bubble height (–) and bubble tip velocity (−−) of the three-dimensional RT instability through the diffusion growth (DG), exponential growth (EG), potential flow growth (PFG) and late-stage growth (LSG). (*b*) Corresponding bubble growth parameter α_b.

regime until $t \approx 1.9\tau$. Then, nonlinearities become important, giving rise to a potential flow growth (PFG) stage where the bubble tip velocity is approximately constant until $t \approx 2.4\tau$. Afterwards, additional nonlinearities cause the bubble tip velocity to decrease. It then reaccelerates at $t \approx 3.9\tau$. The corresponding bubble growth parameter becomes approximately constant for $t > 2.5\tau$, where a self-similar late-stage growth (LSG) regime exists (see Fig. 4.2b). The bubble growth parameter is seen to approach $\alpha_b \approx 0.04$, consistent with values reported in the literature (e.g., Dimonte *et al.*, 2004; Ramaprabhu *et al.*, 2005). Two-dimensional snapshots of the mole fraction within different regimes do not show significant mixing until reaching the PFG stage (see Fig. 4.3).

The conventional measures for RT mixing, defined according to (4.12), (4.14) and (4.15), are compared with the objective functions defined in Chapter 4.3.2 as given by (4.16)–(4.18) (see Fig. 4.4). Each quantity shows relatively small growth during the DG and EG stages, and a rapid increase in mixing after $t \approx 2\tau$, consistent with Figs. 4.2 and 4.3. It is interesting to note that the trend of each objective function is approximately similar. However, the growth of the kinetic energy norm KE (defined using $\mathcal{I} = v^2$) is seen to be delayed until $t \approx 2\tau$ due to diffusion effects. It then increases exponentially according to linear stability theory during the EG regime ($t \gtrapprox 1.6\tau$). Both MIX (defined using $\mathcal{I} = X(1 - X)$) and the mixing width w are observed to evolve in a similar manner, which is not unexpected due to their similarities in definition. The initial growth

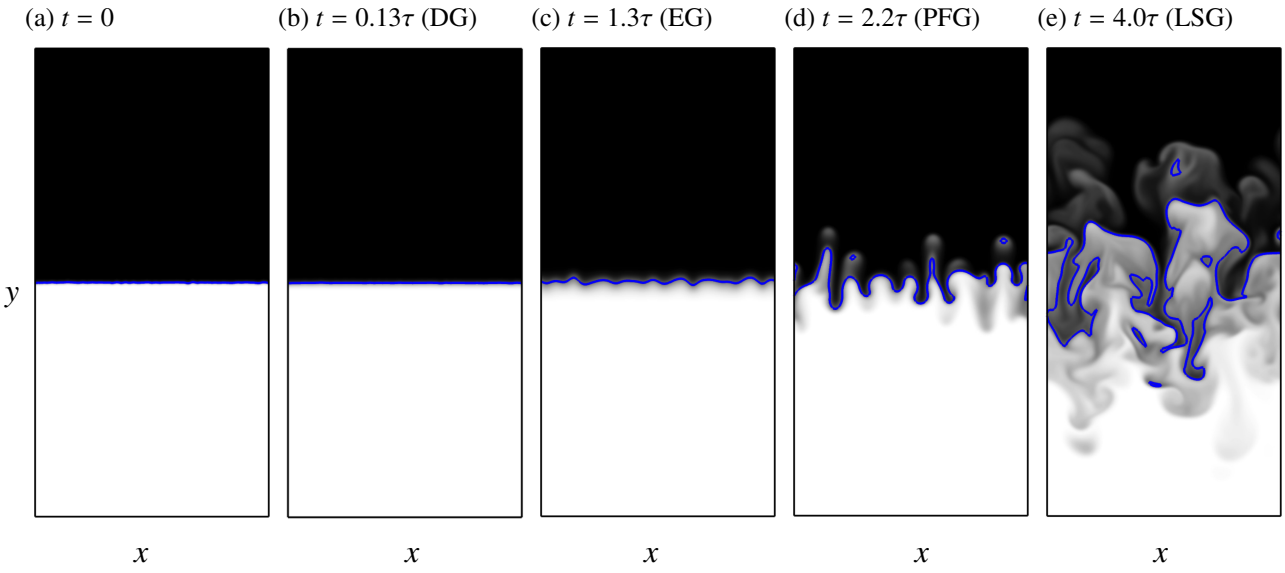

Figure 4.3: Evolution of mole fraction X in the $z = -\pi$ plane. The gray scale shows mole fraction from X =0 (white) to $X = 1$ (black). The blue line depicts the fluid interface ($X = 0.5$).

of bubble-spike distance h_t is similar to that of the mixing height, mixing width and MIX. This suggests the objective functions presented in Chapter 4.3.2 act as good surrogates for quantifying RT growth and mixing. Sensitivity of these quantities to the initial interfacial perturbations will be presented in the following section.

4.4.2 Sensitivities to different measures of mixing

The sensitivity of $\mathcal{J}$ to $\vec{A}$ over duration t_f are evaluated across the averaged perturbation wavenumbers $k = \sqrt{k_x^2 + k_z^2}$ (see Fig. 4.5). It can immediately be seen that at early stages of the RT instability the distribution of sensitivity varies between the different quantities of interest, and collapse at late time. Within the DG stage, VAR and KE are most sensitive to low and intermediate wavenumber perturbations, and are least sensitive at the highest wavenumbers (see Fig. 4.5a). Perhaps surprisingly, MIX exhibits an opposite trend, with sensitivity increasing with increasing k. This suggests that when diffusion dominates, the largest changes to the quantity $X(1 - X)$ can be achieved by perturbing the perturbation amplitude at the highest wavenumbers. This early-time behaviour can be predicted analytically by assuming the mole fraction evolves according to a diffusion equation.

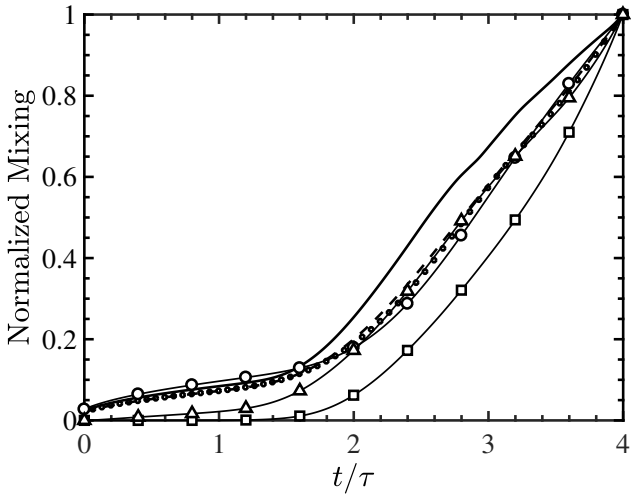

Figure 4.4: Conventional measures for RT mixing: h_t (–), w (−−) and h_m ($\cdots$). Instantaneous values of the objective functions MIX (−◯−), KE (−□−) and VAR (−△−). All data are normalized by their final values (at $t = 4\tau$).

Assuming purely diffusional growth, the distribution of sensitivity with k can be shown to be a consequence of the functional dependence of $\mathcal{J}$ on X and initial conditions. A detailed comparison of the theoretical estimates of early-time sensitivity and the adjoint solution for each objective function is provided in Appendix D.

Inertial effects from buoyancy become more significant as time increases. Linear stability theory predicts that the exponential growth rate within the EG regime, $\sigma_k^{(\mathrm{EG})}$, is given by (Duff *et al.*, 1962)

$$\sigma_k^{(\mathrm{EG})} = \left[\frac{\mathrm{At}k}{\psi \mathrm{Fr}_c} + \frac{k^4}{\rho_I^2 \mathrm{Re}_c^2}\right]^{1/2} - \left(1 + \mathrm{Sc}^{-1}\right)\frac{k^2}{\rho_I \mathrm{Re}_c}, \tag{4.24}$$

where ψ depends on the Atwood number, wavenumber and the thickness of the diffusive layer (see Duff *et al.*, 1962). The above relation predicts $k = 7.58$ as the most unstable wavenumber at $t = 0$. As shown in Fig. 4.5b, this is consistent with the most sensitive wavenumber provided by the adjoint solution in the EG regime. As the time duration increases, the most sensitive modes corresponding to MIX shifts from the highest wavenumbers to lower ones. Within the PFG and LSG regimes, the distribution of sensitivity is similar for all objective functions, with maximum sensitivity remaining close to the most unstable wavenumber predicted by linear stability theory.

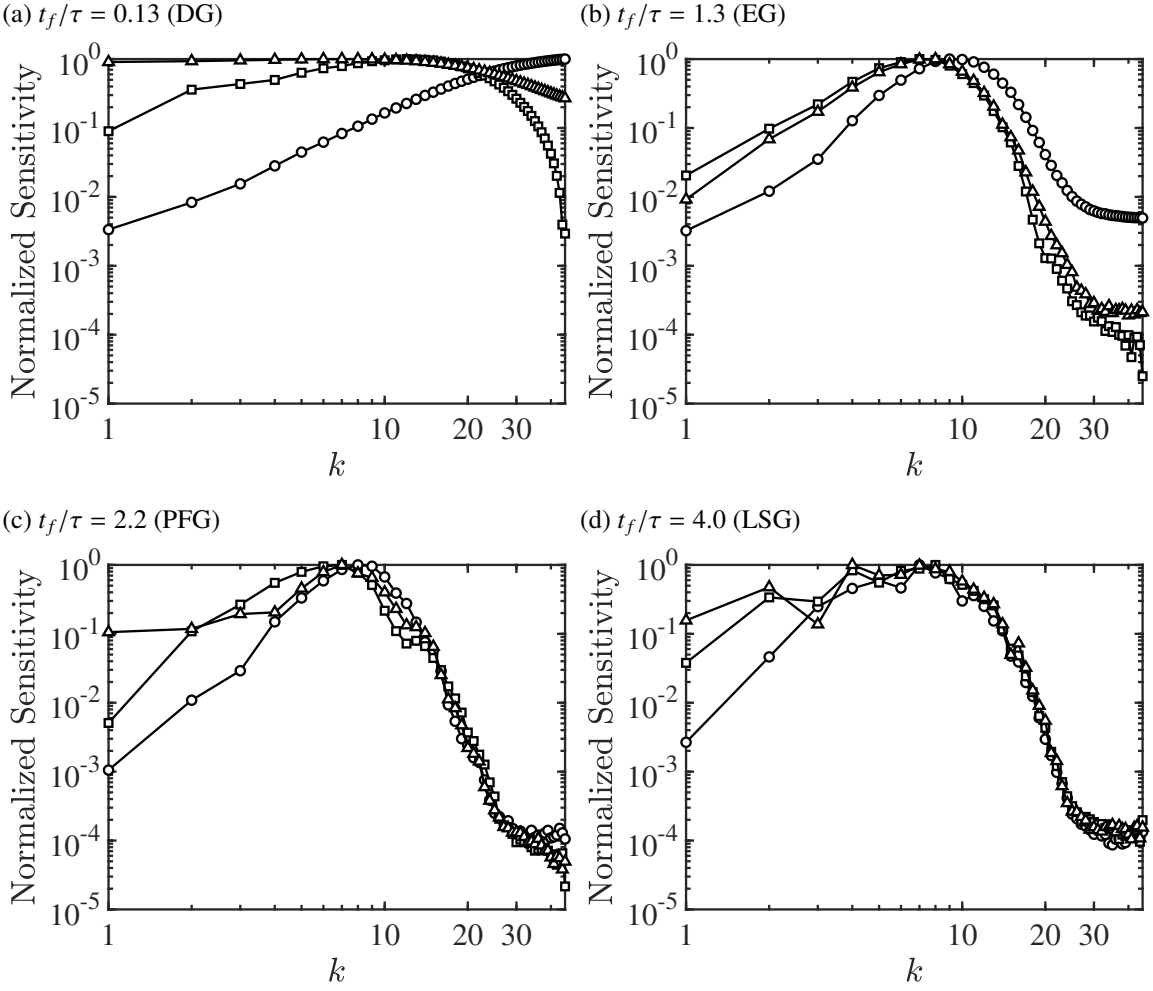

Figure 4.5: Magnitude of sensitivity $|\delta\mathcal{J}/\delta\vec{A}|$ integrated over different durations t_f for MIX ($-\bigcirc-$), KE ($-\square-$) and VAR ($-\ \triangle\ -$). The sensitivities are shown as a function of initial perturbation wavenumber $k = \sqrt{k_x^2 + k_z^2}$ and normalized by their corresponding maximum value.

Except for MIX in the DG regime, the objective functions are generally unaffected by perturbation modes at wavenumbers $k > 20$. Linear stability theory predicts that these modes are damped by diffusion during the EG regime.

It is interesting to note that the most sensitive wavenumber throughout the growth of the RT instability remains approximately constant and consistent with the most unstable wavenumber predicted by linear stability theory. However, its distribution varies. This suggests that employing linear stability theory for manipulating growth of the instability may have only limited success due to the broadband nature of sensitivity. This will be confirmed in Chapter 4.5.

It is important to note that the sensitivity obtained by the adjoint solution in chaotic dynamic systems are known to diverge when measured over long time horizons (e.g., see Lea *et al.*, 2000; Wang & Gao, 2013). Thus, the values used for normalization in Fig. 4.5 will change depending on the duration considered. Following Wang & Gao (2013), its chaotic behaviour is characterized by estimating the first Lyapunov exponent, Λ, for the adjoint solution of each objective function over the duration $t_f = 4.0\tau$, according to

$$\left\| \sum_{i=1}^{6} Q_i^\dagger(\boldsymbol{x}, t) \mathcal{W}_\Gamma(y) \right\|_2 \propto \exp(-\Lambda t), \tag{4.25}$$

where $\|\cdot\|_2$ is a spatial L^2 norm operator, and $i = 1, \ldots, 6$ denotes the i-th component of adjoint variable. The value of Λ estimates the average growth rate in $\delta\mathcal{J}$ due to small changes in initial interfacial perturbations (e.g., see Trevisan & Legnani, 1995). As can be seen in Fig. 4.6, the magnitude of the adjoint variables exponentially increase in inverse time with rates $\Lambda = 3.42\tau^{-1}$, $3.48\tau^{-1}$ and $3.45\tau^{-1}$ for MIX, KE and VAR, respectively. From this, the rate at which sensitivity diverges does not significantly differ among the different objective functions. We note that the positive first Lyapunov exponents of each objective function limits the time horizon that can be considered, which may affect the optimization of the instability during late-time growth. The utility of the adjoint solution for controlling the RT instability will be addressed in Chapter 4.5.3. The next section will analyse local sensitivity at various stages of the instability.

4.4.3 Spatial sensitivity at various stages of the RT instability

In this section we evaluate the spatial distribution of sensitivity at different stages of the instability. The sensitivity gradient defined in (4.20) can be rewritten as

$$\frac{\delta\mathcal{J}}{\delta\vec{Q}_0} = \int_{\mathbb{D}} \int_0^{t_f} \frac{\delta\mathcal{I}}{\delta\vec{Q}_0} \, \mathrm{d}t \, \mathrm{d}\boldsymbol{x} = \int_{\mathbb{D}} \vec{Q}_0^\dagger \, \mathrm{d}\boldsymbol{x}. \tag{4.26}$$

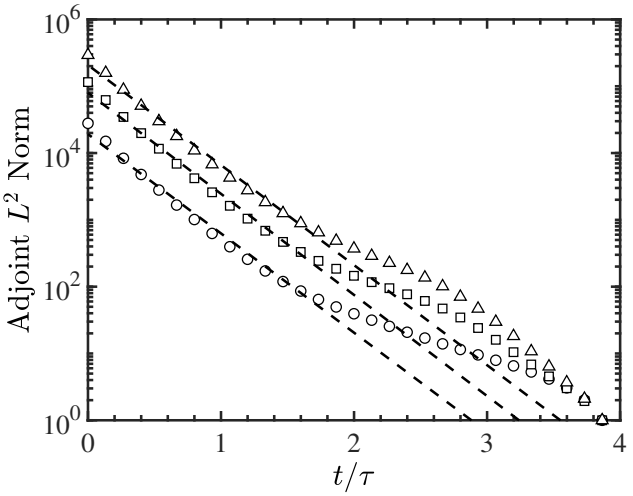

Figure 4.6: The L^2 norm of adjoint solutions for MIX (◯), KE (□) and VAR (△). The L^2 norms are normalized by the corresponding values at $t = 3.87\tau$. The dashed lines estimate the growth in the adjoint solution based on the first Lyapunov exponent, which was found to be $\Lambda = 3.42\tau^{-1}$, $3.48\tau^{-1}$ and $3.45\tau^{-1}$ for MIX, KE and VAR, respectively.

Thus, the local adjoint variables $Q_i^\dagger$ at $t = 0$ provide spatial sensitivity of the mixing norms to the flow state. With this, the local sensitivity of $\mathcal{J}$ with respect to initial mole fraction variations can be expressed as

$$\frac{\delta \mathcal{J}}{\delta X_0} = \rho Y^\dagger \frac{\partial Y}{\partial X}, \tag{4.27}$$

where the chain rule is used, and $\partial Y/\partial X$ can be determined using the relation $Y = XW_1/W$.

The spatial distribution of $\delta\mathcal{J}/\delta X_0$ for VAR integrated over different durations in the vertical plane $z = -\pi$ are compared in Figs. 4.7a–4.7d and at the fluid interface $X = 0.5$ in Figs. 4.7e–4.7h. As can be seen in Figs. 4.7a–4.7d, local sensitivity exhibits a periodic distribution that is maximum near the interface. As was shown in the previous section, the dominant wavenumber of local sensitivity at the interface during the EG stage corresponds to $k \simeq 7$, consistent with the most unstable wavenumber mode predicted by liner stability theory (see Fig. 4.7f). Local sensitivity does not significantly change from EG to PFG (see Fig. 4.7g). However, the sensitivity in the LSG stage exhibits more variations near the interface, suggesting a broader range of modes contribute to mixing. Figures 4.7e– 4.7h show that adjusting the perturbations at the fluid interface could both locally increase (positive sensitivity) or decrease (negative sensitivity) the mixing norm. Non-

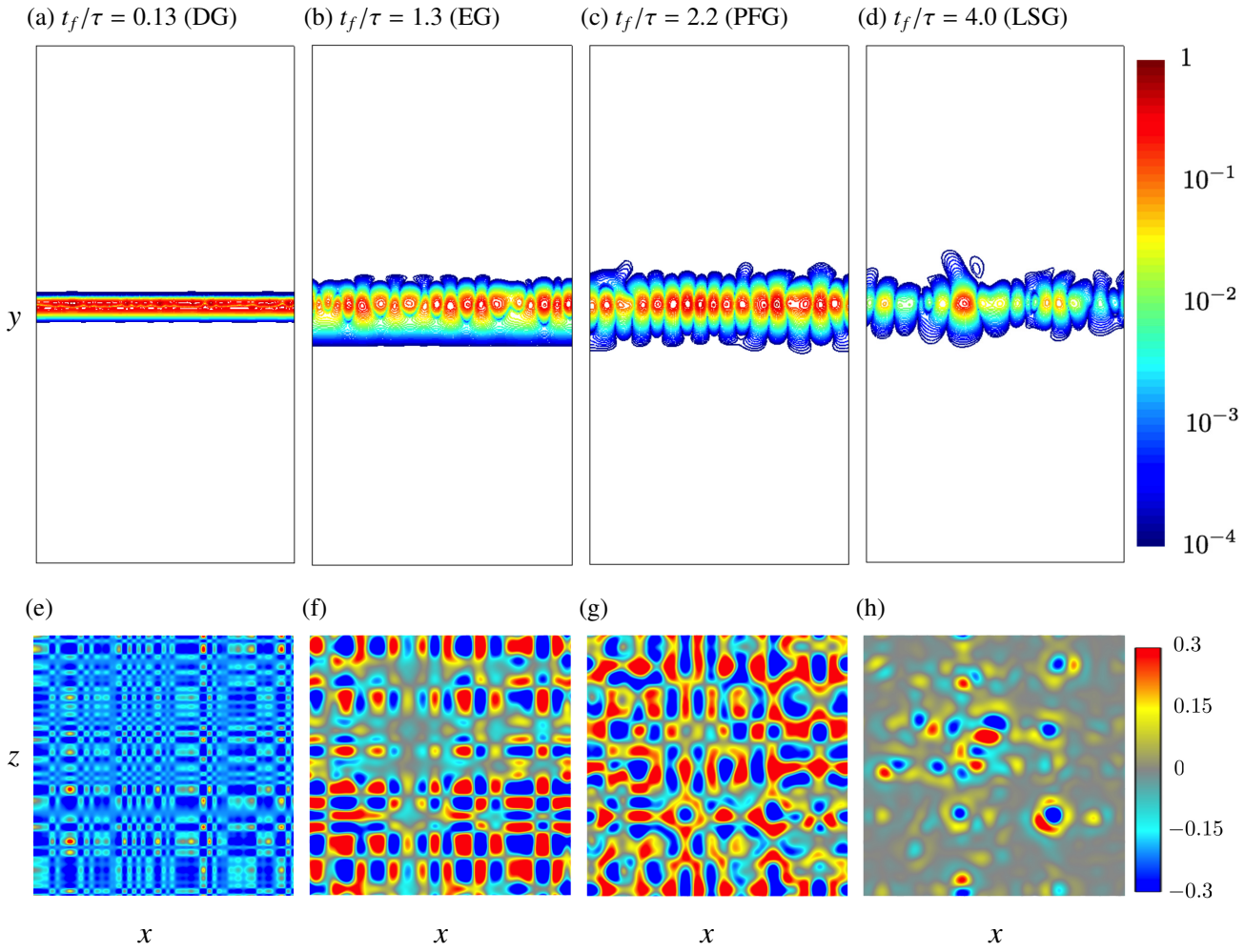

Figure 4.7: Normalized sensitivities of VAR to initial mole fraction ($\delta\mathcal{J}/\delta X_0$) in physical space for different time durations $t \in [0, t_f]$. The sensitivities are normalized by their maximum value. (*a–d*): Normalized sensitivity magnitude at $z = -\pi$. (*e–h*): Normalized sensitivity at the fluid interface ($X = 0.5$).

uniformities in sensitivity observed at the x–z plane suggest that the effects of spatial variations in the initial conditions on mixing persist at late time stages of the growth.

4.4.4 The role of initial conditions on late-time sensitivity

In the previous sections we considered initial interfacial perturbations with uniform amplitude and random phase. In order to evaluate the effects of initial perturbations on different stages of the RT growth, phases $\theta_{x,m}$ and $\theta_{z,n}$ are varied while holding the amplitudes constant. Haan (1989)

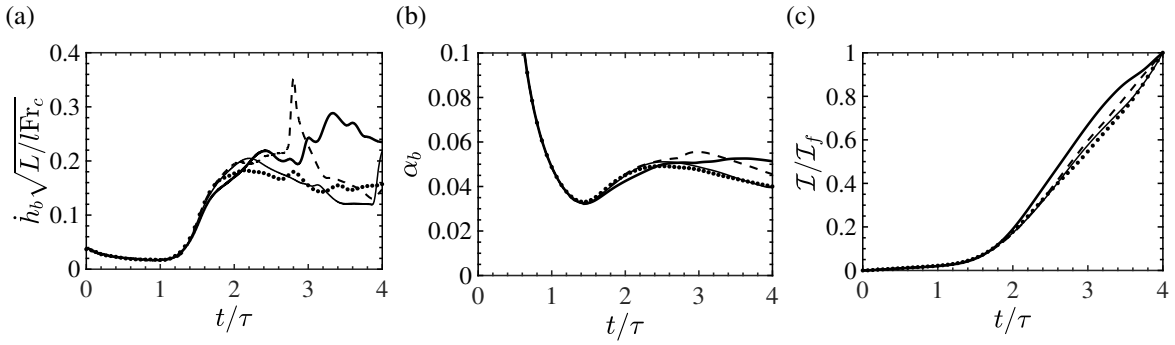

Figure 4.8: Evolution of (a) the bubble tip velocity, (b) bubble growth parameter and (c) instantaneous objective function VAR ($\mathcal{I} = (X - X_\infty)^2$), for four different initial interfacial perturbations of the three-dimensional RT instability.

showed that a group of perturbation modes with similar phases can regionally combine and create a net perturbation amplitude during an RT instability. Thus, we expect that changing the initial perturbation phases while holding the initial amplitudes constant should lead to different nonlinear growth. The evolution of $\dot{h}_b$, α_b and $\mathcal{I} = (X - X_\infty)^2$ with different initial random phases are compared in Fig. 4.8. The bubble growth during the DG and EG stages are insensitive to the initial random phases, while deviations appear during the PFG and LSG regimes (see Fig. 4.8a). The bubble tip velocity corresponding to one of the realization decelerates following a PFG state, and later reaccelerates. On the other hand, another realization exhibits a reacceleration regime after PFG, prior to deceleration. Another realization exhibits a long PFG regime, with a slight deceleration in the bubble growth rate α_b while the other illustrates a combination of short-time accelerations and decelerations during the LSG regime. A chaotic behaviour is observed during the LSG regime. Meanwhile, it can be seen that the bubble growth parameter α_b marginally changes for these initial conditions (see Fig. 4.8b). In addition, the objective function $\mathcal{I} = (X - X_\infty)^2$ corresponding to different initial phases are similar until $t \approx 2\tau$ at which point it diverges (see Fig. 4.8c).

Figure 4.8 shows that the growth is insensitive to initial random phases until $t \approx 2\tau$. For each k, the sensitivity averaged over all realization during early ($t_f = 2.2\tau$) and late ($t_f = 4.0\tau$) nonlinear stages is shown in Fig. 4.9. It can be seen that randomly adjusting the phases leads to significant

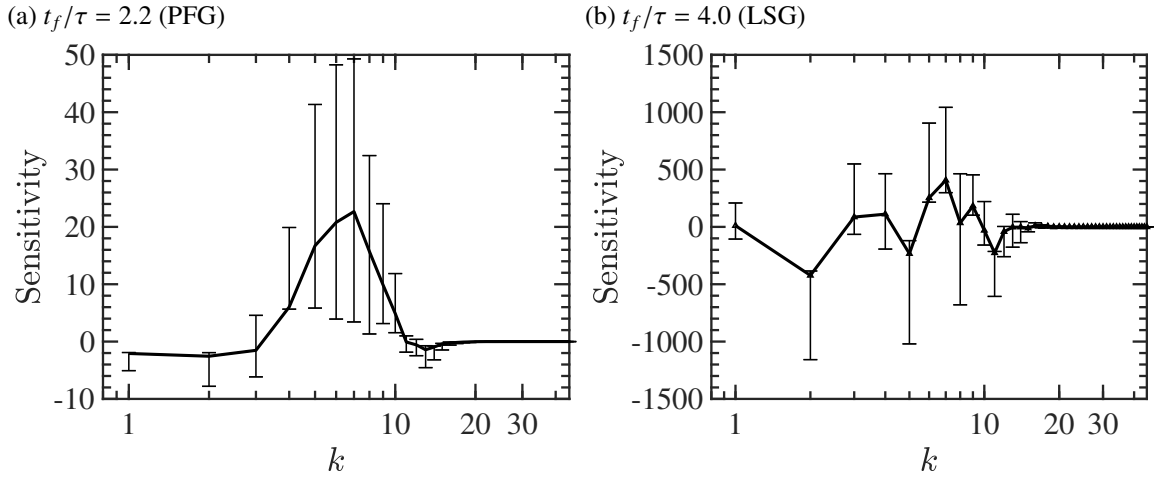

Figure 4.9: Ensemble-averaged sensitivities of VAR ($\delta\mathcal{J}/\delta\vec{A}$) for different random initial phases. The sensitivities are shown as a function of initial perturbation wavenumber $k = \sqrt{k_x^2 + k_z^2}$. The vertical bars illustrate the minimum and maximum sensitivities at each wavenumber.

variations in sensitivity at late stages. A set of modes $2 \leq k \leq 10$ are highly sensitive to initial phases when $t_f = 2.2\tau$ (see Fig. 4.9a). At later times, a broader range of modes are sensitive to the initial phases (see Fig. 4.9b). This is consistent with the positive values of the first Lyapunov exponent discussed in Chapter 4.4.2 (see Fig. 4.6).

4.5 Optimizing a two-dimensional RT instability

In the previous section, sensitivity of multi-mode three-dimensional RT instabilities were analysed. The sensitivity $\delta\mathcal{J}/\delta\vec{A}$ provides the direction towards which the objective function increases (or decreases) with changes to each individual amplitude. In this section, sensitivity obtained from the adjoint solution is employed in a gradient-based optimization framework in order to seek the optimal interfacial perturbations for suppressing and enhancing mixing during the growth of the RT instability. Despite the increased efficiency in computing the sensitivity provided by the adjoint, a direct numerical simulation of three-dimensional multi-mode RT instabilities remain computationally demanding. Thus, optimization of the three-dimensional RT instability would be limited to a small number of iterations. To this end, optimization is performed in two dimen-

sions, with all other parameters considered in Chapter 4.4 kept unchanged. Therefore, only the perturbation amplitudes A_m and phases $\theta_{x,m}$ are varied. In addition, the same RMS of initial perturbation $h_{0,\mathrm{RMS}} = 3.15 \times 10^{-4} L$ is considered. The baseline solution has a uniform distribution of perturbation energy across all wavenumbers, corresponding to an initial amplitude for each mode $A_0 = 7.875 \times 10^{-5} L$.

The optimization procedure can be summarized as

$$\begin{aligned} \text{minimize/maximize} \quad & \mathcal{J}(A_m, \vec{\mathcal{Q}}(A_m)), \\ \text{with respect to} \quad & A_m, \quad m = 1, \ldots, M, \\ \text{subject to} \quad & \sum_{m=1}^{M} A_m^2 = \text{constant}, \\ & |A_m| \leq 4.5 \times 10^{-4} L. \end{aligned} \tag{4.28}$$

The constraint $\sum_{m=1}^{M} A_m^2$ enforces the perturbation energy to be constant, preventing a trivial solution (e.g., $A_m = 0$ or $A_m \gg A_0$). Keeping the perturbation energy constant also provides an upper bound for each amplitude. This bound is imposed on the amplitudes to constrain the optimizer. The amplitudes can take negative values which are interpreted as changes in perturbation phase $\theta_{x,m}$. The optimization procedure (4.28) is solved by a Sequential Least SQuares Programming (SLSQP) algorithm (Kraft, 1988) that leverages the `SciPy minimize` package, an open source Python library (Jones *et al.*, 2001; Oliphant, 2007; Millman & Aivazis, 2011). The tolerance for termination is set to 10^{-6}. The objective function, constraint and gradients are taken as inputs to the optimization library that enforces the amplitude bounds of (4.28).

4.5.1 Selectively assigning the perturbation energy

Before performing the optimization, two-dimensional simulations of RT instabilities are reported with carefully chosen interfacial perturbations for comparison in later sections. As discussed in Chapter 4.4, perturbations with wavenumbers $k > 21$ are suppressed during the EG stage accord-

ing to linear stability theory (Duff *et al.*, 1962). Therefore, it is expected that the optimized solution for minimizing RT mixing corresponds to an interface with all of the energy contained in the highest wavenumbers, leading to pure diffusional growth. Yet, the optimized solution for enhancing mixing is less obvious. In the context of scalar mixing, it is well known that large flow structures are controlled by advection while small length scales are mainly mixed by diffusion (e.g., see Foures *et al.*, 2014b; Miles, 2018). For RT instabilities, it has been observed that assigning more perturbation energy into low wavenumber modes increases the growth parameter α (e.g., see Cook & Dimotakis, 2001; Ristorcelli & Clark, 2004; Youngs, 2009; Banerjee & Andrews, 2009). In addition, Cook & Dimotakis (2001) showed that seeding the lowest wavenumbers leads to 'the largest unmixedness'. In summary, it is expected that increased bubble/spike penetration occurs when more perturbation energy is added to low wavenumbers of the initial interface. When the perturbations are distributed among the highest wavenumber modes mixing is dominated by diffusion.

With this in mind, three different initial conditions are considered: (i) a uniform distribution of modal energy with random phases (similar to the configuration used in Chapter 4.4) serving as the baseline solution for the remainder of the chapter; (ii) all the energy contained in the lowest wavenumber denoted here as Case A; and (iii) all the energy contained in the highest wavenumber referred to here as Case B. As shown in Fig. 4.10, the baseline case yields bubble and spike penetration associated with low perturbation wavenumbers as well as diffusion mixing associated with high wavenumbers. Nonlinear mode-coupling also occurs due to the existence of high wavenumber interfacial perturbations. Case A produces large amounts of penetration through the formation of a bubble and spike. The interfacial perturbation is suppressed in Case B during early-time regimes according to linear stability theory (Duff *et al.*, 1962), and mixing is dominated by diffusion throughout the duration of the simulation.

Values of the corresponding objective functions for the three cases are reported in Table 4.1. Both the lowest and highest wavenumber distributions produce smaller MIX values compared to the uniform distribution. The corresponding integrand, $\mathcal{I} = X(1 - X)$, is maximum for completely

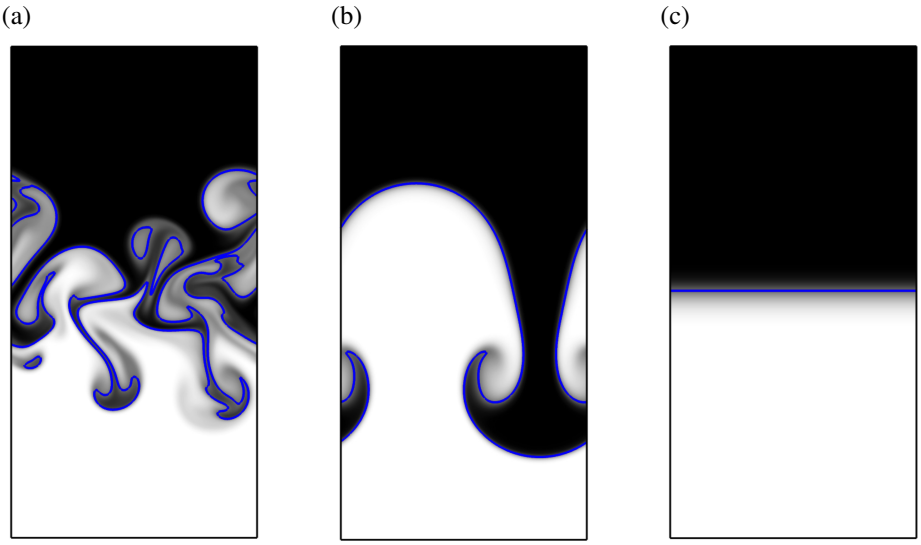

Figure 4.10: Bubble and spike structures of a two-dimensional RT instability at $t = 4.0\tau$ with different initial interfacial perturbations. (a) Baseline (uniform amplitude among all wavenumbers), (b) Case A (all energy contained in the lowest mode) and (c) Case B (all energy contained in the highest mode). Same color scheme as Fig. 4.3.

mixed fluid ($X = 0.5$) and zero for pure fluids. Thus, neither single-mode cases produce as much mixing as in the uniform case as a result of nonlinear mode-coupling. Case A demonstrates solely large-scale fluid penetration, resulting in high interfacial velocity and thus larger values of KE compared to the other objective functions. Assigning the initial perturbation energy into the lowest mode increases KE by almost a factor of 2 compared to the baseline case. Comparatively, putting all the perturbation energy into the highest wavenumber decreases KE by 5 orders of magnitude due to dissipation of kinetic energy by diffusion. Putting all the energy into the lowest mode increases VAR by almost 30% compared to the baseline case. The largest possible value of the VAR integrand, $\mathcal{I}_\infty = (X - X_\infty)^2$, occurs when the two fluids are inverted (i.e., the light fluid on top and heavy fluid on bottom). Thus, larger values of VAR occur in the presence of fluid penetration rather than pure mixing.

Figure 4.11 shows a comparison of the bubble height, bubble tip velocity and mixing width of the two-dimensional RT instability with the three different initial conditions. The bubble tip velocity in Case A approaches the PG regime at a later time compared to the baseline case due to the baseline case containing energy in modes with greater exponential growth rate. In addition,

Normalized objective function	Case A	Case B	$\min_{A_m} \mathcal{J}(\vec{Q}, A_m)$	$\max_{A_m} \mathcal{J}(\vec{Q}, A_m)$
MIX	0.432	0.397	0.397	1.386
KE	1.987	5.13×10^{-5}	6.70×10^{-5}	8.853
VAR	1.266	0.075	0.075	3.111

Table 4.1: Objective functions measured over duration $t_f = 4.0\tau$ normalized by their baseline solution $\mathcal{J}^{(0)}$ (uniformly distributed perturbation energy).

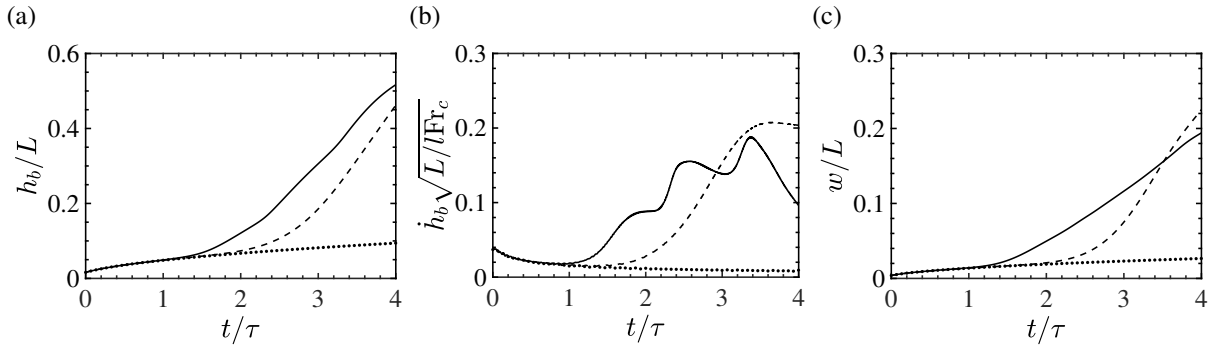

Figure 4.11: Evolution of (*a*) bubble height, (*b*) bubble tip velocity and (*c*) mixing width of the two-dimensional RT instability with different initial interfacial perturbation energy: Baseline (–), Case A (−−) and Case B (··).

nonlinear mode-coupling effects absent in Case A and Case B result in increased growth. The EG stage holds while $h_0 \ll \lambda$, and thus Case A will not exceed the EG regime until a greater time interval has passed compared with the baseline case. In contrast, the bubble tip velocity of Case B decreases due to diffusion.

Finally, it can be seen that the two-dimensional multi-mode RT instability (Figs 4.10 and 4.11) grows more slowly compared to the three-dimensional flow (Figs 4.2 and 4.3). This is consistent with previous work that shows how three-dimensional RT instabilities grow faster than their two-dimensional counterparts during the early nonlinear regime (Layzer, 1955; Hecht *et al.*, 1994; Oron *et al.*, 2001; Goncharov, 2002). This is due to reduced kinematic drag associated with three-dimensional bubbles compared to elongated two-dimensional bubbles, leading to a greater terminal bubble tip velocity in three-dimensions.

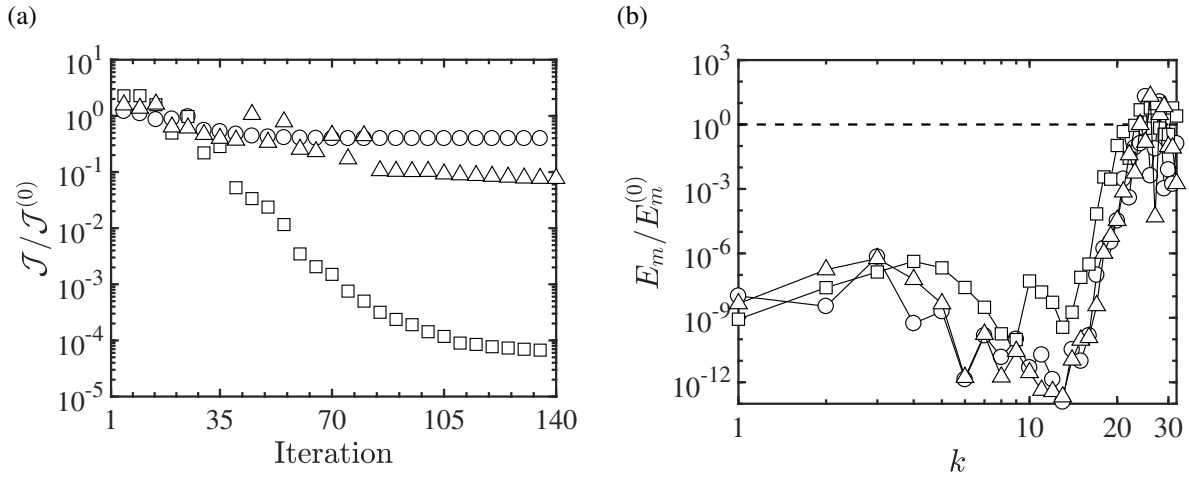

Figure 4.12: (*a*) Reduction of the objective functions normalized by their corresponding baseline values $\mathcal{J}^{(0)}$ for MIX (◯), KE (□), and VAR (△). (*b*) The spectrum of interfacial perturbation energy for the baseline case (−−) and the optimized solution (symbols).

4.5.2 Optimal solution for suppressing mixing

As discussed in the previous section, we expect mixing and growth to be suppressed by transferring all of the perturbation energy into the highest wavenumber modes such that diffusion dominates. In this section, this solution is sought by minimizing the objective functions via the gradient-based optimization method described earlier. Figure 4.12a shows the value of each objective function during the iterative process of the optimization procedure. Different levels of reduction are observed for each objective function. The optimized quantities are listed in Table 4.1. Adjoint-based optimization is capable of reducing KE and VAR by more than an order of magnitude compared to their baseline values while MIX is only reduced by approximately 60%. Due to the initially smooth distribution of mole fraction as defined in (4.5), MIX will remain finite even in the absence of any mixing or growth. As a consequence, its optimal solution approaches the value from Case B and not zero. As expected, the perturbation energy of the optimized solution for each objective function is transferred to high wavenumber modes, resulting in diffusion dominated growth (see Fig. 4.12b).

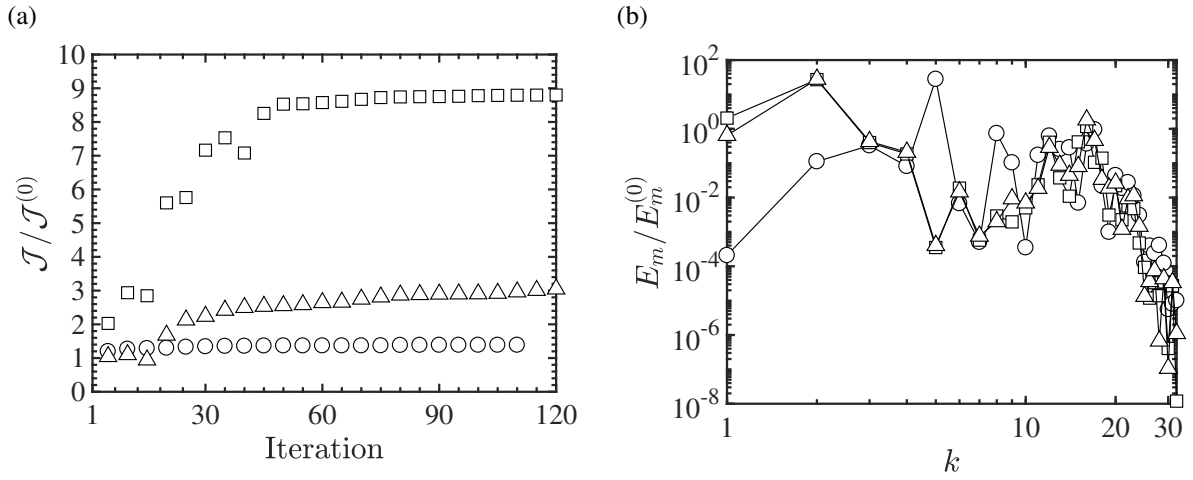

Figure 4.13: (*a*) Enhancement of the objective functions over duration $t_f = 4\tau$ normalized by their corresponding baseline values $\mathcal{J}^{(0)}$ for MIX (◯), KE (□), and VAR (△). (*b*) The spectrum of initial interfacial perturbation energy of the optimized solution.

4.5.3 Optimal solution for enhancing mixing

Based on previous studies of multi-mode RT instabilities (e.g., see Cook & Dimotakis, 2001; Ristorcelli & Clark, 2004; Youngs, 2009; Banerjee & Andrews, 2009), it is anticipated that maximizing late-time growth requires shifting the perturbation energy towards the low wavenumber modes. In this section, we seek the optimal distribution of modal energy that enhances the three objective functions with respect to the baseline case denoted by $\mathcal{J}^{(0)}$ – an interface with uniform amplitude and random phase. It should be noted that gradient-based optimization provides a local extremum and there is no guarantee that such a solution holds globally. To this end, different initial configurations were considered as the starting point in the optimization process. The optimized spectra reported here correspond to an initial distribution of modal energy that was found to produce the greatest changes in $\mathcal{J}$.

The iteration history of the three objective functions shows that MIX is increased by approximately 40%, KE by 900% and VAR by 300% (see Table 4.1 and Fig. 4.13a). The initial interfacial perturbation energy of the three enhanced solutions indicates that low wavenumber modes have a greater contribution to RT growth and mixing (see Fig. 4.13b). It can be seen that the majority of perturbation energy of the high wavenumber modes are transferred to the first five wavenumbers.

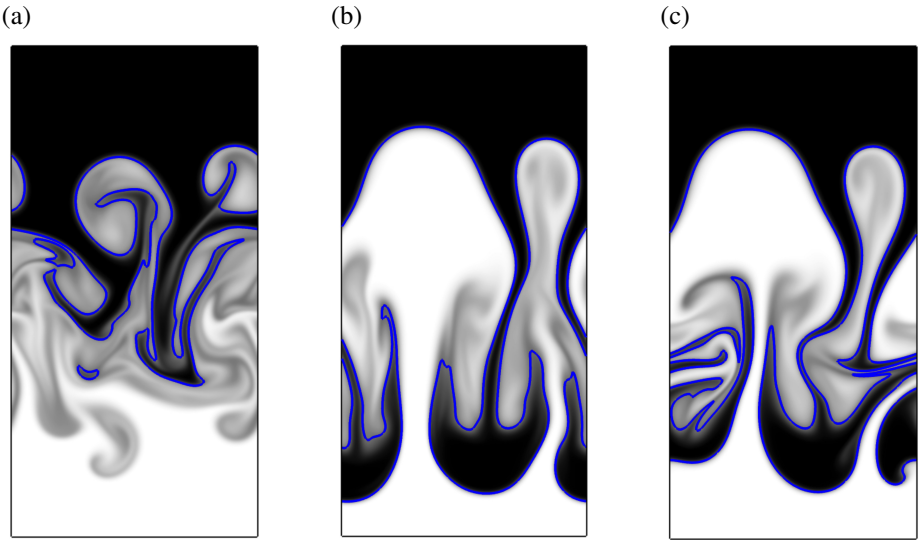

Figure 4.14: Mole fraction at $t = 4.0\tau$ of the optimized solution for enhancing the three objective functions (*a*) MIX, (*b*) KE and (*c*) VAR. Compared to the baseline case, MIX, KE and VAR are enhanced by a factor of 1.4, 8.9, and 3.1, respectively. Same color scheme as Fig. 4.3.

The optimized solutions exhibit non-trivial mode competition and coupling effects that enhance mixing. Nonlinear mode-coupling generates lower wavenumber modes that move faster in the flow during the potential regime. Mode-coupling also creates high wavenumber modes that are diminished by molecular diffusion. These effects are reflected in the optimized initial perturbations shown in Fig. 4.13b, especially for the objective functions that measure the fluid penetration and growth, i.e., KE and VAR. It can be seen that the perturbation energy sharply decreased for $k > 21$, where the exponential growth rate is expected to be negative according to linear stability theory.

The optimized solutions at $t = 4.0\tau$ for KE and VAR exhibit greater fluid penetration compared to the baseline case, while MIX appears qualitatively to be more mixed (see Fig. 4.14). The optimized solutions admit enhancement in conventional measures for RT mixing as well (see Fig. 4.15). The values of α_b at $t = 4\tau$ are increased by 17%, 32% and 31%, with respect to the baseline case for MIX, KE and VAR, respectively. The mixing width w was also increased by as much as 54% compared with the baseline case. It is notable that although $k \approx 8$ corresponds to the most unstable wavenumber according to linear stability theory, and is thus the fastest growing mode during the EG stage, a single-mode initial perturbation of $k = 8$ is not sufficient to optimize

growth at later times.

The effect of the time duration over which the objective function is computed (t_f) on enhancing mixing is also studied. The optimization of the three forms of $\mathcal{J}$ over duration $t_f = 2\tau$ is performed. At this stage of the instability the bubble tip velocity was observed to saturate due to nonlinearities (see Fig. 4.11b). Evolution of RT growth (h_b, $\dot{h}_b$ and α_b) and mixing width w corresponding to the optimal values of $\mathcal{J}$ over duration $t_f = 2\tau$ are compared with the baseline case and the enhanced values over duration $t_f = 4\tau$ (see Fig. 4.15). While the optimized $t_f = 2\tau$ solutions predict larger values for some of the quantities when $t < 2\tau$, they are found to be suboptimal when $t \gtrsim 2\tau$ compared to the solutions optimized for $t_f = 4\tau$. Interestingly, the initial perturbations optimized for $t_f = 2\tau$ were found to be suboptimal compared to the baseline solution when $t \gtrsim 2\tau$ as well. For the baseline case, low wavenumber initial perturbations and nonlinear mode-coupling effects augment RT growth at later times, while they are not as present in the optimal $t_f = 2\tau$ solutions. These differences become more obvious by observing the evolution of the mole fraction of optimal VAR for $t_f = 2\tau$ and $t_f = 4\tau$ (see Fig. 4.16). Initially, there is more fluid penetration in the optimal $t_f = 2\tau$ solution as the initial perturbation assigns more energy to wavenumbers close to the most unstable mode predicted by linear stability theory. However, at later times, the lower wavenumber modes grow faster. These results indicate that optimization of late-time stages of RT instabilities requires late-time sensitivity information.

4.5.4 Enhancing three-dimensional mixing using optimal two-dimensional perturbations

Here we evaluate the ability to enhance mixing of a three-dimensional RT instability using the optimal interfacial perturbations determined from the two-dimensional simulations in Chapter 4.5.3. The initial perturbation energy shown in Fig. 4.13b is used to initialize the three-dimensional configuration presented in Chapter 4.4. The optimized amplitudes A_m in two dimensions are transformed into $A_{m,n}$ in three dimensions by ensuring the average wavenumber components $k = \sqrt{k_x^2 + k_z^2}$ are approximately equal to the values obtained from the two-dimensional enhanced

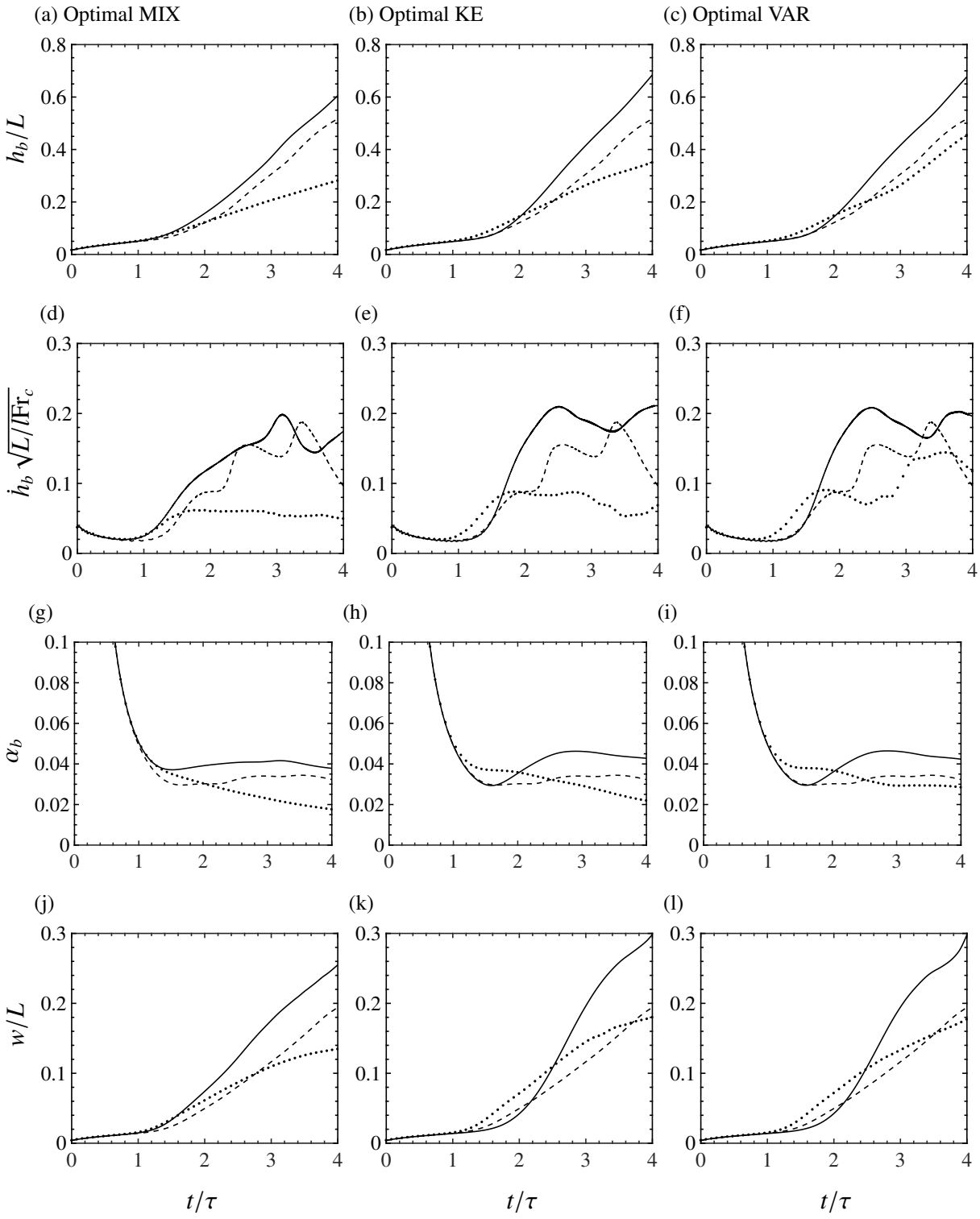

Figure 4.15: Evolution of (*a–c*) bubble height, (*d–f*) bubble tip velocity, (*g–i*) bubble growth parameter and (*j–l*) mixing width of the uniform distribution solution (−−), from the optimized solution over duration $t_f = 2\tau$ ($\cdots$) and $t_f = 4\tau$ (–).

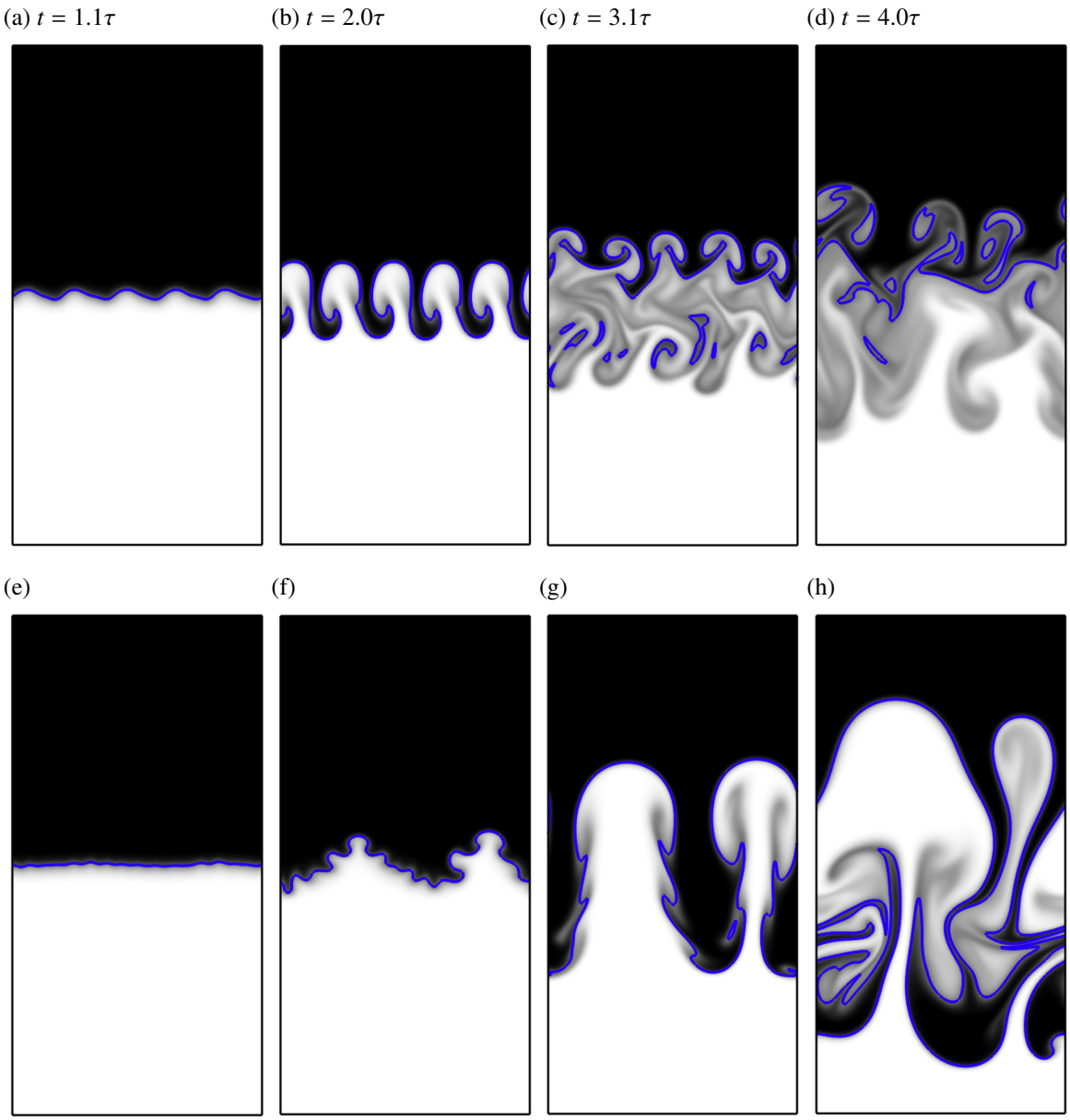

Figure 4.16: Evolution of mole fraction using the optimized perturbation amplitudes that maximize VAR over duration (*a–d*) $t_f = 2\tau$ and (*e–h*) $t_f = 4\tau$. Same color scheme as Fig. 4.3.

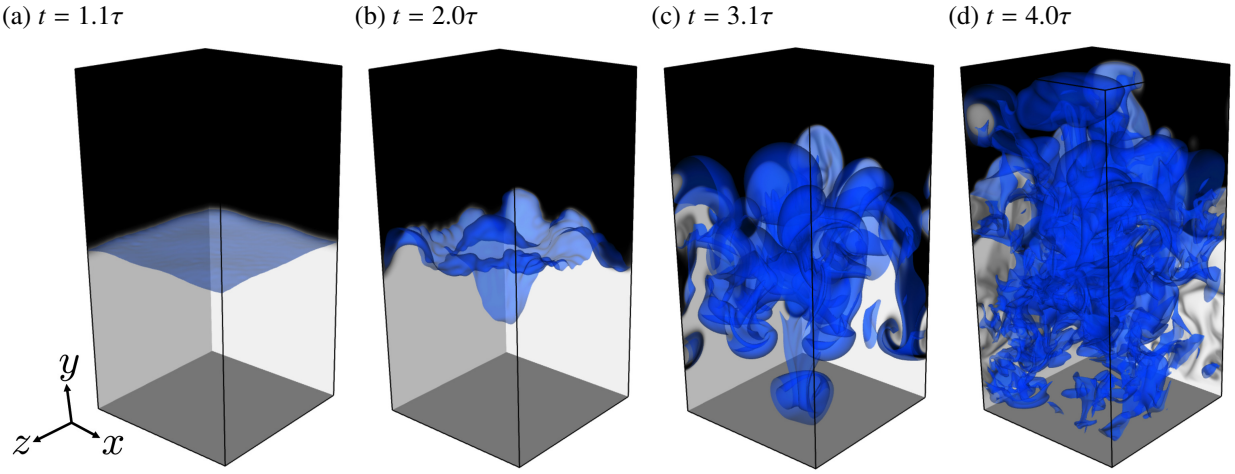

Figure 4.17: Evolution of mole fraction using the optimized perturbation amplitudes that maximize VAR. Same color scheme as Fig. 4.3.

solution.

The evolution of the mole fraction using the interfacial perturbations that optimize VAR is shown in Fig. 4.17. It can immediately be seen that substantial mixing and penetration is achieved compared to the baseline solution over the same time horizon (see Fig. 4.3). Despite being initialized with the same perturbation energy in two dimensions, compared to the evolution in two dimensions (Fig. 4.16e–4.16h), the flow exhibits three-dimensional behaviour as early as $t = 2\tau$, resulting in significantly more mixing compared to its two-dimensional counterpart. Figure 4.18 shows the conventional measures of mixing corresponding to the enhanced objective functions compared to the baseline case. Overall, significant increase in growth and mixing is observed. The objective functions are increased by factors of 1.7, 5.8 and 3.4 for MIX, KE and VAR, respectively, compared to the three-dimensional baseline case reported in Chapter 4.4. Interestingly, greater enhancement is observed for two of the objective functions compared to the enhanced two-dimensional solutions, which were increased by factors of 1.4, 8.9 and 3.1 for MIX, KE and VAR, respectively. As shown in Figs.4.18a and 4.18b, the top and bottom walls act to decelerate the bubble heights and bubble tip velocities at later times. Thus, even greater enhancement might be achieved if a larger domain size was considered.

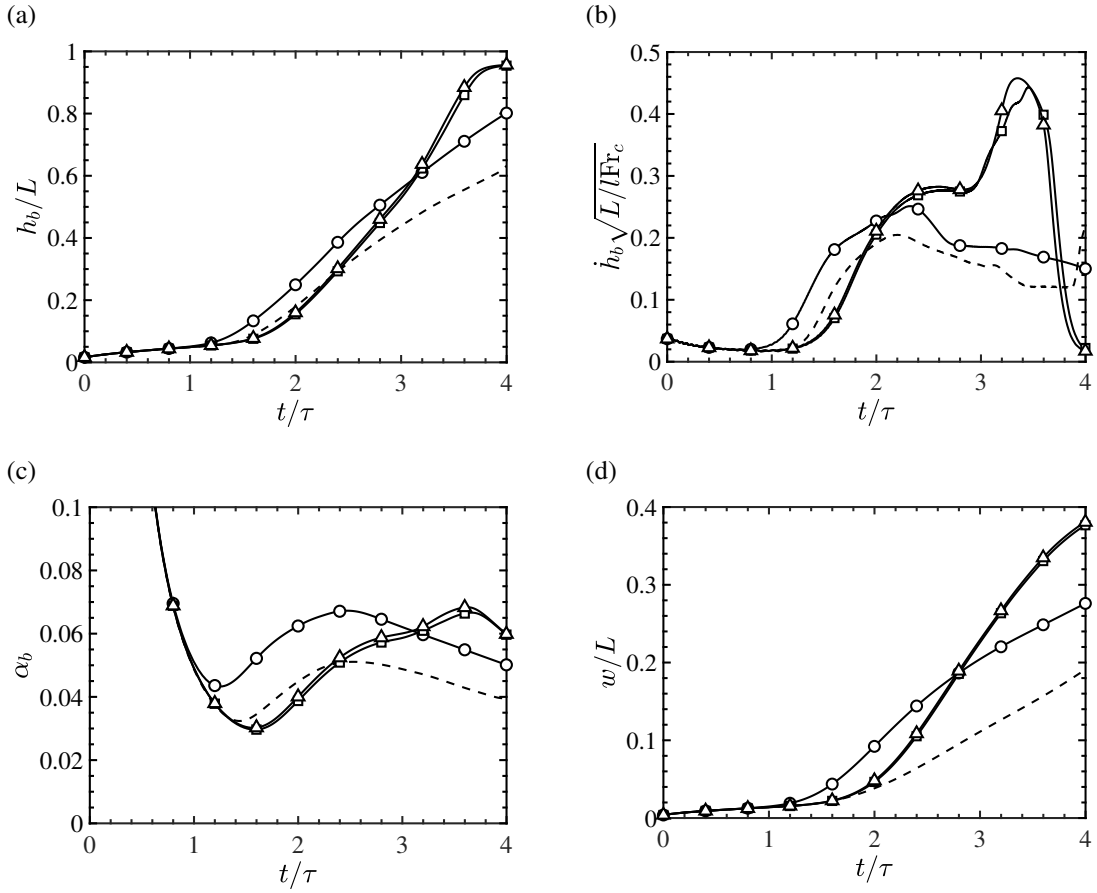

Figure 4.18: Evolution of (*a*) bubble height, (*b*) bubble tip velocity, (*c*) bubble growth parameter and (*d*) mixing width of the three-dimensional RT instabilities with the baseline case (−−) and with the initial interfacial perturbations of the enhanced two-dimensional RT instabilities of MIX (− ◯ −), KE (−□−) and VAR (− △ −).

4.6 Conclusions

We have studied the role of interfacial perturbations on the evolution of a multi-mode Rayleigh–Taylor (RT) instability. The objective was to determine the extent to which the RT growth rate and mixing can be enhanced and suppressed through careful manipulation of the initial conditions. A discrete-adjoint-based method was used to compute sensitivity of mixing and growth to the amplitudes of the initial fluid interface. To quantify RT growth and mixing, three objective functions, $\mathcal{J}$, are defined: (i) a mixing quantity based on the variance of fluid mole fraction (MIX), (ii) a kinetic energy norm based on the vertical velocity (KE) and (iii) an objective function based on the variations of the mole fraction with respect to the unperturbed initial state (VAR). These quantities are integrated in time through different stages of the RT instability.

First, a three-dimensional RT instability was considered with thirty-two perturbation modes and constant amplitude in each horizontal direction. Four main stages during RT growth are observed: a diffusion growth (DG) regime where molecular diffusion dominates, an exponential growth (EG) regime where the perturbations grow exponentially and the growth rate can be estimated by linear stability theory, a potential flow growth (PFG) stage where nonlinearities become important and saturate the bubble tip velocity, and a late-stage growth (LSG) regime where self-similar RT growth ($h_b \propto t^2$) is observed. Except for the DG regime, the most sensitive wavenumber of each objective function approximately equals the most unstable wavenumber predicted by linear stability theory ($k \approx 8$). At early times, the spectrum of interfacial perturbations was found to differ between the different objective functions. However, they were found to collapse at later stages of the instability. It was found that randomly varying the phase distribution of initial perturbations can significantly alter both the growth rate and its sensitivity during the PFG and LSG stages. The sensitivity of the objective function to local mole fraction was also evaluated. Maximum sensitivity exists within the vicinity of the fluid interface, and becomes noisier as the integration time t_f increases. This is attributed to the chaotic behaviour of the instability, characterized by positive values of the first Lyapunov exponent associated with each objective function.

Sensitivity obtained from the adjoint solution is then used to suppress and enhance mixing of two-dimensional multi-mode RT instabilities. First, the objective functions are integrated over a duration $t_f = 4\tau$. The adjoint-based optimization approach was capable of suppressing the instability by shifting all of the initial perturbation energy into the highest wavenumber modes. This result is supported by linear stability theory which predicts that initial perturbation amplitudes exponentially decay for $k > 21$. The optimal solutions for enhancing growth and mixing are less trivial. The optimization procedure was able to enhance MIX, KE and VAR relative to the baseline solution (uniform distributed perturbations) by 40%, 300% and 880%, respectively. This corresponds to a maximum increase in the bubble growth parameter and mixing width by 32% and 54%, respectively. Initial perturbations of all mixing quantities demonstrate that low wavenumbers are favored. The perturbation energy for wavenumber modes $k \gtrsim 20$ is eliminated, as anticipated by linear stability theory.

Enhancing RT growth and mixing over a shorter duration ($t_f = 2\tau$) was also studied. The majority of initial perturbation energy of the optimal solutions shifts towards the most unstable mode predicted by linear stability theory compared with the optimal perturbations when $t_f = 4\tau$. Comparing the optimized solutions for $t_f = 2\tau$ and $t_f = 4\tau$ yields two main conclusions: (i) lower wavenumber modes are more effective in enhancing growth for later times while the modes near the most unstable mode have greater effect in the linear and early nonlinear regimes; and (ii) due to the nonlinear, chaotic behaviour of RT instabilities at late stages of its growth, the optimal solution of early-time growth provides sub-optimal solutions at later times.

The adjoint-based optimization methodology used here demonstrates its capability to enhance and suppress mixing in unsteady multi-component flows. While it is well known that long time horizons can result in diverging adjoint sensitivities due to chaos (e.g., see Lea *et al.*, 2000; Wang & Gao, 2013), we demonstrate that the discrete adjoint approach provides useful sensitivity for optimizing mixing throughout the nonlinear RT regime, despite the existence of positive Lyapunov exponents. It was also shown that the optimized perturbations obtained from two-dimensional simulations admit similar (and sometimes better) improvement when imposed in three-dimensional

configurations, making adjoint-based optimization particularly attractive for controlling large-scale unsteady flows. Such a technique can be extended to study the role of viscous and compressibility effects on the growth of fluid instabilities at late-time nonlinear stages. The utility of such an approach at even later stages must be addressed.

CHAPTER 5

Controlling Scalar Mixing in a Free Shear Flow

5.1 Introduction

In Chapter 4, the adjoint-based solver was applied to the flow fields sufficiently resolved by the computational grids. Thus, it was not required to employ the adaptive dissipation scheme introduced in Chapter 3, and the standard high-order dissipation operators were effective to damp unresolved spurious modes.

In this chapter, we use the adjoint-based optimization framework to control the evolution of a passive scalar $Z \in [0, 1]$ in a spatially evolving mixing layer configuration. The non-reacting compressible Navier–Stokes equations and their discrete adjoint equations are solved. The adaptive dissipation scheme is necessary to preserve scalar boundedness in the considered problem configuration. Both unconditionally- and conditionally stable adaptive dissipation schemes are applied to the predictive simulation. The latter one is more effective in preserving scalar boundedness. Both instantaneous distributions and statistics of the passive scalar are compared with a simulation using a standard high-order dissipation operator. A quantity of interest is defined to measure the evolution of the passive scalar in the mixing layer. Adjoint formulation of conditionally stable adaptive dissipation scheme is used to compute sensitivity to a space-time control field with more than one-hundred million parameters, and its optimal value is obtained with a few dozens of optimization iterations. We demonstrate success in controlling the passive scalar evolution with a tractable computational cost.

5.2 Mixing layer configuration

A two-dimensional mixing layer configuration is considered with an upper stream flow of mixture fraction $Z_u = 0$ and velocity $u_u = 0.6c_\infty$ and lower stream flow of $Z_l = 1$ and $u_l = 0.1c_\infty$ (see Fig. 5.1), where c_∞ denotes the reference speed of sound. Z is taken to be a passive scalar and chemistry is neglected. Both upper and lower streams have density ρ_∞, pressure $1/\gamma$, and temperature $1/(\gamma - 1)$, where $\gamma = 1.4$ denotes the ratio of specific heats. The vorticity thickness separating the two streams at the inflow, $\delta_\omega = \Delta u/|\mathrm{d}u/\mathrm{d}y|_{\max}$ with $\Delta u = u_u - u_l = 0.5c_\infty$, is taken as the reference length scale. The inflow Mach number is defined as $\mathrm{Ma} = \Delta u/c_\infty = 0.5$. The size of the computational domain is $210\delta_\omega$ and $100\delta_\omega$ in streamwise and spanwise directions, respectively, which is discretized with 513×257 grid points. The spanwise grid is smoothly stretched from the middle of the domain towards the lateral boundaries.

The initial distributions of streamwise velocity u and mixture fraction Z are given by

$$\begin{aligned} u &= u_l + \frac{\Delta u}{2}\left\{1 + \tanh\left[\frac{y/\delta_\omega}{2 + 2s\max\left(x/\delta_\omega - x_0, 0\right)}\right]\right\}, \\ Z &= \frac{1}{2} - \frac{1}{2}\mathrm{erf}\left[\frac{y/\delta_\omega}{1 + s\max\left(x/\delta_\omega - x_0, 0\right)}\right], \end{aligned} \tag{5.1}$$

respectively, with $x_0 = 30\delta_\omega$ and growth factor $s = 0.1\delta_\omega^{-1}$.

5.2.1 Governing equations and discretization

The unsteady compressible non-reacting Navier–Stokes equations (2.11) are solved for the conserved variables $\vec{Q} = [\rho,\ \rho u_1,\ \rho u_2,\ \rho E,\ \rho Z]$ with density ρ, velocity components u_i for $i = 1,\ 2$, and specific energy $E = p/[(\gamma - 1)\rho] + u_i u_i/2$, where p denotes pressure, and the Reynolds number is $\mathrm{Re} = \rho_\infty \Delta u \delta_\omega/\mu = 5,000$, where the viscosity remains constant in the domain, i.e., $b = 0$ in (2.7), and the bulk viscosity is $\mu_B = 0$. The Prandtl and Schmidt numbers are given by $\mathrm{Pr} = C_{p,\infty}\mu/\kappa = 0.7$ and $\mathrm{Sc} = \mu/(\rho\mathcal{D}) = 0.7$, respectively, with reference specific heat at constant pressure $C_{p,\infty}$, conductivity κ, and mass diffusivity $\mathcal{D}$. Since the mixture fraction Z is a

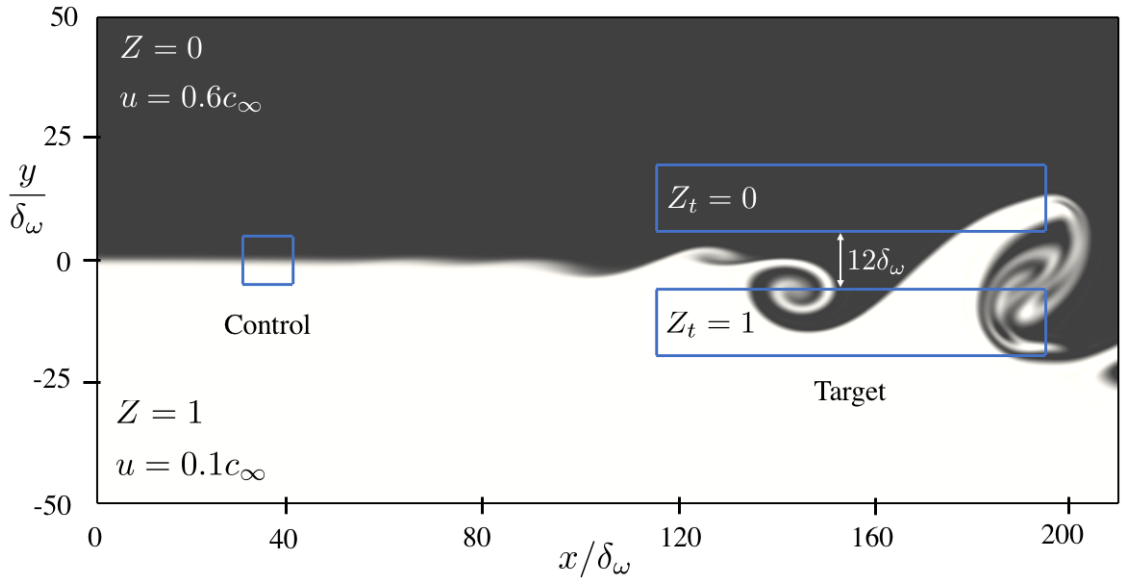

Figure 5.1: Mixing layer configuration. Mixture fraction is shown in gray scale. The QoI is computed in target regions downstream (right blue boxes), and the momentum actuation is applied within the control region upstream (left blue box).

passive scalar, the heat flux and temperature are given by (3.47) and (3.48), respectively. Finally, buoyancy effects are neglected in this configuration, i.e., $\mathrm{Fr}_c \to \infty$.

The governing equations (2.11) are discretized in space via the SBP first-order derivative operators with sixth-order of accuracy interiorly and third-order near the boundaries, resulting in fourth-order global accuracy (see Chapter 3.2.1). Second and mixed derivatives are computed by consecutively applying the first-derivative operators.

The standard sixth-order artificial dissipation operator is applied to the density, momentum, and energy equations, but different dissipation operators are applied to ρZ in different simulations: (*i*) standard sixth-order dissipation operators, (*ii*) unconditionally-, and (*iii*) conditionally stable adaptive dissipation operators presented in 3.2. Since the goal of this study is to ensure boundedness of Z without compromising accuracy of the other flow state variables, adaptive dissipation schemes are only imposed for the ρZ equation.

The non-reflecting boundary conditions are enforced via the SAT boundary treatment (see Svärd *et al.*, 2007; Vishnampet, 2015, and Appendix B.3) for all boundaries, in which the boundary values are weakly imposed to a target solution $\vec{Q}_t$ taken to be the initial condition. In addition,

absorbing sponge regions (Freund, 1997) are applied near the inflow and lateral boundaries via $\sigma_s(\boldsymbol{x})(\vec{Q} - \vec{Q}_t)$, where the sponge strength $\sigma_s(\boldsymbol{x})$ quadratically decreases from $\sigma_s = 0.2$ at the boundary towards zero $6.2\delta_\omega$ away from the inflow and $10.5\delta_\omega$ away from the lateral boundaries. The governing equations are integrated in time by a standard fourth-order Runge–Kutta (RK4) time integration scheme.

5.3 Mixing layer evolution

As explained in the previous section, mixing layer simulations are studied with three different dissipation operators for the ρZ equation: the high-order operator, the unconditionally-, and the conditionally stable adaptive dissipation schemes. Figure 5.2a illustrates maximum boundedness error values (maximum amounts of overshoots/undershoots) of mixture fraction through the mixing layer evolution, given by (3.37).

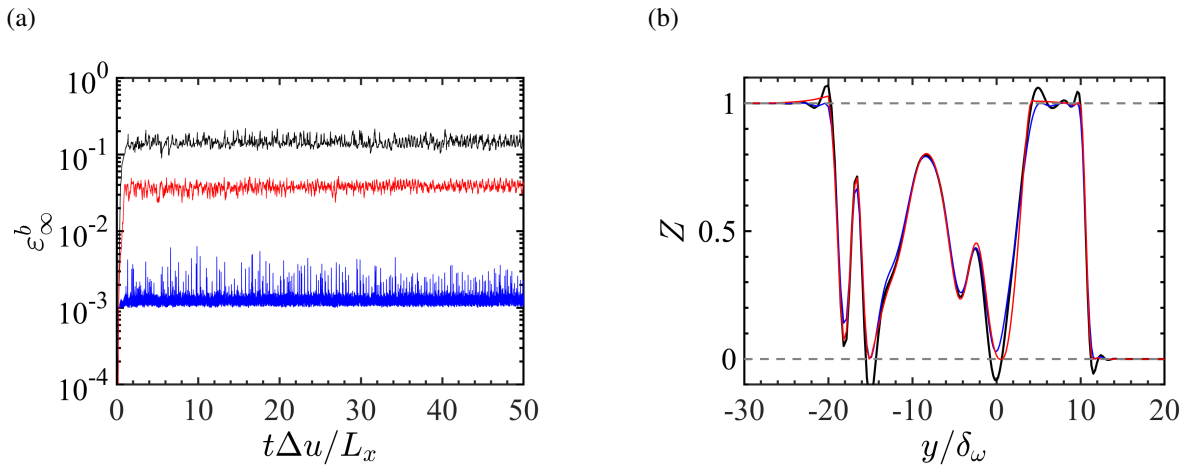

Figure 5.2: (*a*) Boundedness errors of mixture fraction, ε^b_∞ (3.37), associated with the mixing layer simulation, and (*b*) instantaneous distribution of mixture fraction at $x = 186.2\delta_\omega$ when high-order dissipation (black), unconditionally stable (red), and conditionally stable (blue) adaptive dissipation schemes are employed.

The standard high-order dissipation operator is not able to preserve scalar boundedness, and the maximum value of ϵ^b_∞ within all timesteps is 0.220. On the other hand, the conditionally stable adaptive dissipation scheme is able to reduce the excursion errors, i.e. the maximum value of ϵ^b_∞

within all timesteps is 0.006. The unconditionally stable adaptive scheme is not as effective as the conditionally stable scheme (the maximum value of ϵ_∞^b within all timesteps is 0.052), but the scheme improves the boundedness error compared to the simulation with the standard high-order dissipation operator.

The fraction of the grid points that the second-order dissipation is applied is below 0.08% and 10% within all timesteps for conditionally stable and unconditionally stable dissipation schemes, respectively. These results suggest that the unconditionally stable scheme does not sufficiently absorb spurious overshoots and undershoots compared to the conditionally stable scheme, but the the second-order dissipation operator is more activated in the unconditionally stable scheme. As mentioned, the second-order dissipation of conditionally stable scheme is activated only in a negligible fraction of the grid points (maximum of ~0.1%), but it has a significant contribution to suppress the excursion errors.

The error associated with adaptive schemes is evaluated by comparing their mixture fraction distribution with the case using the high-order dissipation operator. An instantaneous distribution of mixture fraction is depicted at $x = 186.2\delta_\omega$ for different dissipation schemes (see Fig. 5.2b). As can be seen, the simulation using the high-order dissipation operator has overshoots/undershoots. Both adaptive schemes are able to approximately capture the mixture fraction distribution (within $0 < Z < 1$) of the simulation with the high-order dissipation operator. Thus, local activation of the second-order dissipation does not significantly destroy instantaneous variations of Z but remarkably reduces unboundedness.

The boundedness capability of different schemes are consistent with one-dimensional numerical tests illustrated in Chapter 3.4 (see Fig. 3.2). We employ the conditionally stable scheme for the rest of this chapter, which has shown great success in preserving scalar boundedness.

We compare the temporal mean and variance of Z, denoted by $\overline{Z}$ and $\overline{Z''^2}$, respectively, between simulations using high-order and conditionally stable adaptive dissipation operators (see Fig. 5.3). The effects of the adaptive dissipation scheme on the accuracy of Z is also studied in two different grid resolutions: the current (coarse) one (513×257) and a fine grid (1025×513), where the

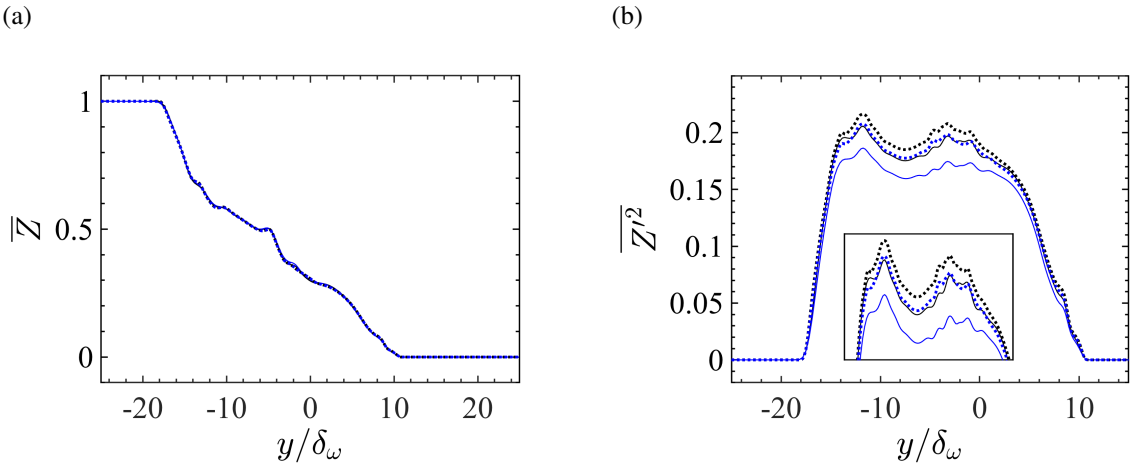

Figure 5.3: Temporal (*a*) mean and (*b*) variance of mixture fraction at $x = 160.0\delta_\omega$ when high-order dissipation (black) and conditionally stable (blue) adaptive dissipation schemes are employed with 513×257 (—) and 1025×513 ($\cdots$) grid points. A zoom-in view near the maximum value of mixture fraction variance was also depicted in (*b*).

physical and numerical parameters and coefficients of these simulations are the same except for the dissipation coefficient $\widetilde{\sigma}^{(\text{diss})}$, which is set to $0.5J$ and $0.2J$ for the coarse and fine grids, respectively, where J is the local Jacobian of the grid, see Eq. (2.11). The higher value for the coarse grid should be considered to keep the scalar excursion error $\epsilon^b_\infty < 0.01$ within all timesteps when the conditionally stable scheme is employed.

As can be seen in Fig. 5.3, the adaptive scheme provides sufficiently close values for the mean and variance of Z compared to the case with the high-order dissipation operator, especially for the fine mesh simulation. The maximum scalar excursion errors within all timesteps on the fine grid (0.188 and 0.005 for high-order and adaptive dissipation schemes, respectively) do not significantly different compared to the corresponding simulations using the coarse one. The fraction of grid points with activated second-order dissipation operator is below 0.03% within all timesteps via the fine grid, compared to below 0.08% for the coarse grid as mentioned before. This lower fraction leads to having a similar scalar variance distribution between the results using the high-order and adaptive dissipation operators in the fine grid according to Fig. 5.3b.

Therefore, we conclude that the adaptive dissipation scheme does not significantly impair the physical fluctuations, and it is able to remarkably decrease spurious overshoots/undershoots asso-

ciated with the unresolved modes.

5.4 Controlling scalar mixing via adjoint-based optimization

To investigate the discrete adjoint framework with conditionally stable adaptive dissipation, we incorporate the adjoint sensitivity into the steepest descent optimizer to suppress mixing. The objective is to constrain mixing of Z within a narrow region downstream (between the two blue boxes shown in Fig. 5.1). To quantify the evolution of Z, the QoI is computed within a time horizon of $[t_0, t_f]$, where $(t_f - t_0)\Delta u/L_x = 4.76$, and the solution reaches a statistically steady-state state prior to t_0. The QoI is given by

$$\mathcal{J} = \int_{t=t_0}^{t=t_f} \int_{\boldsymbol{x}} (Z - Z_t)^2 \mathcal{W}_{\text{Tar}}(x, y)\, \mathrm{d}\boldsymbol{x}\, \mathrm{d}t, \quad \text{with } Z_t = \begin{cases} 0; & y \geq 0, \\ 1; & y < 0, \end{cases} \tag{5.2}$$

which computes the deviation of the local mixture fraction from the target value Z_t according to (5.2) and as depicted in Fig. 5.1. The target weight function $\mathcal{W}_{\text{Tar}}$ spans $[109.9\ \delta_\omega, 200.2\ \delta_\omega] \times [-25.11\ \delta_\omega, 25.11\ \delta_\omega]$, whose value smoothly decays towards zero with $-6\delta_\omega < y < 6\delta_\omega$, i.e., the middle region between the downstream boxes in Fig 5.1. Also, $\mathcal{W}_{\text{Tar}}$ smoothly decays to zero at the prescribed borders via hyperbolic tangent functions. Thus, minimizing (5.2) constrains any mixing $0 < Z < 1$ within the region between the right blue boxes in Fig. 5.1.

A momentum actuator is considered to control the mixing layer evolution. In laboratory experiments, a manipulated momentum actuator can be applied through different techniques such as synthetic jet actuators (e.g., see Smith & Glezer, 1998; Jankee & Ganapathisubramani, 2021). In this work, a momentum actuator is applied upstream by adding a solenoidal source term to the right-hand side of the momentum equations in (2.11), given by

$$\mathcal{N}_2[\vec{Q}] = \frac{\partial \mathcal{W}_{\text{Ctl}} f}{\partial y}, \quad \mathcal{N}_3[\vec{Q}] = -\frac{\partial \mathcal{W}_{\text{Ctl}} f}{\partial x}, \tag{5.3}$$

where $f(x, y, t)$ is a space-time field applied in the control region $\mathcal{W}_{\text{Ctl}}(x, y)$ that spans

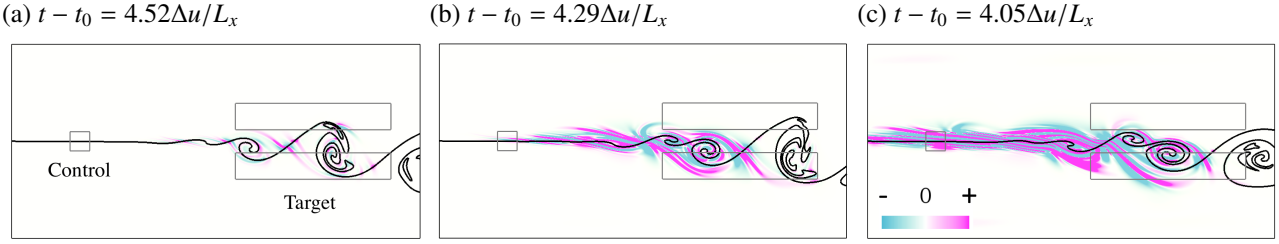

Figure 5.4: The mixture fraction contour of $Z = 0.5$ (black) and evolution of adjoint sensitivity $\partial u_2^\dagger/\partial x - \partial u_1^\dagger/\partial y$ (color) from the target regions (the right gray boxes) to the control region (the left gray box). The momentum actuator f is set to zero (baseline simulation).

$[29.94\ \delta_\omega, 40.20\ \delta_\omega] \times [-4.936\ \delta_\omega, 4.936\ \delta_\omega]$ (see Fig. 5.1). $\mathcal{W}_{\text{Ctl}}$ smoothly decays to zero at the prescribed borders via hyperbolic tangent functions.

Considering governing equations (2.11) with the QoI (5.2), the adjoint equations solving adjoint variables $\vec{Q}^\dagger = \left[\rho^\dagger,\ u_1^\dagger,\ u_2^\dagger,\ E^\dagger,\ Y^\dagger\right]^\mathsf{T}$ and the adjoint sensitivity can be derived as explained in Chapter 3.3 . The space-time adjoint sensitivity of $\mathcal{J}$ to $f(x, y, t)$ is given by

$$g(x, y, t) = \left(\frac{\partial u_2^\dagger}{\partial x} - \frac{\partial u_1^\dagger}{\partial y}\right)\mathcal{W}_{\text{Ctl}}(x, y). \tag{5.4}$$

Similar to momentum actuator $f(x, y, t)$, the adjoint sensitivity $g(x, y, t)$ is also a discrete space-time field, and it is non-zero only in the control region. Note that the fully discrete adjoint method is employed during optimization.

We first study adjoint sensitivity of the primal simulation with zero actuator field, i.e., $f = 0$. Different snapshots of adjoint sensitivity $\partial u_2^\dagger/\partial x - \partial u_1^\dagger/\partial y$ are depicted in Fig. 5.4. According to the adjoint equations in Appendix A, the adjoint solution is generated and forced by the QoI in the target region (see the last term on the left-hand side of (A.17)), and it propagates from the target region through the rest of the computational domain (see Fig. 5.4). Once the adjoint solution reaches the control region, the sensitivity is computed according to (5.4).

Local positive sensitivity as seen in Fig. 5.4 means that a small increment in f at the particular space and time will potentially increase the QoI $\mathcal{J}$. Thus, adjoint sensitivity can also be used to

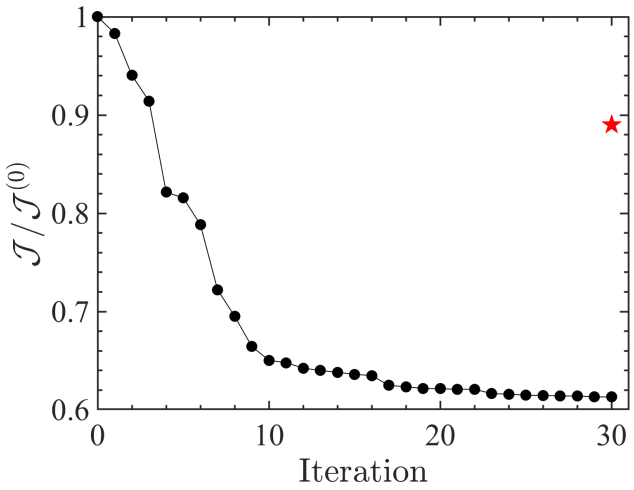

Figure 5.5: Optimization history (–•–) of (5.2) relative to its baseline value, $\mathcal{J}^{(0)}$, corresponding to the mixing layer simulation with no momentum actuation. The red star (★) shows the QoI value when the solenoidal excitation (5.6) and (5.7) is applied with the same amount of energy as the optimized actuator.

update the momentum actuator, e.g., by the steepest descent algorithm according to

$$f^{(n+1)} = f^{(n)} - \alpha^{(n)} g^{(n)}, \tag{5.5}$$

where superscript n denotes the optimization iteration, and $\alpha^{(n)} > 0$ is a step length. Several line searching algorithms exist to obtain an optimal value of $\alpha^{(n)}$. In this work, we use an in-house steepest decent code with backtracking line searching to find optimal values of f to minimize (5.2) (see Chapter 2.6.1 for more details). As mentioned before, the baseline simulation has a zero actuator field. The control region contains 26×53 grid points, and the simulation is performed over $20,000$ timesteps. Considering four sub-steps in the standard RK4 time integrator, the discretized control parameter $f(x, y, t)$ contains more than 10^8 degrees of freedom. The solver writes the space-time field of f to disk after line searching, and it reads f (and also g if required) from and writes g to disk every $2,500$ timesteps during the primal and adjoint simulations, respectively (see Chapter 2.6.1 for more details on data management).

Figure 5.5 shows the optimization history. Using the steepest descent algorithm with backtracking line searching, $\mathcal{J}$ is reduced by 40% compared to the case with no actuation ($f = 0$) within 30

optimization iterations. We also compare the optimized $f(x, y, t)$ (final iteration of Fig. 5.5) with a solenoidal excitation employed by Wei & Freund (2006), which is added to the momentum equations according to (5.3) with a Gaussian weight function $\mathcal{W}_e$ (instead of $\mathcal{W}_{\text{Ctl}}$) and trigonometric function f_e, given by

$$\mathcal{W}_e = e^{-0.2\left[(x-x_0)^2+(y-y_0)^2\right]}, \tag{5.6}$$

and

$$f_e(x, y, t) = \rho_\infty f_{e,0} \sum_{i=1}^{8} \sin\left[\frac{2\pi\omega_i(x - x_0 - U_c t)}{U_c} + \beta_{x,i}\right] \sin\left[\frac{2\pi\omega_i(y - y_0)}{U_c} + \beta_{y,i}\right], \tag{5.7}$$

respectively. The center of solenoidal excitation is $(x_0, y_0) = (35\delta_\omega, 0)$. The mode frequency of excitation is given by $\omega_i = \omega_0(i + \alpha_i)/4$ for $i = 1, \ldots, 8$, where α_i are uniformly distributed random numbers within $[-0.5, 0.5)$, and ω_0 is chosen to give a Strouhal number of $\text{St}_0 = \omega_0\delta_\omega/(4U_c) = 0.032$, which is also used by Wei & Freund (2006), and $U_c = (u_u + u_l)/2 = 0.35c_\infty$. Phase shifts $\beta_{x,i}$ and $\beta_{y,i}$ for $i = 1, \ldots, 8$ are uniformly distributed random number within $[0, 2\pi)$. The amplitude of solenoidal excitation, $f_{e,0}$, is set such that total imposed energy to the mixing layer from the solenoidal excitation and the adjoint-based optimal momentum actuator becomes equal, i.e.,

$$\begin{aligned}
&\int_{t=t_0}^{t=t_f} \int_{\boldsymbol{x}} \left[\left(-\frac{\partial f_e \mathcal{W}_e}{\partial y}\right)^2 + \left(\frac{\partial f_e \mathcal{W}_e}{\partial x}\right)^2\right] \mathrm{d}\boldsymbol{x}\, \mathrm{d}t \approx \\
&\int_{t=t_0}^{t=t_f} \int_{\boldsymbol{x}} \left[\left(-\frac{\partial f^{(30)} \mathcal{W}_{\text{Ctl}}}{\partial y}\right)^2 + \left(\frac{\partial f^{(30)} \mathcal{W}_{\text{Ctl}}}{\partial x}\right)^2\right] \mathrm{d}\boldsymbol{x}\, \mathrm{d}t,
\end{aligned} \tag{5.8}$$

where $f^{(30)}$ is the optimal momentum forcing at iteration $n = 30$ in Fig. 5.5. Such solenoidal excitation provides a new QoI (5.2) which is smaller than the baseline case (no actuator) but much greater than the adjoint-based optimal solution (see Fig. 5.5).

Snapshots of the mixing layer simulations with no actuator (baseline), solenoidal excitation, and the optimized momentum actuator are shown in Fig. 5.6. In the baseline solution, the velocity difference across the shear layer gives rise to a Kelvin–Helmholtz instability that results in growth

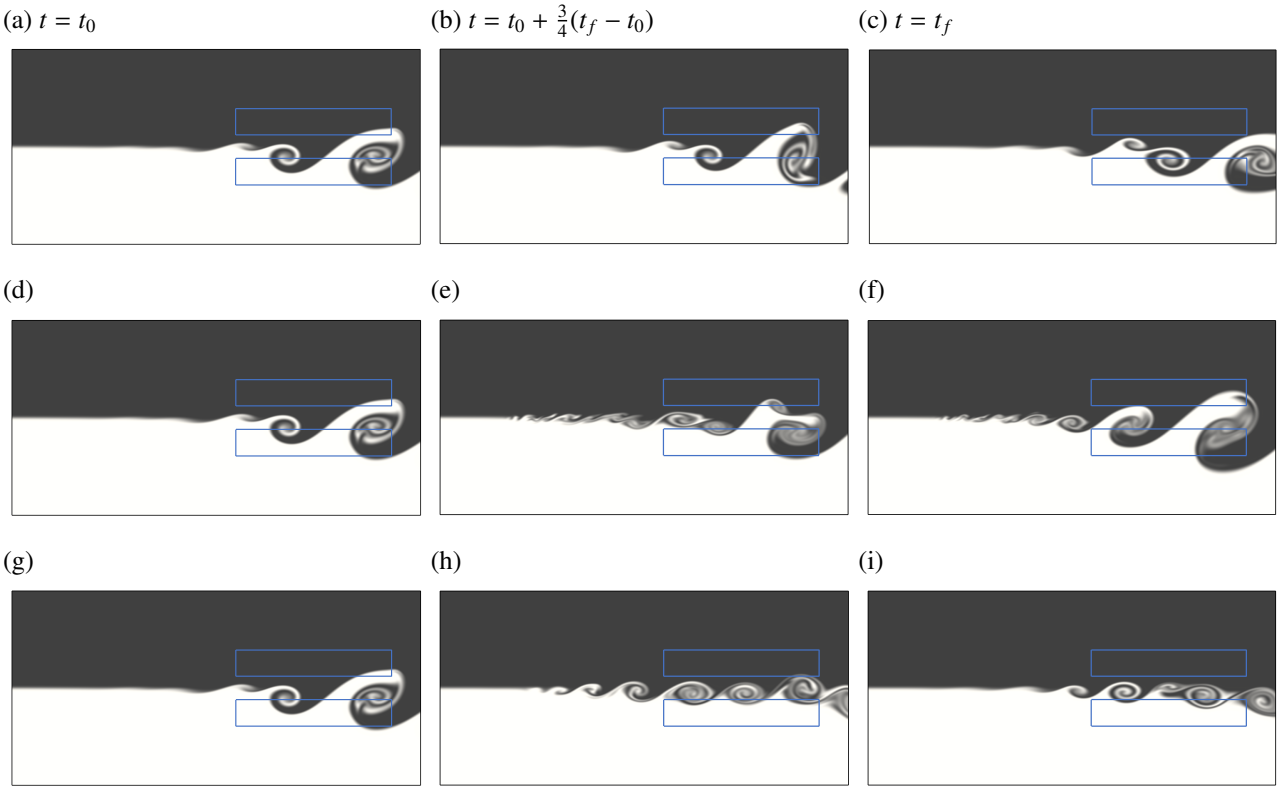

Figure 5.6: Evolution of mixture fraction excited with different momentum actuators: (*a–c*) no actuator (baseline solution), (*d–f*) solenoidal excitation, and (*g–i*) adjoint-based optimal solution after 30 iterations. Same color scheme as Fig. 5.1.

of the mixing layer and penetration of both streams within the target region (see Figs. 5.6a – 5.6c). We can see that the solenoidal excitation generates small perturbations upstream around the $Z = 0.5$ interface, which eventually leads to large vortices downstream. These vortices carry the upper stream into the lower blue box and vise versa (see Figs. 5.6d – 5.6f). On the other hand, the optimized momentum actuator is able to generate perturbations with specific wavelengths and frequencies informed by the adjoint sensitivity field. From Figs. 5.6g – 5.6i, we can see that the optimized momentum actuator is able to constrain mixing between the two boxes. These results demonstrate that the adjoint-based optimization using the proposed conditionally stable adaptive dissipation scheme is successful to control the mixing layer evolution.

5.5 Conclusions

The adjoint-based optimization solver was applied to control the evolution of a passive scalar in a two-dimensional mixing layer configuration. The adaptive dissipation operator was successfully used to preserve scalar boundedness. The unconditionally stable adaptive dissipation was not very effective in reducing scalar boundedness. On the other hand, the conditionally stable scheme was able to significantly reduce the boundedness error. The adjoint-based formulation of the conditionally stable scheme was used to control the evolution of the passive scalar. Momentum forcing with more than one hundred million degrees of freedom was optimized using adjoint sensitivity such that mixing of a passive scalar was constrained within a target region downstream, and the corresponding quantity of interest is reduced by about 40%. This chapter demonstrated the effectiveness of the adaptive dissipation scheme in preserving scalar boundedness in under-resolved flow simulations. Also, its adjoint-based formulation was capable to find optimal forcing with a manageable computational cost when a massive number of control parameters were involved. Extracting physical interpretations from the optimal space-time field, such as obtaining the spatial and temporal modes with greatest influence on flow instabilities and mixing, was beyond the scope of this chapter, and it is suggested for future studies.

CHAPTER 6

Controlling Flame Position in a Turbulent Jet

6.1 Introduction

Flame stabilization is a key factor in designing combustion devices. It is crucial to avoid undesired flame behavior such as flashback (e.g., see Lewis & von Elbe, 1943; von Elbe & Mentser, 1945; Ebi & Clemens, 2016), lifted flames oscillations (e.g., see Nichols & Schmid, 2008; Qadri *et al.*, 2015), and flame extinction. It is well understood that turbulence plays a large role in such behavior.

Flame flashback has been observed in premixed flames such as stationary gas turbine engines. During flashback, the flame front propagates inside the mixing chamber, which affects the efficiency or life endurance of the device. Thus, it is necessary to circumvent such transient effects.

Lifted flame oscillations have been observed in non-premixed flames, where fuel and oxidizer enter the combustion chamber through separate inlets. Thus, the mixing of fuel and oxidizer occurs before igniting the flame. If the momentum of fuel and oxidizer is large compared to the heat release rate of combustion, the flame does not anchor to the fuel nozzle. The ratio of reaction rate to fluid convection rate, i.e., the Damköhler number, plays a significant role in lift-off height and its oscillation frequency (Nichols & Schmid, 2008). Also, the density difference of unburned jet fuel and oxidizer could generate instabilities around the nozzle exit (e.g., see Monkewitz & Sohn, 1988; Nichols *et al.*, 2007), which might grow when traveling downstream and eventually oscillate the lifted flame (e.g., see Nichols & Schmid, 2008). Although detachment of the flame and the fuel nozzle reduces its corrosion, the position of the flame and its oscillations have to be controlled to stabilize it and avoid its blow-off downstream of the jet nozzle.

Several approaches have been proposed within the past two decades for controlling non-reacting and reacting flows (e.g., see Kral, 2000; Cattafesta III & Sheplak, 2011, and references therein). In reacting flows, it is crucial to control the flow for enhancing mixing, stabilizing the flame shape and its position, and reducing emissions (Docquier & Candel, 2002). In general, flow control is categorized into passive (without an external energy source) and active (with an external energy source) techniques. Reacting flows can be controlled passively via modifying a combustion chamber geometry or adding external obstacles on the flowing fluid such as bluff-bodies (Schadow & Gutmark, 1992), which eventually enhances fuel-oxidizer mixing and stabilizes the flame. However, there is less flexibility and fewer degrees of freedom on passive controllers, especially during the operation of the combustion system. On the other hand, active controllers use external energy sources such as loudspeakers, which systematically add energy to the flow and strategically manipulate it. Their input energy value could be predetermined (e.g., certain amplitude and frequency) or instantaneously updated regarding the current flow-flame interactions. Combination of passive (e.g., swirlers and bluff-bodies) with active control techniques (acoustic forcing) was also considered in the previous studies (e.g., see Paschereit *et al.*, 1999; Hardalupas & Selbach, 2002; Balachandran *et al.*, 2005).

Acoustic forcing has been widely imposed to control combustion instabilities, and it can be applied via loudspeakers located upstream of nozzle exits (e.g., see McManus *et al.*, 1993; Baillot & Demare, 2002; Dowling & Morgans, 2005; Baillot & Demare, 2007, and references therein). Acoustic forcing are able of generating both large-scale vortex structures and small-scale turbulent eddies. They could impact fuel-air mixing, modify flame-flow interactions, and eventually change the combustion regime. It can thus enhance flame stability or undermine it (Baillot & Demare, 2002, 2007). Acoustic forcing has been applied on lifted flames to control their stability (Chao *et al.*, 2002; Abdurakipov *et al.*, 2013), reduce emissions (Chao *et al.*, 1996), avoid anchoring the flame (Demare & Baillot, 2004), and modify flame shapes (Kozlov *et al.*, 2013).

In this chapter, we use adjoint sensitivity to control an H_2 lifted flame in a turbulent round jet. The flamelet/progress variable (FPV) approach is used to model the combustion. The adaptive

dissipation scheme developed in Chapter 3 is applied to preserve boundedness of the mixture fraction and progress variable. A quantity of interest is defined to target the flame location, and acoustic forcing is applied upstream of the lifted flame to change its height.

6.2 Turbulent reacting jet configuration

We consider a non-premixed H_2 flame in a three-dimensional turbulent reacting jet to demonstrate the combined features of the proposed adjoint solver. A similar configuration can be found in previous experimental (Markides & Mastorakos, 2005) and numerical (Tyliszczak, 2015a) studies. H_2 ($Y_{H_2} = 0.13$) and N_2 ($Y_{N_2} = 0.87$) enters a rectangular domain of $30D_j \times 15D_j \times 15D_j$ with jet nozzle diameter $D_j = 0.004$ m, jet velocity $U_j = 120$ m/s, and jet temperature $T_j = 691$ K (see Fig. 6.1). A hot co-flow of air is supplied upstream with velocity $U_c = 0.05U_j$ and temperature $T_c = 980$ K. A lookup table is generated via a set of laminar flamelet solutions obtained by solving the laminar counterflow diffusion configuration of H_2-air with the aforementioned mass fractions and temperatures. The FlameMaster solver (Pitsch, 1998) is employed for obtaining the laminar flamelet solutions, and it uses nine species and 19 chemical reactions. The progress variable is defined based on the mass fraction of H_2O.

The mean exit jet velocity $\overline{U}(\boldsymbol{x})$ is given by a top-hat profile distribution, given by (e.g. see Morris, 1976; Michalke, 1984; Tyliszczak, 2018)

$$\overline{U}(\boldsymbol{x}) = \frac{U_j + U_c}{2} - \frac{U_j - U_c}{2} \tanh\left[\frac{1}{4}\frac{R}{\delta_\theta}\left(\frac{r}{R} - \frac{R}{r}\right)\right], \tag{6.1}$$

where r is the radial coordinate, and $R = D_j/2$ denotes the jet radius. An overbar denotes a time averaged quantity. $\delta_\theta = 0.05R$ is the momentum thickness of the initial shear layer, and its value is taken to be consistent with previous works using similar Reynolds numbers (da Silva & Métais, 2002; Tyliszczak & Geurts, 2014; Tyliszczak, 2015b,a, 2018). A similar top-hat profile is taken for

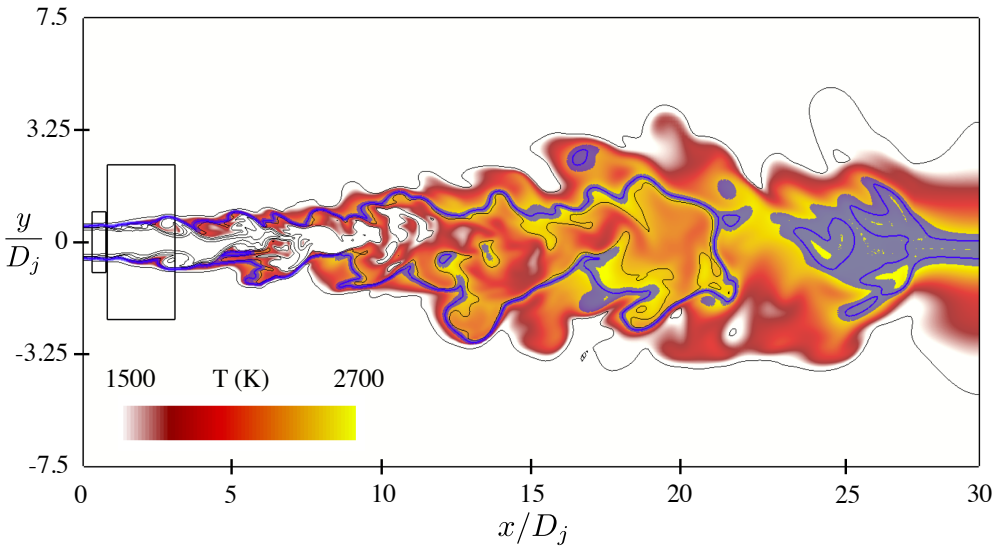

Figure 6.1: Instantaneous snapshot of the three-dimensional turbulent jet showing temperature (red/yellow) and mixture fraction contours (black lines) at the $z = 0$ plane. The $Z = Z_{st}$ contour is depicted by dark blue line and the burning zone ($Z \approx Z_{st}$) is shown by light blue. The small and large boxes correspond to the control and target regions, respectively.

the mixture fraction distribution at the inflow (Nichols *et al.*, 2007; Tyliszczak, 2018), given by

$$Z = \frac{1}{2} - \frac{1}{2}\tanh\left[\frac{1}{4}\frac{R}{\delta_\theta}\left(\frac{r}{R} - \frac{R}{r}\right)\right]. \tag{6.2}$$

To seed turbulent fluctuations at the inlet plane, time-varying three-dimensional pseudo-turbulent velocity fluctuations are superimposed to (6.1) in a region of $-D_j < y,z < D_j$ using a digital filtering technique (Klein *et al.*, 2003). The generated velocity fluctuations are multiplied by a weight function to decay smoothly towards zero outside of $r > R$, given by $0.5\{1 + \tanh[R/(4\delta_\theta)(R/r - r/R)]\}$. The turbulent intensity and integral length scale for the digital filtering are taken to be $0.125U_j$ (Tyliszczak, 2015a) and $\approx 0.2D_j$ (Wang *et al.*, 2010a,b), respectively. The mean and perturbations of radial velocity are set to zero at the jet exit.

The computational domain is discretized using a Cartesian mesh of $396 \times 241 \times 241$ grid points. The grid spacing in the axial direction decreases exponentially towards the inlet plane with a minimum grid spacing of $\Delta x = 0.04D_j$. The cross-flow grid spacing is smoothly stretched from $\Delta y = \Delta z = 0.02D_j$ at the jet centerline towards the lateral boundaries.

The compressible Navier–Stokes equations (2.11) are solved for conserved variables $\vec{Q} = [\rho,\ \rho\boldsymbol{u},\ \rho E,\ \rho Z,\ \rho C]^\mathsf{T}$ with density ρ, velocity vector $\boldsymbol{u} = [u_1,\ u_2,\ u_3]^\mathsf{T}$, total specific energy E, mass fraction Z, and progress variable C. In this work, we assume that all sub-grid scales are resolved by the computational grid. Thus, the mixture fraction variance $\widetilde{Z''^2}$ is taken to be zero when the lookup table is used. Linear interpolation is employed to compute species mass fractions and the progress variable source term from the lookup table. Pressure is obtained via (2.4) with $\gamma = 1.32$. In this work, γ is taken to be constant, corresponding to the mean value obtained from the lookup table. The stress tensor is given by (2.6), and the jet Reynolds number is $\mathrm{Re} = \rho_j U_j D_j/\mu_j \approx 3,000$ with the corresponding Mach number $\mathrm{Ma} = 0.14$. The jet density ρ_j and viscosity μ_j are taken as reference values, which are obtained from the lookup table with $Z = 1$ and $C = 0$, i.e., the mixture of $Y_{\mathrm{H}_2} = 0.13$ and $Y_{\mathrm{N}_2} = 0.87$. The bulk viscosity $\mu_B = 0$, and the first viscosity has a temperature dependence according to (2.7) with $b = 0.78$. The value of b is taken based on the variations of the viscosity with respect to the temperature from the lookup table. The Prandtl number is given by $\mathrm{Pr} = C_{p,\infty}\mu/\kappa = 0.7$ with reference specific heat at constant pressure $C_{p,\infty}$ and thermal conductivity κ. As common with the FPV approach, we take a unity Lewis number among all species, leading to $\mathrm{Pr} = \mathrm{Sc} = 0.7$, where the Schmidt number is given by $\mathrm{Sc} = \mu/(\rho\mathcal{D}) = 0.7$ with mass diffusivity $\mathcal{D}$. Finally, buoyancy effects are neglected in this configuration, i.e., $\mathrm{Fr}_c \to \infty$.

The governing equations are discretized in space via the narrow-stencil finite difference operators satisfying the summation-by-parts (SBP) property (Kreiss & Scherer, 1974; Strand, 1994) with sixth-order of accuracy for the interior grid points and third-order of accuracy near the boundaries, leading to fourth-order global accuracy. Second- and mixed-derivatives are obtained by consecutively applying the first-derivative operators. The conditionally stable adaptive dissipation scheme proposed in Chapter 3.2.3.2 is applied to all governing equations to damp any spurious unresolved modes and ensure boundedness of $Z \in [0, 1]$ and $C \in [0, 1]$, and the Heaviside sensor (3.13) is taken with $\epsilon = 0.001$, which activates the low-order dissipation operator. The maximum value of boundedness error (3.37) of Z and C within all timesteps is $\varepsilon^b_\infty < 0.0021$. The governing equations

are advanced in time using the standard fourth-order Runge–Kutta (RK4) time integration scheme.

The SBP operators are combined with the simultaneous-approximation-term (SAT) boundary treatment that weakly imposes the boundary conditions. Non-reflecting SAT boundary treatment (see Svärd *et al.*, 2007; Vishnampet, 2015, and Appendix B.3) is enforced at the lateral boundaries. A modified SAT treatment is employed to impose an inflow boundary condition at the inlet and the convective (Neumann) condition at the outlet (see Appendices B.4 and B.5, respectively). The proposed SAT inflow-outflow boundaries are able to handle turbulent fluctuations at the inlet and outlet planes; otherwise, a longer computational domain is required to avoid boundary effects on the intermediate numerical solution (see Appendix B.7). Also, turbulence-flame interactions are avoided at the outflow by taking a buffer region with a size of $2D_j$ near the outlet plane, where only the low-order artificial dissipation operator is applied. The low-order artificial dissipation strongly damps any fluctuations, which leads to a smooth and laminar flow near the exit of the domain. In addition, absorbing sponge regions (Freund, 1997) are added to the governing equations (2.11) via a $\sigma_s(\boldsymbol{x})(\vec{Q} - \vec{Q}_t)$ source term that damps acoustic waves, where the coefficient $\sigma_s(\boldsymbol{x})$ quadratically decreases from 0.2 at the lateral boundaries towards zero within a region of $1.2D_j$ away from the boundaries, and $\vec{Q}_t$ is taken to be the initial conserved variables.

6.3 Control force

During the forward simulation, the lift-off height of the flame is located at $x \approx x_B = 1.5D_j$ after a transient regime. Then, thermal forcing is applied upstream of the flame to relocate its position. The external source term mimics an acoustic actuator, which is added to the energy equation as an external source term according to

$$\mathcal{N}_5[\vec{Q}] = \mathcal{W}_{\text{Ctl}}(\boldsymbol{x}) f_E(\boldsymbol{x}, t), \tag{6.3}$$

where a weighting function $\mathcal{W}_{\text{Ctl}}$ is taken to specify a region of interest where f_E applies. The control region, depicted by the small box in the left of the domain in Fig. 6.1, is located within

$[0.32D_j, 0.70D_j]\times[-1.00D_j, 1.00D_j]\times[-1.00D_j, 1.00D_j]$, discretized using 10×97×97 grid points. The weighting function $\mathcal{W}_{\text{Ctl}}(\boldsymbol{x})$ decays to zero at the prescribed borders via hyperbolic tangent functions. The control force is applied over 10,000 timesteps (corresponding to $(t_f - t_0)U_j/D_j = 14.10$), each containing four sub-steps in the RK4 time integrator. Thus, f_E contains $> 3 \times 10^9$ degrees of freedom that has to be optimized in order to modify the flame location.

6.4 Quantity of interest

The target flame location is defined using a QoI similar to the one proposed by Capecelatro *et al.* (2016), which measures the difference between the current temperature distribution to a desired one, according to

$$\mathcal{J}(\vec{Q}; \vec{f}) = \int_t \int_{\boldsymbol{x}} \left(\frac{T - T_{\text{Tar}}(\boldsymbol{x})}{T_{\text{F}} - T_\infty} \right)^2 \mathcal{W}_Z(Z)\, \mathcal{W}_{\text{Tar}}(\boldsymbol{x})\, \mathrm{d}\boldsymbol{x}\, \mathrm{d}t, \tag{6.4}$$

where the weight function $\mathcal{W}_Z$ specifies a burning zone around the stoichiometric mixture fraction, $Z_{st} = 0.184$, where the majority of heat is released, given by

$$\mathcal{W}_Z(Z) = e^{-(Z-Z_{st})^2/2r_{\text{F}}^2}, \tag{6.5}$$

where $r_{\text{F}} = 0.1R_j$ is the burning zone radius. The target temperature T_{Tar} is given by

$$T_{\text{Tar}}(\boldsymbol{x}) = \frac{T_{\text{F}} + T_0}{2} + \frac{T_{\text{F}} - T_0}{2} \tanh\left[s_{\text{F}}\,(x - x_{\text{F}})\right], \tag{6.6}$$

where $s_{\text{F}} = 10D_j^{-1}$ and $x_{\text{F}} = 1.2D_j$ denote a user-defined slope and flame location, respectively. T_0 is set to T_f^0 as defined in (2.4), and the flame temperature T_{F} is set as the maximum value obtained from the lookup table. A weighting function $\mathcal{W}_{\text{Tar}}(\boldsymbol{x})$ is applied in (6.4) to cover a target region $[0.82D_j, 3.01D_j]\times[-2.53D_j, 2.53D_j]\times[-2.53D_j, 2.53D_j]$ (larger box in Fig. 6.1), and it decays to zero at the prescribed borders via hyperbolic tangent functions. Thus, $\mathcal{J}$ is forced to zero outside

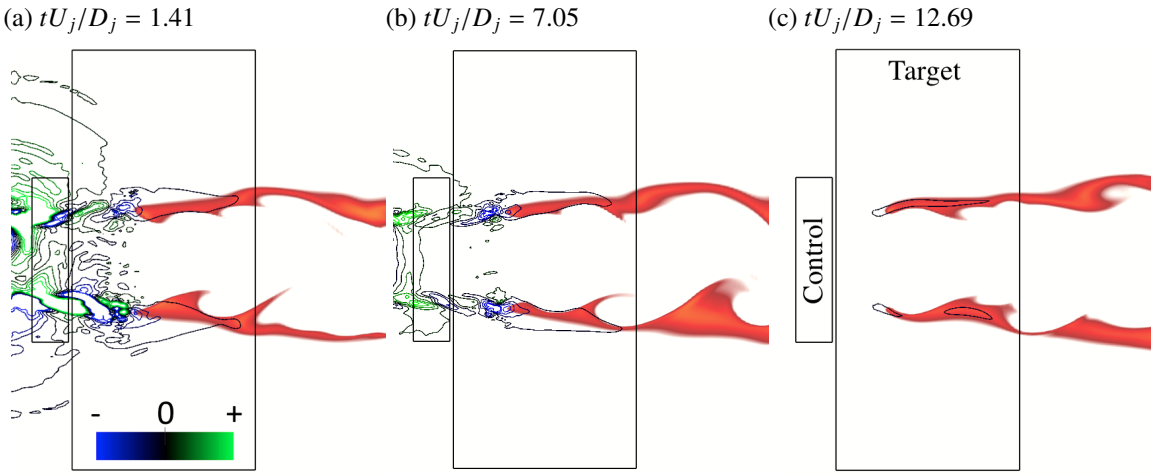

Figure 6.2: Instantaneous snapshots of $E^\dagger$ (adjoint variable corresponding to local sensitivity, blue: negative, green: positive) of the baseline solution (without forcing) at the $z = 0$ plane near the target and control regions. Same coloring as Fig. 6.1.

of the target region.

6.5 Adjoint sensitivity and optimization

Adjoint sensitivity of the QoI (6.4) to f_E is given by Eq. (2.16), i.e.,

$$g = \mathcal{W}_{\text{Ctl}} E^\dagger, \tag{6.7}$$

where $E^\dagger$ is the adjoint variable corresponding to the energy equation. Instantaneous snapshots of $E^\dagger$ are shown in Fig. 6.2. The adjoint sensitivity is generated in the vicinity of the flame and propagates in the reverse flow direction to the control region. Its instantaneous values at the control region are used as a search direction to impose acoustic forcing via a steepest descent algorithm, given by (2.53). A backtracking line searching is employed, as described in Chapter 2.6.1 and Eq. (2.54), to identify the step size for updating the control parameter. The history of optimization iterations are provided in Fig. 6.3. As can be seen, the value of QoI is reduced by more than 10% compared to the baseline case with no forcing after eight optimization iterations. Instantaneous snapshots of temperature are compared in Fig. 6.4, where the baseline (i.e., without forcing) and

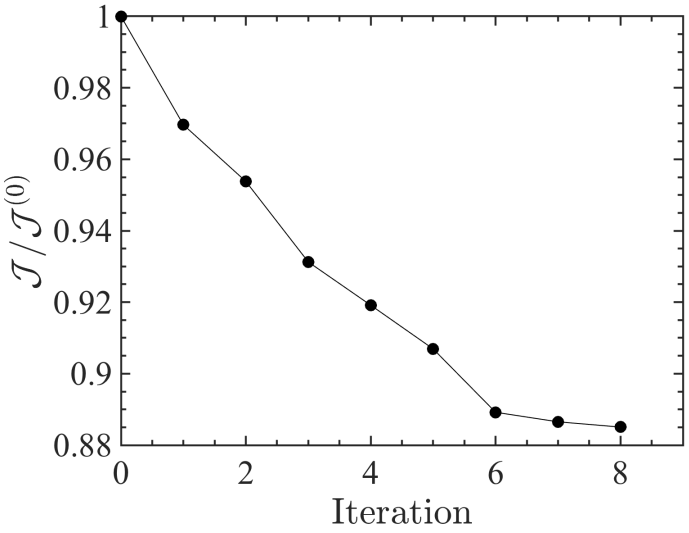

Figure 6.3: Optimization history of (6.4) with respect to the baseline solution, $\mathcal{J}^{(0)}$, i.e., the reacting jet with no thermal actuation.

the optimal control forcing are applied to the turbulent jet. As can be seen, the adjoint-based optimization algorithm is able to retard the lift-off height from $x \approx x_{\mathrm{B}}$ to the desired location $x \approx x_{\mathrm{F}}$ via manipulating the thermal actuator (see the middle vertical lines in Fig. 6.4, which are depicted at $x = x_{\mathrm{F}}$ and $x = x_{\mathrm{B}}$). Although the distance between the optimal and baseline lift-off heights is small ($< 0.5D_j$), this numerical study shows the capability of the adjoint sensitivity in finding optimal forcing of a turbulent reacting jet, in which a massive number of control parameters exist.

6.6 Conclusions

In this chapter, we used the FPV approach and corresponding adjoint solution to control a lifted H_2 flame in a turbulent round jet. A lookup table was generated via detailed chemistry of the H_2-air reaction, i.e., nine chemical species and 19 chemical reactions. Acoustic forcing was optimized using the discrete adjoint sensitivity to alter the flame location. The controller was a discrete space-time field with more than three billion degrees of freedom. Thus, it was not practical to use a brute-force approach to find the optimal forcing. However, the adjoint sensitivity combined

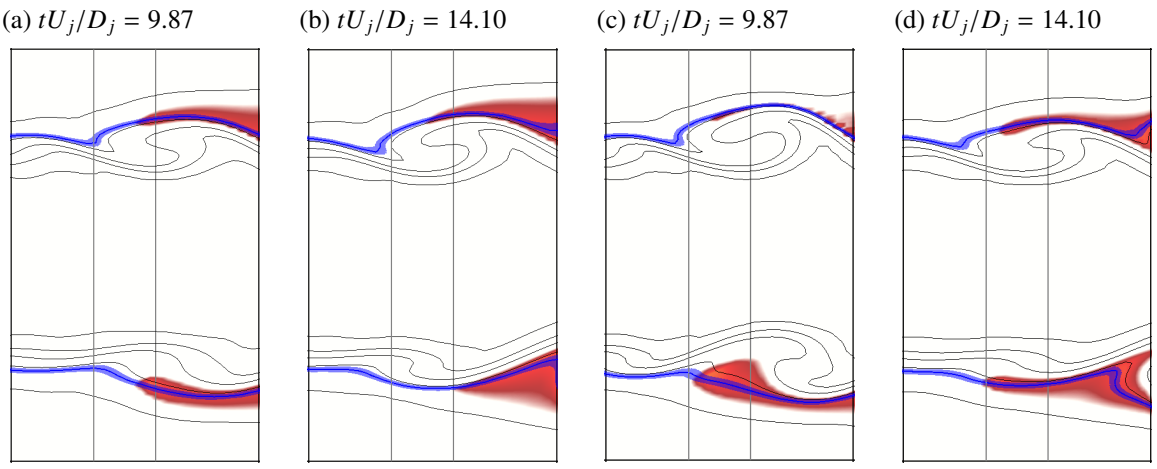

Figure 6.4: Instantaneous snapshots of the turbulent reacting jet at the $z = 0$ plane near the lift-off height of the flame: (*a–b*) no actuator (baseline solution), and (*c–d*) adjoint-based optimal solution after eight iterations. The vertical lines are located at $x = x_{\mathrm{F}}$ (left) and $x = x_{\mathrm{B}}$ (right). Same color scheme as Fig. 6.1.

with the steepest descent algorithm and backtracking line searching was able to obtain the optimal forcing with a tractable computational cost (i.e., the QoI was reduced by more than 10% after eight optimization iterations). Although the flame location was retarded slightly (i.e., $< 0.5D_j$), this demonstrates the ability of the adjoint solver for controlling a high-fidelity simulation of a turbulent reacting jet. The optimal forcing can be analyzed to obtain the spatial and temporal frequencies that modify the lift-off height of the flame and have greatest influence on the hydrodynamic and combustion instabilities associated with the turbulent jet. This post-processing step is beyond the scope of this work and is considered for future studies.

CHAPTER 7

Conclusions

7.1 Summary of achievements

The main contribution of this work is the development of a discrete-adjoint framework for computing sensitivity of high-fidelity simulations associated with turbulent reacting flows. Many engineering systems involve this class of flows, and the ability to actively control such flows has impacts on the economy, public health, and the environment. The developed adjoint-based method provides sensitivity to a large number of input parameters with a tractable computation cost. The adjoint solver was implemented by using analytic Jacobians, and the cost of the combined forward-adjoint simulation was about 3–3.5 times the cost of the forward run. In addition, the sensitivity obtained from the discrete adjoint solver was combined with gradient-based optimization techniques to strategically manipulate design/input parameters for improving various quantities of interest.

In summary, the following achievements were made: (*i*) A discrete-adjoint framework was developed for computing sensitivity of a quantity of interest (QoI) associated with a high-fidelity turbulent reacting flow simulation; (*ii*) An adaptive artificial dissipation scheme was introduced to preserve scalar boundedness with negligible effects on accuracy of the results, which is compatible with adjoint formulation; (*iii*) Flexible combustion modeling was achieved using the flamelet/progress variable (FPV) approach, which avoids transporting a large number of chemical species and reformulating adjoint sensitivity whenever new chemistry is desired; and (*iv*) The capability of the adjoint framework was demonstrated on several representative examples, including flow instabilities and turbulent combustion.

In Chapter 2, the governing equations of multi-component flows were provided, and their adjoint formulation was derived. In this chapter, we presented the FPV approach and its adjoint derivation. Finally, the adjoint-based sensitivity was combined with external and in-house optimization packages, and specific data management was employed when the controller is a discrete space-time field.

In Chapter 3, the adaptive dissipation scheme and its adjoint sensitivity were presented to preserve scalar boundedness. We first reviewed the standard low-order and high-order dissipation operators. The former is able to absorb a broad spectrum of spurious oscillation modes, and the latter is only effective for high-order wavenumbers. Thus, we combined these operators using a sensor that locally activates the low-order operator where the solution is unbounded, and the high-order operator is applied through the rest of the domain. Two formulations were introduced, corresponding to unconditionally- and conditionally stable schemes. The unconditionally stable method ensures energy stability of the numerical framework. Although the conditionally stable adaptive dissipation cannot guarantee energy stability, it has negligible effects on it if an appropriate sensor is employed. We assessed the capability of both schemes and their adjoint formulation in a series of numerical tests. Also, adjoint-based sensitivity was used to design a sensor in a one-dimensional problem. Finally, a turbulent round jet was considered to demonstrate the utility of the adaptive scheme on preserving scalar boundedness and retaining accuracy of the solution.

In Chapter 4, adjoint-based sensitivity analysis and optimization were performed for unsteady multi-component non-reacting flows before considering the complexities associated with chemical reactions and under-resolved simulations. Summary of outcomes of this chapter includes

(i) Sensitivity analysis of a three-dimensional multi-mode Rayleigh–Taylor (RT) instability showed that except for the diffusion growth regime, the most sensitive wavenumber of each objective function approximately equals the most unstable wavenumber predicted by linear stability theory ($k \approx 8$).

(ii) The adjoint-based optimization approach was capable of suppressing the instability by shifting all of the initial perturbation energy into the highest wavenumber modes as expected by

linear stability theory.

(iii) The optimization procedure was able to enhance mixing and growth relative to the baseline solution (uniform distributed perturbations) to a maximum increase in the bubble growth parameter and mixing width by 32% and 54%, respectively. Initial perturbations of all mixing quantities demonstrate that low wavenumbers are favored.

(iv) We also showed that the optimized perturbations obtained from two-dimensional simulations admit similar (and sometimes better) improvement when imposed in three-dimensional configurations, making adjoint-based optimization particularly attractive for controlling large-scale unsteady flows.

After computing adjoint sensitivity in well-resolved flow simulations, we employed the flow and adjoint framework on a free shear flow transporting a passive scalar in Chapter 5. We intentionally considered an under-resolved configuration. This required the use of the adaptive dissipation scheme to preserve scalar boundedness. The adaptive dissipation scheme significantly reduced the excursion errors (i.e., artificial overshoots and undershoots). Also, a discrete space-time field with more than a hundred million parameters was applied to control the evolution of the passive scalar. Combining the discrete adjoint sensitivity with the steepest descent algorithm and backtracking line searching was able to reduce the QoI, associated with the mixing layer evolution, by about 40% compared to the uncontrolled one.

Finally in Chapter 6, the adjoint solver was employed to control a lifted H_2 flame in a turbulent reacting jet. The detailed chemistry is applied to generate the lookup table, where nine chemical species and 19 chemical reactions are involved. A control field with discrete space-time values is applied upstream of the lifted flame, and the total number of parameters was more than a billion. A QoI was defined to measure the discrepancy of the lift-off height with the desired position, and the discrete adjoint optimizer was able to reduce the QoI by more than 10% within a few optimization iterations. Although the high-fidelity simulations were computationally expensive, the discrete-adjoint framework was able to relocate the flame with a tractable computational cost.

The proposed adjoint-based framework has shown great success in determining optimal space-time fields that control quantities of interest associated with turbulent reacting flows. The optimal solution can be further analyzed to precisely investigate the underlying physical mechanisms that contribute to flow instabilities. For instance, it can be used to identify the most active physical modes or frequencies. Other suggestions for future studies are provided in the following section.

7.2 Future prospectives

7.2.1 Accelerating data-driven methods

In recent years, data-driven methods such as machine learning and data assimilation have gained in popularity among the fluid dynamics community (e.g., see Brenner *et al.*, 2019; Duraisamy *et al.*, 2019; Duraisamy, 2021, and references therein), especially for constructing and developing turbulence models. In these methods, the discrepancy between numerical results and 'trusted' data is defined as a QoI that is minimized to extract new models or manipulate some user-defined parameters. The trusted data can be obtained from high-fidelity simulations or experiments. Adjoint sensitivity can thus be employed to accelerate the gradient-based optimization and to minimize the QoI via obtaining the model parameters. For instance, adjoint sensitivity was used to accelerate neural network models that learn sub-filter closures for LES (Sirignano *et al.*, 2020; MacArt *et al.*, 2021). Adjoint-based methods have been widely used with data assimilation techniques in different applications (e.g., see Le Dimet & Talagrand, 1986; Foures *et al.*, 2014a; Lemke & Sesterhenn, 2016) including combustion. For instance, Gray *et al.* (2017) introduced an adjoint-based variational data framework, which manipulates Arrhenius-based chemistry parameters and diffusion coefficients associated with the reactive Navier–Stokes equations, which solves the laminar flow inside of a pulse detonation combustor model. Reducing the number of inputs to a machine learning framework, also called feature reduction, can be performed by analyzing their adjoint sensitivities.

Developing reduced-order models that provide high-fidelity solutions for turbulent reacting

flows is also attractive. The present dissertation provided a discrete-adjoint solver that can be combined with data-driven methods. This framework can be used to improve current LES sub-grid scale models, introduce new ones, or manipulate their user-defined parameters. Combustion and turbulence models involve many model parameters, and accuracy of simulations typically relies on them. Although 'dynamic' approaches exist for adapting some of these parameters, these techniques usually increase computational cost. Adjoint sensitivity will investigate how much the numerical solution is sensitive with variations of these parameters. Also, the adjoint solver will be employed to accelerate the gradient-based optimization to obtain the optimal parameters. Moreover, spatial and temporal dependence on the model parameters can be studied via adjoint fields. These approaches will enhance the accuracy of reduced-order numerical simulations of turbulent reacting flows by strategically manipulating their model parameters via adjoint sensitivity.

7.2.2 Chaos and adjoint-based optimization

In Chapter 1.4.3, we reviewed challenges of adjoint-based optimization on chaotic dynamical systems and turbulent flows, which are divergence of adjoint sensitivity and non-convexity of QoIs (e.g., see Chung & Freund, 2021, and references therein). Several approaches were proposed to address the divergence of adjoint sensitivity (e.g., see Lea *et al.*, 2000, 2002; Eyink *et al.*, 2004; Thuburn, 2005; Wang, 2013; Wang *et al.*, 2014; Blonigan, 2017; Ni & Talnikar, 2019). However, their utility for optimization techniques is still in question regarding their computational cost and accuracy of adjoint sensitivity. Also, Chung & Freund (2021) introduced a multi-step penalty method and combined it with adjoint sensitivity to overcome the non-convexity of QoIs associated with chaos. However, its capability of overcoming extreme chaotic effects in turbulent flows over long time intervals is still unknown.

Although we did not employ the aforementioned approaches in this dissertation, the adjoint-method proposed by this work was successful in controlling representative multi-component flow instabilities and turbulent reacting flows within relatively short time horizons. However, the method has to be extended for overcoming chaotic effects within longer simulations.

Appendices

Appendix A

Continuous Adjoint Equations

In this appendix, the continuous adjoint equations are derived for three-dimensional reacting flows combined with the flamelet/progress variable approach. Adjoint equations of non-reacting flows and reacting flows with a single-step chemistry model can be found in Vishnampet (2015) and Capecelatro *et al.* (2018), respectively. As mentioned in Chapter 2.4, the first line of (2.15) must vanish to exclude the variations of $\vec{Q}$ in $\delta\mathcal{J}$, leading to

$$\vec{Q}^{\dagger\mathsf{T}}\frac{\partial\vec{\mathcal{N}}}{\partial\vec{Q}}\delta\vec{Q}-\left(\frac{\partial\mathcal{I}}{\partial\vec{Q}}\right)^{\mathsf{T}}\delta\vec{Q}\mathcal{W}_{\mathrm{Tar}}=0. \tag{A.1}$$

Variations of the governing equations (2.11) with respect to $\vec{Q}$ are given by

$$\begin{aligned}\frac{\partial\vec{\mathcal{N}}}{\partial\vec{Q}}\delta\vec{Q}=\frac{\partial\delta\vec{Q}}{\partial t}+J\frac{\partial}{\partial\xi_i}\Big\{&\mathcal{A}_i[\vec{Q}]\delta\vec{Q}-\mathcal{B}_{ij}[\vec{Q}_p]\frac{\partial}{\partial\xi_j}\left(C[\vec{Q}]\delta\vec{Q}\right)\\&-\mathcal{B}^{\mathrm{FPVA}}_{ij}[\vec{Q}_p]\frac{\partial}{\partial\xi_j}\left(C^{\mathrm{FPVA}}[\vec{Q}]\delta\vec{Q}\right)\Big\}-\frac{\partial\vec{S}}{\partial\vec{Q}}\delta\vec{Q}=0,\end{aligned} \tag{A.2}$$

where operators $\mathcal{A}$, $\mathcal{B}$, $\mathcal{B}^{\mathrm{FPVA}}$ are derived by considering variations of the inviscid and viscous fluxes (2.3) with respect to $\vec{Q}$, given by

$$\frac{\partial\vec{F}^I_i}{\partial\vec{Q}}\delta\vec{Q}=\widehat{\mathcal{A}^I_j}[\vec{Q}]\delta\vec{Q}, \tag{A.3}$$

and

$$\frac{\partial \vec{F}_i^V}{\partial \vec{Q}} \delta \vec{Q} = \widehat{\mathcal{A}_j^V}[\vec{Q}]\delta\vec{Q} + \widehat{\mathcal{B}_{ij}}[\vec{Q}_p]\frac{\partial}{\partial x_j}\left(C[\vec{Q}]\delta\vec{Q}\right) + \widehat{\mathcal{B}_{ij}^{\mathrm{FPVA}}}[\vec{Q}_p]\frac{\partial}{\partial x_j}\left(C^{\mathrm{FPVA}}[\vec{Q}]\delta\vec{Q}\right), \tag{A.4}$$

respectively, and the variation of the source term with respect to $\vec{Q}$ is given by

$$\frac{\partial \vec{S}}{\partial \vec{Q}} = \begin{bmatrix} 0 & 0 & 0 & 0 & 0 & 0 & 0 \\ -1/\mathrm{Fr}_c & 0 & 0 & 0 & 0 & 0 & 0 \\ 0 & 0 & 0 & 0 & 0 & 0 & 0 \\ 0 & 0 & -1/\mathrm{Fr}_c & 0 & 0 & 0 & 0 \\ 0 & 0 & 0 & 0 & 0 & 0 & 0 \\ 0 & 0 & 0 & 0 & 0 & 0 & 0 \\ -\frac{1}{\rho}\left(Z\frac{\partial \dot{\omega}_C}{\partial Z} + C\frac{\partial \dot{\omega}_C}{\partial C}\right) & 0 & 0 & 0 & 0 & \frac{1}{\rho}\frac{\partial \dot{\omega}_C}{\partial Z} & \frac{1}{\rho}\frac{\partial \dot{\omega}_C}{\partial C} \end{bmatrix}, \tag{A.5}$$

where (2.45) is employed for obtaining $\partial\dot{\omega}_C/\partial\vec{Q}$. $\partial\dot{\omega}_C/\partial Z$ and $\partial\dot{\omega}_C/\partial C$ are computed according to (2.46) and (2.47), respectively. Note that $\mathcal{A} = \mathcal{A}_i^I - \mathcal{A}_i^V$, $\mathcal{A}_i^I[\vec{Q}] = M_{ij}\widehat{\mathcal{A}_j^I}[\vec{Q}]$, $\mathcal{A}_i^V[\vec{Q}] = M_{ij}\widehat{\mathcal{A}_j^V}[\vec{Q}]$, $\mathcal{B}_{ij}[\vec{Q}_p] = M_{ik}\widehat{\mathcal{B}_{kj}}[\vec{Q}_p]$, and $\mathcal{B}_{ij}^{\mathrm{FPVA}}[\vec{Q}_p] = M_{ik}\widehat{\mathcal{B}_{kj}^{\mathrm{FPVA}}}[\vec{Q}_p]$. $\vec{Q}_p = [\rho, \boldsymbol{u}, T, Z, C]^\mathsf{T}$ is the list of primitive variables, and $\vec{Q}_Y = [Y_1, \ldots, Y_N]^\mathsf{T}$ is the list of species mass fractions. Jacobian matrices $C[\vec{Q}]$ and $C^{\mathrm{FPVA}}[\vec{Q}]$ are given by

$$C = \frac{\partial \vec{Q}_p}{\partial \vec{Q}} = \begin{bmatrix} 1 & 0 & 0 & 0 & 0 & 0 & 0 \\ -u_1/\rho & 1/\rho & 0 & 0 & 0 & 0 & 0 \\ -u_2/\rho & 0 & 1/\rho & 0 & 0 & 0 & 0 \\ -u_3/\rho & 0 & 0 & 1/\rho & 0 & 0 & 0 \\ \frac{\partial T}{\partial \rho} & \frac{\partial T}{\partial \rho u_1} & \frac{\partial T}{\partial \rho u_2} & \frac{\partial T}{\partial \rho u_3} & \frac{\partial T}{\partial \rho E} & \frac{\partial T}{\partial \rho Z} & \frac{\partial T}{\partial \rho C} \\ -Z/\rho & 0 & 0 & 0 & 0 & 1/\rho & 0 \\ -C/\rho & 0 & 0 & 0 & 0 & 0 & 1/\rho \end{bmatrix}, \tag{A.6}$$

and

$$C^{\text{FPVA}} = \frac{\partial \vec{Q}_Y}{\partial \vec{Q}} = \begin{bmatrix} -\frac{1}{\rho}\left(Z\frac{\partial Y_1}{\partial Z} + C\frac{\partial Y_1}{\partial C}\right) & 0 & 0 & 0 & 0 & \frac{1}{\rho}\frac{\partial Y_1}{\partial Z} & \frac{1}{\rho}\frac{\partial Y_1}{\partial C} \\ -\frac{1}{\rho}\left(Z\frac{\partial Y_2}{\partial Z} + C\frac{\partial Y_2}{\partial C}\right) & 0 & 0 & 0 & 0 & \frac{1}{\rho}\frac{\partial Y_2}{\partial Z} & \frac{1}{\rho}\frac{\partial Y_2}{\partial C} \\ \vdots & \vdots & \vdots & \vdots & \vdots & \vdots & \vdots \\ -\frac{1}{\rho}\left(Z\frac{\partial Y_N}{\partial Z} + C\frac{\partial Y_N}{\partial C}\right) & 0 & 0 & 0 & 0 & \frac{1}{\rho}\frac{\partial Y_N}{\partial Z} & \frac{1}{\rho}\frac{\partial Y_N}{\partial C} \end{bmatrix}, \tag{A.7}$$

respectively, where $\partial Y_n/\partial Z$ and $\partial Y_n/\partial C$ for $n = 1, \ldots, N$ are computed according to (2.46) and (2.47), respectively. Variations of temperature to conserved variables is derived via considering the equation of state (2.10), leading to

$$\frac{\partial T}{\partial \vec{Q}}\delta\vec{Q} = -\frac{T}{\rho}\delta\rho + \frac{T}{p}\frac{\partial p}{\partial \vec{Q}}\delta\vec{Q} + \frac{T}{W}\frac{\partial W}{\partial \vec{Q}}\delta\vec{Q}, \tag{A.8}$$

where variations of mixture molecular weight, given by (2.5), to $\vec{Q}$ is computed considering the chain rule (2.45), leading to

$$\begin{aligned} \frac{\partial W}{\partial \vec{Q}}\delta\vec{Q} = &- \frac{W^2}{\rho}\left[\sum_{n=1}^{N}\frac{1}{W_n}\left(-Z\frac{\partial Y_n}{\partial Z} - C\frac{\partial Y_n}{\partial C}\right)\right]\delta\rho \\ &- \frac{W^2}{\rho}\left(\sum_{n=1}^{N}\frac{1}{W_n}\frac{\partial Y_n}{\partial Z}\right)\delta(\rho Z) \\ &- \frac{W^2}{\rho}\left(\sum_{n=1}^{N}\frac{1}{W_n}\frac{\partial Y_n}{\partial C}\right)\delta(\rho C). \end{aligned} \tag{A.9}$$

Similarly, variations of p, given by (2.4), is obtained according to

$$\begin{aligned} \frac{\partial p}{\partial \vec{Q}}\delta\vec{Q} = &\left[\phi^2 + (\gamma-1)\left(f(Y) - Z\frac{\partial f}{\partial Z} - C\frac{\partial f}{\partial C}\right)\right]\delta\rho - (\gamma-1)u_1\delta(\rho u_1) \\ &- (\gamma-1)u_2\delta(\rho u_2) - (\gamma-1)u_3\delta(\rho u_3) + (\gamma-1)\delta(\rho E) \\ &+ (\gamma-1)\frac{\partial f}{\partial Z}\delta(\rho Z) + (\gamma-1)\frac{\partial f}{\partial C}\delta(\rho Z) \end{aligned} \tag{A.10}$$

with $\phi^2 = (\gamma-1)u_i u_i/2$ and

$$f(\vec{Q}_Y) = \frac{T_f^0}{W} - \sum_{n=1}^{N} \Delta h_{f,n}^0 Y_n = \sum_{n=1}^{N} \left(\frac{T_f^0}{W_n} - \Delta h_{f,n}^0 \right) Y_n. \tag{A.11}$$

The operators $\mathcal{A}$, $\mathcal{B}$, and $\mathcal{B}^{\text{FPVA}}$ are obtained according to (2.3) and (A.3)–(A.4), given by

$$\mathcal{A}_i^I[\vec{Q}] = \begin{bmatrix} 0 & M_{i1} & M_{i2} \\ \frac{\partial p}{\partial \rho} M_{i1} - u_1 \widehat{u_i} & \widehat{u_i} - (\gamma-2) u_1 M_{i1} & u_1 M_{i2} - (\gamma-1) u_2 M_{i1} \\ \frac{\partial p}{\partial \rho} M_{i2} - u_2 \widehat{u_i} & u_2 M_{i1} - (\gamma-1) u_1 M_{i2} & \widehat{u_i} - (\gamma-2) u_2 M_{i2} \\ \frac{\partial p}{\partial \rho} M_{i3} - u_3 \widehat{u_i} & u_3 M_{i1} - (\gamma-1) u_1 M_{i3} & u_3 M_{i2} - (\gamma-1) u_2 M_{i3} \\ (\frac{\partial p}{\partial \rho} - h) \widehat{u_i} & h M_{i1} - (\gamma-1) u_1 \widehat{u_i} & h M_{i2} - (\gamma-1) u_2 \widehat{u_i} \\ -Z \widehat{u_i} & Z M_{i1} & Z M_{i2} \\ -C \widehat{u_i} & C M_{i1} & C M_{i2} \end{bmatrix}$$

$$\begin{bmatrix} M_{i3} & 0 & 0 & 0 \\ u_1 M_{i3} - (\gamma-1) u_3 M_{i1} & (\gamma-1) M_{i1} & (\gamma-1) \frac{\partial f}{\partial Z} M_{i1} & (\gamma-1) \frac{\partial f}{\partial C} M_{i1} \\ u_2 M_{i3} - (\gamma-1) u_3 M_{i2} & (\gamma-1) M_{i2} & (\gamma-1) \frac{\partial f}{\partial Z} M_{i2} & (\gamma-1) \frac{\partial f}{\partial C} M_{i2} \\ \widehat{u_i} - (\gamma-2) u_3 M_{i3} & (\gamma-1) M_{i3} & (\gamma-1) \frac{\partial f}{\partial Z} M_{i3} & (\gamma-1) \frac{\partial f}{\partial C} M_{i2} \\ h M_{i3} - (\gamma-1) u_3 \widehat{u_i} & \gamma \widehat{u_i} & (\gamma-1) \frac{\partial f}{\partial Z} \widehat{u_i} & (\gamma-1) \frac{\partial f}{\partial C} \widehat{u_i} \\ Z M_{i3} & 0 & \widehat{u_i} & 0 \\ C M_{i3} & 0 & 0 & \widehat{u_i} \end{bmatrix}, \tag{A.12}$$

$$\mathcal{A}_i^V[Q] =$$

$$\begin{bmatrix}
0 & 0 & 0 & 0 & 0 & 0 & 0 \\
\frac{b\widehat{\tau}_{1i}}{T}\frac{\partial T}{\partial \rho} & \frac{b\widehat{\tau}_{1i}}{T}\frac{\partial T}{\partial \rho u_1} & \frac{b\widehat{\tau}_{1i}}{T}\frac{\partial T}{\partial \rho u_2} & \frac{b\widehat{\tau}_{1i}}{T}\frac{\partial T}{\partial \rho u_3} & \frac{b\widehat{\tau}_{1i}}{T}\frac{\partial T}{\partial \rho E} & \frac{b\widehat{\tau}_{1i}}{T}\frac{\partial T}{\partial \rho Z} & \frac{b\widehat{\tau}_{1i}}{T}\frac{\partial T}{\partial \rho C} \\
\frac{b\widehat{\tau}_{2i}}{T}\frac{\partial T}{\partial \rho} & \frac{b\widehat{\tau}_{2i}}{T}\frac{\partial T}{\partial \rho u_1} & \frac{b\widehat{\tau}_{2i}}{T}\frac{\partial T}{\partial \rho u_2} & \frac{b\widehat{\tau}_{2i}}{T}\frac{\partial T}{\partial \rho u_3} & \frac{b\widehat{\tau}_{2i}}{T}\frac{\partial T}{\partial \rho E} & \frac{b\widehat{\tau}_{2i}}{T}\frac{\partial T}{\partial \rho Z} & \frac{b\widehat{\tau}_{2i}}{T}\frac{\partial T}{\partial \rho C} \\
\frac{b\widehat{\tau}_{3i}}{T}\frac{\partial T}{\partial \rho} & \frac{b\widehat{\tau}_{3i}}{T}\frac{\partial T}{\partial \rho u_1} & \frac{b\widehat{\tau}_{3i}}{T}\frac{\partial T}{\partial \rho u_2} & \frac{b\widehat{\tau}_{3i}}{T}\frac{\partial T}{\partial \rho u_3} & \frac{b\widehat{\tau}_{3i}}{T}\frac{\partial T}{\partial \rho E} & \frac{b\widehat{\tau}_{3i}}{T}\frac{\partial T}{\partial \rho Z} & \frac{b\widehat{\tau}_{3i}}{T}\frac{\partial T}{\partial \rho C} \\
-\frac{u_j\widehat{\tau}_{ij}}{\rho} + \widehat{\Phi}_i\frac{\partial T}{\partial \rho} & \frac{\widehat{\tau}_{1i}}{\rho} + \widehat{\Phi}_i\frac{\partial T}{\partial \rho u_1} & \frac{\widehat{\tau}_{2i}}{\rho} + \widehat{\Phi}_i\frac{\partial T}{\partial \rho u_2} & \frac{\widehat{\tau}_{3i}}{\rho} + \widehat{\Phi}_i\frac{\partial T}{\partial \rho u_3} & \widehat{\Phi}_i\frac{\partial T}{\partial \rho E} & \widehat{\Phi}_i\frac{\partial T}{\partial \rho Z} & \widehat{\Phi}_i\frac{\partial T}{\partial \rho C} \\
-\frac{b\widehat{f}^V_{Z,i}}{T}\frac{\partial T}{\partial \rho} & -\frac{b\widehat{f}^V_{Z,i}}{T}\frac{\partial T}{\partial \rho u_1} & -\frac{b\widehat{f}^V_{Z,i}}{T}\frac{\partial T}{\partial \rho u_2} & -\frac{b\widehat{f}^V_{Z,i}}{T}\frac{\partial T}{\partial \rho u_3} & -\frac{b\widehat{f}^V_{Z,i}}{T}\frac{\partial T}{\partial \rho E} & -\frac{b\widehat{f}^V_{Z,i}}{T}\frac{\partial T}{\partial \rho Z} & -\frac{b\widehat{f}^V_{Z,i}}{T}\frac{\partial T}{\partial \rho C} \\
-\frac{b\widehat{f}^V_{C,i}}{T}\frac{\partial T}{\partial \rho} & -\frac{b\widehat{f}^V_{C,i}}{T}\frac{\partial T}{\partial \rho u_1} & -\frac{b\widehat{f}^V_{C,i}}{T}\frac{\partial T}{\partial \rho u_2} & -\frac{b\widehat{f}^V_{C,i}}{T}\frac{\partial T}{\partial \rho u_3} & -\frac{b\widehat{f}^V_{C,i}}{T}\frac{\partial T}{\partial \rho E} & -\frac{b\widehat{f}^V_{C,i}}{T}\frac{\partial T}{\partial \rho Z} & -\frac{b\widehat{f}^V_{C,i}}{T}\frac{\partial T}{\partial \rho C}
\end{bmatrix}, \tag{A.13}$$

$$\mathcal{B}_{ij}[Q_p] = \frac{J}{\mathrm{Re}_c}\begin{bmatrix} 0 & 0 \\ 0 & \mu M_{ik}M_{jk} + (\mu+\lambda)M_{i1}M_{j1} \\ 0 & \mu M_{i1}M_{j2} + \lambda M_{i2}M_{j1} \\ 0 & \mu M_{i1}M_{j3} + \lambda M_{i3}M_{j1} \\ 0 & \mu u_1 M_{ik}M_{jk} + \mu\widehat{u}_j M_{i1} + \lambda\widehat{u}_i M_{j1} \\ 0 & 0 \\ 0 & 0 \end{bmatrix}$$

$$\begin{bmatrix} 0 & 0 \\ \mu M_{i2}M_{j1} + \lambda M_{i1}M_{j2} & \mu M_{i3}M_{j1} + \lambda M_{i1}M_{j3} \\ \mu M_{ik}M_{jk} + (\mu+\lambda)M_{i2}M_{j2} & \mu M_{i3}M_{j2} + \lambda M_{i2}M_{j3} \\ \mu M_{i2}M_{j3} + \lambda M_{i3}M_{j2} & \mu M_{ik}M_{jk} + (\mu+\lambda)M_{i3}M_{j3} \\ \mu u_2 M_{ik}M_{jk} + \mu\widehat{u}_j M_{i2} + \lambda\widehat{u}_i M_{j2} & \mu u_3 M_{ik}M_{jk} + \mu\widehat{u}_j M_{i3} + \lambda\widehat{u}_i M_{j3} \\ 0 & 0 \\ 0 & 0 \end{bmatrix}$$

$$\begin{bmatrix} 0 & 0 & 0 \\ 0 & 0 & 0 \\ 0 & 0 & 0 \\ 0 & 0 & 0 \\ \mu M_{ik}M_{jk}/\mathrm{Pr} & 0 & 0 \\ 0 & \mu M_{ik}M_{jk}/\mathrm{Sc}_Z & 0 \\ 0 & 0 & \mu M_{ik}M_{jk}/\mathrm{Sc}_C \end{bmatrix}, \tag{A.14}$$

and

$$\mathcal{B}_{ij}^{\mathrm{FPVA}}[\vec{Q}_p] = \frac{JM_{ik}M_{jk}\mu}{\mathrm{Re}_c}\begin{bmatrix} 0 & \dots & 0 \\ 0 & \dots & 0 \\ 0 & \dots & 0 \\ 0 & \dots & 0 \\ \frac{1}{\mathrm{Sc}_1}\left(\frac{T-T_f^0}{W_1}+\Delta h_{f,1}^0\right) & \dots & \frac{1}{\mathrm{Sc}_N}\left(\frac{T-T_f^0}{W_N}+\Delta h_{f,N}^0\right) \\ 0 & \dots & 0 \\ 0 & \dots & 0 \end{bmatrix}, \tag{A.15}$$

respectively, with total enthalpy $h = E + p/\rho$, and the contravariant velocity $\widehat{u_i} = M_{ij}u_j$, and $\widehat{\tau}_{ij} = M_{ik}\tau_{kj}$, $\widehat{q_i} = M_{ij}q_j$, $\widehat{f_{Z,i}^V} = M_{ij}f_{Z,j}^V$, $\widehat{f_{C,i}^V} = M_{ij}f_{C,j}^V$, and

$$\widehat{\Phi}_i = \frac{b\left(u_j\widehat{\tau}_{ij} - \widehat{q_i}\right)}{T} + M_{ij}\frac{\mu}{\mathrm{Re}_c}\sum_{n=1}^{N}\frac{1}{W_n\mathrm{Sc}_n}\frac{\partial Y_n}{\partial \xi_j}. \tag{A.16}$$

Substituting $\partial\vec{\mathcal{N}}/\partial\vec{Q}$ from (A.2) into (A.1), employing integration-by-parts, and decomposing each component of $\delta\vec{Q}$ yields the following adjoint equations

$$\begin{aligned}&\frac{\partial\vec{Q}^\dagger}{\partial t} + J\left\{\mathcal{A}_i^{\mathsf{T}}[\vec{Q}]\frac{\partial\vec{Q}^\dagger}{\partial\xi_i} + \mathcal{C}^{\mathsf{T}}[\vec{Q}]\frac{\partial}{\partial\xi_j}\left(\mathcal{B}_{ij}^{\mathsf{T}}[\vec{Q}_p]\frac{\partial\vec{Q}^\dagger}{\partial\xi_i}\right) + \mathcal{C}^{\mathrm{FPVA}\,\mathsf{T}}[\vec{Q}]\frac{\partial}{\partial\xi_j}\left(\mathcal{B}_{ij}^{\mathrm{FPVA}\,\mathsf{T}}[\vec{Q}_p]\frac{\partial Q^\dagger}{\partial\xi_i}\right)\right\} \\ &+\left(\frac{\partial\vec{S}}{\partial\vec{Q}}\right)^{\mathsf{T}}\vec{Q}^\dagger + \frac{\partial\mathcal{I}}{\partial\vec{Q}}\mathcal{W}_{\mathrm{Tar}} = 0.\end{aligned} \tag{A.17}$$

Appendix B

SAT Boundary Conditions and Its Adjoint Formulation

In this appendix, a review of employed SAT boundary treatment with corresponding adjoint formulation is provided, and two new boundary conditions are introduced. More details can be found in Vishnampet (2015).

B.1 Notation

The SAT boundary treatment is added to the right-hand-side of the governing equation (2.11) discretized with the SBP operators according to

$$\frac{\mathrm{d}\vec{Q}}{\mathrm{d}t} = \vec{\mathrm{R}}[\vec{Q}] + \sum_{\alpha=1}^{3} \left(\vec{\mathrm{R}}^{+}_{\mathrm{SAT},\alpha}[\vec{Q}] + \vec{\mathrm{R}}^{-}_{\mathrm{SAT},\alpha}[\vec{Q}] \right). \tag{B.1}$$

In this Appendix, $\vec{Q}$ denotes the conserved flow variables that are discretized in space, and $\vec{\mathrm{R}}$ contains all inviscid and viscous fluxes, external source, artificial dissipation, and damping (absorbing sponge) terms. The SAT boundary treatment is denoted by $\vec{\mathrm{R}}^{\pm}_{\mathrm{SAT},\alpha}$, which enforces a boundary condition for a boundary with a normal vector along the $\pm\xi_\alpha$-direction for $\alpha = 1, 2, 3$ (if it is not a periodic boundary condition). Throughout this chapter, Einstein notation is not implied for repeated or non-repeated indices of the Greek letter α. A diagonal matrix $\vec{\mathrm{E}}^{\pm}_{\alpha}$ is used in the following sections, whose diagonal components are not zero only at the desired boundary point of the computational grid, e.g., $\vec{\mathrm{E}}^{+}_{1} = \mathrm{diag}[1, 0, \ldots, 0] \in \mathbb{R}^{N_x \times N_x}$ and $\vec{\mathrm{E}}^{-}_{1} = \mathrm{diag}[0, \ldots, 0, 1] \in \mathbb{R}^{N_x \times N_x}$ in a one-dimensional grid of size N_x. $\vec{\mathrm{E}}^{\pm}_{\alpha}$ can be easily constructed for higher dimensions using

Kronecker product.

The corresponding adjoint formulation of (B.1) is given by

$$\frac{\mathrm{d}\vec{Q}}{\mathrm{d}t} = \vec{\mathrm{R}}^{\dagger}[\vec{Q}]\vec{Q}^{\dagger} - \sum_{\alpha=1}^{3}\left(\vec{\mathrm{R}}^{\dagger+}_{\mathrm{SAT},\alpha}[\vec{Q}]\vec{Q}^{\dagger} + \vec{\mathrm{R}}^{\dagger-}_{\mathrm{SAT},\alpha}[\vec{Q}]\vec{Q}^{\dagger}\right), \tag{B.2}$$

where the adjoint formulation of the SAT boundary treatment are given by

$$\vec{\mathrm{R}}^{\dagger\pm}_{\mathrm{SAT},\alpha}[\vec{Q}] = \vec{\mathrm{P}}^{-1}\left(\frac{\partial\vec{\mathrm{R}}^{\pm}_{\mathrm{SAT},\alpha}}{\partial\vec{Q}}\right)^{\mathsf{T}}\vec{\mathrm{P}}. \tag{B.3}$$

The SBP norm matrix is denoted by $\vec{\mathrm{P}}$.

B.2 No-penetration wall

An impenetrable wall boundary condition is introduced by Svärd & Nordström (2008), and a different form is provided by Vishnampet (2015). We use the latter approach, which weakly enforces the normal component of the momentum to zero, given by

$$\vec{\mathrm{R}}^{\pm}_{\mathrm{impenetrable},\alpha} = \mp\,\sigma_I^{\mathrm{SAT}}J\vec{\mathrm{P}}^{-1}\vec{\mathrm{E}}^{\pm}_{\alpha}M_{\alpha i}\left[\rho u_i,\ \rho u_i u_1,\ \rho u_i u_2,\ \rho u_i u_3,\ \rho u_i h,\ \rho u_i Y_1,\ \ldots,\ \rho u_i Y_{N-1}\right]^{\mathsf{T}}, \tag{B.4}$$

where the specific enthalpy is given by $h = E + p/\rho$. Energy stability of (B.4) has been verified as $\sigma_I^{\mathrm{SAT}} \geq 1/2$ (Vishnampet, 2015) for single-component flows. Note that the vector $[\rho u_i,\ \rho u_i u_1,\ \rho u_i u_2,\ \rho u_i u_3,\ \rho u_i h,\ \rho u_i Y_1,\ \ldots,\ \rho u_i Y_{N-1}]^{\mathsf{T}}$ in (B.4) is the same with the inviscid flux term (2.3) excluding the pressure term in the momentum fluxes. Thus, adjoint formulation of (B.4)

is given by

$$\vec{\mathrm{R}}^{\dagger\pm}_{\text{impenetrable},\alpha} = \mp\,\sigma_I^{\mathrm{SAT}} J\vec{\mathrm{P}}^{-1}\vec{\mathrm{E}}^{\pm}_{\alpha}\left\{\mathcal{A}^I_\alpha - \begin{bmatrix} 0 \\ M_{\alpha 1} \\ M_{\alpha 2} \\ M_{\alpha 3} \\ 0 \\ 0 \\ \vdots \\ 0 \end{bmatrix}\left[\frac{\partial p}{\partial \rho}, \frac{\partial p}{\partial \rho u_1}, \frac{\partial p}{\partial \rho u_2}, \frac{\partial p}{\partial \rho u_3}, \frac{\partial p}{\partial \rho E}, \frac{\partial p}{\partial \rho Y_1}, \ldots, \frac{\partial p}{\partial \rho Y_{N-1}}\right]\right\}^{\mathsf{T}}. \tag{B.5}$$

B.3 Far-field

The SAT boundary treatment that enforces a non-reflecting boundary condition is given by (Svärd *et al.*, 2007; Vishnampet, 2015)

$$\vec{\mathrm{R}}^{\pm}_{\text{far-field},\alpha} = \mp\,\sigma_I^{\mathrm{SAT}} J\vec{\mathrm{P}}^{-1}\vec{\mathrm{E}}^{\pm}_{\alpha}\mathcal{A}_{\alpha,inc}[\vec{Q}_b](\vec{Q}-\vec{Q}_b) \pm \sigma_V^{\mathrm{SAT}} J\vec{\mathrm{P}}^{-1}\vec{\mathrm{E}}^{\pm}_{\alpha} M_{\alpha i}\left(\vec{\mathrm{F}}^V_i[\vec{Q}] - \vec{\mathrm{F}}^V_i[\vec{Q}_b]\right), \tag{B.6}$$

where $\vec{Q}_b$ is a desired value at the far-field boundary, and the inviscid and viscous penalty parameters are denoted by σ_I^{SAT} and σ_V^{SAT}, respectively. $\mathcal{A}_{\alpha,inc}$ is the Jacobian of inviscid fluxes in which the outgoing characteristic waves are forced to zero, where more details can be found in Pulliam & Chaussee (1981) for single-component and in Fedkiw *et al.* (1997) for multi-component reacting flows. The above SAT treatment requires that $\sigma_I^{\mathrm{SAT}} \geq 1/2$ and $\sigma_V^{\mathrm{SAT}} = 1$ for being stable (Svärd *et al.*, 2007) in single-component flows. Its adjoint formulation is given by

$$\begin{aligned}\vec{\mathrm{R}}^{\dagger\pm}_{\text{far-field},\alpha} = {} & \mp\,\sigma_I^{\mathrm{SAT}} J\vec{\mathrm{P}}^{-1}\vec{\mathrm{E}}^{\pm}_{\alpha}\mathcal{A}^{\mathsf{T}}_{\alpha,inc}[\vec{Q}_b] \\ & \pm \sigma_V^{\mathrm{SAT}} J\vec{\mathrm{P}}^{-1}\vec{\mathrm{E}}^{\pm}_{\alpha}\left(\mathcal{A}^{V^{\mathsf{T}}}_{\alpha}[\vec{Q}] + C^{\mathsf{T}}[\vec{Q}]\mathrm{D}^{\mathsf{T}}_i\mathcal{B}^{\mathsf{T}}_{\alpha i}[\vec{Q}] + C^{\mathrm{FPVA}^{\mathsf{T}}}[\vec{Q}]\mathrm{D}^{\mathsf{T}}_i\mathcal{B}^{\mathrm{FPVA}^{\mathsf{T}}}_{\alpha i}[\vec{Q}_p]\right),\end{aligned} \tag{B.7}$$

where $\mathcal{A}_V$, $\mathcal{B}_{ij}$, C, $\mathcal{B}_{ij}^{\text{FPVA}}$, and C^{FPVA} are defined in Appendix A. D_i denotes the first-derivative operator in direction ξ_i, satisfying the SBP property. Note that the term $C^{\text{FPVA}^\mathsf{T}}[\vec{Q}]\mathrm{D}_i^\mathsf{T}\mathcal{B}_{\alpha i}^{\text{FPVA}^\mathsf{T}}[\vec{Q}_p]$ is used with FPVA.

The proposed SAT term (B.6) can also be used to enforce inflow and outflow boundary conditions. In these cases, the SAT non-reflecting treatment weakly enforces the state values $\vec{Q}$ to the boundary value $\vec{Q}_b$ at the inlet or outlet planes. However, $\vec{Q}$ might not sufficiently remain close to $\vec{Q}_b$, especially when $\vec{Q}_b$ varies in time, such as seeding time-dependent velocity perturbations at the inlet. Also, the target value $\vec{Q}_b$ is typically set to a mean value in turbulent flows. Thus, such SAT boundary term could suppress inflow/outflow fluctuations, necessitating a longer simulation domain to avoid domain size effects on the interior solution. We present new SAT inflow/outflow treatment in the following sections to address the aforementioned issues.

B.4 Inflow

To account for a time-dependent inflow, we consider a modified version of the SAT no-penetration boundary treatment of (B.4) to provide a desired normal momentum, given by (Kord & Capecelatro, 2021)

$$\vec{\mathrm{R}}_{\text{inflow},\alpha}^{\pm} = \mp\,\sigma_I^{\text{SAT}} J\vec{\mathrm{P}}^{-1}\vec{\mathrm{E}}_\alpha^{\pm} M_{\alpha i}\left(\begin{bmatrix}\rho u_i\\ \rho u_i u_1\\ \rho u_i u_2\\ \rho u_i u_3\\ \rho u_i h\\ \rho u_i Y_1\\ \vdots,\\ \rho u_i Y_{N-1}\end{bmatrix} - \begin{bmatrix}\rho_b u_{i,b}\\ \rho_b u_{i,b} u_{b,1}\\ \rho_b u_{i,b} u_{b,2}\\ \rho_b u_{i,b} u_{b,3}\\ \rho_b u_{i,b} h_b\\ \rho_b u_{i,b} Y_{1,b}\\ \vdots,\\ \rho_b u_{\alpha,b} Y_{N-1,b}\end{bmatrix}\right), \tag{B.8}$$

where superscript b denotes the desired inflow values. Note that if the normal inflow velocity $M_{\alpha i}u_{i,b} = 0$, the no-penetration SAT boundary treatment given by (B.4) will be recovered. To impose (B.8), the inflow $\vec{Q}_b(t)$ has to be known, and a desired velocity and mass fraction distributions at the inlet plane have to be taken. These values can be set constant, or vary in space and time via trigonometric functions (e.g., see da Silva & Métais, 2001; Tyliszczak & Geurts, 2014), or be seeded by a time-dependent three-dimensional pseudo-turbulent algorithm (e.g., see Klein *et al.*, 2003). The target energy E_b and enthalpy $h_b = E_b + p_b/\rho_b$ are then updated according to (2.4) when u_b changes while the target pressure p_b could be considered constant. Also, since $\vec{Q}_b$ is updated independently of $\vec{Q}$, the adjoint formulation of (B.8) is the same as the adjoint formulation of the no-penetration wall, i.e., (B.4).

B.5 Outflow

We employ only the inviscid term of the non-reflecting far-field SAT (B.6) to impose the new outflow boundary condition, but $\vec{Q}_b$ is carefully selected at the outflow to make the non-reflecting SAT treatment consistent with convective (Neumann) boundary conditions and to avoid suppressing outflow perturbations (Kord & Capecelatro, 2021). In this work, $\vec{Q}_b$ is chosen such that $u_{\alpha,b} = \max(u_{\alpha,b-1}, 0)$, where $b-1$ is the grid point next to the outlet plane through its normal direction. The tangent components of the velocity in $\vec{Q}_b$ are set the same with the corresponding value at the grid point $b-1$. In addition, $\rho_b = \rho_{b-1}$, $p_b = p_{b-1}$, and $Y_{n,b} = Y_{n,b-1}$ for $n = 1, \ldots, N$. This strategy ensures that the flow can only convect out of the domain and prevents recirculation.

The adjoint formulation of the proposed outflow treatment is more complicated since $\vec{Q}_b$ is also updated based on the flow state variables. The outflow velocity condition $u_{\alpha,b} = \max(u_{\alpha,b-1}, 0)$ can generate discontinuity with respect to $\vec{Q}$. Thus, for adjoint simulations, we only set $u_{\alpha,b} = u_{\alpha,b-1}$. Considering this $\vec{Q}_b$ and taking variations of (B.6) with respect to $\vec{Q}$ yields the adjoint formulation

of the SAT outflow term, given by

$$\begin{aligned}\vec{\mathrm{R}}^{\dagger\pm}_{\mathrm{outflow},\alpha} &= \mp \sigma_I^{\mathrm{SAT}} J\vec{\mathrm{P}}^{-1}\vec{\mathrm{E}}^{\pm}_{\alpha}\mathcal{A}^{\mathsf{T}}_{\alpha,inc}[\vec{Q}_b] \\ &\pm \sigma_I^{\mathrm{SAT}} J\vec{\mathrm{P}}^{-1}\vec{\mathrm{E}}^{\pm}_{\alpha-1}\mathcal{A}^{\mathsf{T}}_{\alpha,inc}[\vec{Q}_b] \\ &\mp \sigma_I^{\mathrm{SAT}} J\vec{\mathrm{P}}^{-1}\vec{\mathrm{E}}^{\pm}_{\alpha-1}\left[\frac{\partial\mathcal{A}_{\alpha,inc}[\vec{Q}_b]}{\partial\vec{Q}}(\vec{Q}-\vec{Q}_b)\right]^{\mathsf{T}},\end{aligned} \tag{B.9}$$

where $\vec{\mathrm{E}}^{\pm}_{\alpha-1}$ is similar to $\vec{\mathrm{E}}^{\pm}_{\alpha}$ except that its unity value is shifted to the grid point next to the outflow boundary in its normal direction, e.g., $\vec{\mathrm{E}}^{+}_{\alpha-1} = \mathrm{diag}[0,1,0,\ldots,0] \in \mathbb{R}^{N_x\times N_x}$ and $\vec{\mathrm{E}}^{-}_{\alpha-1} = \mathrm{diag}[0,\ldots,0,1,0] \in \mathbb{R}^{N_x\times N_x}$ in a one-dimensional grid of size N_x.

B.6 Isothermal wall

An isothermal stationary wall is achieved via a SAT term of (Svärd & Nordström, 2008; Vishnampet, 2015)

$$\vec{\mathrm{R}}^{\pm}_{\mathrm{isothermal},\alpha} = \vec{\mathrm{R}}^{\dagger\pm}_{\mathrm{impenetrable},\alpha} - \sigma_V^{\mathrm{SAT}} J^2\vec{\mathrm{P}}^{-1}\vec{\mathrm{E}}^{\pm}_{\alpha}M_{\alpha i}M_{\alpha i}\begin{bmatrix} 0 \\ \rho u_1 \\ \rho u_2 \\ \rho u_3 \\ \rho E - \frac{\rho T_{\mathrm{W}}}{\gamma W} \\ \rho Y_1 - \rho Y_{1,\mathrm{W}} \\ \vdots \\ \rho Y_{N-1} - \rho Y_{N-1,\mathrm{W}} \end{bmatrix} \tag{B.10}$$

with target wall temperature and mass fraction values of T_{W}, $Y_{1,\mathrm{W}}$, ..., and $Y_{N-1,\mathrm{W}}$, respectively. More details can be found in Svärd & Nordström (2008) and Vishnampet (2015) for single-

component flows. Its adjoint term is computed according to

$$\vec{\mathrm{R}}^{\dagger\pm}_{\mathrm{isothermal},\alpha} = \vec{\mathrm{R}}^{\dagger\pm}_{\mathrm{impenetrable},\alpha}$$
$$- \sigma_V^{\mathrm{SAT}} J^2 \vec{\mathrm{P}}^{-1} \vec{\mathrm{E}}^{\pm}_{\alpha} M_{\alpha i} M_{\alpha i} \begin{bmatrix} 0 & 0 & 0 & 0 & 0 & 0 & \dots & 0 \\ 0 & 1 & 0 & 0 & 0 & 0 & \dots & 0 \\ 0 & 0 & 1 & 0 & 0 & 0 & \dots & 0 \\ 0 & 0 & 0 & 1 & 0 & 0 & \dots & 0 \\ -\frac{T_W}{\gamma W_N} & 0 & 0 & 0 & 1 & -\frac{T_W}{\gamma}\left(\frac{1}{W_1} - \frac{1}{W_N}\right) & \dots & -\frac{T_W}{\gamma}\left(\frac{1}{W_{N-1}} - \frac{1}{W_N}\right) \\ -Y_{1,W} & 0 & 0 & 0 & 0 & 1 & \dots & 0 \\ \vdots & \vdots & \vdots & \vdots & \vdots & \vdots & \ddots & \vdots \\ -Y_{N-1,W} & 0 & 0 & 0 & 0 & 0 & \dots & 1 \end{bmatrix}^{\mathsf{T}}. \tag{B.11}$$

B.7 Demonstration of proposed SAT Inflow-Outflow

We consider the three-dimensional turbulent jet configuration introduced in Chapter 3.5 with the standard inviscid SAT far-field boundary conditions at the inflow and outflow, and we compare the solution with simulation using the proposed inflow and outflow terms.

Comparing with the desired target velocity, the proposed inflow treatment is seen to correctly enforce the target solution at the time plotted in Fig. B.1a. Note that the target velocity contains perturbations generated via the digital filtering technique (Klein *et al.*, 2003) that is updated every timestep (see Chapter 3.5.2 for more details). It is possible to improve the boundary error either via increasing the SAT penalty magnitude or decreasing the frequency at which the target perturbations are updated. It can also be seen that the traditional far-field SAT term at the outlet significantly reduces the fluctuations at the outlet since the target velocity contains zero perturbations (see Fig. B.1b). On the other hand, the modified outflow gives a finite value at the outlet, which is similar to a simulation with a longer domain ($30D_j \times 15D_j \times 15D_j$ with $396 \times 241 \times 241$

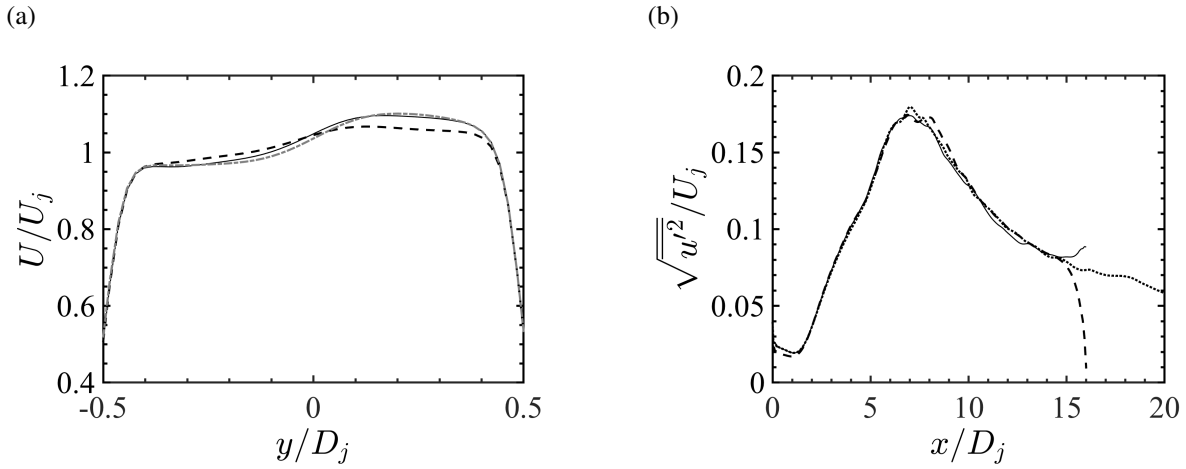

Figure B.1: (*a*) Instantaneous inflow velocity at $x = 0$ and $z = 0$ when an inflow (–) and a far-field (−−) SAT is applied. The target velocity is also plotted (−·). (*b*) Axial-component of the Reynolds stress at the jet centerline for different boundary conditions. Simulation with a larger domain (. . .).

grid points).

Appendix C

Stability of the Adaptive Dissipation Scheme

In this appendix, we assess the stability of the high-order dissipation term in (3.16). Following what was done in Chapter 3.2.3.2 (i.e., multiplying (3.16) by u and neglecting advection, the low-order dissipation term, and boundary term that arise after integrating by parts) with $s = 2$, yields

$$\begin{aligned}
&\frac{1}{2}\frac{\mathrm{d}}{\mathrm{d}t}\|u\|^2 = -\int_{-l}^{l}(1-\psi)u\frac{\partial^4 u}{\partial x^4}\,\mathrm{d}x = \\
&-\int_{-l}^{l}\left(\frac{\partial^2 u}{\partial x^2}\right)^2\,\mathrm{d}x + \int_{-l}^{l}\frac{\partial^2 \psi u}{\partial x^2}\frac{\partial^2 u}{\partial x^2}\,\mathrm{d}x = \\
&-\int_{-l}^{l}\left(\frac{\partial^2 u}{\partial x^2}\right)^2\,\mathrm{d}x + \int_{-l}^{l}\psi\left(\frac{\partial^2 u}{\partial x^2}\right)^2\,\mathrm{d}x + 2\int_{-l}^{l}\frac{\partial \psi}{\partial x}\frac{\partial u}{\partial x}\frac{\partial^2 u}{\partial x^2}\,\mathrm{d}x + \int_{-l}^{l}u\frac{\partial^2 \psi}{\partial x^2}\frac{\partial^2 u}{\partial x^2}\,\mathrm{d}x = \\
&-\int_{-l}^{l}(1-\psi)\left(\frac{\partial^2 u}{\partial x^2}\right)^2\,\mathrm{d}x + 2\int_{-l}^{l}\frac{\mathrm{d}\psi}{\mathrm{d}u}\left(\frac{\partial u}{\partial x}\right)^2\frac{\partial^2 u}{\partial x^2}\,\mathrm{d}x + \int_{-l}^{l}u\frac{\mathrm{d}\psi}{\mathrm{d}u}\left(\frac{\partial^2 u}{\partial x^2}\right)^2\,\mathrm{d}x \\
&+\int_{-l}^{l}u\frac{\mathrm{d}^2\psi}{\mathrm{d}u^2}\left(\frac{\partial u}{\partial x}\right)^2\frac{\partial^2 u}{\partial x^2}\,\mathrm{d}x, \qquad \text{(C.1)}
\end{aligned}$$

where it was assumed that $\psi = \psi(u)$. As previously mentioned, the sensor ψ is taken to be combinations of Heaviside functions of u according to (3.13). Without loss of generality, we assume ψ is comprised of a single Heaviside function such that $\mathrm{d}\psi/\mathrm{d}u = \delta(u)$, and $u\mathrm{d}^2\psi/\mathrm{d}u^2 = -\mathrm{d}\psi/\mathrm{d}u$. Thus,

we simplify (C.1) according to

$$\frac{1}{2}\frac{\mathrm{d}}{\mathrm{d}t}\|u\|^2 = -\int_{-l}^{l}(1-\psi)\left(\frac{\partial^2 u}{\partial x^2}\right)^2 \mathrm{d}x + \int_{-l}^{l}\frac{\mathrm{d}\psi}{\mathrm{d}u}\left(\frac{\partial u}{\partial x}\right)^2\frac{\partial^2 u}{\partial x^2}\,\mathrm{d}x + \int_{-l}^{l}u\frac{\mathrm{d}\psi}{\mathrm{d}u}\left(\frac{\partial^2 u}{\partial x^2}\right)^2 \mathrm{d}x. \tag{C.2}$$

The first term on the right-hand side of (C.2) is always non-positive since $0 \leq \psi \leq 1$. Also, if $\mathrm{d}\psi/\mathrm{d}u$ is only non-zero where the value of sensor changes, it would not significantly affect the stability of the system (similar to discussion about stability of the first term on the right-hand side of (3.16) in Chapter 3.2.3.2). A similar procedure could be performed for cases with $s = 3$ and 4.

Appendix D

Theoretical Estimates of Early-Time RT Sensitivity

In Chapter 4.4.2, the adjoint sensitivities of mixing and growth to initial interfacial perturbations were reported for different stages of the RT instability. In this appendix, we employ established theories that describe the early-time RT growth rates to estimate sensitivity and compare with the adjoint solutions. During the DG regime, the flow is dominated by molecular diffusion. During the diffusion dominated regime, the diffusion thickness broadens according to $\sqrt{\delta_D^2 + 4\mathcal{D}t}$ (Duff *et al.*, 1962; Cook & Dimotakis, 2001). In addition, the amplitude of an initial perturbation with wavenumber k at the interface decays in time with an exponential rate of $-k^2\mathcal{D}$ (Duff *et al.*, 1962). With this, the mole fraction evolution in a diffusion dominated flow can be expressed as

$$X(x,y,z,t) \approx \frac{1}{2}\left\{1 + \text{erf}\left[\frac{y - h(x,z,t)}{\sqrt{\delta_D^2 + 4\mathcal{D}t}}\right]\right\}, \tag{D.1}$$

where the evolution of the interface is

$$h(x,z,t) = \sum_{m=1}^{M}\sum_{n=1}^{N} A_{m,n}\cos\left(k_{x,m}x + \theta_{x,m}\right)\cos\left(k_{z,n}z + \theta_{z,n}\right)\exp\left[\sigma_{m,n}t\right]. \tag{D.2}$$

The interfacial growth rate during the diffusion regime is given by

$$\sigma_{m,n}^{(\text{DG})} = -\mathcal{D}(k_{x,m}^2 + k_{z,n}^2), \tag{D.3}$$

where $k_{x,m}$ and $k_{z,n}$ are wavenumbers in the x and z-directions, respectively.

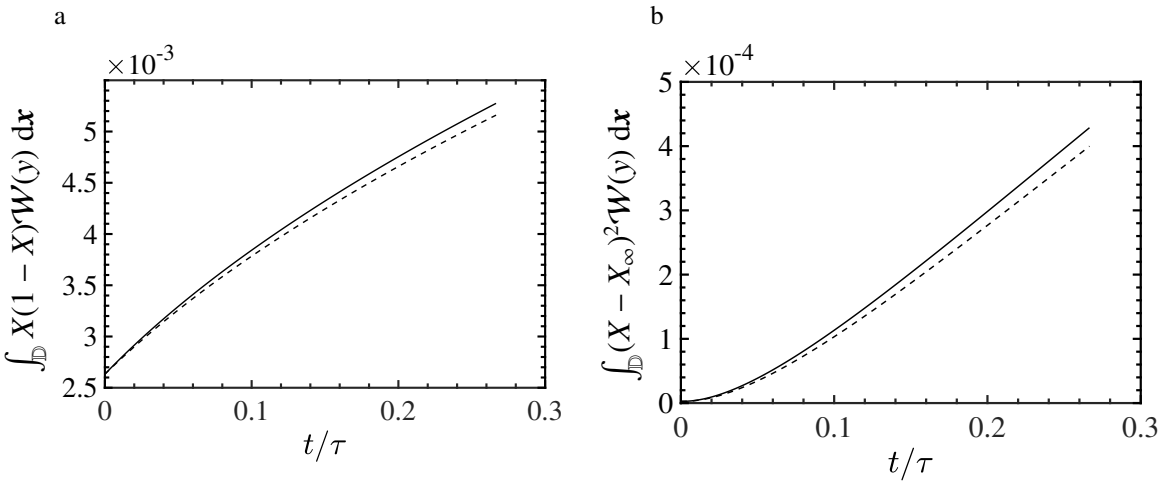

Figure D.1: Temporal evolution of the objective functions of a three-dimensional multi-mode RT instability from the simulation (–) and the model given by (D.1) (−−).

Figure D.1 compares the integral of $\mathcal{IW}(y)$ over the entire domain from the numerical simulations and the model (D.1) for both MIX and VAR. As can be seen, the model solution deviates from the simulation with increasing t. As time increases, the inertial effects of the fluid become more important due to buoyancy, and in this regime, the diffusion model approximation is less robust at capturing these effects. However, as can be seen, the model provides an excellent approximation of the objective functions when $t < 0.2\tau$.

Recalling (4.18), the sensitivity of VAR is obtained by taking its derivative with respect to the initial interfacial amplitudes, given by

$$\frac{\delta\mathcal{J}}{\delta A_{m,n}} = \int_0^{t_f}\int_{\mathbb{D}} 2\frac{\delta X}{\delta A_{m,n}}\,(X-X_\infty)\,\mathcal{W}(y)\,\mathrm{d}\boldsymbol{x}\,\mathrm{d}t, \quad \text{for } \mathcal{J} = \text{VAR}, \tag{D.4}$$

where $\delta X/\delta A_{mn}$ is derived according to (D.1) and (D.2), which yields

$$\frac{\delta X}{\delta A_{m,n}} \approx -\frac{\cos\left(k_{x,m}x+\theta_{x,m}\right)\cos\left(k_{z,n}z+\theta_{z,n}\right)}{\sqrt{\pi\left(\delta_D^2+4\mathcal{D}t\right)}}\exp\left\{-\frac{\left[y-h(x,z)\right]^2}{\delta_D^2+4\mathcal{D}t}+\sigma_{m,n}^{(\mathrm{DG})}t\right\}. \tag{D.5}$$

The VAR sensitivities computed by substituting (D.1) and (D.5) into (D.4) are compared with the adjoint sensitivity for early-time durations (see Fig. D.2a). The sensitivity predicted by the model

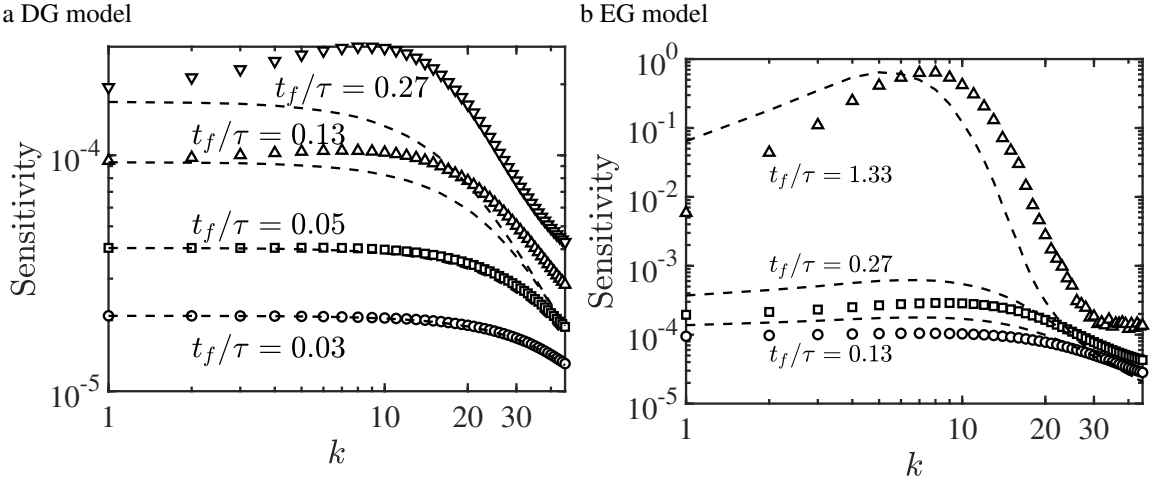

Figure D.2: Magnitude of VAR sensitivity $|\delta\mathcal{J}/\delta\vec{A}|$ integrated over different durations t_f from adjoint simulations (symbols) and the model given by (D.5) (−−) with the growth rate applicable to (*a*) the DG regime, i.e., (D.3) and (*b*) the EG regime, i.e., (4.24). The sensitivities are shown as a function of initial perturbation wavenumber $k = \sqrt{k_x^2 + k_z^2}$.

closely matches the adjoint-based sensitivity at early times and deviates at later times. This effect is more evident at low wavenumbers since they have more substantial growth in the EG regime according to (4.24). In order to include the fluid inertial effects in the model, the diffusion growth rate of the interface $\sigma^{(\mathrm{DG})}$ in (D.2) can be replaced by the exponential growth rate predicted by linear stability theory, i.e., $\sigma^{(\mathrm{EG})}$ given by (4.24) (see Fig. D.2b). Even with these simplifications, the model is able to predict the trends in sensitivity with respect to wavenumber reasonably well.

Similarly, the sensitivity of MIX is obtained by taking derivatives of (4.16) with respect to initial interfacial amplitudes, given by

$$\frac{\delta\mathcal{J}}{\delta A_{m,n}} = \int_0^{t_f}\int_{\mathbb{D}} \frac{\delta X}{\delta A_{m,n}}\,(1-2X)\,\mathcal{W}(y)\,\mathrm{d}\boldsymbol{x}\,\mathrm{d}t, \quad \text{for } \mathcal{J} = \mathrm{MIX}, \tag{D.6}$$

where $\delta X/\delta A_{mn}$ is given by (D.5). However, directly employing the model described in (D.1) results in zero sensitivity. This can be shown by substituting (D.1) and (D.5) into (D.6) and rear-

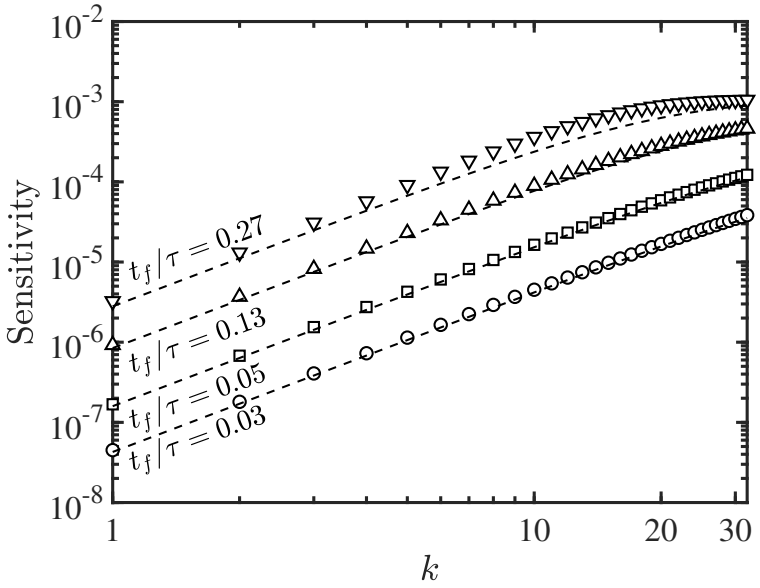

Figure D.3: Sensitivity $\delta\mathcal{J}/\delta\vec{A}$ for $\mathcal{J}$ = MIX integrated over different durations t_f from adjoint simulations (symbols) and model (−−) obtained by (D.6).

ranging, giving

$$\frac{\delta\mathcal{J}}{\delta A_{m,n}} = \int_{t=0}^{t_f} \exp\left[-\mathcal{D}(k_{x,m}^2 + k_{z,n}^2)t\right] \int_{x=-\pi}^{\pi} \cos\left(k_{x,m}x + \theta_{x,m}\right) \int_{z=-\pi}^{\pi} \cos\left(k_{z,n}z + \theta_{z,n}\right)$$
$$\int_{y'=(-2\pi-h)/\sqrt{\delta_D^2+4\mathcal{D}t}}^{(2\pi-h)/\sqrt{\delta_D^2+4\mathcal{D}t}} \exp(-y'^2)\mathrm{erf}(y')\mathcal{W}(y'\Delta(t) + h(x,z,t))\,\mathrm{d}y'\,\mathrm{d}z\,\mathrm{d}x\,\mathrm{d}t, \quad \text{for } \mathcal{J} = \text{MIX}, \tag{D.7}$$

where $y' = y - h(x,z,t)/\sqrt{\delta_D^2 + 4\mathcal{D}t}$. Since h is sufficiently small at early times, the integrand reduces to an odd function with respect to y'. Due to the symmetry of the domain, the resulting integral is null. Alternatively, the sensitivity can be provided via a numerical solution to the following diffusion equation

$$\frac{\partial X}{\partial t} = \mathcal{D}\frac{\partial^2 X}{\partial x_i \partial x_i}, \tag{D.8}$$

where $\mathcal{D}$ denotes the mass diffusivity. This is derived by neglecting fluid inertia and taking the density and molecular weight of the mixture to be constant in ρY equation of (2.2). As shown in

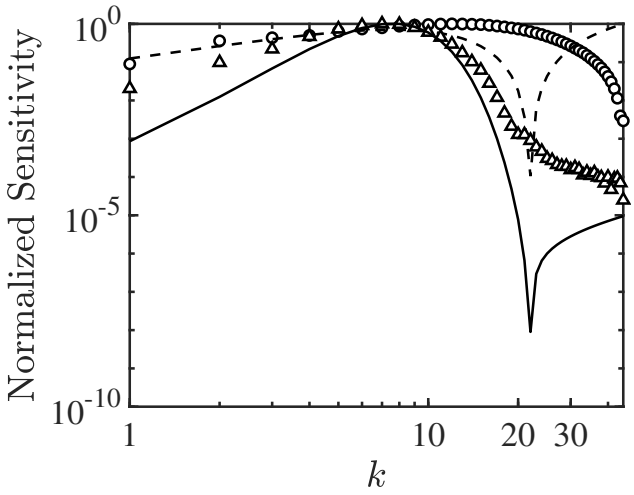

Figure D.4: Magnitude of sensitivity $|\delta\mathcal{J}/\delta\vec{A}|$ for $\mathcal{J}$ = KE integrated over different durations, $t_f = 0.13\tau$ from simulation (◯) and (D.10) (−−) and $t_f = 1.33\tau$ from simulation (△) and (D.10) (–). The sensitivities are shown as a function of initial perturbation wavenumber $k = \sqrt{k_x^2 + k_z^2}$ and normalized by their corresponding maximum value.

Fig. D.3, the resulting sensitivity obtained by solving (D.8) closely matches the adjoint solution. The small differences can be related to assumptions of constant density, diffusivity and molecular weight, and neglecting inertial forces and gravity effects.

It is also possible to find an estimate for the sensitivity of KE with respect to k. Assuming the dominant vertical velocity at early time is located at the interface, the objective function can be rewritten as

$$\text{KE} = \int_0^{t_f}\int_{\mathbb{D}} v^2 \mathcal{W}(y)\,\mathrm{d}\boldsymbol{x}\,\mathrm{d}t \propto \int_0^{t_f}\int_{\mathbb{D}} \left(\frac{\mathrm{d}h}{\mathrm{d}t}\right)^2 \mathcal{W}(y)\,\mathrm{d}\boldsymbol{x}\,\mathrm{d}t. \tag{D.9}$$

Substituting (D.2) into (D.9) and taking the derivative with respect to $A_{m,n}$ yields

$$\frac{\delta\mathcal{J}}{\delta A_{m,n}} \propto A_{m,n}\sigma_{m,n}^{(EG)}\left[\exp\left(2\sigma_{m,n}^{(EG)}t_f\right) - 1\right], \quad \text{for } \mathcal{J} = \text{KE}, \tag{D.10}$$

where the growth rate is estimated from linear stability theory. In (D.9), $\sigma_{m,n}^{(EG)}$ is taken to be time independent even though the EG growth rate (4.24) might vary with time according to Duff *et al.* (1962). As can be seen in Fig. D.4, the model is able to predict the sensitivity behaviour

with respect to wavenumber. The differences between the adjoint sensitivities and the model is attributed to neglecting velocities farther from the interface and also from any errors that might arise in (4.24).

BIBLIOGRAPHY

Aamo, O. M., Krstić, M., & Bewley, T. R. 2003. Control of mixing by boundary feedback in 2D channel flow. *Automatica*, **39**(9), 1597–1606.

Abbas, Q., van der Weide, E., & Nordström, J. 2009. Accurate and stable calculations involving shocks using a new hybrid scheme. *Page 3985 of: 19th AIAA Computational Fluid Dynamics*.

Abbas, Q., van der Weide, E., & Nordström, J. 2010. Energy stability of the MUSCL scheme. *Pages 61–68 of: Numerical Mathematics and Advanced Applications 2009*. Springer.

Abdurakipov, S. S., Dulin, V. M., Markovich, D. M., & Hanjalic, K. 2013. Expanding the stability range of a lifted propane flame by resonant acoustic excitation. *Combustion Science and Technology*, **185**(11), 1644–1666.

Alon, U., Hecht, J., Mukamel, D., & Shvarts, D. 1994. Scale invariant mixing rates of hydrodynamically unstable interfaces. *Physical Review Letters*, **72**(18), 2867.

Anuchina, N. N., Kucherenko, Y. A., Neuvazhaev, V. E., Ogibina, V. N., Shibarshov, L. I., & Yakovlev, V. G. 1978. Turbulent mixing at an accelerating interface between liquids of different density. *Fluid Dynamics*, **13**(6), 916–920.

Babchin, A. J., Frenkel, A. L., Levich, B. G., & Sivashinsky, G. I. 1983. Nonlinear saturation of Rayleigh–Taylor instability in thin films. *Physics of Fluids*, **26**(11), 3159–3161.

Baillot, F., & Demare, D. 2002. Physical mechanisms of a lifted nonpremixed flame stabilized in an acoustic field. *Combustion Science and Technology*, **174**(8), 73–98.

Baillot, F., & Demare, D. 2007. Responses of a lifted non-premixed flame to acoustic forcing. Part 2. *Combustion Science and Technology*, **179**(5), 905–932.

Baker, L., & Freeman, J. R. 1981. Heuristic model of the nonlinear Rayleigh–Taylor instability. *Journal of Applied Physics*, **52**(2), 655–663.

Balachandran, R., Ayoola, B. O., Kaminski, C. F., Dowling, A. P., & Mastorakos, E. 2005. Experimental investigation of the nonlinear response of turbulent premixed flames to imposed inlet velocity oscillations. *Combustion and Flame*, **143**(1-2), 37–55.

Banerjee, A., & Andrews, M. J. 2009. 3D simulations to investigate initial condition effects on the growth of Rayleigh–Taylor mixing. *International Journal of Heat and Mass Transfer*, **52**(17), 3906–3917.

Blonigan, P. J. 2017. Adjoint sensitivity analysis of chaotic dynamical systems with non-intrusive least squares shadowing. *Journal of Computational Physics*, **348**, 803–826.

Bode, M., Collier, N., Bisetti, F., & Pitsch, H. 2019. Adaptive chemistry lookup tables for combustion simulations using optimal B-spline interpolants. *Combustion Theory and Modelling*, **23**(4), 674–699.

Bodony, D. J. 2010. Accuracy of the simultaneous-approximation-term boundary condition for time-dependent problems. *Journal of Scientific Computing*, **43**(1), 118–133.

Braman, K., Oliver, T. A., & Raman, V. 2015. Adjoint-based sensitivity analysis of flames. *Combustion Theory and Modelling*, **19**(1), 29–56.

Brenner, M. P., Eldredge, J. D., & Freund, J. B. 2019. Perspective on machine learning for advancing fluid mechanics. *Physical Review Fluids*, **4**(10), 100501.

Cabot, W. 2006. Comparison of two-and three-dimensional simulations of miscible Rayleigh–Taylor instability. *Physics of Fluids*, **18**(4), 045101.

Cabot, W. H., & Cook, A. W. 2006. Reynolds number effects on Rayleigh–Taylor instability with possible implications for type-Ia supernovae. *Nature Physics*, **2**(8), 562–568.

Capecelatro, J., Vishnampet, R., Bodony, D. J., & Freund, J. B. 2016. Adjoint-based sensitivity analysis of localized ignition in a non-premixed hydrogen-air mixing layer. *Page 2153 of: 54th AIAA Aerospace Sciences Meeting*.

Capecelatro, J., Bodony, D. J., & Freund, J. B. 2017. Adjoint-based sensitivity analysis of ignition in a turbulent reactive shear layer. *Page 0846 of: 55th AIAA Aerospace Sciences Meeting*.

Capecelatro, J., Bodony, D. J., & Freund, J. B. 2018. Adjoint-based sensitivity and ignition threshold mapping in a turbulent mixing layer. *Combustion Theory and Modelling*, 1–33.

Carles, P., Huang, Z., Carbone, G., & Rosenblatt, C. 2006. Rayleigh–Taylor instability for immiscible fluids of arbitrary viscosities: A magnetic levitation investigation and theoretical model. *Physical Review Letters*, **96**(10), 104501.

Carnarius, A., Thiele, F., Oezkaya, E., & Gauger, N. R. 2010. Adjoint approaches for optimal flow control. *AIAA Paper*, **5088**, 2010.

Carpenter, M. H., Gottlieb, D., & Abarbanel, S. 1994. Time-stable boundary conditions for finite-difference schemes solving hyperbolic systems: Methodology and application to high-order compact schemes. *Journal of Computational Physics*, **111**(2), 220–236.

Cattafesta III, L. N., & Sheplak, M. 2011. Actuators for active flow control. *Annual Review of Fluid Mechanics*, **43**, 247–272.

Chandrasekhar, S. 1961. *Hydrodynamic and hydromagnetic stability*. International Series of Monographs on Physics. Clarendon Press.

Chao, Y. C., Yuan, T., & Tseng, C. S. 1996. Effects of flame lifting and acoustic excitation on the reduction of nox emissions. *Combustion Science and Technology*, **113**(1), 49–65.

Chao, Y. C., Wu, C. Y., Yuan, T., & Cheng, T. S. 2002. Stabilization process of a lifted flame tuned by acoustic excitation. *Combustion Science and Technology*, **174**(5-6), 87–110.

Chung, S. W., & Freund, J. B. 2021. An optimization method for chaotic turbulent flow. *Available at SSRN 3954911*.

Cimpeanu, R., Papageorgiou, D. T., & Petropoulos, P. G. 2014. On the control and suppression of the Rayleigh–Taylor instability using electric fields. *Physics of Fluids*, **26**(2), 022105.

Cook, A. W. 2007. Artificial fluid properties for large-eddy simulation of compressible turbulent mixing. *Physics of Fluids*, **19**(5), 055103.

Cook, A. W. 2009. Enthalpy diffusion in multicomponent flows. *Physics of Fluids*, **21**(5), 055109.

Cook, A. W., & Dimotakis, P. E. 2001. Transition stages of Rayleigh–Taylor instability between miscible fluids. *Journal of Fluid Mechanics*, **443**, 69–99.

Cook, A. W., Riley, J. J., & Kosály, G. 1997. A laminar flamelet approach to subgrid-scale chemistry in turbulent flows. *Combustion and Flame*, **109**(3), 332–341.

Craig P., David A., & Zingg, D. W. 2018. High-order artificial dissipation operators possessing the summation-by-parts property. *Page 4165 of: 2018 Fluid Dynamics Conference*.

Cuenot, B, & Poinsot, T. 1996. Asymptotic and numerical study of diffusion flames with variable Lewis number and finite rate chemistry. *Combustion and Flame*, **104**(1-2), 111–137.

da Silva, C. B., & Métais, O. 2001. *Coherent structures in excited spatially evolving round jets*. Dordrecht: Springer Netherlands. Pages 205–212.

da Silva, C. B., & Métais, O. 2002. Vortex control of bifurcating jets: a numerical study. *Physics of Fluids*, **14**(11), 3798–3819.

Demare, D., & Baillot, F. 2004. Acoustic enhancement of combustion in lifted nonpremixed jet flames. *Combustion and Flame*, **139**(4), 312–328.

Diener, P., Dorband, E. N., Schnetter, E., & Tiglio, M. 2007. Optimized high-order derivative and dissipation operators satisfying summation by parts, and applications in three-dimensional multi-block evolutions. *Journal of Scientific Computing*, **32**(1), 109–145.

Dimonte, G. 2004. Dependence of turbulent Rayleigh–Taylor instability on initial perturbations. *Physical Review E*, **69**(5), 056305.

Dimonte, G., Youngs, D. L., Dimits, A., Weber, S., Marinak, M., Wunsch, S., Garasi, C., Robinson, A., Andrews, M. J., Ramaprabhu, P., *et al.*. 2004. A comparative study of the turbulent Rayleigh–Taylor instability using high-resolution three-dimensional numerical simulations: the Alpha-Group collaboration. *Physics of Fluids*, **16**(5), 1668–1693.

Docquier, N., & Candel, S. 2002. Combustion control and sensors: A review. *Progress in energy and combustion science*, **28**(2), 107–150.

Dowling, A. P., & Morgans, A. S. 2005. Feedback control of combustion oscillations. *Annual Review of Fluid Mechanics*, **37**, 151–182.

Dowling, D. R., & Dimotakis, P. E. 1990. Similarity of the concentration field of gas-phase turbulent jets. *Journal of Fluid Mechanics*, **218**, 109–141.

Ducros, F., Ferrand, V., Nicoud, F., Weber, C., Darracq, D., Gacherieu, C., & Poinsot, T. 1999. Large-eddy simulation of the shock/turbulence interaction. *Journal of Computational Physics*, **152**(2), 517–549.

Duff, R. E., Harlow, F. H., & Hirt, C. W. 1962. Effects of diffusion on interface instability between gases. *Physics of Fluids*, **5**(4), 417–425.

Duraisamy, K. 2021. Perspectives on machine learning-augmented Reynolds-averaged and large eddy simulation models of turbulence. *Physical Review Fluids*, **6**(5), 050504.

Duraisamy, K., & Alonso, J. 2012. Adjoint based techniques for uncertainty quantification in turbulent flows with combustion. *Page 2711 of: 42nd AIAA Fluid Dynamics Conference and Exhibit*.

Duraisamy, K., Iaccarino, G., & Xiao, H. 2019. Turbulence modeling in the age of data. *Annual Review of Fluid Mechanics*, **51**, 357–377.

Ebi, D., & Clemens, N. T. 2016. Experimental investigation of upstream flame propagation during boundary layer flashback of swirl flames. *Combustion and Flame*, **168**, 39–52.

Eriksson, S., & Nordström, J. 2018. Finite difference schemes with transferable interfaces for parabolic problems. *Journal of Computational Physics*, **375**, 935–949.

Eriksson, S., Abbas, Q., & Nordström, J. 2011. A stable and conservative method for locally adapting the design order of finite difference schemes. *Journal of Computational Physics*, **230**(11), 4216–4231.

Eyink, G. L., Haine, T. W. N., & Lea, D. J. 2004. Ruelle's linear response formula, ensemble adjoint schemes and Lévy flights. *Nonlinearity*, **17**(5), 1867.

Fedkiw, R. P., Merriman, B., & Osher, S. 1997. High accuracy numerical methods for thermally perfect gas flows with chemistry. *Journal of Computational Physics*, **132**(2), 175–190.

Fernández, D. C., Hicken, J. E., & Zingg, D. W. 2014. Review of summation-by-parts operators with simultaneous approximation terms for the numerical solution of partial differential equations. *Computers and Fluids*, **95**, 171–196.

Foures, D. P. G., Dovetta, N., Sipp, D., & Schmid, P. J. 2014a. A data-assimilation method for Reynolds-averaged Navier–Stokes-driven mean flow reconstruction. *Journal of Fluid Mechanics*, **759**, 404–431.

Foures, D. P. G., Caulfield, C. P., & Schmid, P. J. 2014b. Optimal mixing in two-dimensional plane Poiseuille flow at finite Péclet number. *Journal of Fluid Mechanics*, **748**, 241–277.

Freund, J. B. 1997. Proposed inflow/outflow boundary condition for direct computation of aerodynamic sound. *AIAA Journal*, **35**(4), 740–742.

Fujimoto, M. Y. 1993. The evolution of accreting stars with turbulent mixing. *The Astrophysical Journal*, **419**, 768.

Goncharov, V. N. 2002. Analytical model of nonlinear, single-mode, classical Rayleigh–Taylor instability at arbitrary atwood numbers. *Physical Review Letters*, **88**(13), 134502.

Gray, J. A. T., Lemke, M., Reiss, J., Paschereit, C. O., Sesterhenn, J., & Moeck, J. P. 2017. A compact shock-focusing geometry for detonation initiation: Experiments and adjoint-based variational data assimilation. *Combustion and Flame*, **183**, 144–156.

Haan, S. W. 1989. Onset of nonlinear saturation for Rayleigh–Taylor growth in the presence of a full spectrum of modes. *Physical Review A*, **39**(11), 5812.

Halpern, D., & Frenkel, A. L. 2001. Saturated Rayleigh–Taylor instability of an oscillating Couette film flow. *Journal of Fluid Mechanics*, **446**, 67–93.

Hardalupas, Y., & Selbach, A. 2002. Imposed oscillations and non-premixed flames. *Progress in Energy and Combustion Science*, **28**(1), 75–104.

Harten, A. 1978. The artificial compression method for computation of shocks and contact discontinuities. III. Self-adjusting hybrid schemes. *Mathematics of Computation*, **32**(142), 363–389.

Hassan, A., Sayadi, T., Le Chenadec, V., Pitsch, H., & Attili, A. 2021. Adjoint-based sensitivity analysis of steady char burnout. *Combustion Theory and Modelling*, **25**(1), 96–120.

Hecht, J., Alon, U., & Shvarts, D. 1994. Potential flow models of Rayleigh–Taylor and Richtmyer–Meshkov bubble fronts. *Physics of fluids*, **6**(12), 4019–4030.

Herrmann, M., Blanquart, G., & Raman, V. 2006. Flux corrected finite volume scheme for preserving scalar boundedness in reacting large-eddy simulations. *AIAA journal*, **44**(12), 2879–2886.

Hicken, J. E., & Zingg, D. W. 2011. Superconvergent functional estimates from summation-by-parts finite-difference discretizations. *SIAM Journal on Scientific Computing*, **33**(2), 893–922.

Hicken, J. E., & Zingg, D. W. 2014. Dual consistency and functional accuracy: A finite-difference perspective. *Journal of Computational Physics*, **256**, 161–182.

Huang, Z., De Luca, A., Atherton, T. J., Bird, M., Rosenblatt, C., & Carlès, P. 2007. Rayleigh–Taylor instability experiments with precise and arbitrary control of the initial interface shape. *Physical Review Letters*, **99**(20), 204502.

Ihme, M., & Pitsch, H. 2008a. Modeling of radiation and nitric oxide formation in turbulent nonpremixed flames using a flamelet/progress variable formulation. *Physics of Fluids*, **20**(5), 055110.

Ihme, M., & Pitsch, H. 2008b. Prediction of extinction and reignition in nonpremixed turbulent flames using a flamelet/progress variable model: 1. A priori study and presumed PDF closure. *Combustion and Flame*, **155**(1), 70–89.

Ihme, M., & Pitsch, H. 2008c. Prediction of extinction and reignition in nonpremixed turbulent flames using a flamelet/progress variable model: 2. Application in LES of Sandia flames D and E. *Combustion and Flame*, **155**(1), 90–107.

Jameson, A. 1989. Aerodynamic design via control theory. *Pages 377–401 of: Recent Advances in Computational Fluid Dynamics*. Springer.

Jameson, A., & Martinelli, L. 2000. Aerodynamic shape optimization techniques based on control theory. *Pages 151–221 of: Computational Mathematics Driven by Industrial Problems*. Springer.

Jameson, A., Schmidt, W., & Turkel, E. 1981. Numerical solution of the Euler equations by finite volume methods using Runge Kutta time stepping schemes. *Page 1259 of: 14th Fluid and Plasma Dynamics Conference*.

Janka, H. T., & Müller, E. 1996. Neutrino heating, convection, and the mechanism of type-II supernova explosions. *Astronomy and Astrophysics*, **306**, 167.

Jankee, G. K., & Ganapathisubramani, B. 2021. Interaction and vectoring of parallel rectangular twin jets in a turbulent boundary layer. *Physical Review Fluids*, **6**(4), 044701.

Jiang, G. S., & Shu, C. W. 1996. Efficient implementation of weighted ENO schemes. *Journal of Computational Physics*, **126**(1), 202–228.

Johnsen, E., Larsson, J., Bhagatwala, A. V., Cabot, W. H., Moin, P., Olson, B. J., Rawat, P. S., Shankar, S. K., Sjögreen, B., Yee, H. C., *et al.*. 2010. Assessment of high-resolution methods for numerical simulations of compressible turbulence with shock waves. *Journal of Computational Physics*, **229**(4), 1213–1237.

Jones, E., Oliphant, T., & Peterson, P. 2001. *SciPy: Open source scientific tools for Python*. http://www.scipy.org/.

Kawai, S., & Lele, S. K. 2008. Localized artificial diffusivity scheme for discontinuity capturing on curvilinear meshes. *Journal of Computational Physics*, **227**(22), 9498–9526.

Klein, M., Sadiki, A., & Janicka, J. 2003. A digital filter based generation of inflow data for spatially developing direct numerical or large eddy simulations. *Journal of Computational Physics*, **186**(2), 652–665.

Kolla, H., & Chen, J. H. 2018. *Turbulent combustion simulations with high-performance computing*. Singapore: Springer Singapore. Pages 73–97.

Kord, A., & Capecelatro, J. 2019. Optimal perturbations for controlling the growth of a Rayleigh–Taylor instability. *Journal of Fluid Mechanics*, **876**, 150–185.

Kord, A., & Capecelatro, J. 2021. Adaptive energy stable artificial dissipation for preserving scalar boundedness in turbulent flows. *Journal of Computational Physics*, **Submitted**.

Kord, A., & Capecelatro, J. 2022. A discrete-adjoint framework for optimizing high-fidelity simulations of turbulent reacting flows. *Proceedings of the Combustion Institute*, **Submitted**.

Kozlov, V. V., Grek, G. R., Katasonov, M. M., Korobeinichev, O. P., Litvinenko, Y. A., & Shmakov, A. G. 2013. Stability of subsonic microjet flows and combustion. *Journal of Flow Control, Measurement and Visualization*, **1**(3), 108–111.

Kraft, D. 1988. A software package for sequential quadratic programming. *Forschungsbericht-Deutsche Forschungs- und Versuchsanstalt fur Luft- und Raumfahrt*.

Kral, L. D. 2000. Active flow control technology. *ASME Fluids Engineering Technical Brief*.

Kreiss, H. O., & Scherer, G. 1974. Finite element and finite difference methods for hyperbolic partial differential equations. *Pages 195–212 of: Mathematical aspects of finite elements in partial differential equations*. Elsevier.

Larsson, J., Lele, S. K., & Moin, P. 2007. Effect of numerical dissipation on the predicted spectra for compressible turbulence. *Annual Research Briefs*, 47–57.

Layzer, D. 1955. On the instability of superposed fluids in a gravitational field. *Astrophysical Journal*, **122**, 1.

Le Dimet, F. X., & Talagrand, O. 1986. Variational algorithms for analysis and assimilation of meteorological observations: theoretical aspects. *Tellus A: Dynamic Meteorology and Oceanography*, **38**(2), 97–110.

Lea, D. J., Allen, M. R., & Haine, T. W. N. 2000. Sensitivity analysis of the climate of a chaotic system. *Tellus A: Dynamic Meteorology and Oceanography*, **52**(5), 523–532.

Lea, D. J., Haine, T. W. N., Allen, M. R., & Hansen, J. A. 2002. Sensitivity analysis of the climate of a chaotic ocean circulation model. *Quarterly Journal of the Royal Meteorological Society: A journal of the atmospheric sciences, applied meteorology and physical oceanography*, **128**(586), 2587–2605.

Lemke, M., & Sesterhenn, J. 2016. Adjoint-based pressure determination from PIV data in compressible flows – Validation and assessment based on synthetic data. *European Journal of Mechanics B/Fluids*, **58**, 29–38.

Lemke, M., Reiss, J., & Sesterhenn, J. 2014. Adjoint based optimisation of reactive compressible flows. *Combustion and Flame*, **161**(10), 2552–2564.

Lewis, B., & von Elbe, G. 1943. Stability and structure of burner flames. *The Journal of Chemical Physics*, **11**(2), 75–97.

Li, J., Zhao, Z., Kazakov, A., & Dryer, F. L. 2004. An updated comprehensive kinetic model of hydrogen combustion. *International Journal of Chemical Kinetics*, **36**(10), 566–575.

Lindl, J. 1995. Development of the indirect-drive approach to inertial confinement fusion and the target physics basis for ignition and gain. *Physics of Plasmas (1994-present)*, **2**(11), 3933–4024.

Liu, W. 2006. Mixing enhancement via flow optimization. *Pages 5323–5328 of: Decision and Control, 2006 45th IEEE Conference on*. IEEE.

Livescu, D. 2004. Compressibility effects on the Rayleigh–Taylor instability growth between immiscible fluids. *Physics of Fluids*, **16**(1), 118–127.

Livescu, D. 2013. Numerical simulations of two-fluid turbulent mixing at large density ratios and applications to the Rayleigh–Taylor instability. *Philosophical Transactions of the Royal Society of London A: Mathematical, Physical and Engineering Sciences*, **371**(2003), 20120185.

Livescu, D., Wei, T., & Petersen, M. R. 2011. Direct numerical simulations of Rayleigh–Taylor instability. *Page 082007 of: Journal of Physics: Conference Series*, vol. 318. IOP Publishing.

Lopez-Zazueta, A., Fontane, J., & Joly, L. 2016. Optimal perturbations in time-dependent variable-density Kelvin–Helmholtz billows. *Journal of Fluid Mechanics*, **803**, 466–501.

MacArt, J. F., Sirignano, J., & Freund, J. B. 2021. Embedded training of neural-network subgrid-scale turbulence models. *Physical Review Fluids*, **6**(5), 050502.

Markides, C. N., & Mastorakos, E. 2005. An experimental study of hydrogen autoignition in a turbulent co-flow of heated air. *Proceedings of the Combustion Institute*, **30**(1), 883–891.

Martins, J. R. R. A., & Ning, A. 2021. *Engineering design optimization*. Cambridge University Press.

Martins, J. R. R. A., Kroo, I. M., & Alonso, J. J. 2000. An automated method for sensitivity analysis using complex variables. *Page 689 of: 38th Aerospace Sciences Meeting and Exhibit*.

Martins, J. R. R. A., Sturdza, P., & Alonso, J. J. 2001. The connection between the complex-step derivative approximation and algorithmic differentiation. *Page 921 of: 39th Aerospace Sciences Meeting and Exhibit*.

Martins, J. R. R. A., Sturdza, P., & Alonso, J. J. 2003. The complex-step derivative approximation. *ACM Transactions on Mathematical Software (TOMS)*, **29**(3), 245–262.

Martins, J. R. R. A., Alonso, J. J., & Reuther, J. J. 2004. High-fidelity aerostructural design optimization of a supersonic business jet. *Journal of Aircraft*, **41**(3), 523–530.

Matheou, G., & Dimotakis, P. E. 2016. Scalar excursions in large-eddy simulations. *Journal of Computational Physics*, **327**, 97–120.

Mathew, G., Mezić, I., & Petzold, L. 2005. A multiscale measure for mixing. *Physica D: Nonlinear Phenomena*, **211**(1-2), 23–46.

Mathew, G., Mezić, I., Grivopoulos, S., Vaidya, U., & Petzold, L. 2007. Optimal control of mixing in stokes fluid flows. *Journal of Fluid Mechanics*, **580**, 261–281.

Mattsson, K. 2017. Diagonal-norm upwind SBP operators. *Journal of Computational Physics*, **335**, 283–310.

Mattsson, K., Svärd, M., & Nordström, J. 2004. Stable and accurate artificial dissipation. *Journal of Scientific Computing*, **21**(1), 57–79.

Mattsson, K., Svärd, M., Carpenter, M., & Nordström, J. 2007. High-order accurate computations for unsteady aerodynamics. *Computers and Fluids*, **36**(3), 636–649.

McManus, K. R., Poinsot, T., & Candel, S. M. 1993. A review of active control of combustion instabilities. *Progress in energy and combustion science*, **19**(1), 1–29.

Michalke, A. 1984. Survey on jet instability theory. *Progress in Aerospace Sciences*, **21**, 159–199.

Miles, C. J. 2018. *Optimal control of the advection-diffusion equation for effective fluid mixing*. Ph.D. thesis, University of Michigan.

Millman, K. J., & Aivazis, M. 2011. Python for scientists and engineers. *Computing in Science and Engineering*, **13**(2), 9–12.

Monkewitz, P. A., & Sohn, K. D. 1988. Absolute instability in hot jets. *AIAA Journal*, **26**(8), 911–916.

Morris, P. J. 1976. The spatial viscous instability of axisymmetric jets. *Journal of Fluid Mechanics*, **77**(3), 511–529.

Movahed, P. 2014. *High-fidelity numerical simulations of compressible turbulence and mixing generated by hydrodynamic instabilities*. Ph.D. thesis, University of Michigan.

Mueller, M. E., & Pitsch, Heinz. 2012. LES model for sooting turbulent nonpremixed flames. *Combustion and Flame*, **159**(6), 2166–2180.

Nadarajah, S., & Jameson, A. 2000. A comparison of the continuous and discrete adjoint approach to automatic aerodynamic optimization. *Page 667 of: 38th Aerospace Sciences Meeting and Exhibit*.

Nadarajah, S., & Jameson, A. 2001. Studies of the continuous and discrete adjoint approaches to viscous automatic aerodynamic shape optimization. *Page 2530 of: 15th AIAA Computational Fluid Dynamics Conference*.

Nakai, S., & Takabe, H. 1996. Principles of inertial confinement fusion-physics of implosion and the concept of inertial fusion energy. *Reports on Progress in Physics*, **59**(9), 1071.

Ni, A., & Talnikar, C. 2019. Adjoint sensitivity analysis on chaotic dynamical systems by non-intrusive least squares adjoint shadowing (NILSAS). *Journal of Computational Physics*, **395**, 690–709.

Nichols, J. W., & Schmid, P. J. 2008. The effect of a lifted flame on the stability of round fuel jets. *Journal of Fluid Mechanics*, **609**, 275–284.

Nichols, J. W., Schmid, P. J., & Riley, J. J. 2007. Self-sustained oscillations in variable-density round jets. *Journal of Fluid Mechanics*, **582**, 341–376.

Nordström, J. 2006. Conservative finite difference formulations, variable coefficients, energy estimates and artificial dissipation. *Journal of Scientific Computing*, **29**(3), 375–404.

Nordström, J., Gong, J., van der Weide, E., & Svärd, M. 2009. A stable and conservative high order multi-block method for the compressible Navier–Stokes equations. *Journal of Computational Physics*, **228**(24), 9020–9035.

Oliphant, T. E. 2007. Python for scientific computing. *Computing in Science and Engineering*, **9**(3), 10–20.

Oron, D., Arazi, L., Kartoon, D., Rikanati, A., Alon, U., & Shvarts, D. 2001. Dimensionality dependence of the Rayleigh–Taylor and Richtmyer–Meshkov instability late-time scaling laws. *Physics of Plasmas*, **8**(6), 2883–2889.

Panchapakesan, N. R., & Lumley, J. L. 1993. Turbulence measurements in axisymmetric jets of air and helium. Part 1. Air jet. *Journal of Fluid Mechanics*, **246**, 197–223.

Paschereit, C. O., Gutmark, E., & Weisenstein, W. 1999. Coherent structures in swirling flows and their role in acoustic combustion control. *Physics of Fluids*, **11**(9), 2667–2678.

Peters, N. 1983. Local quenching due to flame stretch and non-premixed turbulent combustion. *Combustion Science and Technology*, **30**(1-6), 1–17.

Peters, N. 1984. Laminar diffusion flamelet models in non-premixed turbulent combustion. *Progress in Energy and Combustion Science*, **10**(3), 319–339.

Peters, N. 1986. Laminar flamelet concepts in turbulent combustion. *Pages 1231–1250 of: 21th Symposium (International) on Combustion/The Combustion Institute*.

Peters, N. 2000. *Turbulent Combustion*. Cambridge University Press.

Pierce, C. D. 2001. *Progress-variable approach for large-eddy simulation of turbulent combustion*. Ph.D. thesis, Stanford University.

Pierce, C. D., & Moin, P. 1998. A dynamic model for subgrid-scale variance and dissipation rate of a conserved scalar. *Physics of Fluids*, **10**(12), 3041–3044.

Pierce, C. D., & Moin, P. 2004. Progress-variable approach for large-eddy simulation of non-premixed turbulent combustion. *Journal of Fluid Mechanics*, **504**, 73–97.

Piro, A. L., & Bildsten, L. 2007. Turbulent mixing in the surface layers of accreting neutron stars. *The Astrophysical Journal*, **663**(2), 1252.

Pitsch, H. 1998. Flamemaster v4. 1: A C++ computer program for 0D combustion and 1D laminar flame calculations. *available from https://web.stanford.edu/group/pitsch/FlameMaster.htm*.

Pitsch, H. 2000. Unsteady flamelet modeling of differential diffusion in turbulent jet diffusion flames. *Combustion and Flame*, **123**(3), 358–374.

Pitsch, H. 2006. Large-eddy simulation of turbulent combustion. *Annual Review of Fluid Mechanics*, **38**, 453–482.

Pitsch, H., & Steiner, H. 2000. Large-eddy simulation of a turbulent piloted methane/air diffusion flame (Sandia flame D). *Physics of Fluids*, **12**(10), 2541–2554.

Pitsch, H., Chen, M., & Peters, N. 1998. Unsteady flamelet modeling of turbulent hydrogen-air diffusion flames. *Pages 1057–1064 of: Symposium (International) on Combustion*, vol. 27. Elsevier.

Poinsot, T., & Veynante, D. 2005. *Theoretical and Numerical Combustion*. RT Edwards, Inc.

Poinsot, T., Veynante, D., & Candel, S. 1991. Quenching processes and premixed turbulent combustion diagrams. *Journal of Fluid Mechanics*, **228**, 561–606.

Pope, S. B. 2000. *Turbulent flows*. Cambridge University Press.

Pulliam, T. H., & Chaussee, D. S. 1981. A diagonal form of an implicit approximate-factorization algorithm. *Journal of Computational Physics*, **39**(2), 347–363.

Qadri, U. A., Chandler, G. J., & Juniper, M. P. 2015. Self-sustained hydrodynamic oscillations in lifted jet diffusion flames: origin and control. *Journal of Fluid Mechanics*, **775**, 201–222.

Qadri, U. A., Magri, L., Ihme, M., & Schmid, P. J. 2021. Using adjoint-based optimization to enhance ignition in non-premixed jets. *Proceedings of the Royal Society A*, **477**(2245), 20200472.

Ramaprabhu, P., Dimonte, G., & Andrews, M. J. 2005. A numerical study of the influence of initial perturbations on the turbulent Rayleigh–Taylor instability. *Journal of Fluid Mechanics*, **536**, 285–319.

Ranocha, H., Glaubitz, J., Öffner, P., & Sonar, T. 2018. Stability of artificial dissipation and modal filtering for flux reconstruction schemes using summation-by-parts operators. *Applied Numerical Mathematics*, **128**, 1–23.

Read, K. I. 1984. Experimental investigation of turbulent mixing by Rayleigh–Taylor instability. *Physica D: Nonlinear Phenomena*, **12**(1-3), 45–58.

Reckinger, S. J., Livescu, D., & Vasilyev, O. V. 2016. Comprehensive numerical methodology for direct numerical simulations of compressible Rayleigh–Taylor instability. *Journal of Computational Physics*, **313**, 181–208.

Ren, Y. X., Liu, M., & Zhang, H. 2003. A characteristic-wise hybrid compact-WENO scheme for solving hyperbolic conservation laws. *Journal of Computational Physics*, **192**(2), 365–386.

Ristorcelli, J. R., & Clark, T. T. 2004. Rayleigh–Taylor turbulence: self-similar analysis and direct numerical simulations. *Journal of Fluid Mechanics*, **507**, 213–253.

Roberts, M. S., & Jacobs, J. W. 2016. The effects of forced small-wavelength, finite-bandwidth initial perturbations and miscibility on the turbulent Rayleigh–Taylor instability. *Journal of Fluid Mechanics*, **787**, 50–83.

Saghafian, A., Terrapon, V. E., & Pitsch, H. 2015. An efficient flamelet-based combustion model for compressible flows. *Combustion and Flame*, **162**(3), 652–667.

Sayadi, T., & Schmid, P. J. 2021. Frequency response analysis of a (non-)reactive jet in crossflow. *Journal of Fluid Mechanics*, **922**.

Schadow, K. C., & Gutmark, E. 1992. Combustion instability related to vortex shedding in dump combustors and their passive control. *Progress in Energy and Combustion Science*, **18**(2), 117–132.

Schmitt, M., Frouzakis, C. E., Wright, Y. M., Tomboulides, A. G., & Boulouchos, K. 2016. Investigation of wall heat transfer and thermal stratification under engine-relevant conditions using DNS. *International Journal of Engine Research*, **17**(1), 63–75.

Sharan, N., Matheou, G., & Dimotakis, P. E. 2018. Mixing, scalar boundedness, and numerical dissipation in large-eddy simulations. *Journal of Computational Physics*, **369**, 148–172.

Sharp, D. H. 1984. An overview of Rayleigh–Taylor instability. *Physica D: Nonlinear Phenomena*, **12**(1), 3–18.

Singh, A. P., Medida, S., & Duraisamy, K. 2017. Machine-learning-augmented predictive modeling of turbulent separated flows over airfoils. *AIAA Journal*, 2215–2227.

Sirignano, J., MacArt, J. F., & Freund, J. B. 2020. DPM: A deep learning PDE augmentation method with application to large-eddy simulation. *Journal of Computational Physics*, **423**, 109811.

Sirkes, Z., & Tziperman, E. 1997. Finite difference of adjoint or adjoint of finite difference? *Monthly Weather Review*, **125**(12), 3373–3378.

Skene, C. S., & Schmid, P. J. 2019. Adjoint-based parametric sensitivity analysis for swirling M-flames. *Journal of Fluid Mechanics*, **859**, 516–542.

Skene, C. S., Eggl, M. F., & Schmid, P. J. 2021. A parallel-in-time approach for accelerating direct-adjoint studies. *Journal of Computational Physics*, **429**, 110033.

Smith, B. L., & Glezer, A. 1998. The formation and evolution of synthetic jets. *Physics of fluids*, **10**(9), 2281–2297.

Squire, W., & Trapp, G. 1998. Using complex variables to estimate derivatives of real functions. *SIAM review*, **40**(1), 110–112.

Strand, B. 1994. Summation by parts for finite difference approximations for d/dx. *Journal of Computational Physics*, **110**(1), 47–67.

Subbareddy, P. K., Kartha, A., & Candler, G. V. 2017. Scalar conservation and boundedness in simulations of compressible flow. *Journal of Computational Physics*, **348**, 827–846.

Svärd, M. 2004. On coordinate transformations for summation-by-parts operators. *Journal of Scientific Computing*, **20**(1), 29–42.

Svärd, M., & Mishra, S. 2009. Shock capturing artificial dissipation for high-order finite difference schemes. *Journal of Scientific Computing*, **39**(3), 454–484.

Svärd, M., & Nordström, J. 2008. A stable high-order finite difference scheme for the compressible Navier–Stokes equations: No-slip wall boundary conditions. *Journal of Computational Physics*, **227**(10), 4805–4824.

Svärd, M., Mattsson, K., & Nordström, J. 2005. Steady-state computations using summation-by-parts operators. *Journal of Scientific Computing*, **24**(1), 79–95.

Svärd, M., Carpenter, M. H., & Nordström, J. 2007. A stable high-order finite difference scheme for the compressible Navier–Stokes equations, far-field boundary conditions. *Journal of Computational Physics*, **225**(1), 1020–1038.

Thiffeault, J. L. 2012. Using multiscale norms to quantify mixing and transport. *Nonlinearity*, **25**(2), R1.

Thuburn, J. 2005. Climate sensitivities via a Fokker–Planck adjoint approach. *Quarterly Journal of the Royal Meteorological Society*, **131**(605), 73–92.

Trevisan, A., & Legnani, R. 1995. Transient error growth and local predictability: A study in the Lorenz system. *Tellus A*, **47**(1), 103–117.

Tyliszczak, A. 2015a. LES–CMC study of an excited hydrogen flame. *Combustion and Flame*, **162**(10), 3864–3883.

Tyliszczak, A. 2015b. Multi-armed jets: A subset of the blooming jets. *Physics of Fluids*, **27**(4), 041703.

Tyliszczak, A. 2018. Parametric study of multi-armed jets. *International Journal of Heat and Fluid Flow*, **73**, 82–100.

Tyliszczak, A., & Geurts, B. J. 2014. Parametric analysis of excited round jets-numerical study. *Flow, Turbulence and Combustion*, **93**(2), 221–247.

Tyliszczak, A., Boguslawski, A., & Nowak, D. 2016. Numerical simulations of combustion process in a gas turbine with a single and multi-point fuel injection system. *Applied Energy*, **174**, 153–165.

van Oijen, J. A., Lammers, F. A., & de Goey, L. P. H. 2001. Modeling of complex premixed burner systems by using flamelet-generated manifolds. *Combustion and Flame*, **127**(3), 2124–2134.

Vermach, L., & Caulfield, C. P. 2018. Optimal mixing in three-dimensional plane Poiseuille flow at high Péclet number. *Journal of Fluid Mechanics*, **850**, 875–923.

Vervisch, L., & Poinsot, T. 1998. Direct numerical simulation of non-premixed turbulent flames. *Annual Review of Fluid Mechanics*, **30**(1), 655–691.

Vikhansky, A. 2002. Enhancement of laminar mixing by optimal control methods. *Chemical Engineering Science*, **57**(14), 2719–2725.

Vishnampet, R. 2015. *An exact and consistent adjoint method for high-fidelity discretization of the compressible flow equations*. Ph.D. thesis, University of Illinois at Urbana-Champaign.

Vishnampet, R., Bodony, D. J., & Freund, J. B. 2015. A practical discrete-adjoint method for high-fidelity compressible turbulence simulations. *Journal of Computational Physics*, **285**, 173–192.

von Elbe, G., & Mentser, M. 1945. Further studies of the structure and stability of burner flames. *The Journal of Chemical Physics*, **13**(2), 89–100.

Wang, Q. 2013. Forward and adjoint sensitivity computation of chaotic dynamical systems. *Journal of Computational Physics*, **235**, 1–13.

Wang, Q., & Gao, J. H. 2013. The drag-adjoint field of a circular cylinder wake at Reynolds numbers 20, 100 and 500. *Journal of Fluid Mechanics*, **730**, 145–161.

Wang, Q., Duraisamy, K., Alonso, J. J., & Iaccarino, G. 2012. Risk assessment of scramjet unstart using adjoint-based sampling methods. *AIAA journal*, **50**(3), 581–592.

Wang, Q., Hu, R., & Blonigan, P. 2014. Least squares shadowing sensitivity analysis of chaotic limit cycle oscillations. *Journal of Computational Physics*, **267**, 210–224.

Wang, Z., He, P., Lv, Y., Zhou, J., Fan, J., & Cen, K. 2010a. Direct numerical simulation of subsonic round turbulent jet. *Flow, Turbulence and Combustion*, **84**(4), 669–686.

Wang, Z., Lv, Y., He, P., Zhou, J., & Cen, K. 2010b. Fully explicit implementation of direct numerical simulation for a transient near-field methane/air diffusion jet flame. *Computers and Fluids*, **39**(8), 1381–1389.

Wei, M., & Freund, J. B. 2006. A noise-controlled free shear flow. *Journal of Fluid Mechanics*, **546**, 123–152.

Wei, T., & Livescu, D. 2012. Late-time quadratic growth in single-mode Rayleigh–Taylor instability. *Physical Review E*, **86**(4), 046405.

White, J., Baurle, R., Fisher, T., Quinlan, J., & Black, W. 2012. Low-dissipation advection schemes designed for large eddy simulations of hypersonic propulsion systems. *Page 4263 of: 48th AIAA/ASME/SAE/ASEE Joint Propulsion Conference and Exhibit*.

Woosley, S. E., & Weaver, T. A. 1986. The physics of supernova explosions. *Annual Review of Astronomy and Astrophysics*, **24**(1), 205–253.

Xie, C. Y., Tao, J. J., Sun, Z. L., & Li, J. 2017. Retarding viscous Rayleigh–Taylor mixing by an optimized additional mode. *Physical Review E*, **95**(2), 023109.

Yamaleev, N. K., & Carpenter, M. H. 2009a. A systematic methodology for constructing high-order energy stable WENO schemes. *Journal of Computational Physics*, **228**(11), 4248–4272.

Yamaleev, N. K., & Carpenter, M. H. 2009b. Third-order energy stable WENO scheme. *Journal of Computational Physics*, **228**(8), 3025–3047.

Yang, S., Lew, J. K., & Mueller, M. E. 2019. Large eddy simulation of soot evolution in turbulent reacting flows: Presumed subfilter PDF model for soot–turbulence–chemistry interactions. *Combustion and Flame*, **209**, 200–213.

Youngs, D. L. 1984. Numerical simulation of turbulent mixing by Rayleigh–Taylor instability. *Physica D: Nonlinear Phenomena*, **12**(1-3), 32–44.

Youngs, D. L. 2003. Application of MILES to Rayleigh–Taylor and Richtmyer-Meshkov mixing. *Page 4102 of: 16th AIAA Computational Fluid Dynamics Conference*.

Youngs, D. L. 2009. Application of monotone integrated large eddy simulation to Rayleigh–Taylor mixing. *Philosophical Transactions of the Royal Society of London A: Mathematical, Physical and Engineering Sciences*, **367**(1899), 2971–2983.

Zhao, G. Y., Sun, M. B., & Pirozzoli, S. 2020. On shock sensors for hybrid compact/WENO schemes. *Computers and Fluids*, **199**, 104439.